Advanced Photodetector for Athlete Monitoring

Flavie Durand de Gevigney

Flavie Durand de Gevigney. Advanced Photodetector for Athlete Monitoring. Signal and Image Processing. INSA de Rennes, 2024. English. ⟨NNT : 2024ISAR0025⟩. ⟨tel-05577742⟩

HAL Id: tel-05577742
https://theses.hal.science/tel-05577742v1
Submitted on 2 Apr 2026

COLLEGE MATHS, TELECOMS
DOCTORAL INFORMATIQUE, SIGNAL
BRETAGNE SYSTEMES, ELECTRONIQUE

INSA INSTITUT NATIONAL
DES SCIENCES
APPLIQUÉES
RENNES

THÈSE DE DOCTORAT DE

L'INSTITUT NATIONAL DES
SCIENCES APPLIQUÉES DE RENNES

ÉCOLE DOCTORALE Nº 601
Mathématiques, Télécommunications, Informatique, Signal, Systèmes, Électronique
Spécialité : *AST*

Par
Flavie DURAND DE GEVIGNEY

Advanced Photodetector for Athlete Monitoring

Thèse présentée et soutenue à INSA, Rennes, le 12 décembre 2024
Unité de recherche : IETR
Thèse Nº : 24ISAR 27 / D24 - 27

Rapporteurs avant soutenance :

Sylvain FERUGLIO	Maitre de conférences, Lip6, Sorbonne Université
François BERRY	Professeur d'université, Institut Pascal, Université Clermont Auvergne et CNRS

Composition du Jury :

Président :	Yannick BENEZETH	Professeur d'université, ImViA, Université de Bourgogne
Examinateurs :	Taous-Meriem LALEG KIRATI	Chargé de recherche, INRIA, Université de Rennes
	Sylvain FERUGLIO	Maitre de conférences, Lip6, Sorbonne Université
	François BERRY	Professeur d'université, Institut Pascal, Université Clermont Auvergne et CNRS
Dir. de thèse :	Jean-François NEZAN	Professeur d'université, IETR, Université de Rennes
Encadrant :	Mickael DARDAILLON	Maitre de conférences, IETR, Université de Rennes

Invité(s) :

Slaheddine ARIDHI	Sensoria Analysis

REMERCICEMENTS

Je tiens à remercier mes encadrants, pour tous leurs conseils et leur soutien pendant mes années de thèse : Jeff, Mickael, Éric et Julien. Je remercie tout particulièrement Éric, pour tout le temps qu'il a consacré à se pencher sur le capteur avec moi, Jeff et Mickael pour leur précieuse aide. Merci aussi à tous les membres du labo IETR pour leur bienveillance. Je tiens également à remecier mes collègues de FOTON, et en particulier Thomas.

À Christophe, Pedro et Mouath, mes camarades de bureau, merci pour les tournées et votre amitié !

Merci à ma famille, pour avoir toujours soutenu que j'étais la plus belle, la plus intelligente et la plus forte. Vous aviez raison.

Enfin, merci à Elise d'exister, et encore mieux, d'exister à mes côtés.

TABLE OF CONTENTS

ACRONYMS

ABG arterial blood gas. 34

AC alternating current. 12, 13, 33, 34, 43, 44, 47, 58, 59, 65, 67, 79, 82–86, 89, 90, 95, 96, 105, 110, 112, *Glossary:* ac

ACG Accelerometer. 143

ADC Analog-to-Digital Converter. 43, 58–61, 79, 82–86, 124, 125, 148

AM Amplitude Modulation. 40, 124

BW Baseline Wander. 40, 124

DAC Digital-to-Analog Converter. 43

DC direct current. 6, 12, 20, 22, 43, 44, 47, 58, 59, 65, 67, 70–72, 82–85, 124, 147, *Glossary:* dc

DDR Double Data Rate. 60

DMA Direct Memory Access. 60

ECG Electrocardiography. 14, 31, 122–124, 143

EMG Electromyography. 143

EPFL École Polytechnique Fédérale de Lausanne. 51, 71, 142, 144, 148

ESL Embedded Systems Laboratory. 7, 15, 142, 143, 145

EV kit Evaluation kit. 43

FIFO First in, first out. 60

FM Frequency Modulation. 40, 124

FPGA Field Programmable Gate Arrays. 6, 12, 51, 52, 59, 60, 62, 64, 70–72

Hb Hemoglobin. 12, 35, 37, 131

HbCO Carboxyhemoglobin. 12, 35–37, 53, 121, 128, 132

HbO$_2$ Oxyhemoglobin. 12, 35, 37, 121, 131

HR Heart Rate. 14, 31, 33, 34, 42, 44, 123, 124
HRV Heart Rate Variation. 31–34, 42

IMU Inertial Measurement Unit. 143
IR Infrared. 43, 46, 53

KTE Kaiser-Teager Energy. 135, 137

LED Light-Emitting Diode. 5, 6, 12–14, 17–22, 27, 29, 36–38, 43, 45–49, 51–56, 58, 59, 61–63, 65–68, 70, 73, 74, 76–113, 115–117, 122, 124, 147, 148, 176

mARD Mean Absolute Relative Deviation. 16, 137–140
MCU Microcontroller Unit. 6, 71
MetHb Methemoglobin. 12, 35, 37, 53, 121, 128, 132
MSE Mean Squared Error. 16, 137, 138, 140

PI Perfusion Index. 15, 47, 48, 112, 176–182
PPG photoplethysmography. 6, 12, 14, 17–22, 25–27, 29–31, 33–36, 39–46, 48, 49, 51, 53, 63, 65, 69–74, 79, 87–89, 96–98, 105–108, 115, 117, 118, 121–126, 132, 133, 140, 142–144, 146–148, 190, *Glossary:* ppg
PRV Pulse Rate Variation. 33
PSD Power Spectral Density. 135–137
PWM Pulse Width Modulation. 13, 55, 73, 75, 76, 85, 86

RSA Respiratory Sinus Arrhythmia. 40
RSP Respiration. 143

SEI Signal Effect Index. 6, 14, 48, 111–119
SkT Skin Temperature. 143
SNR Signal-to-Noise Ratio. 15, 47, 48, 112, 176, 183–188
SPI Serial Peripheral Interface. 71, 160
SpO_2 Peripheral oxygen saturation. 7, 17–19, 21, 27, 29, 34, 36, 38, 42, 44, 121, 125–127, 129, 131, 132, 146, 147
SQI Signal Quality Index. 44
SVR Support Vector Regression. 137, 140, 141

GLOSSARY

ac Pulsed, alternating component of the signal. 12

dc Constant component of the signal. 6

dyshemoglobin Hemoglobin that doesn't participate to the transport of oxygen. 35, 36

ppg Optical technology to measure volume change in arterial blood. 6, 29

LIST OF FIGURES

LIST OF TABLES

RÉSUMÉ

Introduction

La technologie de la photopléthysmographie (PPG) est devenue un outil essentiel dans le domaine de la surveillance non invasive des paramètres physiologiques. Grâce à sa capacité à mesurer des signaux biologiques à travers des variations de l'absorption lumineuse dans les tissus, elle permet de suivre en temps réel des indicateurs tels que la fréquence cardiaque, la saturation en oxygène (SpO_2), et potentiellement le taux de glucose sanguin. Cependant, malgré les progrès réalisés, des défis persistent, notamment en termes de précision des mesures, de sensibilité aux interférences, et de calibration des capteurs en fonction des variations physiologiques individuelles.

Avec l'essor des dispositifs portables de santé, tels que les montres connectées et les trackers d'activité, la demande pour des technologies de mesure plus précises et plus fiables n'a jamais été aussi forte. Ces dispositifs, bien qu'efficaces pour le suivi quotidien des activités physiques et des paramètres de base, rencontrent souvent des limites lorsqu'il s'agit de fournir des données de haute précision nécessaires pour des applications médicales plus critiques. C'est dans ce contexte que se situe notre recherche, visant à développer un capteur PPG avancé capable de surmonter ces limitations et de répondre aux exigences croissantes des utilisateurs.

L'objectif principal de cette thèse est d'améliorer la qualité du signal PPG afin d'augmenter la précision des mesures des paramètres vitaux. Pour ce faire, nous avons exploré diverses approches, telles que la multiplication des longueurs d'onde utilisées, l'amélioration de la distance entre les LEDs et les photodétecteurs, et le développement d'algorithmes et d'électroniques d'autocalibration. Ces innovations ont pour but non seulement de perfectionner la précision des mesures, mais aussi de rendre le capteur plus adaptable aux environnements variés et aux caractéristiques individuelles des sujets testés.

État de l'art

L'état de l'art dans le domaine de la photopléthysmographie (PPG) révèle un large éventail de technologies et de méthodes utilisées pour la surveillance des paramètres physiologiques. Les dispositifs de mesure physiologique, tels que les capteurs PPG, sont largement utilisés pour suivre la fréquence cardiaque, la variabilité de la fréquence cardiaque, la saturation en oxygène (SpO_2). Ces dispositifs fonctionnent en capturant les variations de la lumière absorbée par les tissus cutanés, qui sont ensuite interprétées pour extraire des informations sur les paramètres vitaux.

Parmi les plateformes déjà disponibles sur le marché, on trouve les trackers d'activité et les montres connectées qui, bien qu'abordables et accessibles au grand public, présentent des limitations en termes de précision des données et d'accès aux données brutes pour une analyse plus poussée. D'autre part, des kits d'évaluation plus avancés offrent des capacités analytiques accrues et permettent, pour certains, un accès plus direct aux signaux PPG bruts, mais leur coût et leur complexité les rendent moins accessibles pour une utilisation quotidienne par le grand public et manquent aussi de paramétrisation pour pouvoir être pleinement utilisés dans le domaine scientifique.

La qualité des mesures PPG est un facteur critique qui dépend de plusieurs paramètres. La longueur d'onde de la lumière utilisée, la distance entre les LEDs et la photodiode, et la calibration de l'appareil jouent un rôle déterminant dans la précision des résultats obtenus. Le mode réflexion et transmission du PPG offrent des avantages et des inconvénients spécifiques en fonction du contexte d'application et doivent être choisi avec soin.

Enfin, les défis associés à la calibration des capteurs PPG sont peu explorés. La calibration doit être suffisamment efficace pour s'adapter aux variations individuelles des utilisateurs. La multiplicité des longueurs d'onde et l'optimisation de la distance entre les composants optiques sont également essentielles pour améliorer la qualité du signal et, par conséquent, la fiabilité des données biologiques ainsi collectées.

En résumé, l'état de l'art met en évidence les progrès réalisés dans le domaine des dispositifs PPG, tout en soulignant les défis techniques qui subsistent. L'objectif de cette thèse est l'amélioration de la précision des mesures, l'accès à la paramétrisation des paramètres et aux données brutes pour la communauté scientifique et l'amélioration de l'accessibilité des technologies PPG pour une utilisation à grande échelle, tant dans des contextes médicaux que grand public.

Description technique de la plateforme et de ses innovations

Dans le cadre de cette thèse, une plateforme expérimentale avancée a été développée pour surmonter les limitations des dispositifs PPG existants. Cette plateforme a été conçue avec une attention particulière à la portabilité, à la précision des mesures, et à l'intégration des fonctionnalités logicielles et matérielles.

La conception physique du capteur a fait l'objet d'une réflexion approfondie, aboutissant à une sonde optimisée pour capter les signaux PPG avec une sensibilité accrue. Le design de la sonde a été pensé pour inclure huit LEDs avec des longueurs d'onde différentes. Plusieurs sondes ont été créées afin de laisser le choix à l'utilisateur, afin que la sonde puisse répondre à ses besoins spécifiques.

Le développement électronique de la plateforme a inclus l'intégration du traitement de plusieurs longueurs d'onde, une fréquence d'échantillonnage élevé et une résolution augmentée. Ces caractéristiques permettent une analyse plus fine des signaux PPG, particulièrement pour la mesure de la saturation en oxygène (SpO_2) et d'autres paramètres hémodynamiques. La carte logique, quant à elle, a été choisie pour gérer efficacement l'acquisition de données, tout en étant suffisamment polyvalente pour supporter des algorithmes de traitement du signal embarqués.

Sur le plan logiciel, l'architecture développée vise à offrir une interface utilisateur intuitive tout en assurant des fonctionnalités avancées pour la paramétrisation, l'acquisition de mesures, la gestion des données et leur visualisation. Un cadre de paramétrisation flexible permet aux utilisateurs de configurer facilement les différents aspects du dispositif en fonction des besoins spécifiques des expériences ou des tests cliniques. L'acquisition des données et leur stockage ont été optimisés pour garantir la préservation de l'intégrité des signaux bruts, facilitant ainsi une analyse approfondie a posteriori.

Le logiciel prend également en charge plusieurs modes de fonctionnement, permettant de basculer entre différents types de mesures ou de conditions d'expérimentation. L'intégration de modules d'analyse et de visualisation des données permet aux chercheurs de tirer rapidement des conclusions à partir des données collectées, sans nécessiter de traitement externe complexe.

En résumé, la plateforme expérimentale développée dans cette thèse représente une avancée significative dans le domaine des dispositifs PPG. Elle combine une conception matérielle innovante avec des capacités logicielles avancées, offrant ainsi un outil puissant et versatile pour la recherche et le développement dans le domaine de la surveillance des paramètres physiologiques. Cette plateforme se distingue par sa capacité à capter des données de haute qualité, tout en étant adaptable à une grande variété de situations expérimentales et cliniques.

Amélioration de la qualité du signal

L'amélioration de la qualité du signal, avant la numérisation, est un aspect crucial pour maximiser la précision des mesures effectuées par les dispositifs de PPG. De plus cette approche est complémentaire avec celle qui consiste à améliorer le signal après la captation. Dans cette étude, plusieurs approches ont été explorées pour surmonter les défis de la technologie PPG, afin de garantir des résultats fiables et cohérents.

La première étape a consisté en la vérification du matériel, en examinant la relation linéaire entre la commande des LEDs et l'illumination produite. Cette vérification est essentielle pour assurer que les LEDs fonctionnent de manière optimale et génèrent un signal suffisamment fort pour être détecté par les photodétecteurs, sans introduire de distorsion ou de bruit dans les mesures.

Ensuite, une comparaison de la qualité du signal entre différentes générations de capteurs a été réalisée. Cette comparaison a permis d'identifier les améliorations apportées par les nouvelles conceptions et d'évaluer leur efficacité par rapport aux versions antérieures. Les résultats ont montré que les nouvelles générations de capteurs PPG offrent une qualité de signal supérieure, grâce à des optimisations tant au niveau du matériel que du logiciel.

L'une des innovations majeures de cette étude est l'introduction d'un système d'autocalibration pour déterminer les paramètres optimaux. Ce système permet d'ajuster automatiquement le niveau DC et le courant des LEDs, en fonction des conditions spécifiques de l'utilisateur et de l'environnement. Cette approche réduit les erreurs dues à une mauvaise calibration et améliore considérablement la précision des mesures.

Parallèlement, des simulations ont été menées pour déterminer la meilleure distance entre les LEDs et les photodiodes. Cette distance est un paramètre clé pour maximiser la sensibilité du capteur tout en minimisant les interférences et les artefacts. Les calculs effectués ont pris en compte les spécificités optiques des tissus humains, permettant d'optimiser le positionnement des composants optiques pour chaque configuration de capteur.

Enfin, une investigation expérimentale a été menée pour valider les résultats des simulations et affiner davantage la configuration du capteur. Les tests ont confirmé que l'optimisation de la distance entre les LEDs et les photodétecteurs améliore de manière significative la qualité du signal, rendant le capteur plus performant et plus fiable pour une large gamme d'applications.

En somme, cette étude a permis d'identifier et mettre en uvre plusieurs stratégies d'amélioration de la qualité du signal PPG, contribuant à la conception de dispositifs plus précis et plus adaptés aux besoins des utilisateurs, tant dans des environnements cliniques que pour un usage dans le domaine du sport.

Mesures physiologiques

La mesure des paramètres physiologiques à l'aide de la technologie de photopléthysmographie (PPG) est au cur de cette thèse, avec un accent particulier sur l'évaluation des paramètres cardio-respiratoires, de la concentration en hémoglobines, de la saturation périphérique en oxygène (SpO_2), ainsi que sur le potentiel de suivi du glucose sanguin.

Les paramètres cardio-respiratoires ont été évalués en utilisant les signaux PPG pour extraire des informations sur la fréquence cardiaque et la variabilité de celle-ci, ainsi que sur les motifs respiratoires. Les résultats obtenus valident l'utilisation de notre plateforme pour le suivi de ces indicateurs vitaux. Ces mesures permettent de mieux comprendre l'état de santé global et l'efficacité respiratoire des sujets testés.

En ce qui concerne la concentration en hémoglobines et la SpO_2, l'application des modèles basés sur la loi de Beer-Lambert a permis de démontrer la capacité de notre capteur à fournir des estimations précises de ces paramètres. Bien que les résultats obtenus ne soient pas encore comparés au standard de référence, ils sont encourageants et montrent que la plateforme pourrait être utilisée pour des évaluations fiables dans un contexte clinique ou sportif.

Le suivi du glucose à l'aide de la technologie PPG représente un défi important, en raison des complexités liées à l'optique des tissus et à la calibration des capteurs. Bien que les essais préliminaires réalisés aient montré des résultats prometteurs, des collectes de données sur une plus grande population sont nécessaires pour valider ceux-ci. Avec des expériences à plus grande échelle, il est possible que cette plateforme puisse être utilisée pour une surveillance non invasive du glucose, offrant ainsi une alternative aux méthodes invasives actuelles.

En résumé, cette section démontre le potentiel de la technologie PPG pour la mesure de divers paramètres physiologiques, en particulier dans les domaines de la santé cardiovasculaire et métabolique. Bien que certains aspects nécessitent encore des améliorations, les résultats obtenus jusqu'à présent suggèrent que notre plateforme pourrait jouer un rôle clé dans l'avenir de la surveillance médicale et sportive, en offrant des mesures précises, non invasives et adaptables aux besoins spécifiques des utilisateurs.

Conclusion et Perspectives

Au terme de cette thèse, les travaux réalisés ont permis de démontrer l'efficacité et le potentiel de la technologie PPG pour la mesure non invasive de divers paramètres physiologiques. La plateforme expérimentale développée se distingue par ses innovations tant matérielles que logicielles, permettant une amélioration significative de la qualité des signaux captés et, par conséquent, une plus grande précision des mesures obtenues.

L'amélioration de la qualité du signal PPG grâce à des stratégies telles que l'autocalibration des niveaux DC et l'optimisation de la distance entre les LEDs et les photodiodes a montré des résultats prometteurs. Ces avancées ont non seulement renforcé la fiabilité des mesures cardio-respiratoires et des concentrations d'hémoglobine, mais ont également ouvert la voie à des applications potentielles dans le suivi du glucose sanguin, bien que ce dernier domaine nécessite encore des recherches approfondies pour surmonter les défis restants.

Les perspectives offertes par ces travaux sont multiples. Dans un avenir proche, il est prévu de constituer un ensemble de données (dataset) en utilisant notre capteur ainsi que d'autres dispositifs comparables, afin d'enrichir la base de connaissances et d'améliorer encore les algorithmes de traitement des signaux PPG.

Les recherches se poursuivront dans le cadre d'un postdoctorat, avec un accent particulier sur l'acceptation de l'appareil par les utilisateurs, en tenant compte des besoins des personnes en situation de handicap, notamment dans le cadre de la chaire IH2A. Des tests seront effectués dans le domaine du handisport, avec pour objectif d'évaluer des paramètres tels que le stress et le glucose.

En parallèle, des collaborations avec des partenaires industriels comme *Innove* pourraient permettre d'intégrer la technologie de capteur dans leurs plateformes IoT pour le suivi sportif ou médical en temps réel.

Enfin, le programme EUR Digisport, qui a financé une partie de ce travail, a permis de développer une plateforme qui servira de base à des projets futurs, notamment avec des efforts de miniaturisation pour faciliter son adoption dans les domaines sportifs et médicaux.

INTRODUCTION

Context

In recent years, there has been a significant surge in the development and adoption of wearable devices designed to monitor health and athletic performance. These devices, which include fitness trackers, smartwatches, and specialized health monitoring equipment, have become increasingly popular among consumers and healthcare providers alike. They provide users with real-time data on various physiological parameters, such as heart rate, oxygen saturation, physical activity, and sleep quality, enabling individuals to make informed decisions about their health and wellness.

This trend is driven by several factors, including a growing public interest in personal health management, advances in wearable technology, and the increasing integration of digital health solutions into everyday life. The ability to monitor health metrics continuously and non-invasively is particularly appealing in the context of chronic disease management, early detection of health issues, and the optimization of athletic performance. As a result, the market for wearable health devices has expanded rapidly, with projections suggesting continued growth in the coming years.

One of the key technologies enabling these devices is PPG, an optical method used to detect blood volume changes in the microvascular bed of tissue. PPG sensors are widely used in wearable devices due to their ability to measure vital signs such as heart rate and blood oxygen levels with relative ease and accuracy.

The context of this research is set against this backdrop of increasing demand for advanced wearable health monitoring devices and the ongoing challenges faced by existing sensor technologies.

Motivation

As the demand for more sophisticated and accurate monitoring capabilities increases, there is a growing need to enhance the performance of PPG sensors.

Current PPG sensors face several challenges, including limitations in accuracy during physical activity, sensitivity to motion artifacts, and performance issues under varying environmental conditions. These challenges are particularly relevant in the context of sports and fitness, where accurate real-time data is crucial for monitoring performance and ensuring the safety of athletes. Moreover, as wearable devices become more compact and power-efficient, there is a pressing need for sensors that operates effectively under these constraints while maintaining high performance.

This thesis focuses on the development of a new advanced photodetector for PPG applications, aimed at improving the accuracy, reliability, and versatility of health monitoring devices. By addressing the limitations of current PPG technology, this research seeks to contribute to the evolution of wearable devices, enhancing their capability to monitor health and athletic performance in a wide range of settings.

The motivation behind this thesis is deeply inspired by collaborations with key partners who are at the forefront of innovation in sports technology and health monitoring. DIGISPORT, as a leading European University Research School, emphasizes the integration of sports science and digital technology, funding half of this research endeavor. Their commitment to advancing the application and effectiveness of digital technologies in sports reinforces the importance of this work in meeting the evolving demands of athletes, coaches, and the broader socio-economic context. Insiders, a Swiss sports technology company, empowers athletes and teams by providing high-precision data devices that enhance performance insights. Their focus on detailed performance metrics drives the need for innovative solutions to optimize training and competition strategies. Finally, Sensoria Analytics highlights the critical importance of cardiovascular health through their biomedical signal analysis. Their tools, such as CardioSensys, underscore the potential to detect cardiovascular risks early, thus preventing health issues and promoting overall well-being. Together, these organizations inspire the pursuit of a thesis that seeks to bridge the gap between advanced sensor technologies and practical applications in sports and health, ultimately contributing to improved athletic performance and health outcomes.

Objectives

The primary objectives of this thesis are focused on advancing the capabilities of PPG technology for wearable health monitoring devices. Specifically, the research aims to:

— Enhance the quality of the PPG signal by developing a new dedicated hardware.

— Develop an adaptive sensor technology that dynamically adjust to varying environmental conditions and individual user characteristics, optimizing the accuracy and reliability of the sensor across diverse scenarios.

- Evaluate new biological parameters, for example the concentration of dyshemoglobins (such as carboxyhemoglobin and methemoglobin), through enhanced PPG sensor technology, ensuring more accurate assessments of SpO_2 and related vital parameters.
- Validate the performance of the platform created through extensive testing, ensuring its effectiveness in accurately measuring a large variety of physiological parameters.

Outline

This thesis is organized into five main chapters, each building upon the previous to provide a comprehensive exploration of the development and enhancement of an advanced photodetector for wearable health monitoring devices, with a particular focus on improving the precision of physiological measurements.

The first chapter, **State-of-the-Art**, provides a thorough review of the current technologies and methodologies used in wearable health monitoring, with an emphasis on PPG sensors. It begins with an introduction to the physiological measurements relevant to PPG, including cardiac rhythm, oxygen saturation, and glucose levels. The chapter then discusses the commercially available platforms, such as activity trackers and smartwatches, highlighting their capabilities and limitations. Finally, the chapter examines key factors that influence the quality of PPG signals, including the type of PPG used (reflected vs. transmitted), calibration methods, wavelength selection, and the distance between the photodetector and LEDs.

The second chapter, **Developed Experimental Platform**, outlines the design and development of the experimental platform used for this research. It details the physical platform, including probe design, electronic components, and logic board, as well as the software architecture and functionalities. The software discussion covers the parametrization framework, measurement and data acquisition processes, data management and storage, operating modes, and the tools used for data analysis and visualization. Finally, the platform's evolution and the key insights gained throughout its development are thoroughly examined. This chapter provides the foundational technical framework upon which the subsequent experiments and investigations are based.

In third chapter, **Study for Enhancement of the Signal Quality**, the focus shifts to improving the quality of the PPG signal. It begins with material verification, examining the relationship between LED command signals and the resulting illumination quality. The chapter then explores the development of an auto-calibration mechanism designed to optimize the sensor's operating parameters. Following this, simulations are presented to determine the best distance between the LEDs and photodiode, which is crucial for maximizing signal quality. The chapter concludes with an experimental investigation aimed at refining this distance, providing insights into the optimal configuration for the PPG sensor.

The fourth chapter, **Measures of Physiological Parameters**, presents the methods and results of measuring key physiological parameters using the developed PPG sensor. It starts with an analysis of cardio-respiratory parameters, such as heart rate and breathing patterns. The chapter then delves into the measurement of hemoglobin concentrations and peripheral oxygen saturation (SpO2), including a review of the Beer-Lambert Law and its application in this context. Lastly, the chapter discusses the protocols and results related to glucose measurement, demonstrating the sensor's capabilities across a range of physiological metrics.

The final chapter, **Conclusion and Future Work**, summarizes the key findings of the thesis, highlighting the advancements made in the development and optimization of the PPG sensor. It also discusses the implications of these findings for wearable health monitoring technology and outlines potential directions for future research, including further enhancements to sensor accuracy, the integration of additional physiological measurements, and the exploration of new application areas for the technology.

Chapter 1

STATE-OF-THE-ART

1.1 Introduction

Understanding the Mechanics of PPG The etymology of photoplethysmography (PPG) reveals its essence: "photo" for light, "plethysmo" for changes in volume, and "graphy" for measurement or recording. Therefore, at its core, photoplethysmography involves using light to measure changes in volume, particularly in blood, offering insights into vascular dynamics and physiology. The PPG is a non-invasive optical technique used to detect blood volume changes in tissue microvasculature. It operates on the principle of light absorption by blood.

In PPG, a light source, typically a LED emitting red or infrared light, is directed into the tissue. This light interacts with tissue components, including melanin, water, and hemoglobin. Indeed, the hemoglobin, the oxygen-carrying protein in red blood cells, absorbs light differently depending on its oxygenation state.

A photodetector placed a few millimeters apart from a light source detects the light that is transmitted or reflected from the tissue. This detected signal is processed to isolate the pulsatile component corresponding to changes in blood volume with each heartbeat, as shown in Figure 1.1. The waveform of a PPG signal displays characteristic peaks and troughs corresponding to the cardiac cycle.

By analyzing the PPG signal, various physiological parameters can be inferred, such as heart rate, arterial oxygen saturation (SpO_2), and glucose level. It is for its versatility that the PPG is widely used in clinical settings for, among other things, cardiovascular monitoring.

Additionally, this technique finds integration into wearable devices, enabling continuous monitoring of vital signs. This advancement extends its utility beyond clinical settings to applications in sports and fitness, providing real-time insights into physiological parameters during physical activity without the constraints of traditional monitoring systems such as the lack of availability outside the medical setting or the difficulty to use.

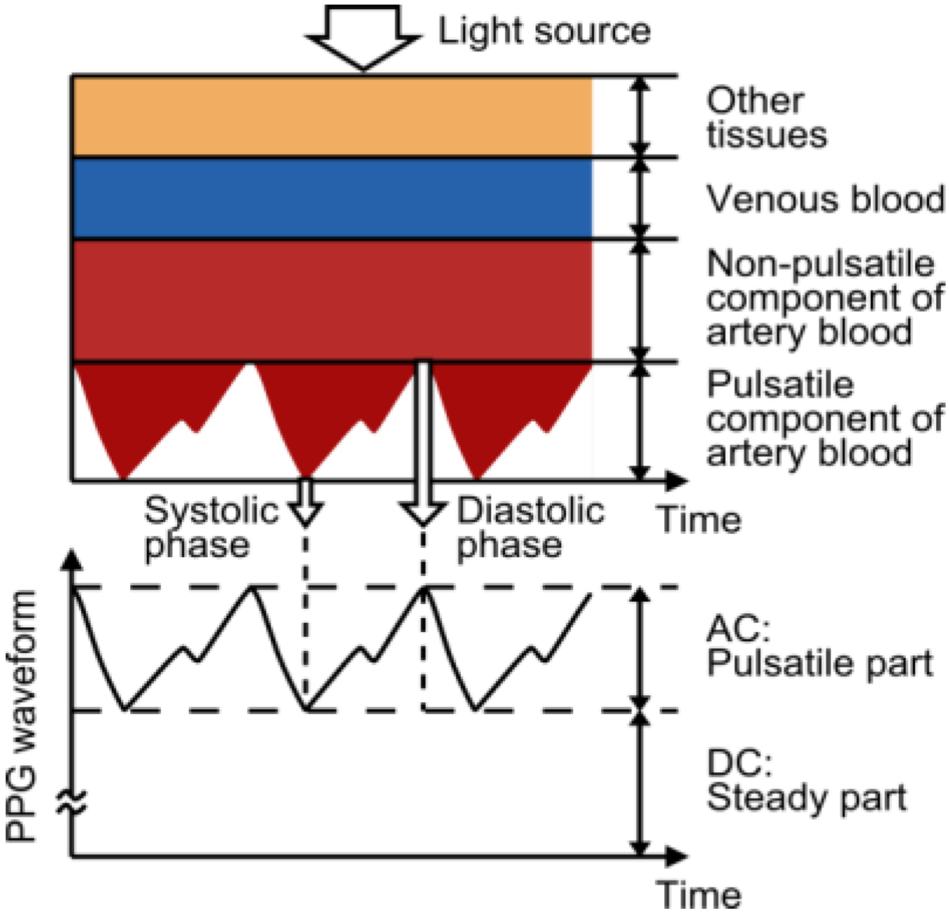

Figure 1.1 – Variation in light attenuation by tissue [47]

1.2 Physiological Measurements

In this section, we'll explore how PPG technology helps measure various aspects of physiology. From tracking heart rhythm and oxygen levels to observing breathing patterns and glucose levels, PPG provides convenient, real-time insights into the body's workings. Indeed, the information that can be extracted from a PPG signal go way beyond simply the heart rate [15]. We'll also discuss the basic principles, practical uses, clinical implications, and common challenges associated with this technology.

1.2.1 Cardiac Rhythm and Variability

PPG technology plays a significant role in monitoring cardiac rhythm and variability. When the heart pumps blood, each contraction of the heart causes an increase in the amount of blood in the capillaries in the skin's surface, resulting in more light absorption. The blood then travels back to the heart through the venous network, leading to a decrease of blood volume in the surface capillaries, resulting in less light absorption as showed in Figure 1.1 [47].

As monitoring heart health is crucial for assessing overall well-being, various technologies are employed to measure HR and Heart Rate Variation (HRV). The most well-known and gold standard method is the ECG, which relies on detecting the electrical activity of the heart. While highly accurate, ECG systems often require electrode placement on the skin and is cumbersome or uncomfortable for continuous use. Another method, the phonocardiography, is based on capturing the sounds produced by the heart with each beat. However, phonocardiography is affected by external noise and may not provide the same level of detail as ECG. In contrast, PPG offers a more convenient and non-invasive alternative. PPG can be integrated into wearable devices such as smartwatches and fitness trackers, providing continuous heart rate monitoring without the need for electrode placement or cumbersome equipment. The correspondence between the different technologies is shown in Figure 1.2.

In the atrial pressure plot: wave "a" corresponds to atrial contraction, wave "c" corresponds to an increase in pressure from the mitral valve bulging into the atrium after closure, and wave "v" corresponds to passive atrial filling.

In the electrocardiogram: wave "P" corresponds to atrial depolarization, waves "QRS" correspond to ventricular depolarization, and wave "T" corresponds to ventricular repolarization.

In the phonocardiogram: The sound labeled 1st contributes to the S1 heart sound and is the reverberation of blood from the sudden closure of the mitral valve (left A-V valve) and the sound labeled "2nd" contributes to the S2 heart sound and is the reverberation of blood from the sudden closure of the aortic valve.

It's important to note that both HR and HRV offer valuable insights into cardiovascular health. While HR provides a straightforward measure of the number of heartbeats per minute, HRV delves deeper by quantifying the variation between these beats. This distinction is particularly relevant in sports, where HRV is monitored to assess the body's stress levels during exercise and recovery afterward. The HRV feature is used to analyze

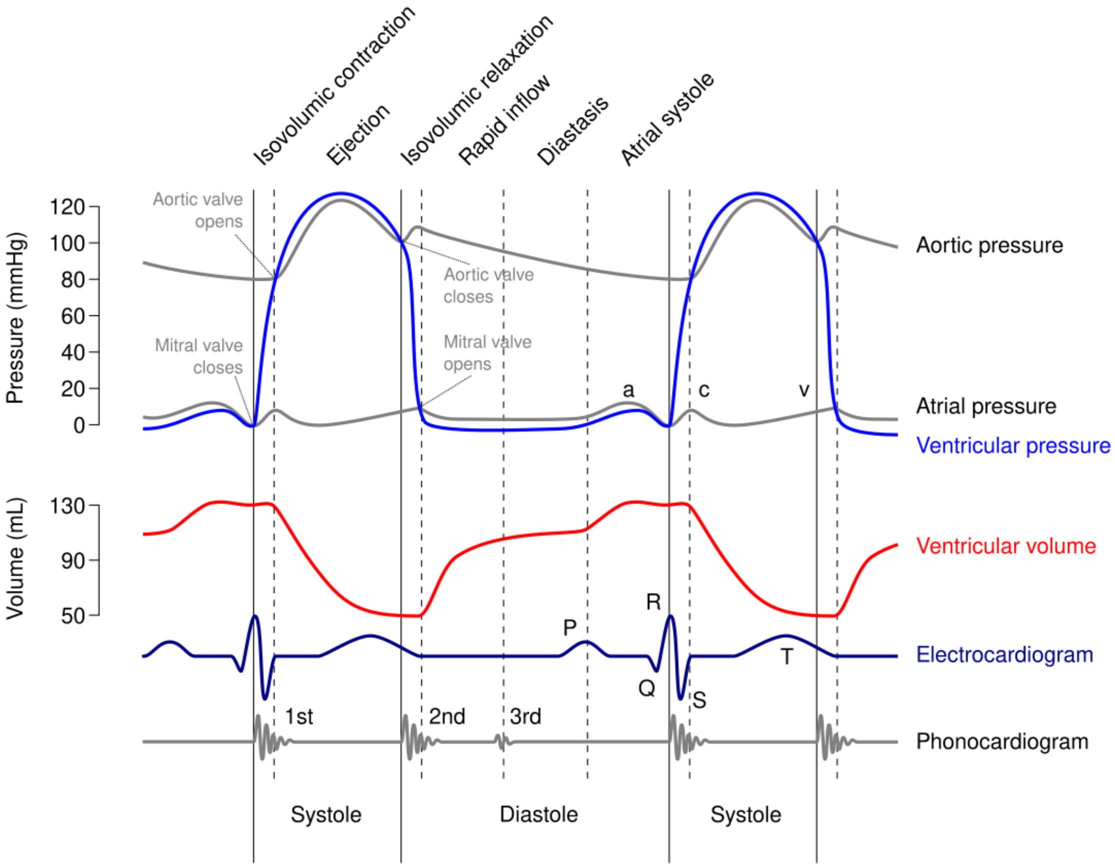

Figure 1.2 – A Wiggers diagram, showing the cardiac cycle events occurring in the left ventricle [17].

the stress the body experiences during training and to gain insight into physiological recovery after training. Information regarding the extent to which the body recovers after training provides useful data for the personalization of sports training, training loads, and recovery time. HRV monitoring of athletes is frequently applied to the prevention and diagnosis of overtraining syndrome [27].

HRV serves as a significant indicator of cardiac regulation influenced by both sympathetic and vagal branches of the autonomic nervous system (ANS). While traditionally HRV is linked to predicting sudden cardiac death and evaluating the progression of cardiovascular and metabolic diseases, recent studies have highlighted its potential in the context of physical exercise training. HRV is increasingly recognized as a valuable tool for monitoring the progression of training adaptation or maladaptation in athletes and for determining optimal training loads to enhance performance. Despite this, there is limited understanding of the role of HRV and the internal impacts of physical exercise on athletes, which could be beneficial for designing fitness programs that ensure adequate training loads tailored to an athlete's specific capabilities [10].

It is also interesting to note that the Pulse Rate Variation (PRV), which is obtained with the PPG signal, is sometimes considered correlated enough to the heart rate to be used for its evaluation [42, 23, 7]. Occasionally, it is regarded as a closely related parameter that provides additional information. For example, research has shown that the relationship between HRV and PRV is not yet fully understood, and that PRV may be influenced not only by technical aspects, but also by physiological factors that may affect the measurements obtained from the pulse-to-pulse time series extracted from pulse waves [29]. Consequently, PRV should not be considered a valid substitute for HRV in all scenarios, and care should be taken if the two are to be used interchangeably.

A PPG signal and its components are shown in Figure 1.3.

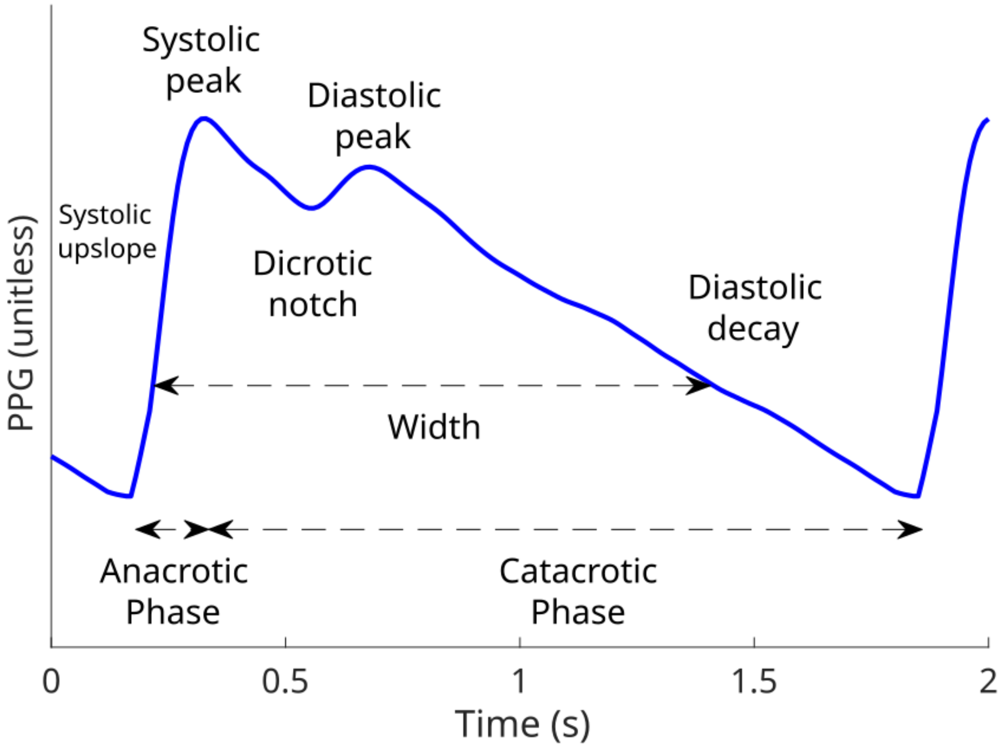

Figure 1.3 – Typical PPG signal and its components.

The HR and HRV computation accuracy is tied to the AC component of the captured

PPG signal as it is in this component that lies the information about the HR. Indeed, the simplest method for the evaluation of the HR and thus the HRV, is to identify the peaks of the PPG signal, that are contained in the AC part of the signal. The peaks of the signal correspond to a heart beat, and the time measured between two of them give the instantaneous heart rate. A demonstration of this technique is done in Section 4.2. High sample rate and high quantization accuracy of the signal are necessary for this metric.

1.2.2 Oxygen Saturation and Hemoglobin Variants

While HR is a vital aspect of monitoring an athlete's condition, it is equally important to consider other parameters, such as SpO_2. SpO_2 levels provide insights into how effectively the lungs are delivering oxygen to the bloodstream, which is crucial for muscle function and endurance during physical activity. Maintaining optimal SpO_2 is essential for ensuring that muscles receive the oxygen they need to perform efficiently, thereby supporting peak athletic performance.

Next, we consider how PPG technology is utilized to monitor oxygen saturation and the different hemoglobin variants in the blood. The control of human body oxygenation is crucial for assessing the health status of individuals. Adequate monitoring helps prevent serious respiratory issues often caused by infections. Pulse oximeters, that use the PPG technologies, are devices that measure blood oxygen saturation, are widely used in the medical field as they present several advantages over the gold standard method, the arterial blood gas (ABG) analysis.

ABG analysis requires a blood sample taken directly from an artery, which is a more invasive procedure compared to pulse oximetry. The arterial puncture needed for ABG can be painful and uncomfortable for the patient. It is also associated with a risk of complications such as bruising, bleeding, and, in rare cases, arterial injury. This is avoided when using a PPG since it is a non-invasive technology, making it more comfortable and safer for the patient. The process of drawing arterial blood and analyzing it takes more time compared to the almost instantaneous reading provided by a pulse oximeter. ABG sampling and interpretation require trained healthcare professionals. PPG are easy to use and can be operated by a wider range of people. ABG analysis involves more resources and higher costs, including the need for specialized equipment and personnel. In contrast, pulse oximetry is generally less expensive and requires minimal equipment. ABG cannot be performed continuously and is typically done intermittently, providing a snapshot of the patient's status rather than continuous monitoring. Pulse oximeters, however, provides continuous, real-time monitoring of oxygen saturation.

The use of the PPG technology has also extended to the sports domain for monitoring athletes' respiration during physical exertion. In the context of athletic training, monitoring blood oxygen saturation during exertion allows for better control of effort. The use of a pulse oximeter enables tracking oxygen supply during intense effort, allowing adjustments in critical situations to maintain speed, endurance, and efficiency. Additionally, a pulse oximeter can help prevent hypoxia, resulting from poor respiration, during training.

For athletes training at high altitudes, where oxygen levels are significantly reduced, PPG technology becomes even more valuable. Monitoring SpO2 in these conditions allows athletes and trainers to better adapt training intensity and recovery strategies, preventing altitude sickness and optimizing performance through altitude adaptation. This insight into blood oxygen saturation helps manage the body's acclimatization process, crucial for endurance athletes aiming to improve performance under low-oxygen environments.

Oxygenation monitoring is carried out by studying the arterial proteins responsible for oxygen transport: Hemoglobin (Hb). There are primarily four types of hemoglobins in the human body:

- Oxyhemoglobin (HbO_2)
- Reduced Hemoglobin, (RHb)
- Methemoglobin (MetHb)
- Carboxyhemoglobin (HbCO)

The first two types, Oxyhemoglobin (HbO_2) and reduced hemoglobin (RHb), are responsible for oxygen transport in the blood and are related by the following formula 1.1:

$$O_2 + RHb = HbO_2 \tag{1.1}$$

Methemoglobin and Carboxyhemoglobin do not participate in oxygen transport and are referred to as dyshemoglobin. However, elevated levels of these dyshemoglobin in the blood can lead to health problems. Rapid and non-invasive monitoring of their concentrations would allow for an initial diagnosis of the issue.

Methemoglobin forms naturally through the oxidation of iron atoms present in hemoglobin molecules, preventing oxygen binding. Thus, it is naturally present in small quantities in human blood. Elevated levels of MetHb, known as methemoglobinemia, can result from exposure to certain chemicals, medications (such as nitrates or local anesthetics), or genetic conditions. This condition decreases the blood's ability to deliver oxygen, leading to symptoms such as cyanosis, dizziness, and in severe cases, death.

Carboxyhemoglobin, on the other hand, forms when carbon monoxide is inhaled. Carbon monoxide binds more easily to hemoglobin, preventing oxygen transport and potentially leading to poisoning. In non-smokers, normal Carboxyhemoglobin levels are below 2%. Elevated levels of HbCO are dangerous, as they can result in carbon monoxide poisoning. Carbon monoxide detectors, often found in home alarms, are used to monitor and alert to dangerous levels of this gas, which can otherwise be fatal.

However, current oximeters have significant limitations. They use only two wavelengths and rely on a calibration-based model to provide results. Therefore, they cannot detect the presence of dyshemoglobins, and in cases of high dyshemoglobin concentration, the calculated saturation value may be incorrect. Moreover, these devices are sensitive to movement, which distorts measurements, particularly during training.

The oxygenation level of blood can be inferred from the PPG signal. This is because each type of hemoglobin exhibits a distinct absorption pattern, in particular the oxygenated hemoglobin compared to deoxygenated hemoglobin, as showed in Figure 1.4.

Typically, other hemoglobin types are disregarded, as their presence in the blood is minimal under normal conditions. The determination of SpO_2 levels via light absorption follows the Beer-Lambert Law, as in Equation 1.2. This law states that the concentration of a solute dissolved in a clear solvent is determined by transmitting light of a known wavelength through the solution.

$$A = \epsilon \cdot c \cdot l \tag{1.2}$$

where:

A = Absorbance

ϵ = Molar absorptivity (extinction coefficient)

c = Concentration of the solution

l = Path length of the light through the solution

One of the method to find SpO_2 is the method with the LED calibration [3]. The ratio called red over infrared is calculated, it is the ratio of the amplitude of signal obtain when emitting with the red LED (divided by its constant component) over the amplitude of the infrared one (divided by its constant component), as in equation 1.3. This value is than adjusted by an empirical linear equation to get the SpO_2 level. The parameters a and b

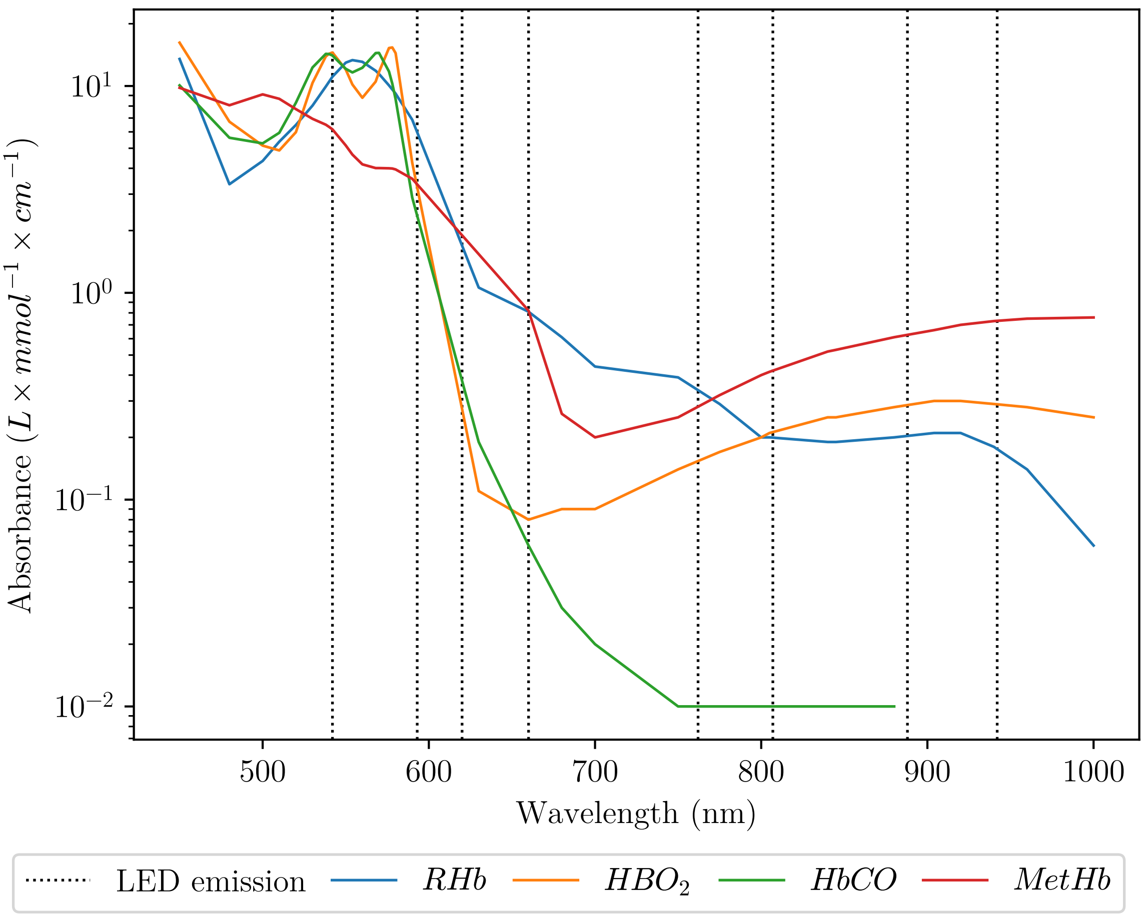

Figure 1.4 – Absorbance of Hb, HbO_2, HbCO, MetHb as tabulated in [52] and wavelength of the LEDs chosen for the platform.

of Equation 1.4 are found by calibration [3].

$$r = \frac{(AC/DC)_{red}}{(AC/DC)_{infra}} \tag{1.3}$$

$$SpO_2 = \frac{(AC/DC)_{red}}{(AC/DC)_{infra}} * a - b \tag{1.4}$$

The primary method for calibrating pulse oximeters involves using reference measurements of oxygen saturation. A group of volunteers or patients is used to collect data. The data collected is used to perform a regression analysis. The empirical data is fitted to a curve that relates the measured absorbance ratios (from the red and infrared LEDs in the oximeter) to the actual oxygen saturation levels. The fitted curve is then translated into an algorithm that the pulse oximeter's software uses to convert raw sensor data into accurate SpO_2 readings. Consequently, each pulse oximeter manufacturer have its own calibration curves depending on the group of volunteers tested [43].

A second method is the calibration free method [43], it allows the SpO_2 calculation to be independent of the patient and the LEDs used. The absorption coefficients of the different hemoglobin is used, in addition of the slope of the curve before the peaks and the value of the peaks. These values must be precise. Therefore, it is crucial to obtain the highest quality signal possible to facilitate accurate extraction. This method has the advantage to be independent of the patient related differences and of the LEDs specificity.

There are some limits to the calibration free methods [36]. One of the calibration free methods neglect the difference in path lengths of the different wavelengths. This can only be done if the wavelengths are close [26, 37, 51].

The interpretation of hemoglobin levels in athletes should be approached with caution due to the possibility of what is called sports anemia [13]. Endurance athletes, in particular, tend to have lower hemoglobin levels compared to normal values in the general population. Since anemia is characterized by low hemoglobin levels, this phenomenon is referred to as sports anemia.

However, this term is not entirely accurate. For most athletes, especially males, the low hemoglobin level is a false anemia. The total red blood cell volume remains normal. The hemoglobin level decreases because aerobic exercise increases the baseline plasma volume, diluting the concentration of red blood cells, which contain hemoglobin. In other words, the naturally lower hemoglobin level in endurance athletes is a dilutional pseudo-anemia.

Pseudo-anemia is an adaptation to the hemoconcentration that occurs during training. Vigorous exercise significantly reduces plasma volume by 10 to 20% in three ways. First, increased blood pressure and muscle compression of venules raise fluid pressure in the capillaries of the active muscles. Second, the release of lactic acid and other metabolites in the muscles increases tissue osmotic pressure. These forces move plasma fluid from the blood to the tissues, but not the red blood cells. Finally, some plasma water is lost through sweating.

In response, renin, aldosterone, and vasopressin are released to conserve water and salt. Albumin is also added to the blood. Consequently, the baseline plasma volume increases. A single intense exercise session can increase plasma volume by 10% within 24 hours.

Pseudo-anemia is key to aerobic capacity. An increased plasma volume, coupled with the athlete's heart adaptation, enhances stroke volume, which more than compensates for the reduced hemoglobin concentration per blood unit. As a result, more oxygen is delivered to the muscles, leading to improved athletic performance.

Despite these complexities, monitoring hemoglobin levels still provides valuable insights into an athlete's physiological status and the progression of their training regimen.

1.2.3 Breathing Patterns

Understanding the nuances of hemoglobin levels and pseudo-anemia in athletes and patients is essential for evaluating their overall health and performance. Equally important is the detection of breathing patterns, which can offer critical insights into a person's respiratory health and endurance capabilities.

Measuring the breathing rate is of significant interest in both medical and sports settings due to its crucial role in assessing respiratory and overall health. In medical contexts, the breathing rate serves as an early indicator of respiratory distress or dysfunction, aiding in the diagnosis and management of conditions such as adverse cardiac events, pneumonia, and clinical deterioration [34]. Regular monitoring allows for timely interventions, improving patient outcomes. In sports settings, an athlete's breathing rate provides valuable information about their respiratory efficiency and aerobic capacity. It helps in optimizing training regimens, preventing overtraining, and enhancing performance. Furthermore, understanding breathing patterns aids in the development of personalized training programs that maximize oxygen intake and utilization, crucial for endurance sports [32]. Hence, accurate measurement of breathing rate is a vital tool for both medical professionals and sports scientists aiming to ensure health and improve performance.

Breathing patterns provide vital health information and are another critical parameter monitored using PPG technology. There are two different types of methods to obtain these parameters, the firsts are the direct methods and the seconds are indirect. The direct methods directly measure the breathing intake and outtake, those methods are precise and don't rely on other parameters to determine the breathing patterns, but they required invasive device such as a mask. The indirect methods, such as band that are designed to count the chest expansion and contraction, are less invasive because they can be integrated in clothes but are negatively impacted by movement in particular during sleep [45]. Another way to get these parameters is to manually count the chest expansion and contraction, this method is both unreliable and labor-intensive. The PPG on the other hand are already used in both medical and sport settings, they are non-invasive, low-cost, and are used to evaluate reliably this parameter.

Breathing pattern presents a unique challenge in PPG signal processing, as it manifests both as a signal of interest and as background noise.

The respiratory cycle, along with synaptic nerve activity, introduces fluctuations in the signal, complicating analysis alongside other measurements. However, this interference offers an opportunity to extract valuable data, notably the breathing rate [8].

Actually, physiologic effects related to respiratory activity and cardiac cycle induce several modulations of PPG. Albeit not fully understood, the mechanism mainly consists of three modulations that can briefly be described as follows:

- Baseline Wander (BW): also known as respiratory induced intensity variation. In fact, respiration causes blood volume fluctuations in the peripheral vascular bed. The intrathoracic pressure variate as a result of a change in the blood volume and contribution from abdominal and thoracic muscles. This fluctuation induces exchange of blood between the pulmonary and the systemic circulations. This results in a variation of the perfusion baseline [35].
- Amplitude Modulation (AM): also known as respiratory induced amplitude variation. PPG amplitude is also affected by the respiratory rate: it decreases with increased respiratory rate due to variation in peripheral pulse strength [31].
- Frequency Modulation (FM): also known as respiratory induced frequency variation. Heart rate changes induced by respiratory activity is known as Respiratory Sinus Arrhythmia (RSA). In fact, the heart rate increases during inspiration and decreases during expiration [5].

The different modulations are illustrated in Figure 1.5.

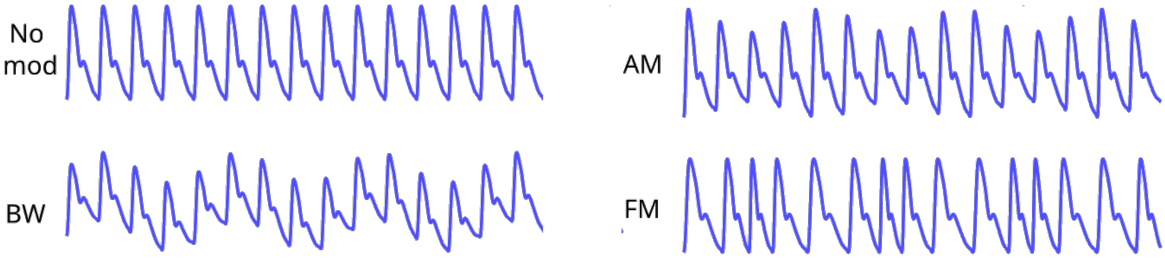

Figure 1.5 – Different modulations in the PPG signal induced by breathing.

Understanding and monitoring breathing rate is essential for assessing respiratory efficiency and overall health.

1.2.4 Blood Glucose Monitoring

Equally critical in both medical and athletic contexts is the monitoring of blood glucose levels. Blood glucose monitoring provides valuable insights into metabolic health, energy utilization, and the management of conditions such as diabetes. In this Subsection, we explore the potential of PPG technology in non-invasive blood glucose monitoring.

Glucose monitoring using PPG is a promising avenue in non-invasive glucose monitoring. The basic principle involves detecting changes in the optical properties of tissue caused by variations in blood glucose levels [44, 49, 21].

When glucose levels change in the blood, it alters the refractive index and scattering properties of tissue, affecting how light propagates through it. PPG sensors detect these changes by analyzing the intensity of light reflected or transmitted through the tissue.

Using PPG for glucose monitoring offers several distinct advantages. One key advantage is its non-invasive nature, eliminating the need for painful finger pricks associated with traditional glucose monitoring methods. This makes PPG-based glucose monitoring more comfortable and convenient, particularly for individuals who require frequent glucose measurements throughout the day. Moreover, PPG sensors can potentially provide continuous glucose monitoring, allowing for real-time tracking of glucose levels without the need for frequent sensor replacements. Additionally, PPG sensors are often integrated into wearable devices, offering the potential for seamless and unobtrusive glucose monitoring in everyday life. These advantages highlight the potential of PPG-based glucose monitoring to improve patient compliance and overall quality of life for individuals with diabetes.

However, despite its potential, optical glucose sensing via PPG faces several limitations and challenges:

- Achieving accurate glucose measurements remains a significant challenge due to the complex and dynamic nature of tissue optics. Factors like tissue hydration, temperature variations, and motion artifacts affect measurement accuracy.
- PPG-based glucose sensors require robust calibration procedures to establish a correlation between the measured optical signals and actual glucose levels. Calibration must account for individual differences in tissue properties and sensor placement.
- Signal interference from ambient light, motion artifacts, and physiological noise degrade the accuracy and reliability of glucose measurements. Advanced signal processing techniques are necessary to mitigate these sources of interference.
- Wearable PPG-based glucose monitoring devices must be user-friendly, comfortable

to wear, and unobtrusive. Ensuring user acceptance and compliance with continuous monitoring requires addressing issues related to device size, battery life, and data privacy.

In summary, while optical glucose sensing using PPG holds promise for non-invasive glucose monitoring, addressing these limitations and challenges is crucial. Continued research and technological advancements are needed to improve the accuracy, reliability, and user experience of PPG-based glucose monitoring devices.

1.3 Already commercially available platforms

This section surveys some available devices used to extract and study PPG signals. Several technologies are categorized depending on the intended use. Whilst most of these devices allow the visualization, storage, and extraction of parameters from the PPG signal, they offer limited possibilities for additional data extraction and novel signal processing algorithms.

Platforms that allow experimental analysis should be able to make comparisons of different algorithms. Commercial solutions generally do not disclose the details of their hardware and software. From our perspective, existing PPG devices can be categorized in packaged solutions and evaluation systems.

1.3.1 Activities trackers and smartwatches

Nowadays, activity trackers and smartwatches embed PPG sensors to perform HR analysis and SpO_2 measurements. The raw data measured by these devices are generally not accessible by the user; the user only has access to the compiled data (mean, max, or min) or even proprietary analysis including sleep analysis or stress level. These devices are dedicated to consumer applications and do not allow for advanced analysis required for research projects. Despite the acceptable accuracy of the displayed metrics (such as HR, HRV, SpO_2, RR interval, etc...), further analysis is impossible due to inaccessibility of the raw data [46].

1.3.2 Evaluation kits

Some chip manufacturers and companies propose kits for developing projects and applications using physiological sensors. As an example of dedicated company, BITalino proposes a handy plug and play system that allows many physiological measurements [6]. While these kinds of devices are useful to develop projects in a limited time, the performance of sensors are limited to commercial sensor performance, i.e. 500Hz sample rate with 2 or 3 wavelengths. Moreover, they do not allow tuning of all the different building blocks needed for PPG signal acquisition and analysis.

The MAX30101 Evaluation kit (EV kit) from Maxim Integrated allows the evaluation of the MAX30101, which is an integrated pulse oximetry and heart-rate monitor integrated circuit. The MAX30101 includes internal LEDs (green, red and Infrared (IR)), a photodetector together with low-noise electronics including ambient light rejection and digital filtering. The MAX30101 EV kit monitors and stores the recorded PPG signals while allowing the user to modify the sampling rate (up to 3200 Hz), LED currents, and pulse widths. This EV kit board allows the user to fully exploit the MAX30101, which is a 3-wavelengths sensor.

Similarly, the AFE44x0SpO 2 EVM from Texas Instruments is another kit intended for evaluating AFE4400 and AFE4490 devices. The AFE4490 is a complete analog front-end solution targeted for pulse-oximeter applications. The device consists of a low-noise receiver channel, a LED transmit section, and diagnostics for sensor and LED fault detection. The software of the AFE44x0SpO 2 EVM includes a GUI that allows the configuration of the I-V amplifier, the ambient light cancellation Digital-to-Analog Converter (DAC), the analog filtering, the Analog-to-Digital Converter (ADC) sampling and LED pulse and intensity, among many other parameters. This is a very complete evaluation system with highly configurable capabilities that unfortunately only allows two wavelengths.

To the author knowledge, there were no platforms that allow the exploration of multiple signals, higher frequency and higher resolution with respect to the quality of the PPG acquisition at the beginning of this thesis in 2021.

1.4 Quality

As the use of PPG technology continues to grow, it becomes increasingly important to evaluate and enhance the quality of the signal. This is particularly crucial because the PPG signal is prone to noise, which affect its accuracy. Additionally, improving signal quality is essential since PPG is used to assess a variety of biomarkers, providing valuable insights into cardiovascular and overall health.

As shown on Figure 1.1, the signal is decomposed in two parts, the DC and AC.

Each part contains useful information and is used to compute physiological features. To calculate certain biomarkers, it is necessary to have a precise value for the DC and the AC. For example, the extraction of the breathing rhythm is done using either the DC and the AC (to get the best estimation, both should be taken into account), the HR is measured using only the AC and lastly the SpO_2 need the AC and DC together A particular attention should be given to the acquisition of the AC component because its amplitude represents only about 5% of the constant component, as represented in Figure 1.6.

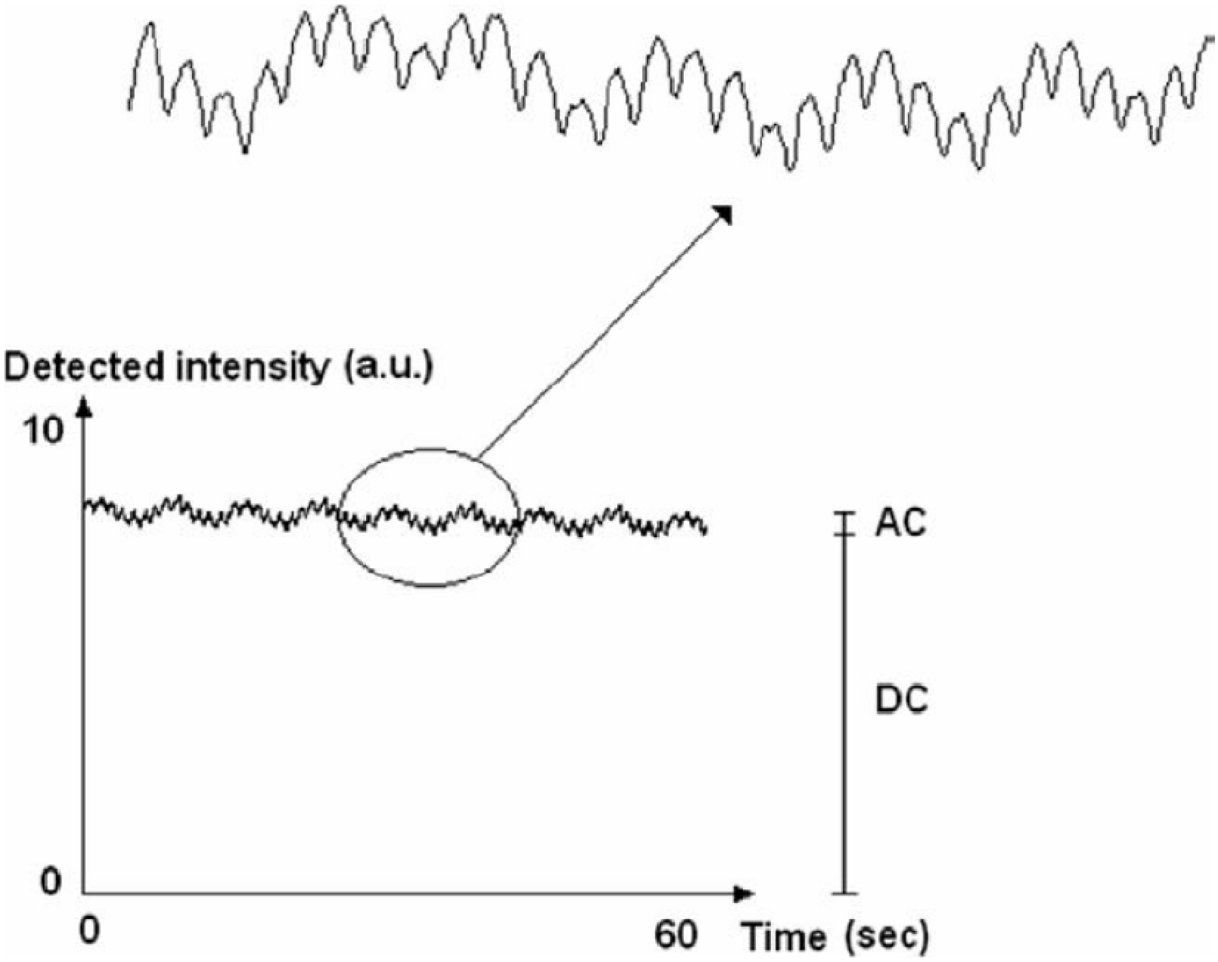

Figure 1.6 – Illustration of the ratio between the AC and the DC component in a PPG signal [18].

There are different Signal Quality Indexes (SQIs), that are used to classify the signal quality [14]. The following are particularly noteworthy:

— perfusion

- kurtosis
- skewness
- relative power
- non-stationarity
- zero crossing
- entropy
- the matching of systolic wave detectors

A lot of effort in the PPG domain is concentrated on the post-processing techniques, but it is our belief that acquiring better signal leads to an enhancement in the evaluation of the vital parameters.

1.4.1 Reflected vs transmitted

PPG signals can be acquired by either transmittance or reflectance, as showed in Figure 1.7. In transmittance mode, the photons leave the LED, pass through the finger and are measured by the photodiode. In reflection mode, the skin and tissues reflect the photons, which are captured by the photodiode placed near the LED. Transmittance mode produces good signals, but can only be used on body sites of limited thickness, such as the fingertips, earlobes or nasal septum. The reflection mode does not have this problem and allows measurements to be taken on other body sites such as the wrists, chest, or forehead.

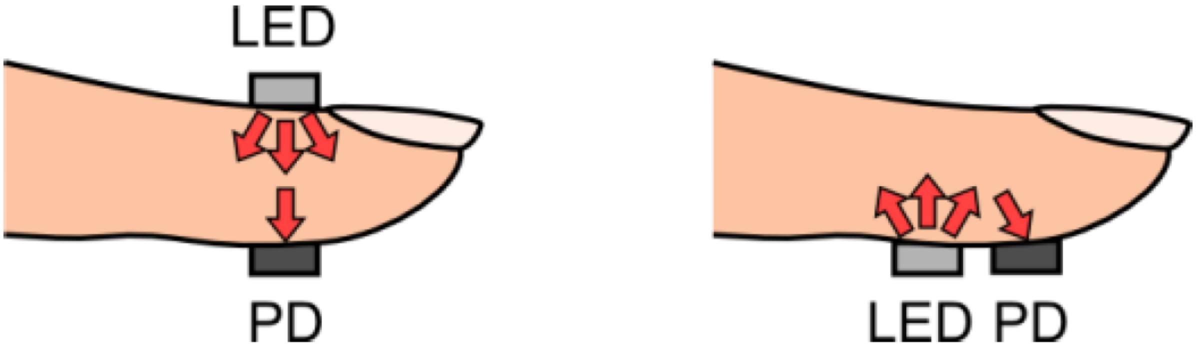

Figure 1.7 – LED and photodetector placement for transmission and reflectance mode PPG, from [47]

It is important to adapt the PPG mode to the usage, meaning the condition of the experiments, the subject, the exterior factors and different requirements of the experiment.

It is valuable for the user, in particular for scientific researches, to be able to choose and change the PPG mode.

1.4.2 Calibration

Various physiological factors, including weight, skin tone [2], vascular health, hydration level, and age [4] can influence the quality and reliability of PPG signals. A darker skin tone indicates a higher melanin content in the epidermis. Melanin exhibits relatively higher absorption in the UV-visible spectrum, and it is anticipated that an increased melanin concentration leads to greater photon absorption. In addition, weight significantly impact on the thickness of various layers of the skin, for example obesity is linked to a higher dermal thickness [2]. In addition, the site of measurement has an influence on the quality of the measurement, due to the different arrangement of the surface vascular system [30]. To mitigate these effects, adjustments to various parameters of the PPG sensors can be made.

1.4.3 Wavelengths

One of the fundamental principles of PPG relies on the higher sensitivity of certain optical wavelengths for blood rather than other tissue components. The red LED (∼660 nm) and IR LED (∼940 nm) are the standard wavelengths used in pulse oximeters for the calculation of oxygen saturation. The green LED wavelength (∼550 nm) is being widely used in reflection-mode applications, since tissue reflects well at this wavelength. As the evaluation of quantity and concentration using PPG is based on Beer-Lambert law (as described in equation 1.2), the more signals with different wavelengths are measured, the more accurate and robust the evaluation is.

In addition, there is a need for multiple wavelengths also because each wavelength has a different sensibility to motion noise. Among other things, the shorter the wavelength, the less the penetration into biological tissues. In addition, the shorter wavelengths of light are strongly absorbed by melanin. A wide range of wavelengths allow variation in light scattering and absorption in the different biological layers at the measurement site.

1.4.4 Distance between photodetector and LEDs

The distance between the photodiode and LEDs in PPG plays a crucial role in the accuracy and reliability of the signal acquisition process. This distance influences the optical path length, determined by the depth of tissue penetration by the emitted light and affects the intensity of the detected signal as showed in Figure 1.8. Optimal placement of the photodiode and LEDs ensures sufficient light transmission through the tissue while minimizing signal attenuation and distortion.

A shorter distance between the photodiode and LEDs enhance signal strength and reduce the risk of signal loss due to tissue absorption and scattering. However, excessively short distances may increase the likelihood of signal saturation, where the photodiode becomes overwhelmed by the intensity of the transmitted light. Conversely, a longer optical path length provides deeper tissue penetration, potentially capturing signals from deeper vascular structures. Still, it may lead to weaker signal intensity and increased susceptibility to motion artifacts and ambient light interference. It also leads to the need to increase the power in the LED to get an exploitable signal.

However, the shorter the distance, the greater the risk of direct illumination of the photodetector by the LEDs. Ideally, an optical isolator should be used between the LEDs and the photodetector, as the LEDs should not directly illuminate the photodetector. Ideally, only the contribution of light reflected by the skin, particularly the AC component, should reach the photodetector [19].

According to simulation, the optimal distance between optical elements is determined to be, for infrared wavelengths (850 nm - 950 nm), 2 mm [25]. In experiments, for green wavelengths (543 nm - 571 nm), the ideal separation is found to be located between 2 and 3.2 mm [22].

However, it is important to note the limitations of these studies. The first study [25] relied solely on simulations, which may not fully capture the complexities of real-world scenarios. Furthermore, this study evaluated the signal quality using only one metric, the PI , which is defined as the ratio of AC to DC components of the signal, as written in the equation 1.5.

$$\mathrm{PI} = \frac{\mathrm{AC}}{\mathrm{DC}} \tag{1.5}$$

While the PI is an important indicator, other critical metrics are not taken into account. One such metric is the SNR, which quantifies the strength of the signal relative to background noise and is calculated as in the equation 1.6.

$$\mathrm{SNR} = 20 \log \left(\frac{\mathrm{AC}}{Nph} \right) \tag{1.6}$$

Where Nph represents the noise level in the signal. Additionally, the SEI, which is a combined measure of both the PI and SNR, are not considered. The SEI is defined as:

$$\text{SEI} = \text{PI} \times \text{SNR} \tag{1.7}$$

The second study [22], while based on experimental data, has its own set of limitations. The exact site of measurement is not specified, which raises concerns about the generalizability of the results to different measurement sites (e.g., finger, wrist). Additionally, neither study addressed the potential differences in signal quality across various measurement sites or used a combination of both simulation and experimental approaches. Both studies also focused on a limited range of wavelengths, which may not encompass the full spectrum of interest for optimizing PPG measurements.

These limitations highlight areas where further research and more comprehensive methodologies are needed to improve the understanding of optimal optical element distances in PPG systems across different wavelengths and measurement sites.

Therefore, determining the ideal distance between the photodiode and LEDs involves a careful balance between maximizing signal strength and minimizing signal distortion. Factors such as the optical properties of the tissue, sensor design, and intended application must be considered when optimizing this distance. Additionally, advancements in sensor technology and signal processing techniques continue to refine our understanding of the optimal configuration for PPG sensors, ultimately improving the accuracy and effectiveness of non-invasive physiological monitoring. In conclusion, it is really important not only to develop good signal processing algorithms but also to develop a PPG-design that allows the best measurement even before the post-processing [30, 19].

1.5 Conclusion

PPG technology offers a valuable, non-invasive approach to monitor various physiological parameters, including heart rate and respiratory rate. PPG's ability to capture modulations related to breathing patterns and cardiac activity makes it useful for assessing respiratory efficiency and overall health. Despite challenges such as signal interference and calibration difficulties, PPG provides insights into both heart rate variability and blood glucose levels.

PPG's application in glucose monitoring shows promise due to its non-invasive nature and potential for continuous tracking. However, achieving accurate glucose measurements

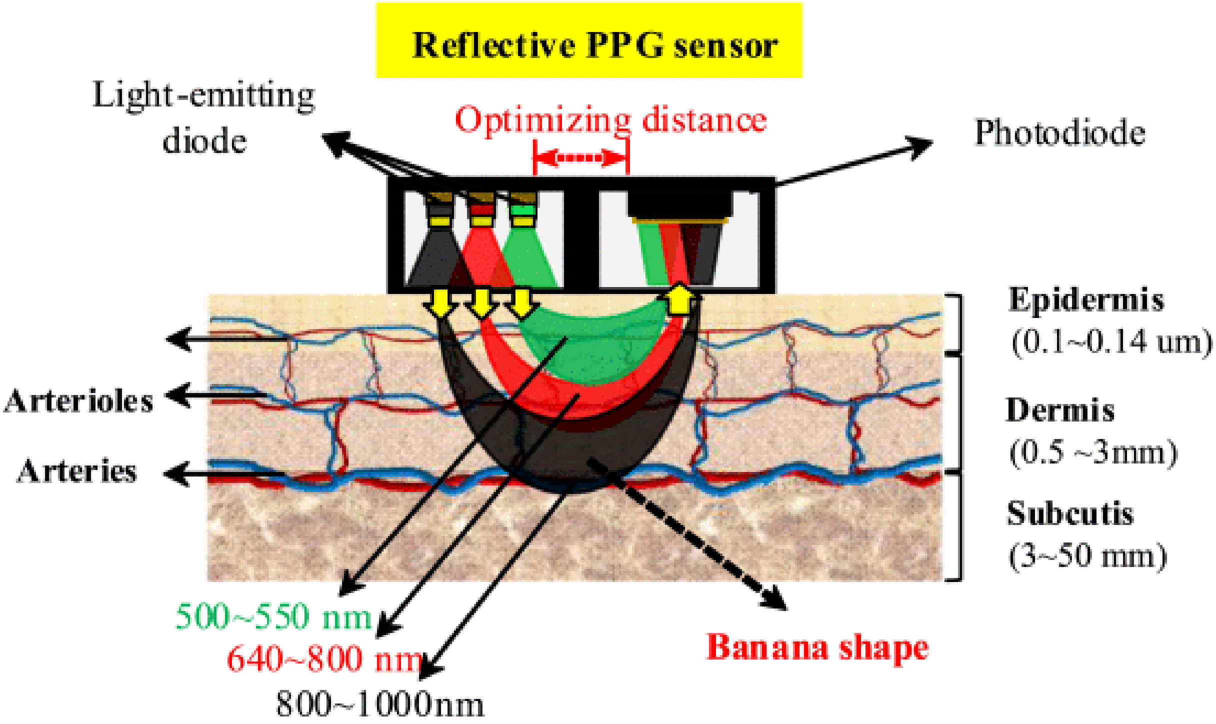

Figure 1.8 – Optimizing the distance for specifics wavelength [24]

requires overcoming challenges related to tissue optics and sensor calibration.

Various devices, ranging from consumer-grade activity trackers to advanced evaluation kits, offer different levels of data access and analytical capabilities. The accuracy of PPG measurements is influenced by factors such as wavelength selection, distance between LEDs and photodetectors, and calibration for individual physiological variations.

Advancements in PPG technology and signal processing are crucial for improving measurement accuracy and reliability. Continued research and development enhance the effectiveness of PPG-based monitoring in both medical and consumer applications.

Chapter 2

DEVELOPED EXPERIMENTAL PLATFORM

2.1 Introduction

The platform described in this chapter is designed to tackle the limits of current devices for PPG analysis, as discussed in Chapter 1. The challenges of improving accuracy, resolution, and flexibility in PPG sensing are addressed here through the development of a reconfigurable hardware solution, specifically leveraging an FPGA. This choice of hardware allows for adaptable signal processing, higher computational power, and scalability, which are crucial in meeting the evolving demands of multi-wavelength sensing and high-frequency data acquisition.

These new directions include multiple wavelengths (more than four), higher frequency, and higher resolution, all while maintaining a mobile device, as shown in Figure 2.1. The decision to incorporate several LED wavelengths stems from the need to capture more detailed physiological data across a broader spectrum. This smart sensor captures and stores raw data, and its FPGA-based architecture enables embedded signal processing with a general-purpose processor, providing flexibility for real-time analysis and potential reconfiguration. In addition, the user experience is taken into account, particularly the ease of using the device.

The mobility aspect of this device is crucial as it is designed for use during physical activity or in long-term medical monitoring scenarios, such as continuous tracking over the course of a day or even a week. The developed system serves as a prototype that can be utilized in validation phases and early measurement campaigns. It is already being tested in projects at École Polytechnique Fédérale de Lausanne (EPFL), demonstrating its applicability in real-world conditions, as discussed in Section 4.5. Additionally, this prototype offers potential for future miniaturization, as explained in Subsection 2.4.5, ensuring it can be adapted into a more compact and user-friendly form for broader applications.

The platform is composed, as shown in Figure 2.1, of a Pynq board embedding a Zynq SoC from Xilinx. The ARM processor running a Petalinux operating system may

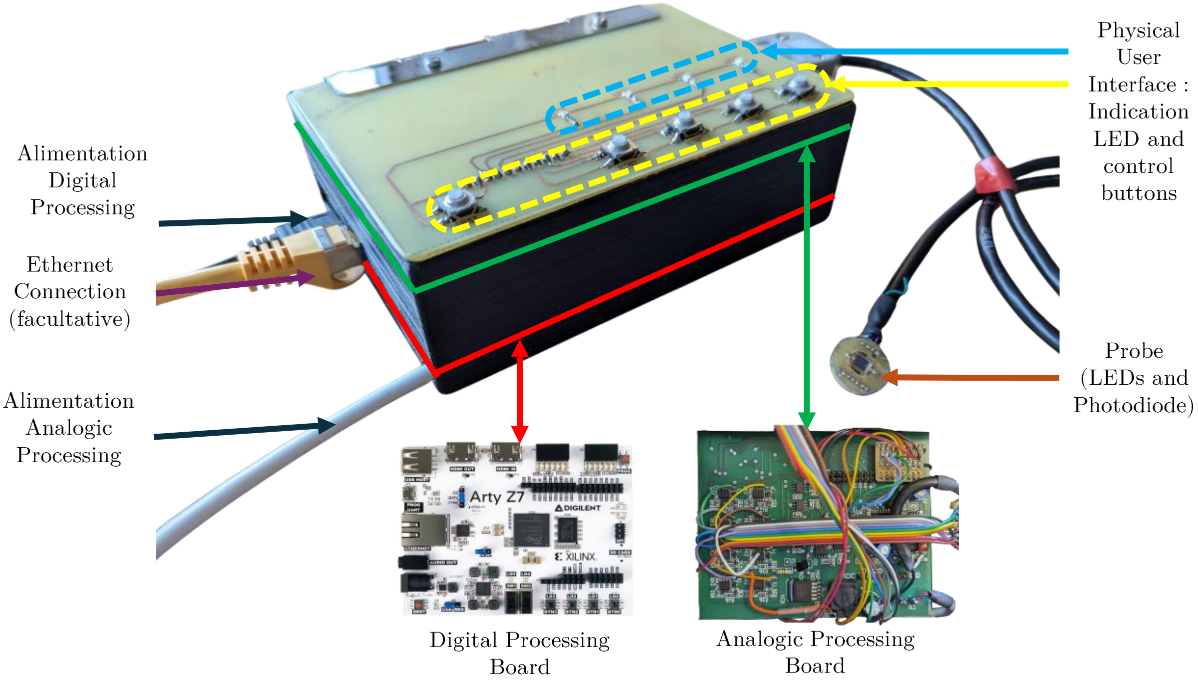

Figure 2.1 – Overview of the platform.

be used as a sandbox for real time signal processing algorithm research. The FPGA of the Zynq platform is used to port the acquisition process to dedicated hardware, making the acquisition reliable and not impacting the ARM processor. A custom analogic processing board is then used to control the physical sensor. Several custom-made probes, composed of LEDs and a photodetector, had been design to be plugged into the board.

This platform is presented, first the physical part including the probes, the analogic electronics and the logic (digital processing) board, then the custom-made software is presented including the user-friendly interface, data management and the interfacing with other sensors. Finally, the platform's evolution is discussed in detail, highlighting the key insights and lessons learned throughout its development.

2.2 Physical platform

This platform uses the custom-made probes, as explained in Subsection 2.2.1, custom electronic design for LED power and signal acquisition explained in Subsection 2.2.2 and finally an integrated logic design called maestro detailed in Subsection 2.2.3.

2.2.1 Probe design

One of the primary goals of the advanced PPG sensor is to provide measurements with more wavelengths than the typical green/red/IR. Consequently, a new sensor has been designed with 8 LEDs allowing 8 wavelengths to be studied.

With the constraints of size, market availability and price, the following 8 LEDs wavelengths have been chosen. The choice fell on 8 non-encapsulated LEDs (300 x 300 ţm), the objective is to minimize the size of the sensor. The ensemble is then covered with a protective resin.

To bring this custom sensor to life, we collaborated closely with the FOTON laboratory, leveraging their expertise in probe development. Thomas BATTE from FOTON was pivotal in assembling the unencapsulated LEDs onto the PCB, a task that required precise bonding, followed by applying a protective resin to safeguard the components. This process was beyond the capabilities of our lab, as FOTON has the specialized machinery and technical knowledge required for such intricate work. Throughout the course of my thesis, FOTON produced numerous iterations of the probes to accommodate technical improvements and specific testing needs. These iterations allowed us to optimize various factors, such as the form factor, connector type, and the distance between the LED and the photodiode, ultimately refining the sensor's performance. The collaboration was critical in overcoming the technical challenges associated with designing a compact, multi-wavelength PPG sensor.

A red LED operating at 660 nm and an IR LED operating at 940 nm have been chosen to allow the comparison with standard oximetry. LEDs operating at 542 nm, 593 nm, 620 nm, 762 nm, 807 nm, 888 nm have also been chosen to allow Carboxyhemoglobin and Methemoglobin to be estimated. The range of the wavelengths of the LED is seen in Figure 1.4.

Two sensor patterns, consisting of the previously mentioned 8 LEDs covering wavelengths from 542 to 940 nm, were manufactured. The first sensor pattern is designed for use in transmittance, and is constituted of two separate boards. The first one contains the 8 LEDs, as showed in Figure 2.2 and the second one contains the photodiode. The second sensor pattern is for use in reflectance, so the 8 LEDs surrounds a photodiode, as in Figure 2.3.

In addition, a large variety of probes, in particular the reflectance pattern, has been developed not only in order to search for the best design but also to evaluate the reproducibility of the best design.

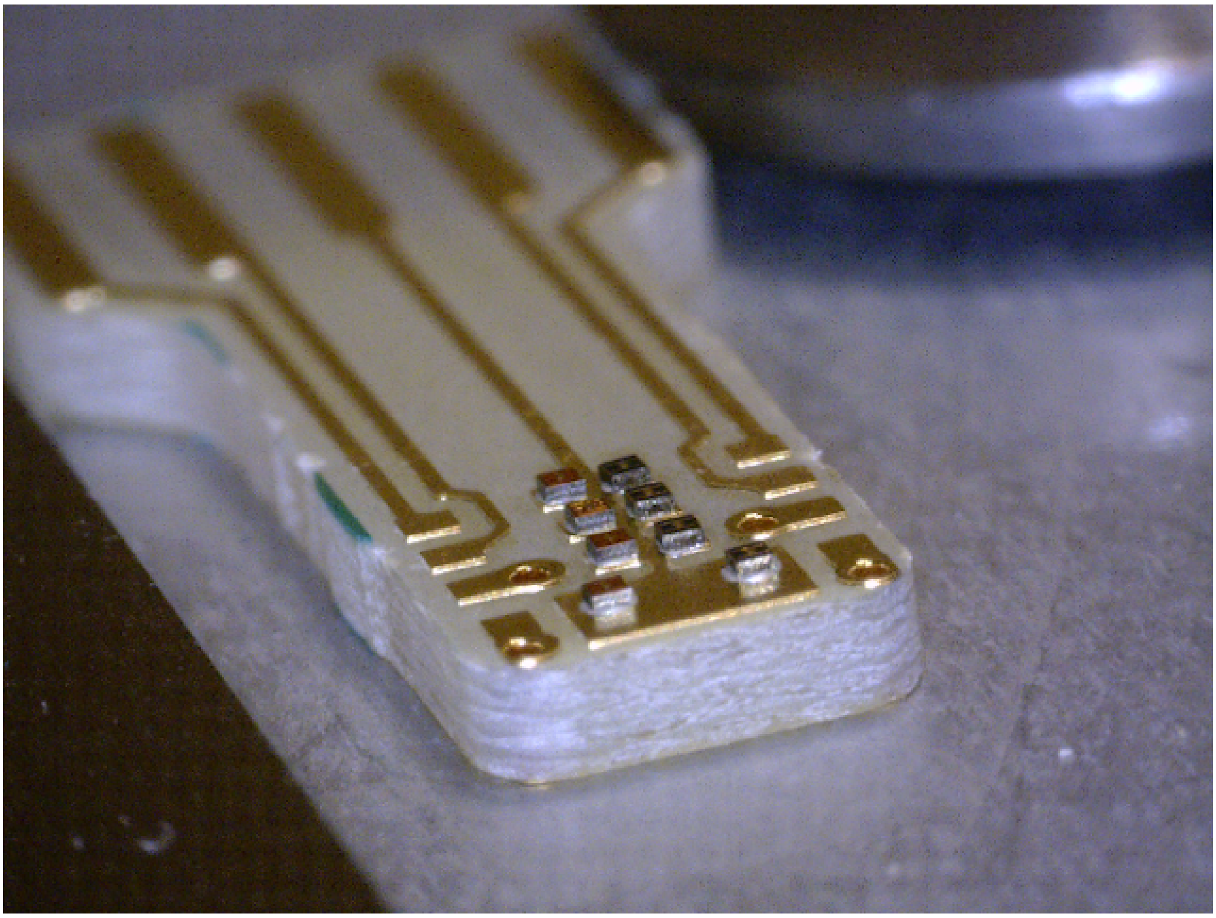

Figure 2.2 – Transmittance pattern before encapsulation.

The differences between the probes is highlighted is Table 2.1. The main difference between the Generation 1 and 2 is the shape of the probes. The main evolution between the Generation 2 and 3 is the distance between the LED and the photodiode. It can also be noted that there is two type of resin used. The optical one is first used and then to comply with the medical requirement, the medical resin is used. Both resins had been extensively tested and for the wavelength used they yield identical results, as showed in Section 3.2. In addition, some tests have done on the usefulness of the wires' shielding. A special connector has been done to be able to plug the probes to other structure, in case of the use of multiple sensors. Some test has been conducted on the placement of the resin to makes the probe easier to clean and less susceptible to break. The test to find the ideal distance between the LED and photodetector, is discussed in Section 3.5.

The Figure 2.4 is the illustration of the evolution of the probes, in addition a sensor

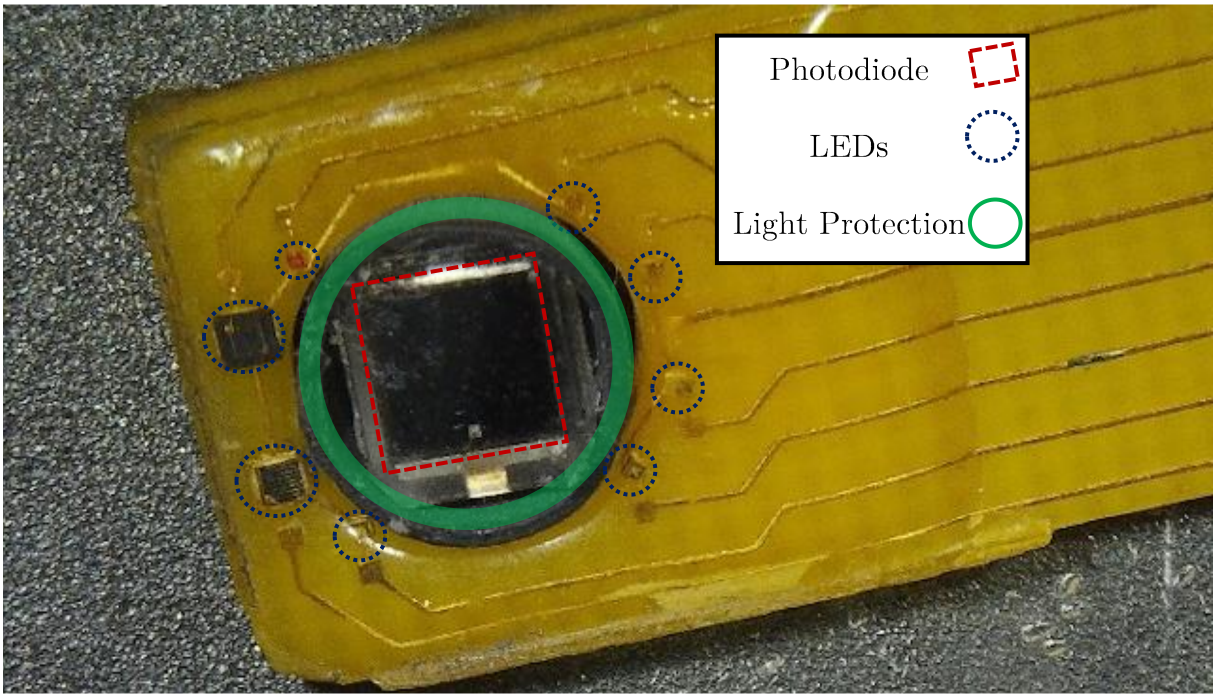

Figure 2.3 – Reflectance pattern encapsulated in a protective resin.

of the third generation is pictured in Figure 3.28.

2.2.2 Electronic design

To enable sample measurements using this sensor, two specific electronic circuits have been designed. The primary goal of the first circuit is to provide a stable and accurate current to the desired LED. The second circuit allows fine measurements of the received current in the photodiode. These two circuits are connected to the LEDs, photodiode and logic as shown in Figure 2.5. Those two circuit are on the analogic board, as shown in Figure 2.1.

LED Power

The first electronic circuit presented here drives the current in a specific LED. For this end, the logic sends 2 types of signals. The Figure 2.6 represents the circuit design for a specific LED. The first signal sent is the *enable* signal. This signal is composed of one wire per LED. When set to a logic 1 (here 3.3 V) it then causes the selected LED to light up. The second signal is the *power* signal. This signal is a PWM signal that is the

	Generation						
	1		2			3	
	1.1	1.2	2.1		2.2	3.1	3.2
			2.1.1	2.1.2			
Form	rect.	rect.	circ.	circ.	circ.	rect.	rect.
Type of resin	opt.	opt.	med.	med.	med.	opt.	med.
Wires shielding	yes	yes	no	n/a	yes	yes	yes
DLP	yes	no	no	no	yes	no	no
Conn.	wires	wires	wires	conn.	wires	wires	wires
Place resin	only LED	every.	every.	every.	only LED	only LED	only LED
$d_{LED/PD}$	3 mm	5 mm	3 mm	3 mm	3 mm	fixed	variable

Table 2.1 – Table of the different generation of probes developed.

Abbreviation	Description
DLP	Direct Light Protection
$d_{LED/PD}$	distance between LED and photodetector
rect.	rectangular
circ.	circular
opt.	optical
med.	medical
n/a	not applicable
conn.	connectors
every.	everywhere
var.	variable

Table 2.2 – Legend for abbreviations used in Table 2.1.

amount of current driven into the LED.

First, the *power* signal passes inside a low pass filter (a basic RC design) that transform the logic signal into an analog waveform. Then, when instructed by the enable signal, an analog switch passes the signal into the current driver. The analog switch chosen is a HCT4066-based circuit. Since the current should be switched off when the switch is disconnected, a pull-down resistor is inserted. Finally, the current driver section then operates the current regulation. The schematic is based on an OpAmp and a transistor (TLC271CP and BC847CW).

(a) Generation 1 (b) Generation 2.1.1

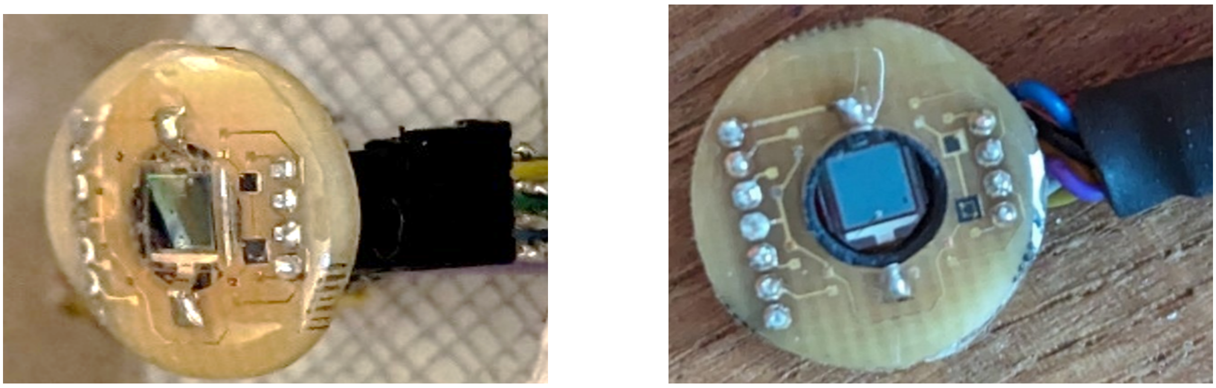

(c) Generation 2.1.2 (d) Generation 2.2

Figure 2.4 – Evolution of the probes.

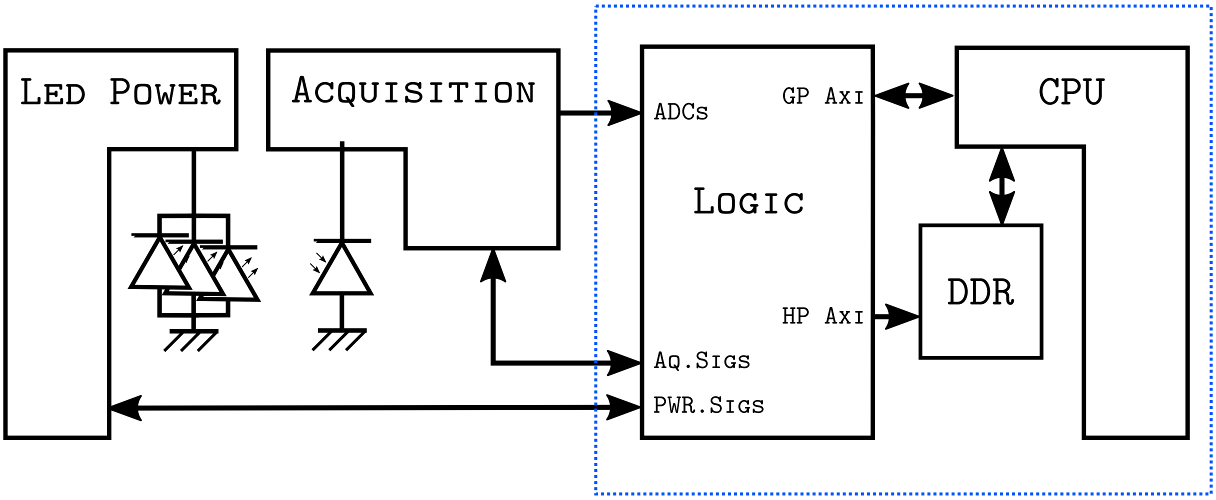

Figure 2.5 – Global schematic of the system.

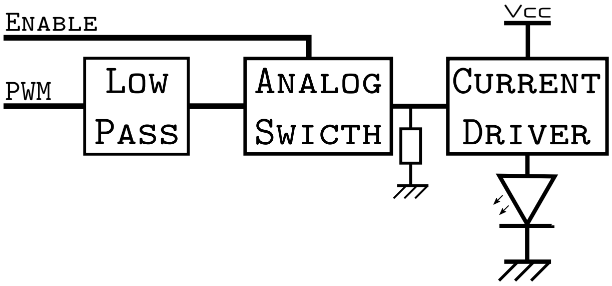

Figure 2.6 – Electronic LED power stage for one LED.

Acquisition

The light emitted by the LED is then attenuated or reflected by the tissue of the subject and captured by the photodiode. Figure 2.7 shows the schematic of the reception circuit.

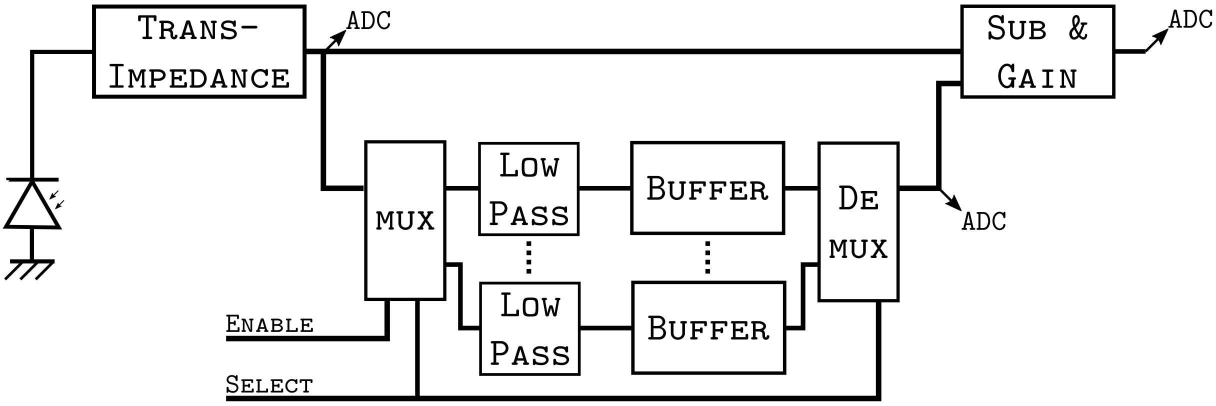

Figure 2.7 – Diode stage for data acquisition.

The first block is a transimpedance block composed of AD8021AR OpAmp that converts the current delivered by the diode to a voltage. This first voltage is measured (after a level adjuster) to one of the ADC pins of the Zynq chip.

This schematic also shows the first version of the circuit responsible to measure the three different output signals. This version is with the analog calibration of the DCs. The ADC engines of the targeted architecture measure in a rapid succession the 3 output signals, which correspond to the AC, DC and total signal. The 2 inputs are a 3-bit *select* that specify which LED is currently measured and a 1-bit *enable* signal that specifies if the device is in the DC calibration mode.

To maximize the signal precision, the signal is amplified. However, since the pulsating level (AC) of the signal is significantly smaller than the steady (DC) component, the choice has been made to subtract an offset value from the signal. This offset value is determined either at the start of the capture by taking the average value of the signal for each LED for the fist version, but in the second digital version, this offset is adapted thought a feedback loop (see Section 3.3).

This operation, for the analog version of the DC calibration, is performed through the first Analogic Mux (74HCT4051) that allows the input signal to charge a low pass RC filter when the *calibration* signal is set. The signal is then buffered using an TLC271 OpAmp used as voltage follower, thus removing the possibility of discharging the filter capacitor. After calibration, DC-offset is measured using the second Analog Mux that outputs to the ADC. The DC calibration part of the circuit is changed from analog to digital. To understand the reasons behind the calibration change, see Section 1.4.

Finally, the main full-signal and the offset are subtracted then amplified using an TLC271 OpAmp in differential amplification mode. Resistors are chosen accordingly to obtain the following output voltage:

$$V_{out} = g * (V_{avg} - V_{in}) + 0.5 \tag{2.1}$$

With g equal to 10, V_{avg} the DC level found by either the analog or digital version of the DC calibration and V_{in} the input tension (full signal). The goal is that $V_{avg} - V_{in} = V_{ac}$, with V_{ac} the tension that represent only the AC component of the signal. Choosing an offset of 0.5V allows maximum signal variation, as the ADC has a range of 0-1V. The value of g is chosen to bring the most enhancement of the signal without saturation or amplification artifacts.

2.2.3 Logic board

Since the Analog/Digital interface is operated with an FPGA, a logic interface is performed to operate the sensor's electronic but also to operate the ADC. Thus, the signal capture is not processor dependent and so guarantees synchronicity of the capture operation as well as less impact on the processor. The logic system is described in Figure 2.8.

A global state machine called Maestro handles the capture process. It outputs the signals for the LED and diode electronics as well as piloting the capture of the ADC using the *convert* and *ADC_enable* signal.

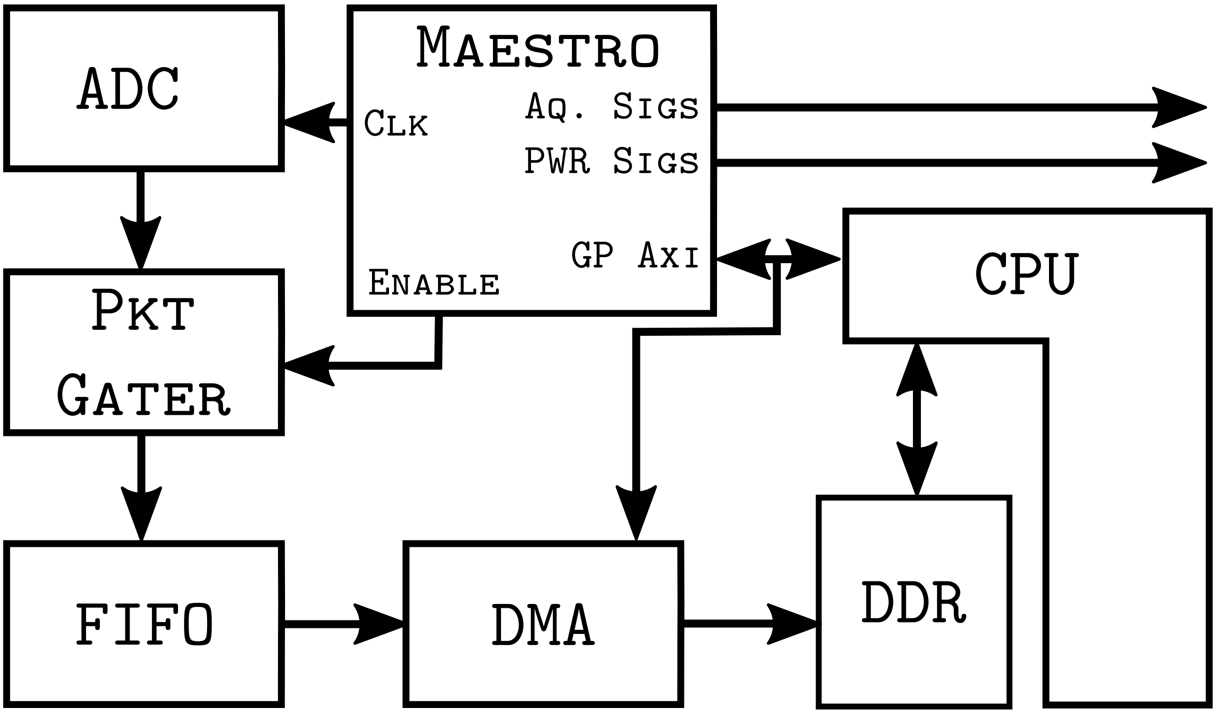

Figure 2.8 – Schematic of the FPGA design.

The processor communicates with the Maestro through a general purpose AXI interface, by writing in specific registers. Samples are stored through a RAM using a DMA.

When performing the capture, the ADC outputs its captured data through an AXI Stream interface. This stream is then gated to allow the sample to flow only when a capture is performed. This is necessary to both prevent the ADC to output a sample at startup when it is not configured correctly but also for debugging (performing dry runs).

Samples are then buffered in a First in, first out (FIFO) before being copied to the Double Data Rate (DDR) using a Direct Memory Access (DMA). This FIFO prevents loss of samples if the DMA doesn't request the sample fast enough.

Finally, when triggered by the processor, the DMA writes the samples to a given address in the DDR. High performance AXI ports of the Zynq architecture are used to achieve a high throughput.

Maestro State Machine Architecture and Operation

Maestro consists of two state machines, with one embedded within the other. The Supervisor State Machine, the larger one, is depicted in Figure 2.9, while the Macro State

Machine is shown in Figure 2.10.

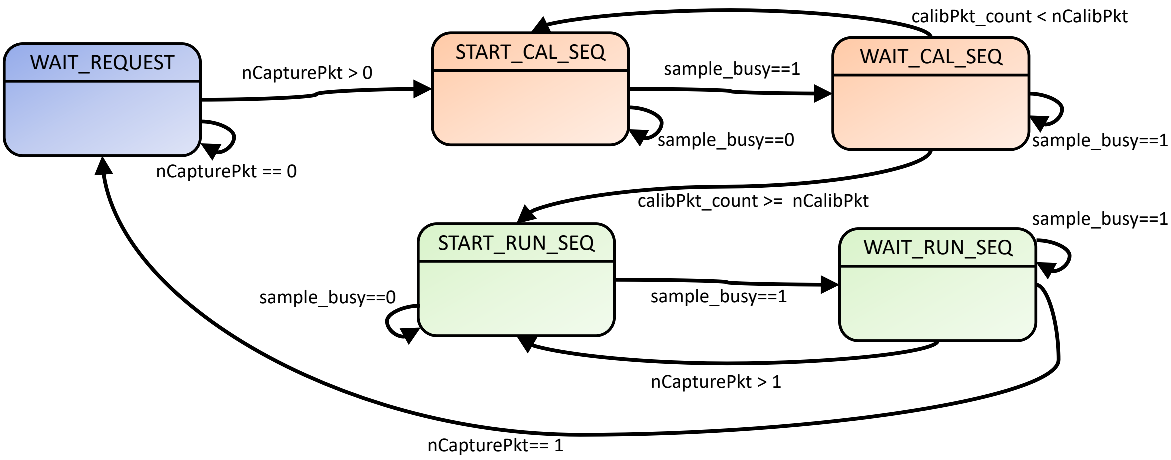

Figure 2.9 – Supervisor State Machine

The Supervisor State Machine operates as follows: Initially, the sensor is in the idle state, **WAIT_REQUEST**. When a request is receivedspecifying the number of packets to capture (`nCapturePkt`)the system transitions to **START_CAL_SEQ**, initiating the calibration phase. It then moves to the **WAIT_CAL_SEQ** state, where it remains until the calibration process concludes. Calibration ends when the number of captured packets (`calibPkt_count`) equals or exceeds the requested number (`nCalibPkt`). At this point, the system transitions to **START_RUN_SEQ**, which initiates the measurement sequence in a manner similar to the calibration phase. The system then enters **WAIT_RUN_SEQ** and waits until the specified number of packets has been captured.

When the Supervisor State Machine triggers either the calibration or measurement sequence (**START_CAL_SEQ** or **START_RUN_SEQ**), the Macro State Machine exits its idle state, **WAIT_START**, and begins the corresponding sequence by transitioning to **WAIT_CLK**. In this state, the state machine waits for a clock tick at the user-defined sampling frequency (`clk_sample`) to ensure precise timing. Once the clock ticks, the state machine moves to **SWITCH_LED_ON**, where the current LED (stored in the variable `led_cur`) is turned on. After the LED remains on for a user-defined duration (`t_led_up`), the system transitions to **START_ADC**, initiating the ADC to measure the voltage.

In the **WAIT_ADC** state, the system waits for confirmation that the ADC has completed the measurement. Once confirmed, the state machine loops back to **START_ADC**

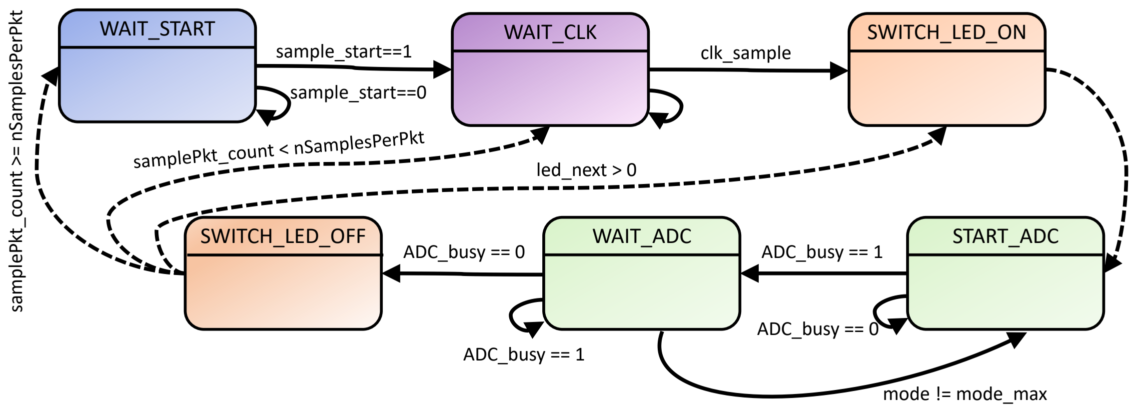

Figure 2.10 – Macro State Machine

to capture the next mode (AC, DC, or AC/DC) of the same LED. This loop repeats three timesone for each modeafter which the system moves to **SWITCH_LED_OFF**. Similar to **SWITCH_LED_ON**, this state turns off the LED and forces the system to wait for a set time (`t_led_down`) before proceeding.

At this point, there are three possible paths: If the last selected LED has not been measured, the system selects the next LED (stored in `led_cur`) and begins a new cycle from **SWITCH_LED_ON**. If the last LED has been measured but there are more packets to capture, the cycle restarts for all LEDs from **WAIT_CLK**. Finally, if all packets have been captured and the last LED has been measured, the Macro State Machine notifies the Supervisor State Machine that the calibration or measurement is complete, returning to **WAIT_START** to await the next request.

A highly configurable platform

The use of an FPGA also provides a wide range of sampling frequencies. The platform support sampling frequencies ranging from 200 Hz to 10 kHz, each measurement comprising a sample for the selected LEDs (up to 8). In addition, various acquisition parameters are configurable.

As mentioned before, the current in the LEDs is specified separately for each LED. A custom software on the processor performs an exhaustive search for the best power value in the LED for each LED, in order to optimize dynamic range during acquisition. This is used to adapt the platform to the experiment environment but also to the experiment subject.

The delay between turning on the LED and the measurement is configurable. There is a compromise to find between the settling time and speed. Similarly, it is possible to configure the fixed delay between turning off the previous LED and turning on the next one. The compromise here is between allowing enough time to avoid inter-LED pollution, as light lingers in the biological tissue, and ensuring speed. The numbers of LEDs used for an experiment can be chosen. Any combination that uses between 1 and 8 LEDs is allowed. The number of samples used for the calibration of the offset can also be adjusted, the compromise in this case is between allowing enough time to have a stable offset and speed.

2.3 Software Architecture and Functionality

The developed software for the PPG device integrates an advanced operating system with a robust file system, facilitating seamless connectivity and control. The software takes advantage of the already installed Jupiter Labs on the board, for more ease to use. Each device is assigned a fixed IP address, enabling direct access and remote management via Ethernet and SSH. This connectivity ensures that users can effortlessly engage with the device, enhancing its utility and adaptability.

2.3.1 Parametrization Framework

The software incorporates a sophisticated parametrization structure, allowing comprehensive measurement customization through an intuitive interface with widgets. This user-friendly design ensures accessibility for users without coding expertise. The parametrization framework is implemented through three primary classes as described in Figure 2.11.

The parameterization structure allows researchers to fine-tune the device for specific experimental requirements, such as varying sampling rates, LED configurations, and measurement modes, which are critical for tailoring measurements to different physiological signals and experimental conditions, as described in subsection 1.4.2.

VisualManager Class

The `VisualManager` class bridges the gap between users and the device's functionality, providing a graphical interface for measurement initiation, visualization of previous

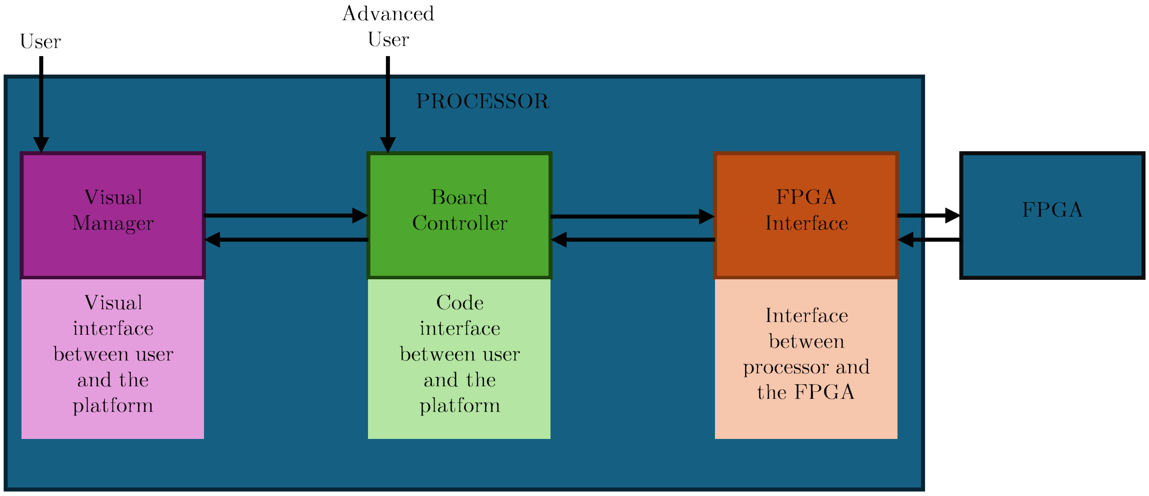

Figure 2.11 – Illustration of developed classes for the parametrization.

measurements, and calibration. It simplifies parameter adjustments, presenting them in an intuitive format. For instance, the sample rate is displayed in a user-friendly manner, abstracting the complexity of the underlying firmware code.

BoardController Class

The `BoardController` class processes data input from the `VisualManager` or directly from users preferring non-graphical interaction. It includes input validation routines that prevent erroneous configurations, such as incompatible sampling rates or LED modes, by cross-checking against device specifications. This ensures that users do not inadvertently configure the system in ways that could compromise measurement integrity or damage hardware.

FPGAInterface Class

The `FPGAInterface` class manages the communication between the processor and the FPGA, accurately writing values to the FPGA registers and initiating measurements.

To demonstrate the usage of these classes, a Jupyter Lab script, named `Launching Board`, has been developed, providing practical examples and enhancing user understanding.

2.3.2 Measurement and Data Acquisition

Standard Measurement

The device supports standard measurement procedures, ensuring high accuracy and reliability in data acquisition.

LEDs' Current Calibration

Calibration routines are integrated to optimize device performance, adapting to varying conditions and ensuring consistent measurement quality. In particular, as described in Section 3.3, calibrating the LED's current improves measurement quality by adapting to individual-specific characteristics, environmental factors, or general experimental conditions. This allows to get the best of the platform, and of the PPG technology in general, in a large variety of scenarios.

2.3.3 Data Management and Storage

Data format

Each sample is a collection of different measurements that happen at each period of the sampling frequency. In each sample, N_{led} LEDs are used where N_{led} is the numbers of LEDs selected by the user. For each of the LEDs, each mode,AC, DC or complete (AC and DC), is measured. The complete structure of a sample is described in Figure 2.12. In this Figure, N_{led} LEDs are selected and all the modes are activated by the user.

The samples are agglomerated together to form packets. The number of sample per packet is configurable by the user, even if we advise to not change the default value that is configured to be the best value to ensure speed in local memory writing and communication of the results with other sensors. These are the units that are exchanged between the logic board and the processor. Next, there is the mega-packets, that are an agglomeration of packets for saving purposes and communication.

Data Saving Protocol

During measurements or calibrations, data is periodically saved every N_{save} samples into new files. This segmented storage approach prevents files from becoming excessively large, enhancing manageability. The N_{save} parameter is configurable by the user. This technological solution allows the use of our platform, that produce a lot of data due to

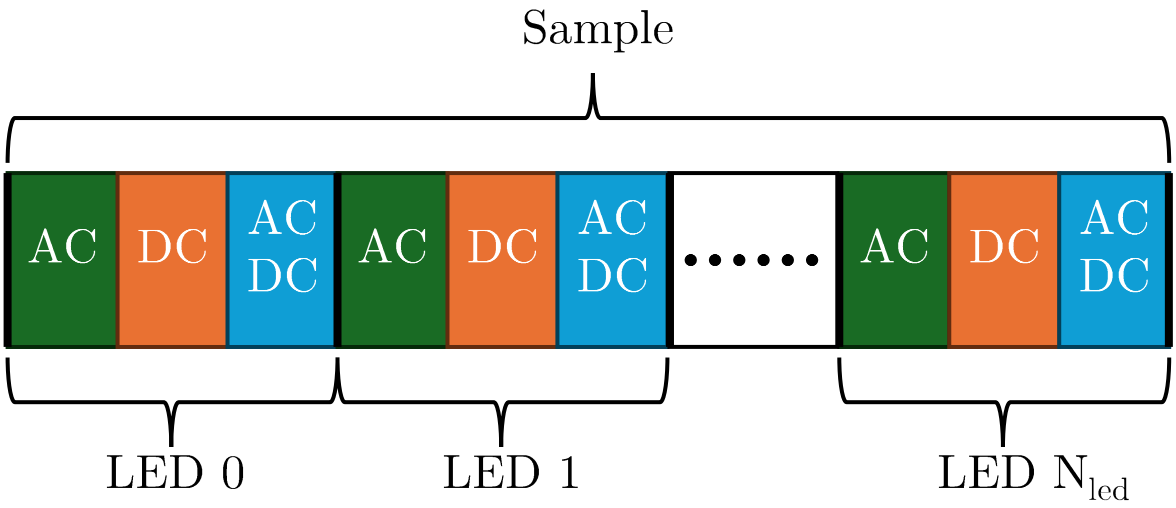

Figure 2.12 – Illustration of the structure of a sample.

the high sampling frequencies possible to configure and the usage of up to 8 LEDs. In addition, its manageability helps make post-processing and offline analysis easier.

In addition, the segmented storage approach mitigates the risk of data loss during long measurements by ensuring that no single file becomes too large or prone to corruption. This method also improves memory management, as smaller file sizes are more manageable for post-processing, especially during high-frequency measurements where large datasets can overwhelm conventional storage systems

Metadata Integration

Metadata accompanying each measurement is stored, providing essential context for data interpretation. First the parameters used for the measurement are always saved. The saved parameters are :

- Unique ID of the measurement.
- Length of the measurement.
- Sample frequency.
- LEDs used.
- Calibration used (current in the LEDs).
- t_{LEDup}, the time between the turn on of the LEDs and the measurement with it.

- $t_{LEDdown}$, the time between the turn off of a LED and the turning on of the next one.
- The Modes used (AC, DC or/and AC/DC)
- The number of sample per packet.
- Time dedicated to the calibration of the DC-offset, as discussed in Section 3.3.

During calibration, it is the same parameters that are saved except that the ID is a calibration ID and the calibration parameters is a range or list rather than a number. This information is also saved to serve as a template, allowing the device to be reconfigured automatically without the need for manual adjustments each time. When the measurement or calibration is launched thought the graphical interface, then some additional information is asked to the user and saved. They are the following :

- Unique ID of the measurement (read-only)
- Date of the measurement
- Placement of the probe on the body
- Name of the person
- Generation of the sensor
- Additional notes

Those additional information allows for a good data organization and analyze.

File Format

Data is stored in a binary format without headers. Metadata is thus crucial for decoding the information, with each measurement of a sample represented as an unsigned 16-bit word. This format allows for the efficient storage of both numerous experiments and extensive individual experiments.

The choice of binary format without headers is motivated by the need for efficient storage and rapid data transfer, especially given the large volume of data generated by the device's high sampling rates and multi-wavelength measurements. By eliminating unnecessary metadata from each sample, we maximize storage efficiency and reduce the computational overhead during real-time data processing.

File Organization

Files are organized into directories based on the parametrization used and the unique ID of each measurement or calibration. This hierarchical structure facilitates efficient data retrieval and management, as measurements and calibrations with the same parameters are grouped together.

2.3.4 Operating Modes

Jupiter Labs and Ethernet

When connecting to the device via Ethernet, the user access the installed Jupyter Labs on the board. All previously mentioned files and software are available within the system's file explorer. They can be used to operate all the device's capabilities.

Jupyter Labs provides a versatile environment where users can interact with the device via Python scripts, enabling real-time data visualization, control, and analysis. The board's fixed IP address ensures stable and consistent access for remote monitoring.

Blind Mode

A blind mode is available for operating the device without a computer or Ethernet connection. Upon startup, the device enters blind mode, enabling functionality through a physical button interface. Users restart the device, initiate pre-configured measurements, or exit blind mode using buttons SRST, BTN3 to BTN0 respectively. The positions of the buttons are seen in Figure 2.1, they are marked as control buttons.

SPI Communication

An SPI interface has been implemented, by Hasna ESSAKALI during an internship under my supervision, to enable device operation without manual button presses, Ethernet connectivity, or SSH. The detailed protocol for SPI communication is provided in the Appendix 4.6.

The custom communication protocol includes various commands essential for configuring the device and managing data transfers. Commands are structured with an opcode followed by arguments, facilitating precise and flexible communication between devices.

2.3.5 Data Analysis and Visualization

LEDs' Current Calibration Analysis

The software includes advanced calibration analysis functions, assisting users in determining optimal LED current parameters. Users have also the option to allow the system to automatically select the best settings based on the analysis.

Real-time Demonstration

A Jupyter Lab notebook has been developed to fully demonstrate the real-time data acquisition and visualization capabilities of the PPG sensor. This tool offers immediate feedback on physiological signals, which is crucial for several reasons.

Real-time feedback allows users to assess the quality of the physiological measurements as they happen. For example, users can immediately identify issues such as sensor misplacement, poor signal-to-noise ratio, or environmental interference (e.g., ambient light or motion artifacts), enabling immediate adjustments. Indeed, in PPG systems, signal integrity varies significantly depending on factors such as probe placement on the skin or individual variability, as described in the subsection 1.4.2. By providing live visual feedback, the system allows for dynamic correction, preventing poor data collection over extended measurement sessions.

In addition to technical uses, the real-time visualization is also an effective tool for demonstrations, teaching, and training purposes. For instance, educators can use the notebook to showcase physiological responses in real time, helping students and researchers understand how PPG technology works.

This Jupyter Lab notebook is an essential tool for leveraging the full potential of the PPG platform. It facilitates immediate feedback, and accelerates parameter tuning, making the system more efficient and adaptable in both experimental and applied settings.

2.4 Evolution of the PPG Platform

The development of the PPG platform went through multiple iterations, each improving on the limitations of previous versions and introducing new features to enhance flexibility, precision, and portability. In this section, we will review the main stages of this evolution and highlight the key learnings from each version.

2.4.1 Texas Instruments-Based Prototype

The initial version of our PPG platform utilized the *Texas Instruments AFE4490SPO2EVM* development kit. This sensor was designed for dual-wavelength applications, which allowed us to work with two distinct wavelengths. We expanded this capability by adding custom electronics, including a multiplexer that enabled alternating between eight wavelengths. This allowed for the activation of eight LEDs, enhancing the accuracy of the PPG measurements via the transmittance method.

The platform was equipped with a dedicated software package, complemented by modifications to the firmware to support LED sequencing. Additionally, MATLAB code was developed to extract and process data, effectively replacing the GUI provided by Texas Instruments.

Key learnings: This version of the platform enabled us to gain hands-on experience with PPG technology. It provided a foundational understanding of the hardware and software requirements, while highlighting the need for more control and flexibility in future iterations. The use of commercial development kits proved limiting in terms of customization, leading us to pursue custom FPGA-based solutions in later stages.

2.4.2 Minized FPGA with Custom Analog Board

The next iteration involved a custom-built analog board interfaced with the *Minized FPGA* (*AES-MINIZED-7Z007-G*). This version gave us complete control over the design, from the FPGA code to the communication protocols between the platform and a host computer. Written in C, the communication software handled data interpretation, which provided increased flexibility and precision in data acquisition and processing.

Key learnings: Transitioning to an FPGA-based platform provided significant advantages in terms of flexibility and control. However, it also introduced complexity, as all hardware and software elements had to be developed from scratch. This phase demonstrated the trade-off between flexibility and development time, reinforcing the need for modularity and ease of use in subsequent versions.

2.4.3 Pynq Z2 with Custom Analog Board (Analog DC Calibration)

A further iteration employed the *Pynq Z2 FPGA*, paired with a custom analog board designed for DC calibration. This version expanded the input/output capacity of the system, enabling the acquisition of three analog voltage signals. We leveraged the Python-based *Jupyter Notebook* interface, which facilitated interaction with the platform and provided a more intuitive environment for controlling and analyzing the data.

Key learnings: This version highlighted the benefits of simplifying user interaction. By incorporating Python-based interfaces, such as Jupyter Notebooks, we made data acquisition and processing more accessible to users. However, this iteration still relied on analog DC calibration, which proved to be a bottleneck in terms of measurement time and overall efficiency.

2.4.4 Pynq Z2 with Custom Analog Board (Digital DC Calibration)

To address the limitations of the previous version, we transitioned to digital DC calibration while still using the *Pynq Z2 FPGA* and the custom analog board. The introduction of digital calibration significantly reduced the time required for calibration and allowed for longer measurement sessions. Indeed, as the calibration is digital, there are no capacitors involved storing the voltage corresponding to the DC and thus no discharging of those capacitors. Unless otherwise stated, this is the version used in the experiments.

Key learnings: This iteration demonstrated the importance of adaptability to real word use. By shifting from analog to digital DC calibration, we optimized the platform for longer measurement sessions, minimizing downtime and improving overall usability.

2.4.5 MCU *STM32F446RE* with Custom Analog Board

The most recent version of the PPG platform is based on the *STM32F446RE* MCU, paired with our custom analog board. The firmware for the MCU was implemented by Hasna ESSAKALI during an internship under my guidance. This iteration was designed with portability and energy efficiency in mind, featuring a smaller form factor and reduced power consumption. To facilitate communication with external systems, such as the EPFL platform, a Serial Peripheral Interface (SPI) was added.

Key learnings: This version represents a significant leap in portability and power efficiency, which are essential for applications that require mobility, such as wearable health monitoring devices. The integration of SPI communication also enhanced the platform's connectivity, laying the groundwork for more versatile applications. However, development on this version is still ongoing, and further testing is required to validate its performance in real-world scenarios.

2.4.6 Summary of Key Transitions and Challenges

Throughout the evolution of the platform, a few key transitions have driven improvements: - The shift from a commercially available sensor to a custom FPGA platform enabled greater control but required extensive development effort. - The move from analog to digital DC calibration improved efficiency and measurement duration, addressing bottlenecks in the acquisition process. - The adoption of Python-based interfaces, such as Jupyter Notebooks, made the platform more user-friendly, simplifying the data analysis process for non-expert users.

Each iteration of the platform brought valuable insights, guiding the design choices for subsequent versions. With each enhancement, the focus shifted towards greater flexibility, improved efficiency, and increased portability to meet the demands of real-world PPG applications.

2.5 Conclusion

The platform introduced in this chapter addresses the limitations of current PPG devices by incorporating multiple wavelengths (more than 4), higher frequency, and higher resolution, all while maintaining portability. The device captures and stores raw data and supports embedded signal processing with a general-purpose processor. User experience is prioritized, particularly ease of use.

The software developed for the PPG device exemplifies a seamless integration of user-friendly interfaces with sophisticated measurement and data management capabilities. Its potential impact on the field includes enhanced usability, precise data acquisition, and comprehensive analysis tools, contributing significantly to advancements in PPG technology.

The platform's evolution, from early prototypes to more advanced custom systems, highlighted key improvements in flexibility, efficiency, and performance.

Chapter 3

STUDY FOR ENHANCEMENT OF THE SIGNAL QUALITY

3.1 Introduction

In order to allow for the best evaluation of the vital parameters using the platform presented in Chapter 2, the raw signal of the PPG must be at the best quality. To achieve this goal, several measures have been made. A lot of study has been focusing on enhance the signal via signal processing method and thus transforming the signal after acquisition. The approach here is both different and complementary as the goal is to enhance the quality of the signal at the acquisition meaning thought careful material design. The initial step is to ensure that individual components and their basic functions are correctly implemented, which is demonstrated in section 3.2. Section 3.3 examine the auto-calibration of the LEDs' current, aiming to improve signal quality across different individuals and experimental conditions. The subsequent sections, section 3.4 and 3.5, focus on determining the optimal distance between the photodiode and the LEDs to enhance signal quality. This investigation are conducted both theoretically and experimentally.

3.2 Hardware Verification

3.2.1 Linear Relationship between LED command and illumination

To ensure the accuracy and reliability of our PPG measurements, we undertake a thorough verification of the PPG platform. A critical aspect of this verification involves confirming the linear relationship between the light output of the LEDs and the current supplied to them, which is electronically controlled by a variable PWM signal. By using a custom-built verification platform, we precisely measure the light intensity. This setup allows us to confirm that the light output increases linearly with increasing current, validating the electronic control mechanisms of the PPG system. Ensuring this linear relationship is vital for accurate PPG signal acquisition, as it directly impacts the consistency and quality of the physiological data collected.

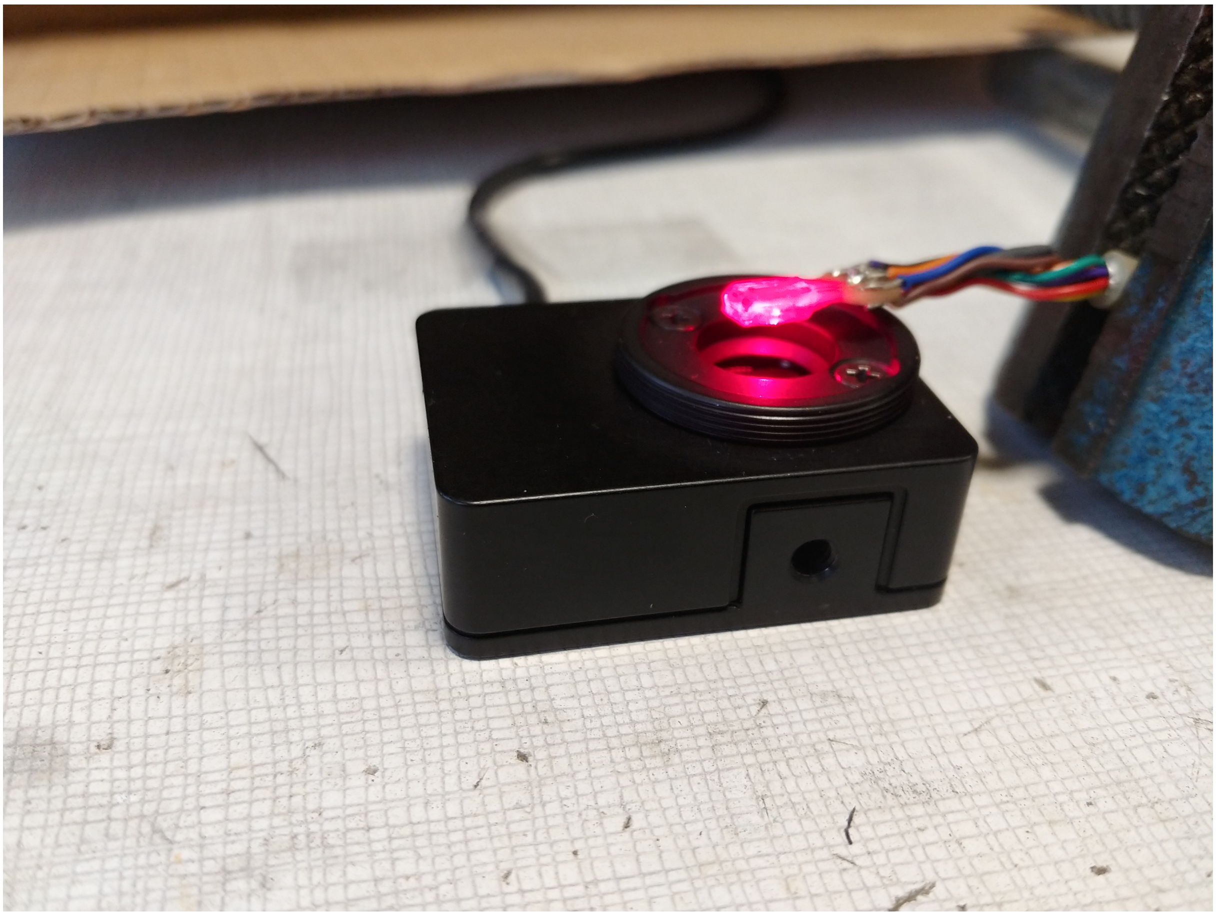

Figure 3.1 – Setup for measuring the linearity.

As we verified the linearity we determined the value of the parameter of the following equation :

$$\mathbf{PWM} \cdot \mathbf{A} + \mathbf{B} = \mathbf{Y} \tag{3.1}$$

All the LEDs's current are between 0 and 50 mA. The LED with a wavelength of 762 nm is tested three times. Two times with the same setup and one time with a different photodiode in order to test the precision of the setup and the influence of the photodiode. The following value written in Table 3.1. Additionally, the R^2 values are as in Table 3.2. The visual representation of the result is in Figure 3.2.

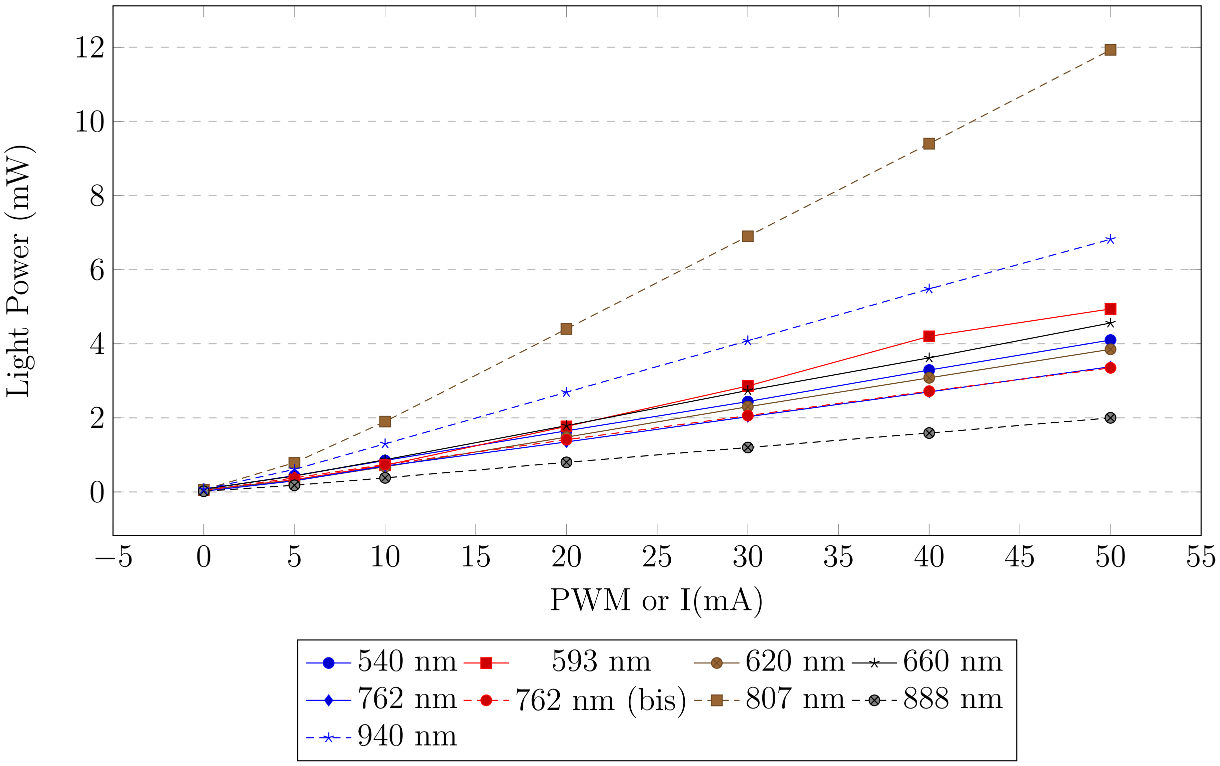

Figure 3.2 – Verification of the linear relationship between the PWM and light power

λ	$\mathbf{A}^\top$	**B**
542 nm	0.081	0.044
593 nm	0.103	-0.216
620 nm	0.078	0.090
660 nm	0.091	0.050
762 nm	0.068	-0.002
762 nm (bis)	0.066	0.060
762 nm (ter)	0.067	-0.009
807 nm	0.242	-0.776
888 nm	0.040	0.050
940 nm	0.137	-0.014

Table 3.1 – Table representation of $\mathbf{A}^\top$ and **B** values.

$\mathbf{R^2}$	**Value**
R^2_{542nm}	0.9998
R^2_{593nm}	0.9933
R^2_{620nm}	0.9987
R^2_{660nm}	0.9994
R^2_{762nm}	0.9997
$R^2_{762nm}(bis)$	0.9998
$R^2_{762nm}(ter)$	0.9994
R^2_{807nm}	0.9981
R^2_{888nm}	0.9996
R^2_{940nm}	0.9996

Table 3.2 – Table representation of $\mathbf{R^2}$ values.

As the R^2 are high, we deduce that the relation between the Light Power of the LED and the PWM input is indeed linear. The result between the different experiments on the LED 762 nm yield similar results, it is deduced that the setup is correct.

3.2.2 Comparison of quality between the probes' generations

We test the different generation of the probes in order to be sure that they give the same quality signal. In particular, it is the resin and the light protection that we want to test. There are two types of tests, one focussing on the performance of the LED and the others on the performance of the photodiodes. The results are as shown in Figure 3.7 and Figure 3.8 for the LEDs and in Figure 3.10 for the photodiodes

To obtain this figure, the following experiment is conducted : the LED is fixed at a given distance of a light sensor[48] (8 mm), as showed in Figure 3.3 and Figure 3.4, and then covers by an opaque box, as in Figure 3.5.

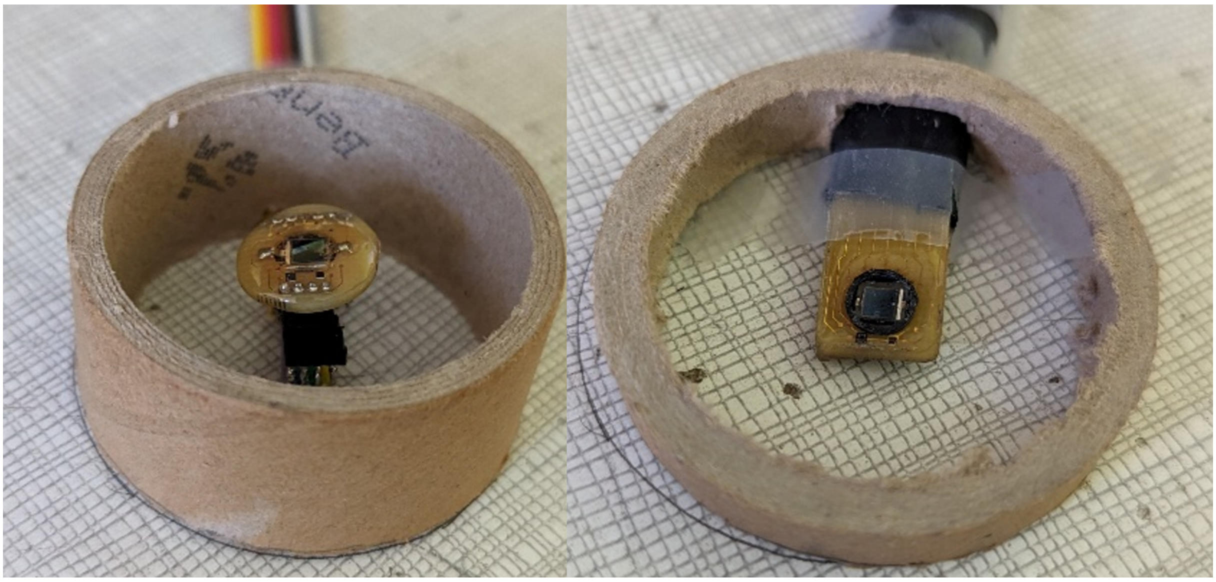

Figure 3.3 – Setup for fixing the distance between the Light Sensor and the LED in function of the connector.

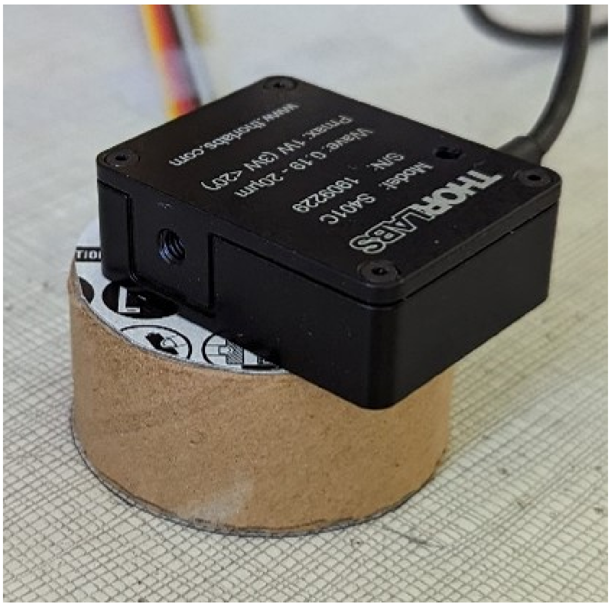

Figure 3.4 – Setup with the Light Sensor.

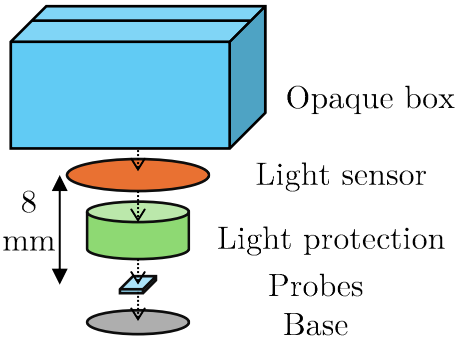

Figure 3.5 – Exploded view of the complete setup.

Then a constant current is applied, thanks to the circuit as represented in Figure 3.6 and once the value on the light sensor is stabilized, the value is written. This measurement is repeated for each LED of each probes of the generation tested.

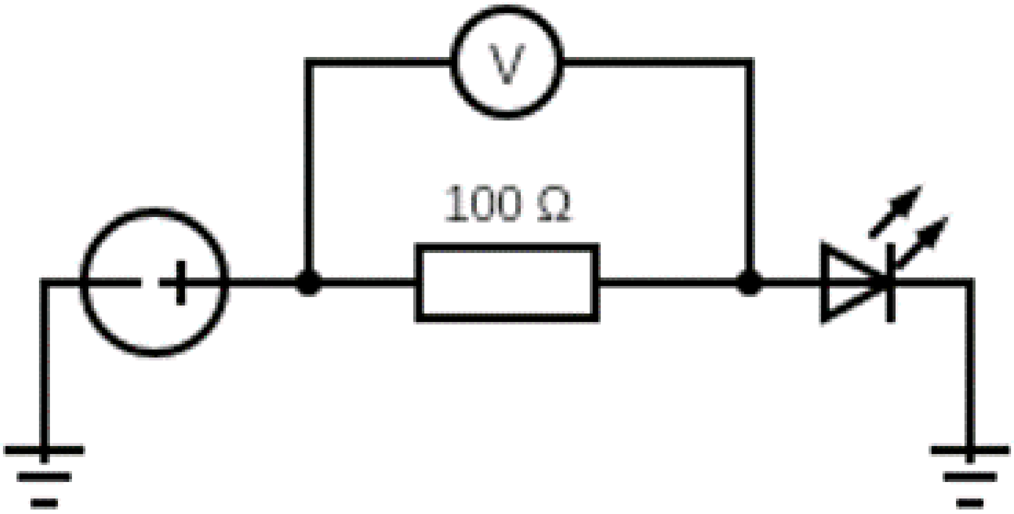

Figure 3.6 – Emission test circuit for the LED.

The generation tested are :

- Generation 1
- Generation 2.1.1

— Generation 2.1.2

Those three generations allowed for the test of the influence of resin, light protection and in addition the form of the probes as the Generation 1 has the optical resin and a rectangular shape whereas the Generation 2 has the medical resin and a circular shape. Additionally, direct light protection is available in some generations while absent in others. For more details, please refer to Table 2.1.

The Figure 3.7 is graphical result of the experiment for the LED with a visible light while Figure 3.8 represent the result for the LED with the infrared light. The current in the LED is represented on the x-axis, and the light intensity output on the y-axis. We observe that the linear relationship between the current in the LED and the light intensity is still true. Both the individual value and parameters of the linear equation of the different generation are close for most plots. One exception is the 660 nm LED, the Generation 1 seems less efficient, meaning that for the same current input, there is less light illumination.

The setup for the test of the photodiodes is similar to the one for the LED. The circuitry necessary to do the experiment change a bit to become as described on Figure 3.9.

On Figure 3.10, we see that the photodiode yield the same results.

3.3 Auto-calibration for finding the optimal parameters

3.3.1 DC calibration

As previously stated, the AC component of a PPG signal is about 5 percents of the full signal. For a lot of parameters, it is important to have a good quality of AC because often the analysis is based on the shape of the AC signal. Beside post acquisition processing, one improves the quality of the signal by carefully designing the PPG sensor itself. In order to achieve a greater quality of AC signal, we implemented two different technique of AC isolation and amplification.

As the signal need to be acquired, an ADC is used. Its limitations, notably in terms of quantification is one of the limiting factor. To overpass this limitation, one could use a ADC with a greater resolution, but this is not ideal for several reasons. Using such ADC, without doing anything else, means that only a small portion of this resolution is being used for useful signal and the greater the resolution the greater the consumption of power.

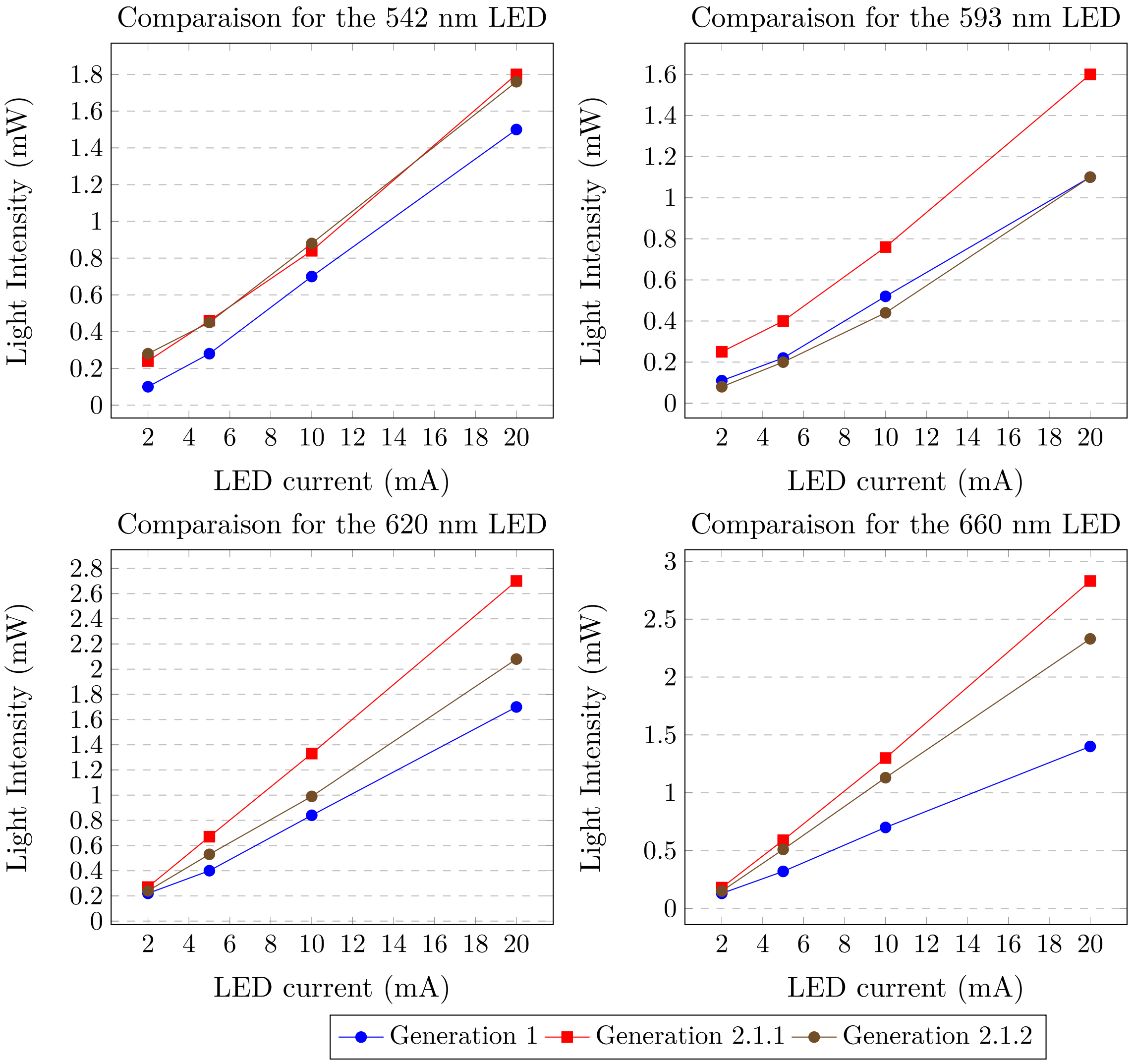

Figure 3.7 – Comparison between generation for the visible LED

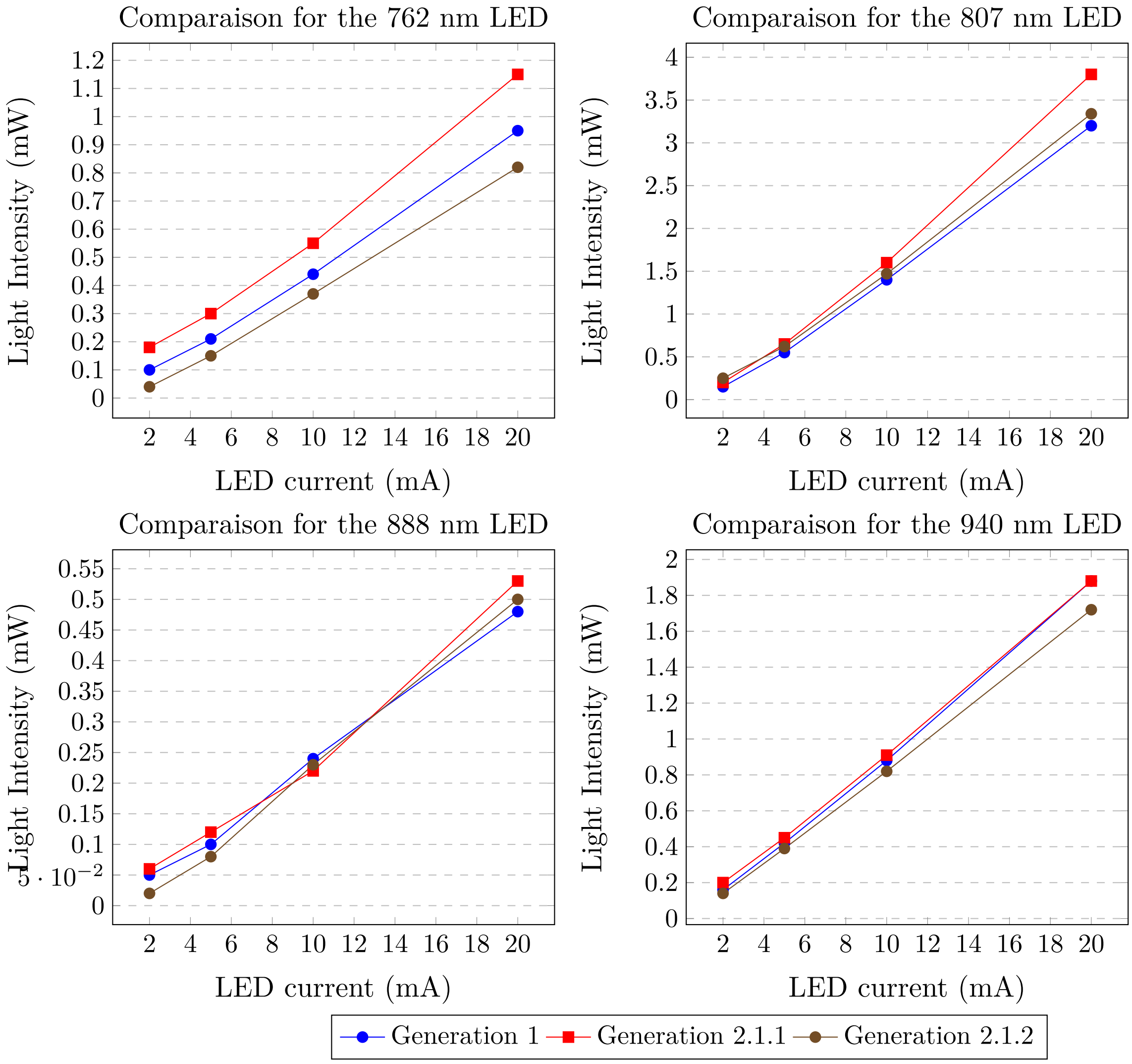

Figure 3.8 – Comparison between generation for the infrared LED

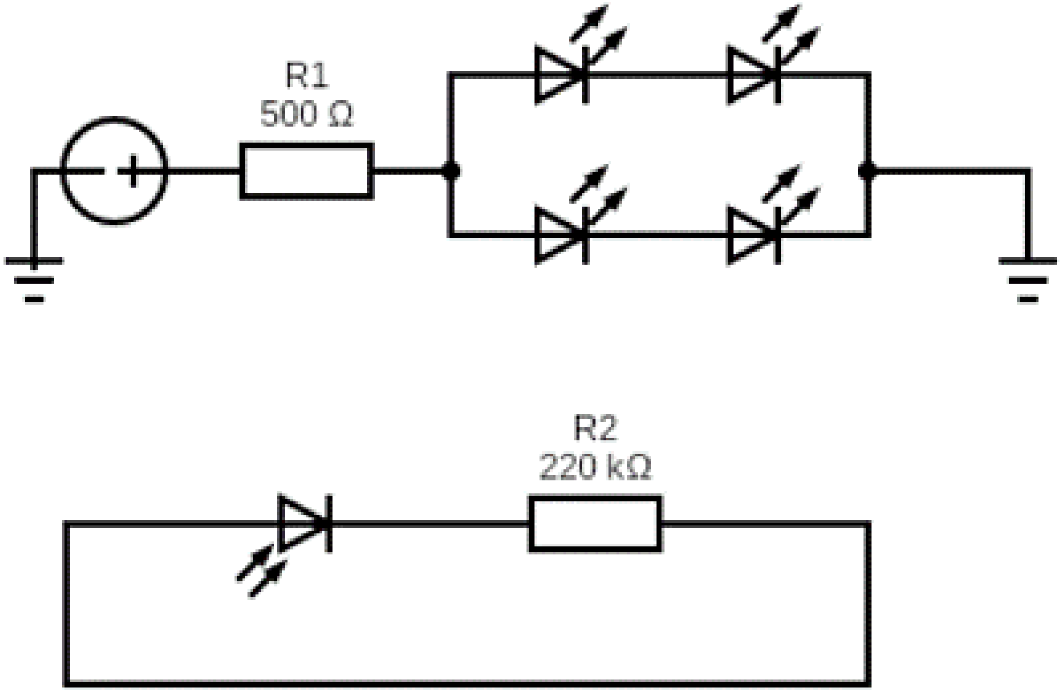

Figure 3.9 – Emission and reception circuit for the photodiode.

Also in some development kit, the ADC is already present and changing it is difficult.

Full Analog solution

Our first technique is to separate the AC from the DC signal and amplifying it before acquiring it. A useful analogy can be drawn from the field of photography. If a photo is taken with a certain lens and then digitally zoomed in using software, the resulting image is of poor quality. In contrast, if the photographer uses a more zoomed-in lens before taking the photo, thereby optimizing the optical setup prior to digitalization, the zoomed-in image has a much better quality.

The fact that we use 8 LEDs complicated the design as it is not possible to just use an analog filter as the signal represents the light coming from the 8 LEDs (after going thought the tissues) one after the other.

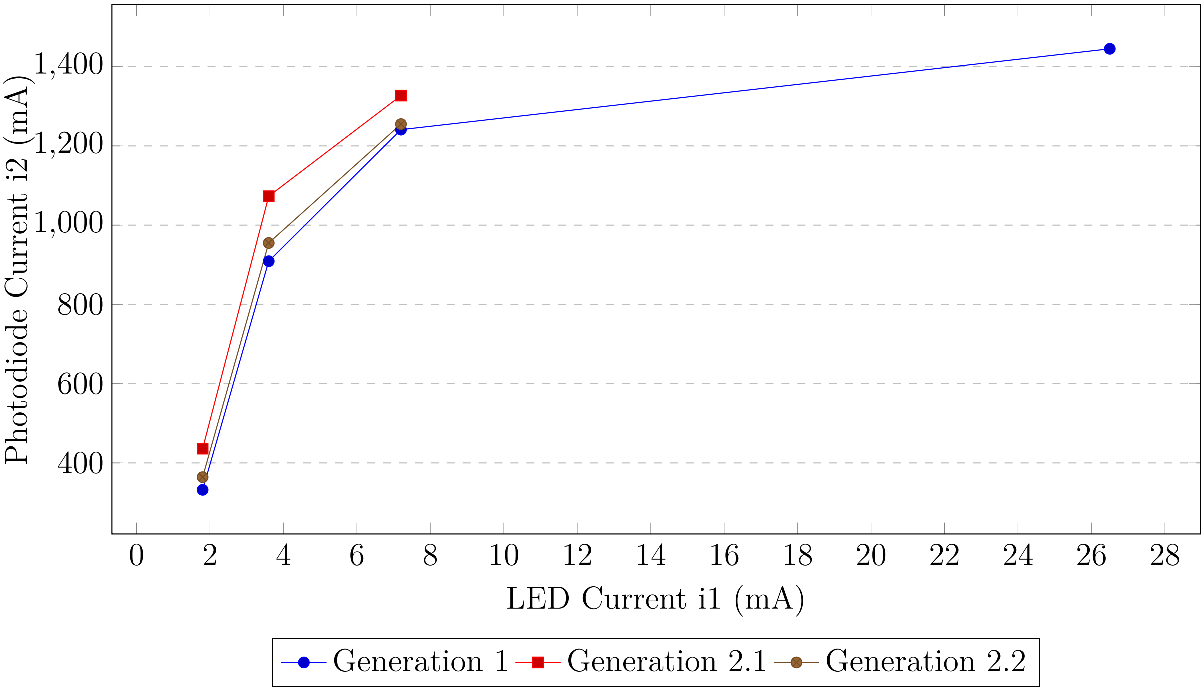

Figure 3.10 – Comparison of the photodiode between different Generations of probes

It is why the following design is created. It consists in 8 different circuits, each containing a capacitor, use as a DC memory. During a calibration phase, the current is going in each capacitor turn by turn (each capacitor is linked to a LED). Then during the measurement phase, the capacitor is used to subtract the DC component to the complete signal in order to obtain the AC part. This signal is then amplified by a factor 10 and centered around the middle of the ADC range (0.5V as the range is 0V to 1V).

This solution allows a good AC signal quality regardless of the DC value. In particular, thanks to the capacitor, even if the DC signal is greater than the maximum value of the ADC, we collect a good AC. The issue of this method is that the DC component used to extract the AC is fixed during the measurement phase however it is known that this value evolve, for example the breathing influence the DC component, so it means that the value of DC stored, after a time, doesn't correspond to the DC component of the signal and that might get the amplified signal out of bound of the ADC. Another inconvenient is that the DC calibration phase need to be long enough to charge each capacitor. Additionally, capacitors discharge gradually over time. For instance, after approximately 10 minutes, the DC output from the capacitors is lower than at the beginning of the experiment. This limitation are mitigated by performing regular recalibrations through consecutive small experiments rather than a single large one. However, a potential drawback is that each time a new experiment is initiated, the signal may not be accurately assessed during the calibration phase.

The difference between the use of the DC calibration and saving the total signal and then removing after the ADC the DC, is illustrated in Figure 3.11. For this experiment, the initial version of the DC calibration is used. A detailed description of the platform employed can be found in Subsection 2.4.3. On the x-axis, the time is measured in seconds, and on the y-axis, the amplitude of the signals ranges from 0 to 1. The blue plot represents the AC component extracted from the full signal measured by the ADC, while the orange plot represents the AC signal as measured directly by the ADC, with values scaled between 0 and 1 for comparison with the full signal. The first row of subplots displays the signals for the first seven LEDs, while the last row shows the results for the LED with a wavelength of 940 nm. It is evident from the figure that the orange plot is narrower and less noisy, indicating that DC calibration reduces quantification noise in the orange plot. This system enables a more precise definition of the signal's shape, allowing for analyze on it.

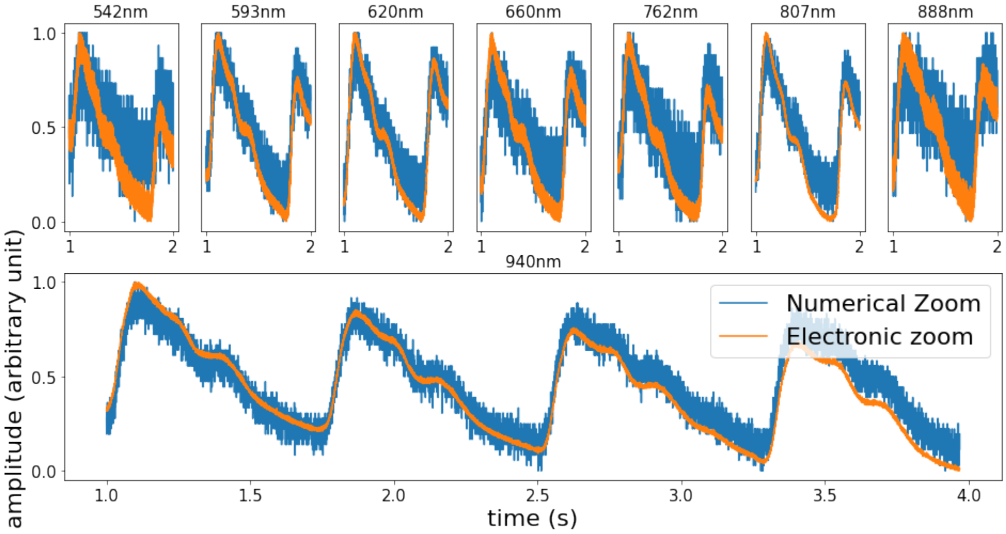

Figure 3.11 – Comparison between zooming before and after the digitalization.

Digital solution

To mitigate the limitations of the ADC, improvements have been made to the previous technique. The circuitry with the capacitors is replaced. Instead, a DC value is generated through a PWM, generated by the logic board, for each LED. Each time the AC signal of a LED is evaluated by the ADC, we look if this value is higher than the maximum (a fixed value) or lower than the minimum (a fixed value) authorized, if it is the case the DC value generated is respectively either decreased or increased. This ensures that the AC value stay within the bound of the fixed range (minimum and maximum). Here the values chosen are respectively 80 and 20 percents of the full range of the ADC

The issue of the method is that it creates "jumps" in the signal when the DC value generated is adjusted. To partially overcome this, a short calibration phase is implemented. During this phase, the lower and upper bound fixed are both 50 percents. This forced the generated DC to have a value that allows the AC to be as close as the middle of the ADC range as possible. During this phase, a lot of jumps occurs, it is why it is separated from the measurement phase.

The error that the "jumps" create is easily recoverable as the DC is also saved during measure. Simple signal processing on this signal can detect and correct the errors.

3.3.2 LEDs' Current Calibration

To accommodate various individuals and experimental conditions, we implement a meticulous light calibration process. This involves adjusting the current supplied to each LED, experimenting with different values to ascertain the optimal current for each LED. Given the unique characteristics and responses of each LED, they undergo independent calibration to identify their specific optimal current values. This individualized approach ensures the highest possible data quality by optimizing the light output for each experimental setup.

The range of current values used for calibration can be tailored to meet the specific requirements of the experiment. For example, if minimizing power consumption is a priority, the range of current values can be restricted accordingly. This flexibility allows us to strike a balance between optimal light quality and energy efficiency. Consequently, the calibration phase, known as LED calibration, is a critical step in our experimental protocol.

A key advantage of this calibration mechanism is its adaptability to a wide variety of experimental conditions. This includes variations in the illumination environment, changes in the distance between the LED and the photodiode, and physiological differences between subjects. By customizing the LED current settings, we ensure consistent and reliable measurements across diverse experimental setups.

Currently, the maximum range of current values that can be tested during calibration is from 0 to 99 mA. This range provides a broad spectrum for identifying the optimal operating point for each LED, ensuring that the platform accommodates a wide range of experimental requirements and conditions without damaging the LEDs.

Several methods have been employed to determine the most effective calibration approach:

- **Using only the AC value**: The AC value is calculated as the difference between the maximum and minimum readings, represented by the formula AC = max−min.
- **Using the inverse of the variation**: The variation is calculated in small windows (1/20 seconds). For each window, the maximum or mean of the variation is determined. The objective is to minimize the variation as it represents the "noise" or fluctuations in the signal, meaning that the inverse should be maximized.
- **Using the AC divided by the variation**: This method combines the AC value and the variation to provide a ratio that could assist in optimizing the calibration.

Among these methods, using only the AC value demonstrates the best results. This straightforward approach effectively maximizes signal strength, thereby enhancing the quality of the data collected.

For this experiment, the calibration is performed within a range of 0 to 99 mA for all LEDs. A 2-second signal is used for each calibration. The subject is seated, and all recordings are conducted on the finger.

In Figures 3.12 and 3.13, the results of the calibration are displayed, showing the results of the two indicators (AC and variation) for all possible calibrations across the 8 LEDs. On the x-axis, there is the current in the LED in mA or alternatively the PWM value as there is a correspondence between them. On the y-axis, the value of the indicators. The value of the variation and the AC, respectively on the left and right y-axis.

Figures 3.14 and 3.15 illustrates the signal selected by each indicator for each LED. For each indicator, the maximum is determined, the current I_{max} used to get this maximum is extracted. The signal obtain during the calibration using the same I_{max} current is chosen and plotted. Those operations are repeated for all the LED. On the x-axis, it is the time in seconds and on the y-axis is the amplitude of the signal, the range is the ADC's one, meaning from 0 to 65535.

This demonstrates that the AC value provides superior calibration results. We see that sometimes the variance indicator select a signal that doesn't contain information, but that has the less noise, as demonstrated, for instance, by the wavelength of 762 nm

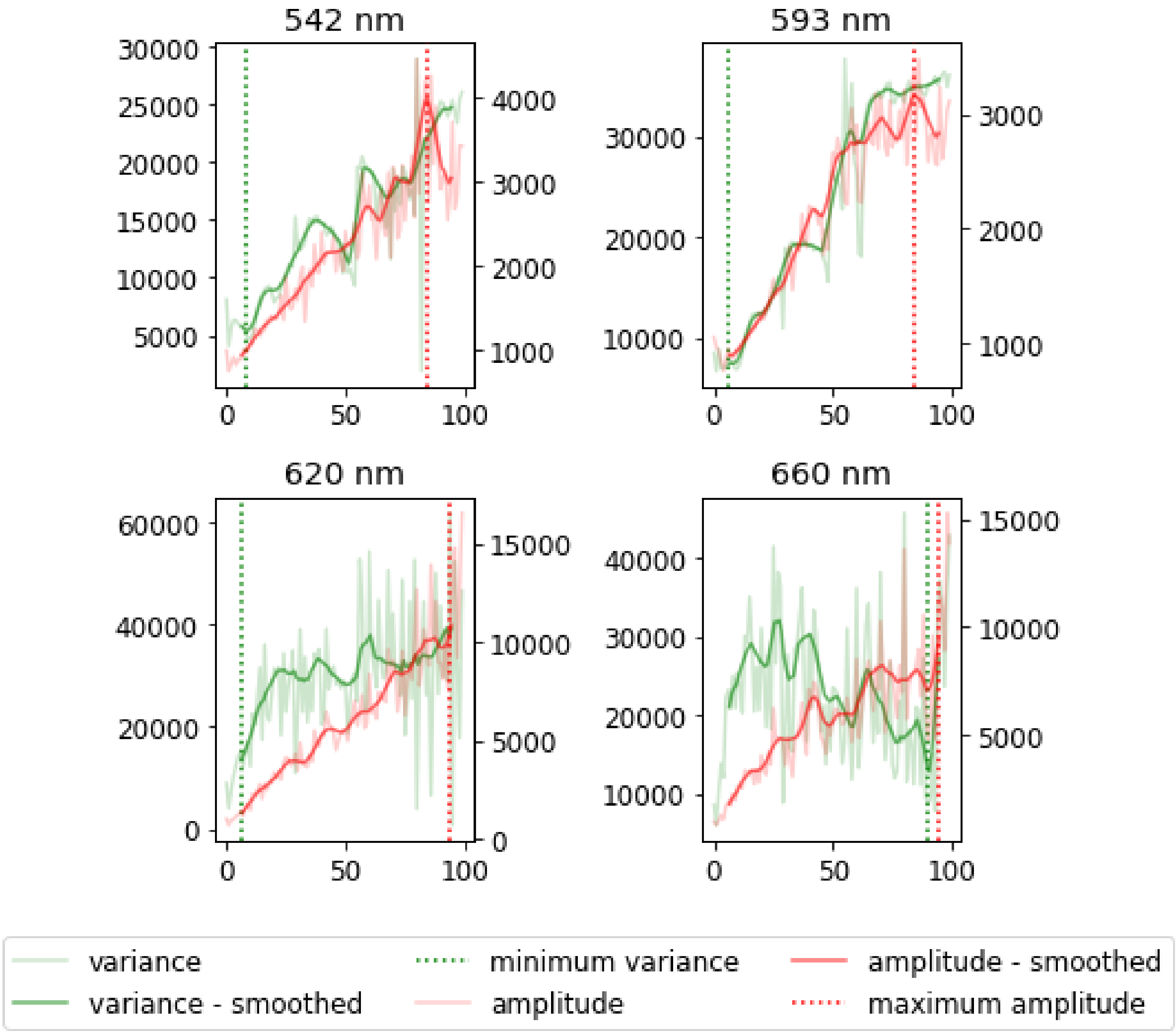

Figure 3.12 – Results of the calibration showing the performance of the three indicators (glsac and variation) for all possible calibrations across the 4 LEDs with visible wavelength.

in Figures 3.15.

To further improve the quality of the PPG signal, an optimal distance between the photodiode and the LED is investigated. This investigation is conducted through two distinct approaches. The first approach involved theoretical analysis using a custom-made simulation model, while the second approach entailed empirical experimentation.

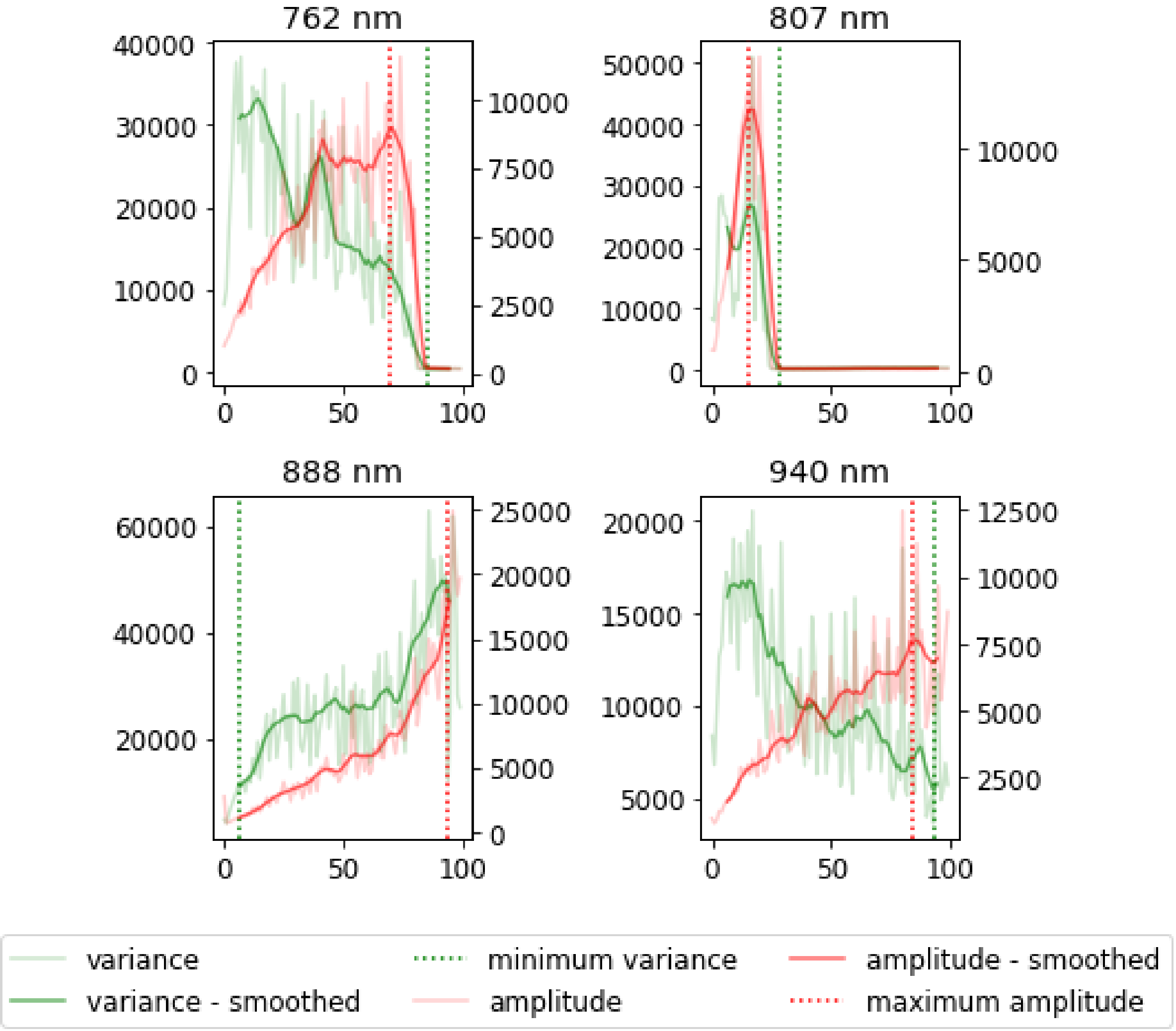

Figure 3.13 – Results of the calibration showing the performance of the three indicators (glsac and variation) for all possible calibrations across the 4 LEDs with infrared wavelengths.

3.4 Optimization of Photodiode-LED distance through simulation

In this section, we explore the simulation of photon propagation within biological tissues, focusing on the reflection-based PPG system. The tissue is modeled as a semi-infinite homogeneous medium to simplify the complexities associated with biological layers. The study uses a Monte-Carlo algorithm to simulate photon interactions within the tissue, capturing essential parameters such as the optical path length, wavelength, and depth of

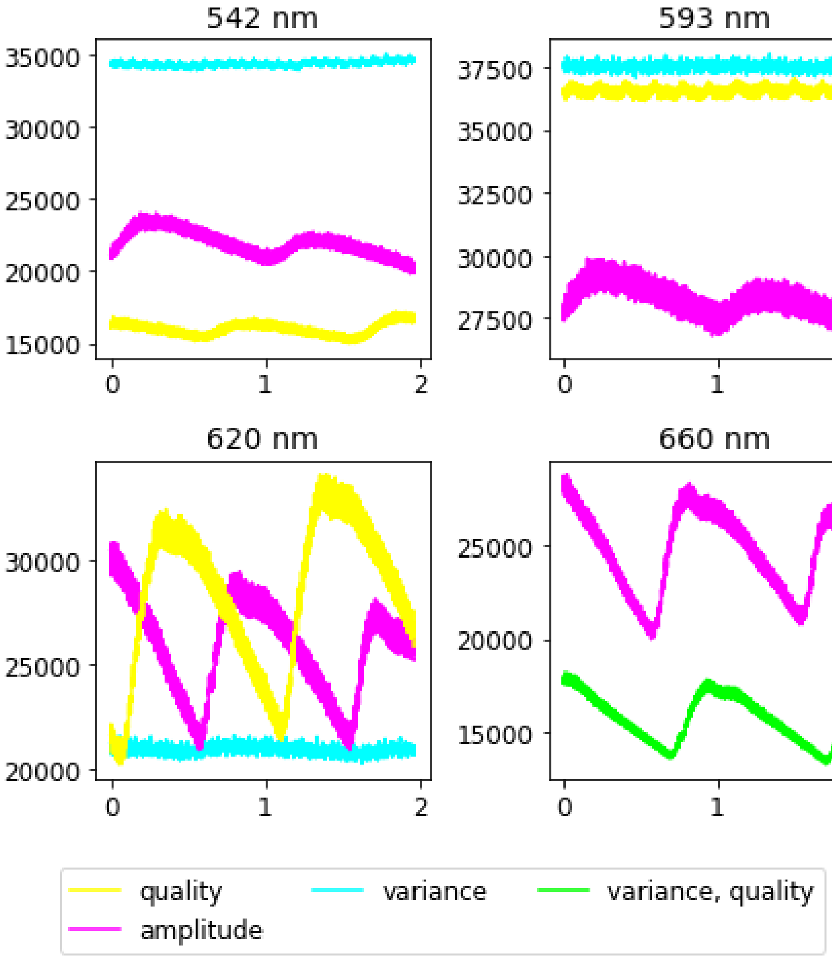

Figure 3.14 – Signal selected by each indicator for each LED (with visible wavelength), demonstrating the superior results provided by using the AC value.

photon trajectories. This algorithm was developed by Théo LANGÉ, during an internship under my supervision. These simulations are crucial for understanding the behavior of light as it interacts with tissue components, including epidermal cells and blood, while providing insights into how factors like blood volume and oxygen saturation influence photon capture. By examining these parameters, we aim to uncover relationships between the biological and physical properties and the efficiency of photon detection in a PPG system.

The tissue is modeled as a semi-infinite homogeneous medium in a Cartesian reference frame, as shown in Figure 3.16. We are considering here the case of a reflection PPG. We are therefore only interested in photons that emerge from tissues on the same side of the skin as the source. Furthermore, we consider that photons don't penetrate the skin

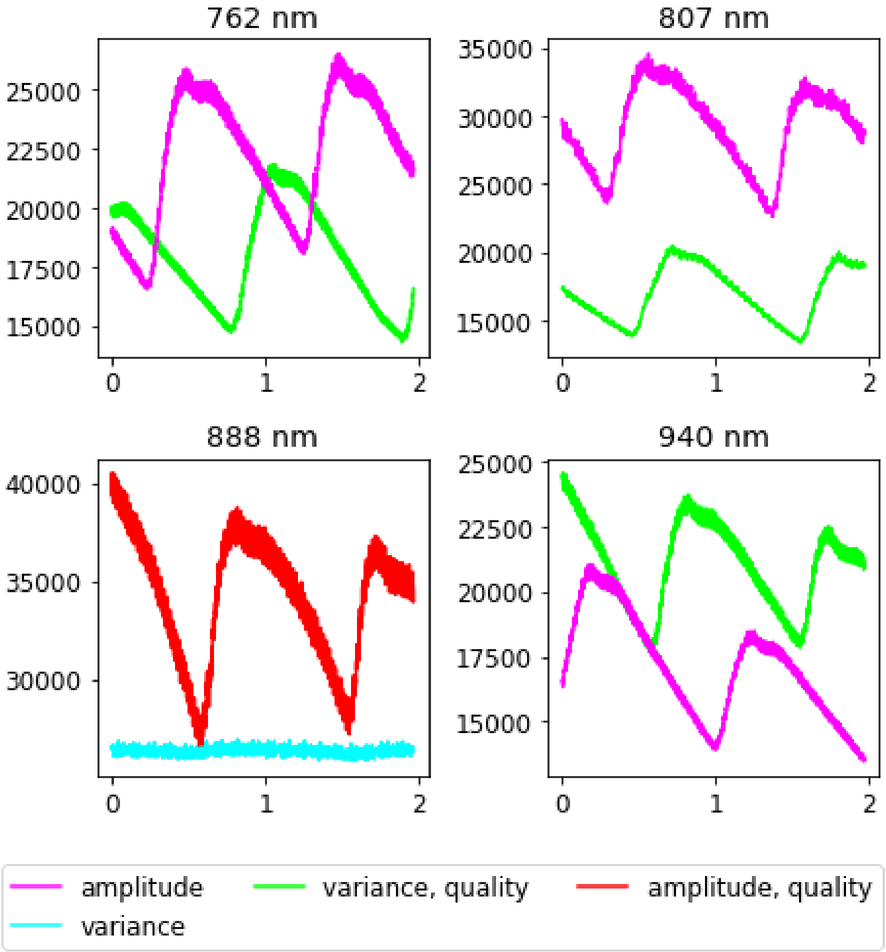

Figure 3.15 – Signal selected by each indicator for each LED (with infrared wavelength), demonstrating the superior results provided by using the AC value.

sufficiently to emerge at the opposite end, even for thin site like the fingers or earlobes. Moreover, to simplify the study, we have chosen to model the tissue as a homogeneous medium composed of epidermal cells and a certain amount of blood. It is possible to consider additional layers of tissue; however, this requires precise data on the layers in question. Determining the exact size and composition of these layers for an individual is challenging, as these values vary significantly. Consequently, we chose to maintain a more generalized approach.

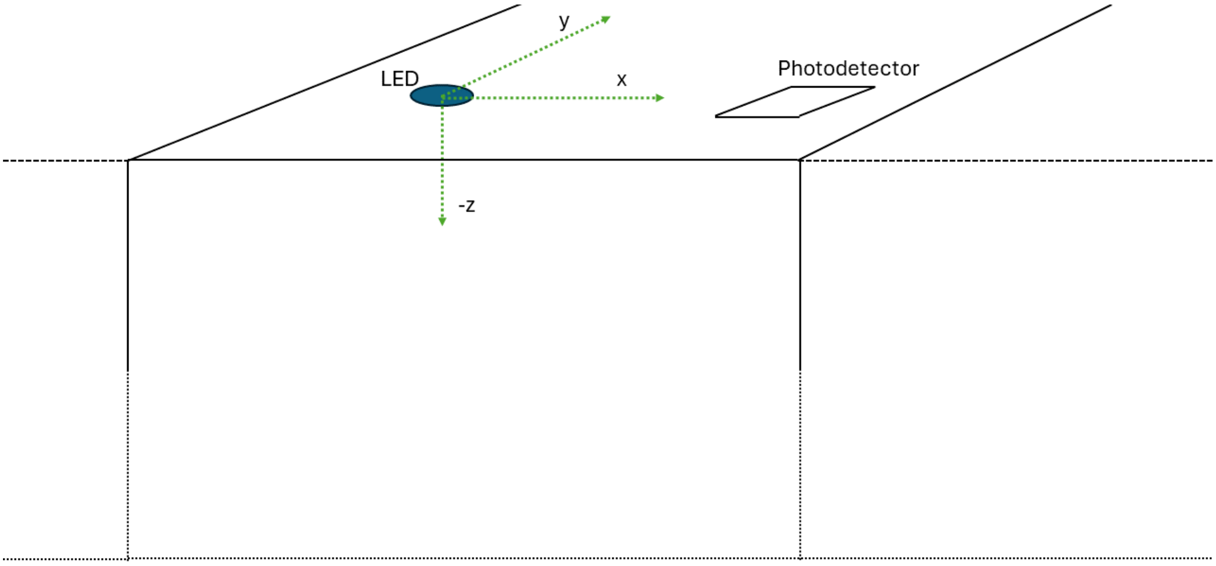

Figure 3.16 – Semi-infinite homogeneous medium with LEDs and photodetector

3.4.1 Calculation method

A Monte-Carlo algorithm is used to simulate the propagation of photons through an absorbing and scattering medium. The aim is to empirically determine the optical path taken by the light before it is captured. The aim of this study is to determine the link between the different parameters such as the distance between the emission and reception of the light, the wavelength of the light, the length, and the depth of the trajectory of the photons and the biological parameters.

3.4.2 Specificity

In the simulation, a total of 380,000 photons was emitted for each wavelength from the position of the LED. The photodetector has a length in x and y of 2.65 mm. A photon is declared captured by the photodetector if its last position respected the conditions written in the equation 3.2 where d is the distance between the photodetector and the

LEDs, x,y and z are its position on the respective axis in millimeters.

$$\begin{pmatrix} abs(x-d) < 1.325 \\ abs(y) < 1.325 \\ z = 0 \end{pmatrix} \tag{3.2}$$

The wavelengths consider are the same as in the device, meaning 542 nm, 593 nm, 620 nm, 660 nm, 762 nm, 807 nm, 888 nm and 942 nm.

3.4.3 Results

Influence of Volumic Fraction of Blood and Oxygen Saturation

In order to establish the blood volumetric fraction in tissue and the oxygen saturation of blood for the remainder of the study, a preliminary analysis was conducted to examine their influence on the number of photons captured by the photodetector.

In our experiments, we investigated the influence of the volumic fraction of blood (V) and oxygen saturation (SpO_2) on the number of photons captured. These experiments are conducted across all the wavelengths. We focused on the effects of V and SpO_2 to determine their impact.

The volumic fraction of blood (V) varied from 0.01 to 0.02 in increments of 0.001 and represent the relative quantity of blood present in the tissue. The oxygen saturation (SpO_2) varied independently, from 0.8 to 1.0 in increments of 0.02. The distance between the photodetector and the LED is set at 3.9 mm, each configuration is tested for each wavelength, and 20,000 photons are sent for each configuration.

To assess the relationship between the blood volumetric fraction (V) and oxygen saturation (SpO_2) with the number of photons captured, we computed the **Pearson correlation coefficients** for each variable at every wavelength. The Pearson correlation coefficient (r_{xy}) quantifies the linear relationship between two variables (x and y), where $r_{xy} = 1$ indicates a perfect positive correlation, $r_{xy} = -1$ indicates a perfect negative correlation, and $r_{xy} = 0$ indicates no linear correlation. The equation used for calculating r_{xy} is given by Equation 3.3.

$$r_{xy} = \frac{\sum(X_i - \bar{X})(Y_i - \bar{Y})}{\sqrt{\sum(X_i - \bar{X})^2 \sum(Y_i - \bar{Y})^2}} \tag{3.3}$$

The correlation values for V and SpO_2 with the number of photons captured (N_p),

λ	542	593	620	660	762	807	888	942
$r_{N_p,V}$	0.008	0.011	0.51	0.003	0.393	0.024	0.037	0.013
r_{N_p,SpO_2}	0.0	0.003	0.016	0.011	0.004	0.0	0.038	0.003

Table 3.3 – Correlation coefficients between input variables and number of photons captured.

respectively $r_{N_p,V}$ and r_{N_p,SpO_2}, presented in Table 3.3, are close to zero for most wavelengths, indicating a weak or no linear relationship between the variables and the number of photons captured.

This analysis reveals that the volumic fraction of blood (V) and oxygen saturation (SpO_2) have minimal influence on the number of photons captured. The correlation coefficients for both variables are low, suggesting that variations in V and SpO_2 do not significantly impact the simulation outcomes.

This finding is crucial for simplifying our model, as it indicates that the number of photons captured is relatively insensitive to changes in V and SpO_2. Therefore, these variables are considered less critical in the context of our simulation, allowing us to focus on other factors that have a more substantial impact on the results, such as the wavelength of the light used.

Figure 3.17 illustrates the scatter plots and affine functions for both V and SpO_2 across the different wavelengths. The solid lines represent the best-fit linear models, highlighting the relationship between each variable and the number of photons captured.

When not separating the results by wavelength, the analysis of the correlation coefficients, as showed in Table 3.4, reveals that the volumic fraction of blood V and oxygen saturation SpO_2 have negligible impacts on the number of photons captured, with correlation coefficients of 0.0018 and -0.0005, respectively. In contrast, the wavelength (λ) exhibits a strong positive correlation with the number of photons captured, with a correlation coefficient of 0.9233. This indicates that variations in wavelength significantly influence photon capture efficiency, whereas changes in the volumic fraction of blood and oxygen saturation do not substantially affect the outcome.

Parameter	V	SpO_2	λ
Correlation Coefficient	0.0018	-0.0005	0.9233

Table 3.4 – Correlation coefficients of parameters with the number of photons captured

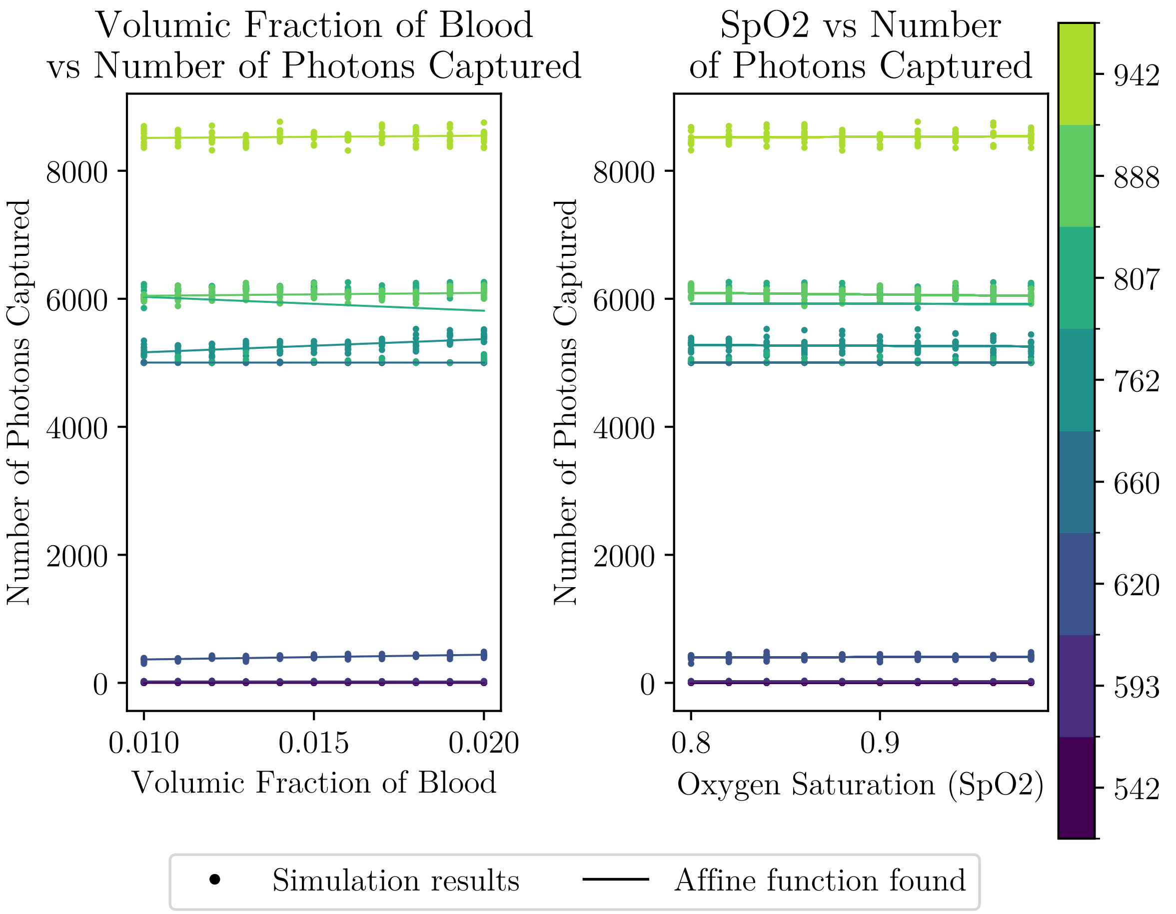

Figure 3.17 – Scatter plots showing the relationship between volumic fraction of blood (V) and oxygen saturation (SpO_2) with the number of photons captured.

Trajectory of the photons

If we look at the trajectory of the photons, we obtain the following Figure 3.18. This is obtained by sending 30000 photons (with the wavelength 542 nm). We observe that the trajectories of the photons create a half sphere with the center being the emission point, the LEDs position.

When only focusing on the photons that are captured, at the end of their trajectory, by the photodiode, we obtain Figure 3.19.

For this experiment, we count the number of photon arrived into the photodetector for each wavelength and calculated the chance for a photon to get to the photodetector for different photodiode/LED distance.

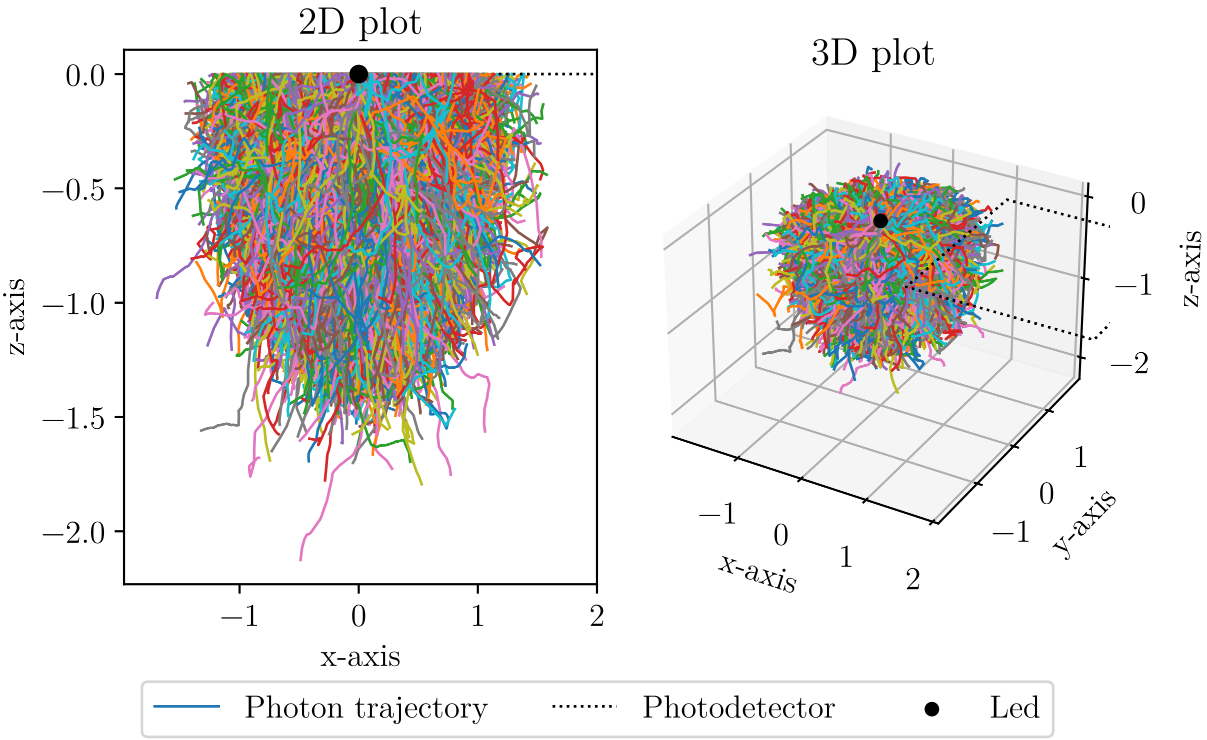

Figure 3.18 – Photons trajectories with a wavelength of 542 nm (simulation)

The Figures 3.20 and 3.21 represent the chance for a photon to be captured by the photodetector. As expected the more distance between the photodetector and the LED, the fewer photons arrived to the photodetector. We also see that the greater the wavelength, the more in depth it penetrates, but it is less efficient at shorter distance(less than 2 mm).

Depth of the photon trajectory

Not all photons captured by the photodetector are relevant. Specifically, those that do not pass through veins or arteries do not affect the AC of the signal, as variations in blood within these vessels do not influence their likelihood of being captured. Therefore, it is essential to study the depth to which the captured photons penetrate.

The Figure 3.22 illustrates the distribution of events in a 2D plane, revealing a characteristic "banana" shape. This indicates that the trajectory of photons within the tissue resembles that of a banana, with the attained depth correlated, among other factors, to the distance between the LED and the photodiode. To explore this phenomenon further,

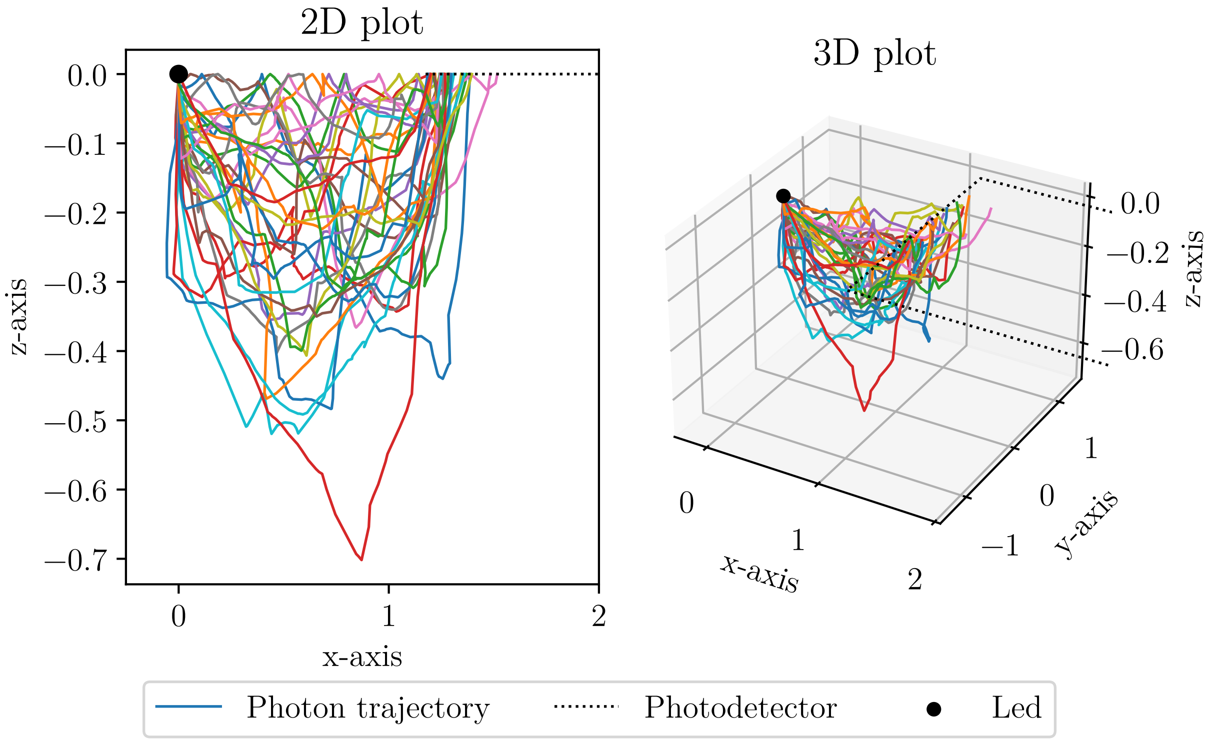

Figure 3.19 – Photons trajectories of the photons captured by the photodetector, being at 2.5 mm of the LEDs and LED with a 542 nm wavelength (simulation)

we examine the maximum depth reached by the photons during their trajectory. We see in Figure 3.23 the distribution of depth. We see the influence of the wavelength on the number of photon going through the vascular system. Indeed, the greater the wavelength, the deeper the penetration into the tissue. Additionally, for longer wavelengths, the number of photons reaching a fixed depth is higher compared to shorter wavelengths.

We also study the influence of the distance between the photodetector and the LED on the depth reached by the photon as shown in Figure 3.24.

We observe that the shorter the LED-photodiode distance, the greater the number of photons reaching any fixed depth. This result was expected, as increasing the distance between the emitter and receiver increases the likelihood of photons being absorbed along the way.

These findings, combined with knowledge of biological tissue structure (such as the depth of the blood vessels), can help estimate the proportion of photons that theoretically contribute to the AC component of the PPG signal. According to our results, regardless of the blood vessel depth, a shorter LED-photodiode distance and longer wavelengths

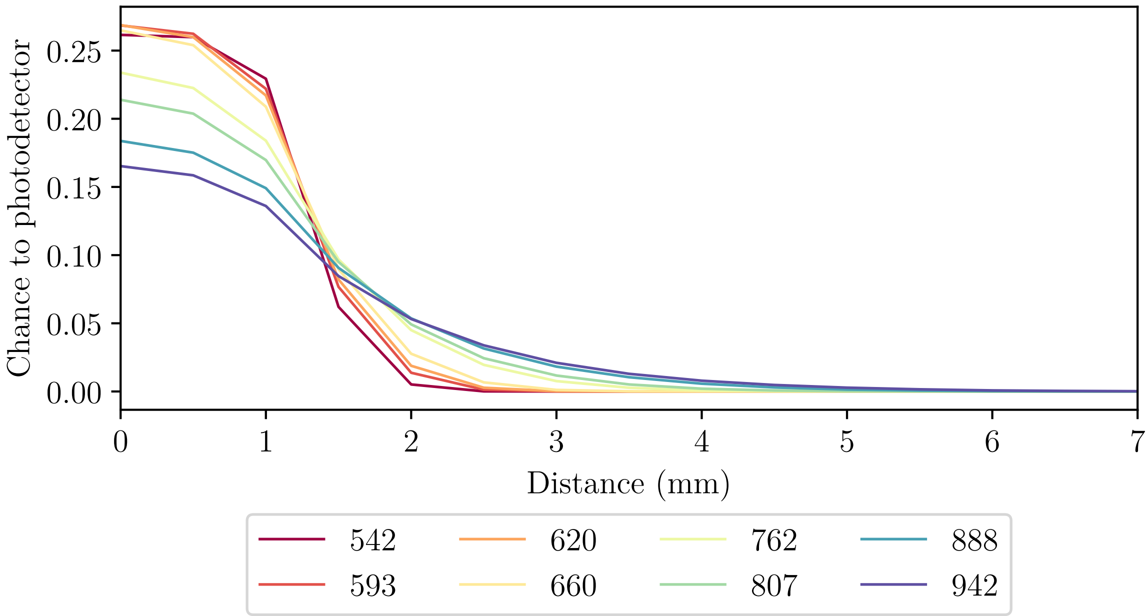

Figure 3.20 – Chance for a photon to be captured (simulation)

should yield the best outcomes.

3.5 Optimization of Photodiode-LED Distance Through Experimentation

3.5.1 Methodology and Sensor Configuration

Our objective is to validate simulation outcomes with empirical data, aiming not only for optimal data quality but also to quantify the associated energy expenditure, particularly in LED usage. Additionally, we sought to characterize the performance of our sensor. To achieve this, we developed a custom sensor and conducted data collection.

Accuracy challenges

To obtain the most accurate data possible, we engineered an adjustable-distance PPG system. This system had a dual purpose: to precisely determine the distance between the LEDs and the photodiode and to maintain this distance throughout the experiment.

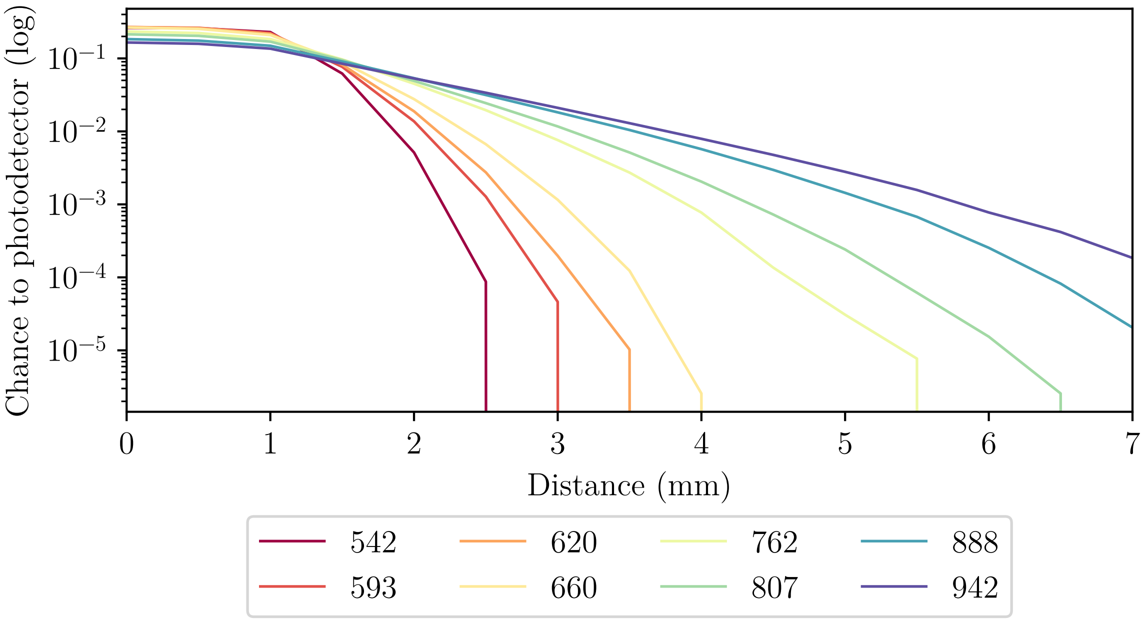

Figure 3.21 – Chance for a photon to be captured (log scale) (simulation)

During initial experiments, it is observed that improper fixation of the LED platform led to movement relative to the photodiode platform, introducing additional uncertainty regarding the distance. Moreover, it is imperative to ensure that there is no angular misalignment between the LED platform and the photodiode platform.

Given that the entire system needed to be affixed to a person, either on the finger or arm, it is essential for it to maintain a slim profile. The component responsible for distance adjustment needed to be easily manipulated while providing secure fixation once the desired distance is set.

3D-Printed Adjustable-Distance PPG

The distance regulation mechanism comprises three components. The first component is a hollowed parallelepiped along its central axis. The second component is a platform connected to the third component, which is a screw.

The screw is securely housed within the hollowed section of the first component. The photodiode's PCB is affixed to the first component, while the LED's PCB is attached to the second component. A railing system is integrated into the first component to prevent

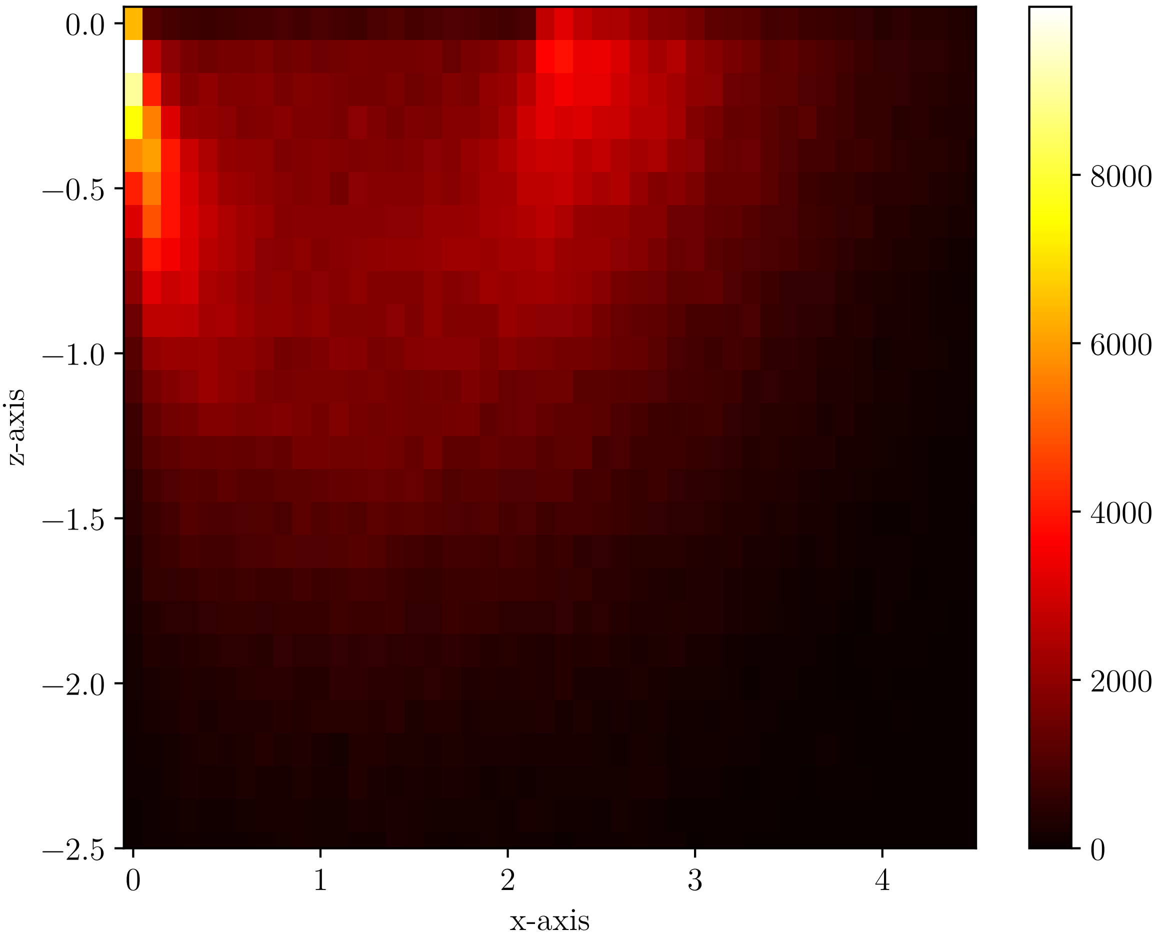

Figure 3.22 – Event Distribution during the Trajectories of Photon (2D) (simulation)

rotation of the second component relative to the first.

By turning the screw, which passes through both platforms, the distance between them can be adjusted. Each rotation of the screwdriver results in incremental convergence or divergence of the two platforms, with adjustments as fine as 0.5 mm per complete screw turn, enabling precise control over the distance between the photodiode and LEDs.

The complete mechanism can be seen in Figure 3.28. In particular, the end of the screw can be seen in Figure 3.27. The sliding PCB and the rail can be best appreciated in Figure 3.25 and Figure 3.26.

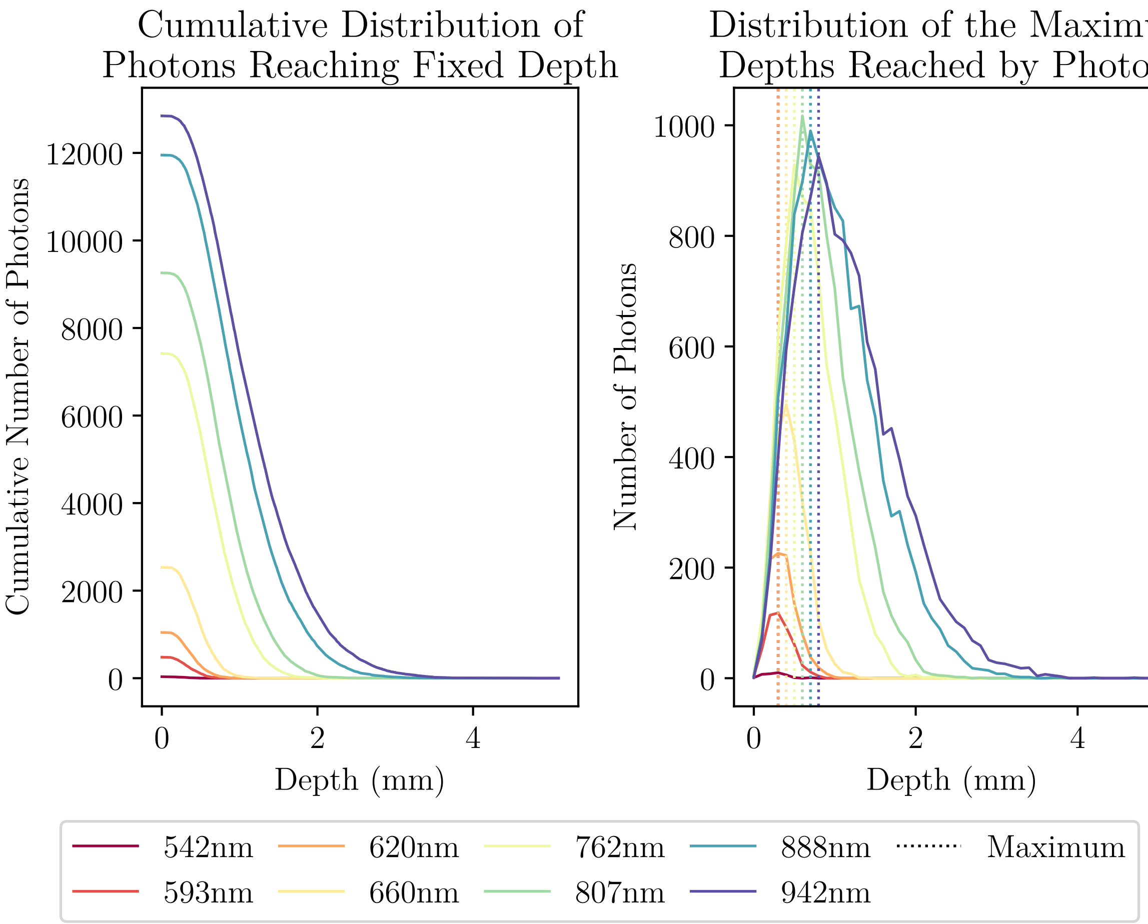

Figure 3.23 – Distribution of the Maximum Depths Reached by Photons (simulation)

Adaptation for Multiple Wavelengths and LED Organization

Recognizing the necessity of spatial organization to accommodate multiple LEDs emitting distinct wavelengths, we devised a strategic arrangement. Due to the eight wavelengths utilized, it is not feasible for all LEDs to be equidistant from the photodiode and aligned with the screw axis. Thus, LEDs are organized into four rows, as depicted in the accompanying Figure 3.29. This figure is the footprint of the PCB on which the LEDs are. In addition, the photography of the PCB is given in Figure 3.30.

Given knowledge of the distance between the LED PCB edge and the photodiode center, determining the distance between the LED PCB edge and each LED allowed calculation of the total distance for all LEDs.

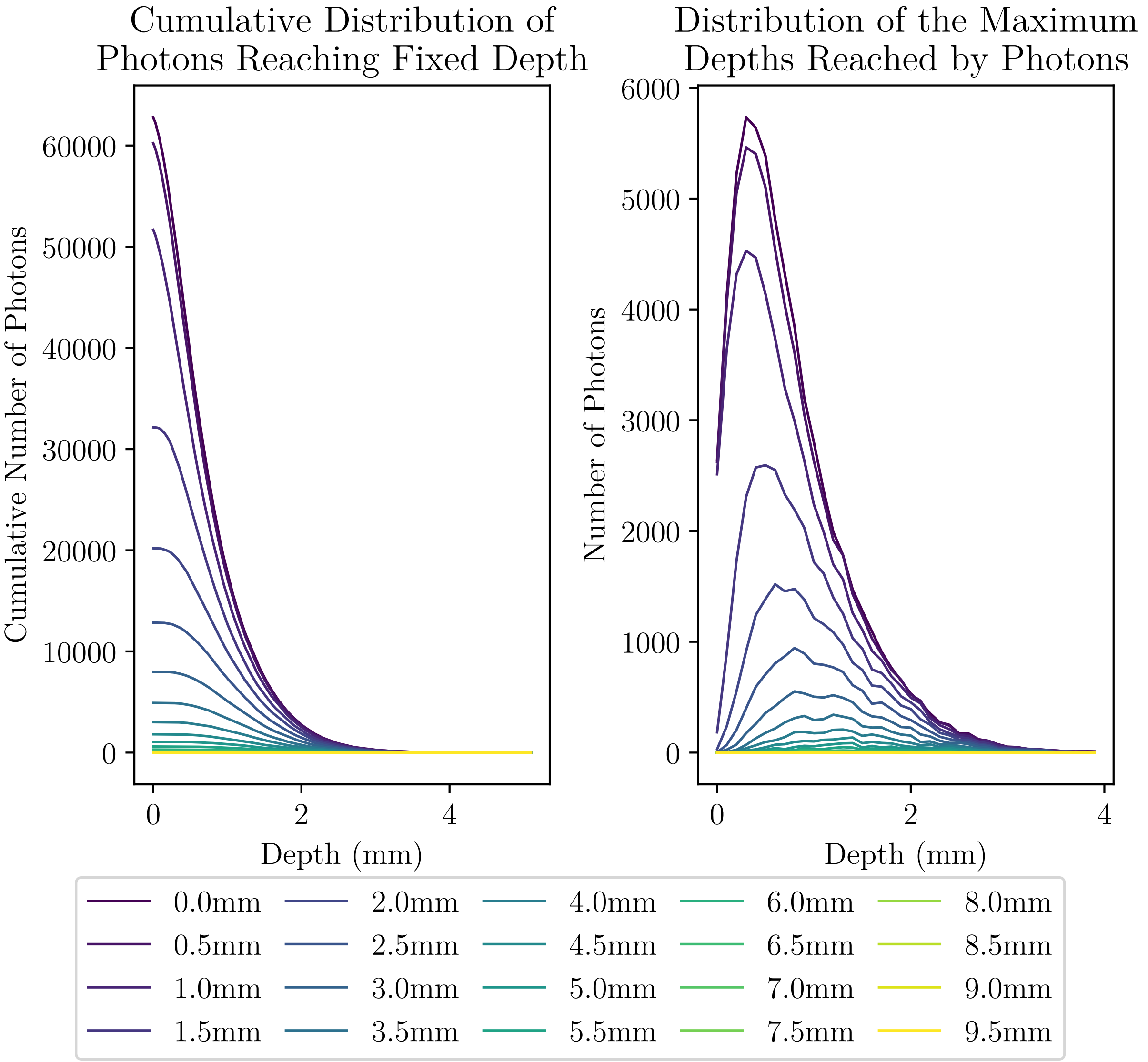

Figure 3.24 – Distribution of the Maximum Depths Reached by Photons (simulation)

Range of Distance

An objective is to ensure a broad range of distances. The distance between the photodiode and the edge of the LEDs' PCB could vary from 3 mm to 12 mm.

Difficulties due to biology

Each current value for the LEDs from 0 mA to 99 mA are tested successively, this is called LEDs' current calibration, for each length between the photodetector and the

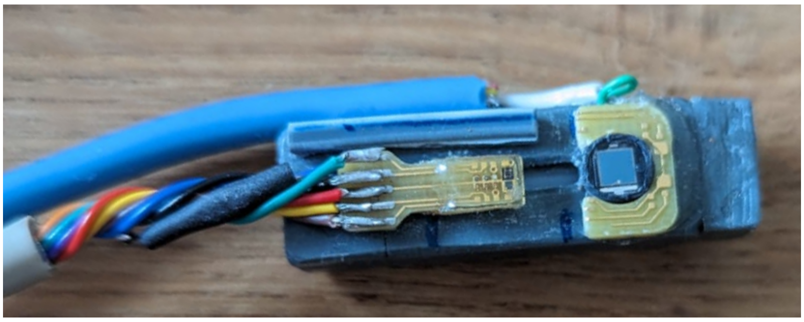

Figure 3.25 – Top of the sensor

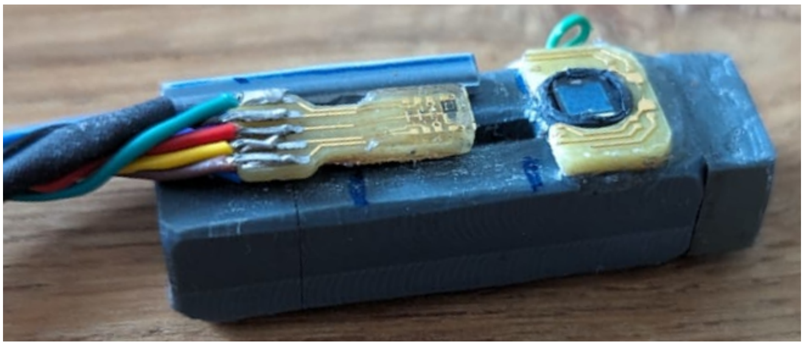

Figure 3.26 – Side of the sensor

Figure 3.27 – Screw side of the sensor

Figure 3.28 – Sensor for evaluating the quality over the distance

LEDs. However, the duration of calibration, currently at five minutes, posed challenges as physiological parameters fluctuate over time. In this experiment, the range of distance is 3 mm to 7.75 mm with a 0.25 mm step, which corresponds to half a revolution of the screw. This means that between the beginning of the experiment and the end, at least 100 minutes passed even without accounting for the time required to adjust the distance between calibrations. This difference could influence signal amplitude, potentially confounding interpretations regarding distance-related quality changes.

Subjects are instructed to minimize movement and abstain from caffeine or other substances known to affect signal stability during experiments.

3.5.2 Comparison with simulation results

Protocol

All measurements and calibrations in this experiment are conducted on the finger. The experiment consists of four distinct phases. In the first phase, a series of calibrations

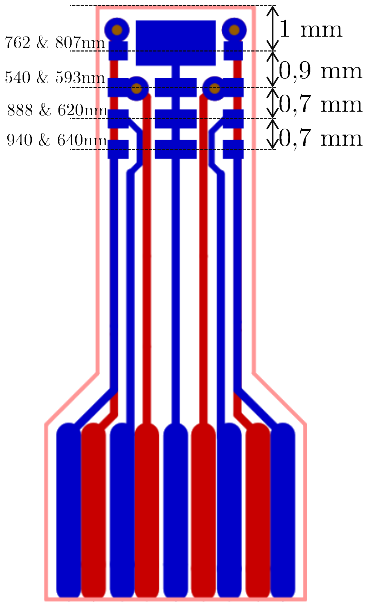

Figure 3.29 – Illustration of the LED's PCB for the distance sensor, highlighting the measured distances between components.

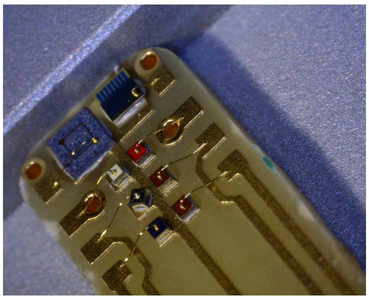

Figure 3.30 – Photo of the LED's PCB for the distance sensor

are performed while progressively increasing the distance between the photodetector and the LED. The third phase follows a similar approach with incremental distance increases. In contrast, the second and fourth phases involve decreasing the distance between the photodetector and LED. The algorithm 1 describes this experiment, where n_{part} represents the part we are currently executing, d_{min} is the distance minimum between the edge of the two PCB, d_{max} is maximum of this distance, d is the current distance, LED_{cur} is the current in mA in the LEDs.

Algorithm 1 Experiment decomposition

```
$d \leftarrow 3$
$d_{min} \leftarrow 3$
$d_{max} \leftarrow 8$
$LED_{cur} \leftarrow 0$
for $n_{part} = 1, 2, 3, 4$ do
    if $n_{part}$ is odd then
        while $d \neq d_{max}$ do
            $d \leftarrow d + 0.25$
            for $LED_{cur} = 0, 1, 2, \ldots, 99$ do
                Test the calibration with the LED currents equal to $LED_{cur}$.
            end for
        end while
    else if $n_{part}$ is even then
        while $d \neq d_{min}$ do
            $d \leftarrow d - 0.25$
            for $LED_{cur} = 0, 1, 2, \ldots, 99$ do
                Test the calibration with the LED currents equal to $LED_{cur}$.
            end for
        end while
    end if
end for
```

Link with the simulation

As shown previously, the current in the LEDs is linearly correlated to the light emitted, but not with the same coefficient for all the LEDs. This makes the comparison between wavelengths somewhat challenging. As the same current in the different LEDs doesn't guaranty the same luminous output, the previous result of Figures 3.31 and 3.32 need to be adjusted to be able to compare the results for the different wavelengths and in particular to compare those results with the simulation described in Section 3.4. Using the result

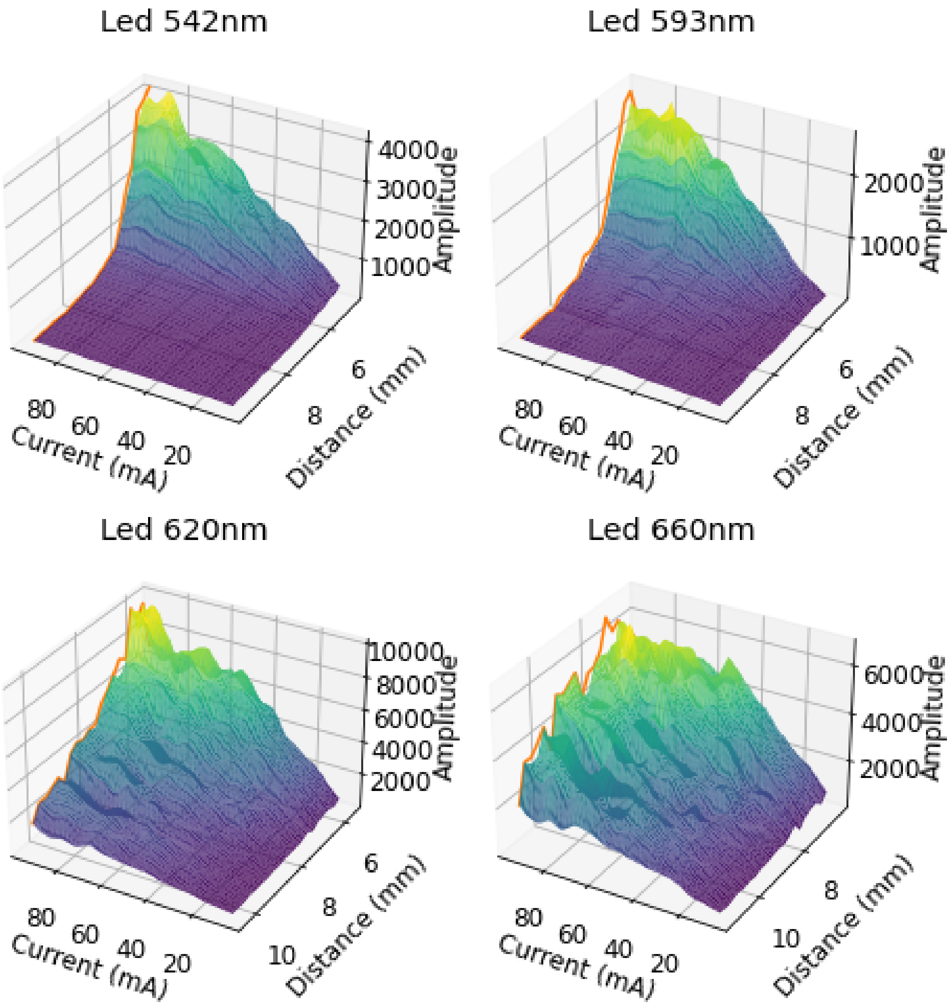

Led 542nm

Led 593nm

Led 620nm

Led 660nm

Figure 3.31 – Influence of distance and current in the LED over the quality of the PPG signal, for the visible wavelengths

of Section 3.2, we adjust the result. Indeed, thanks to the affine function found for each wavelength, we transform the current in the LEDs into the light output. The Figures 3.33 and 3.34, show the influence of the distance (color coded in the figure) and the current in the glsled over the quality (mesured in AC). As the results in the simulation used the number of photon, it is necessary to convert the optical power in number of photons sent. The number of emitted photons N during the time t in seconds (s) is given by :

$$N = \frac{E_{\text{total}}}{E} \tag{3.4}$$

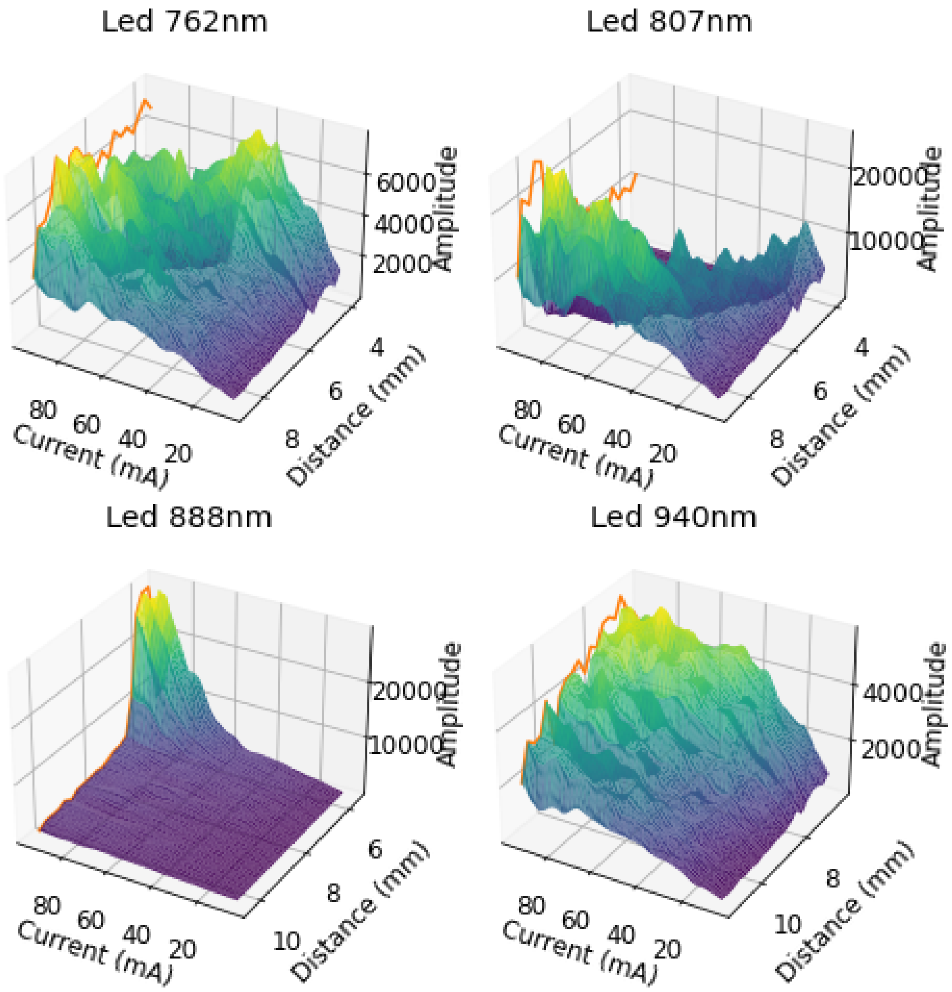

Figure 3.32 – Influence of distance and current in the LED over the quality of the PPG signal, for the infrared wavelengths

where E is the energy of a single photon and E_{total} is the total energy emitted by the LED during the time t.

The energy of a single photon E is given by:

$$E = \frac{hc}{\lambda} \tag{3.5}$$

The total energy E_{total} emitted by the LED over time t is given by:

$$E_{\text{total}} = P \times t \tag{3.6}$$

By combining the equations 3.4, 3.5 and 3.6, we obtain a new equation for the number

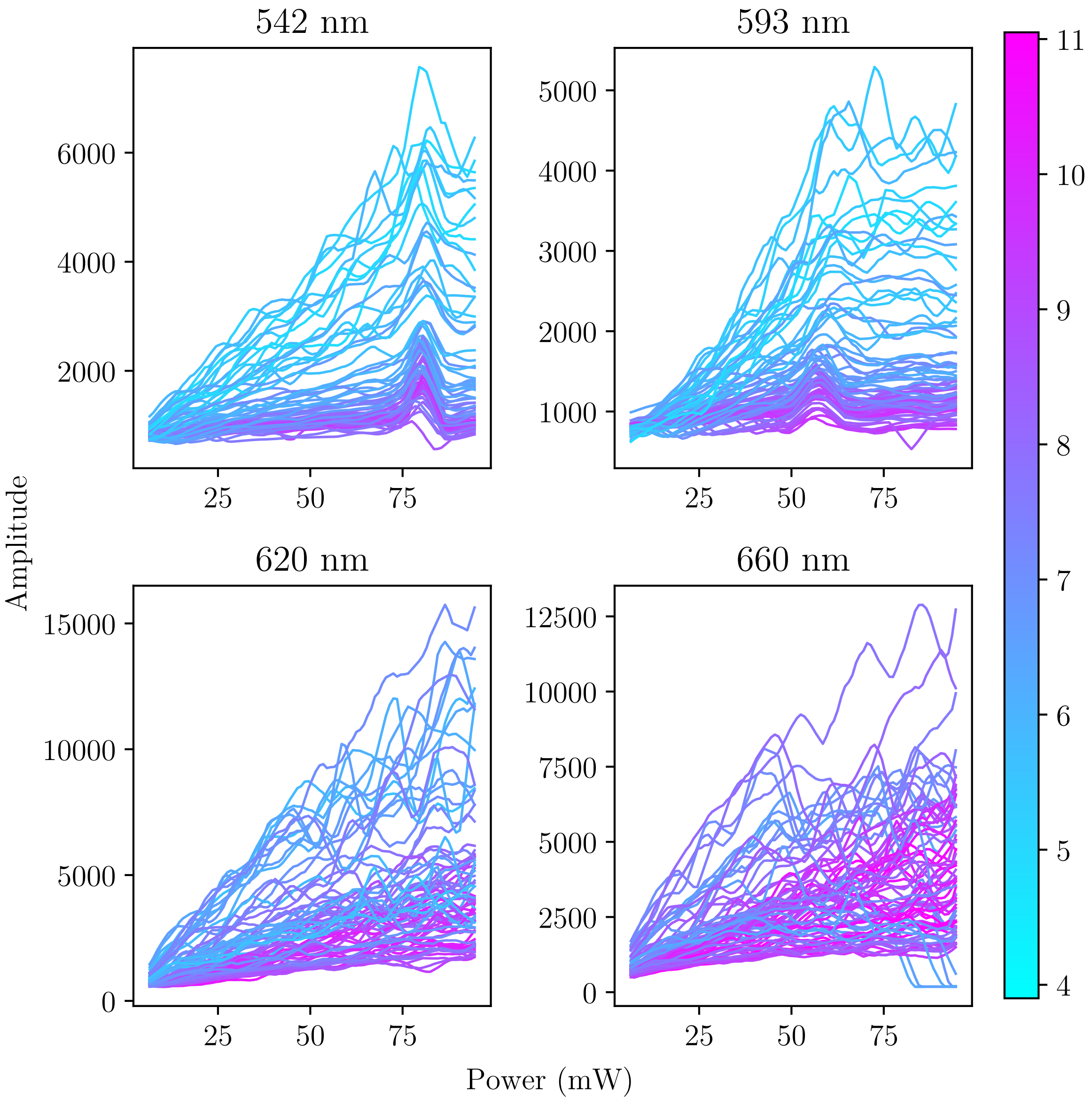

Figure 3.33 – Influence of distance (mm) and current in the LED over the quality of the PPG signal, visible wavelengths

of emitted photons. The number of emitted photons N during the time t in seconds (s) by the LED with power P in watts (W) is given by:

$$N = \frac{P \times \lambda}{hc} \times t \tag{3.7}$$

In addition to that the photodetector is more sensitive to certain wavelengths, it is

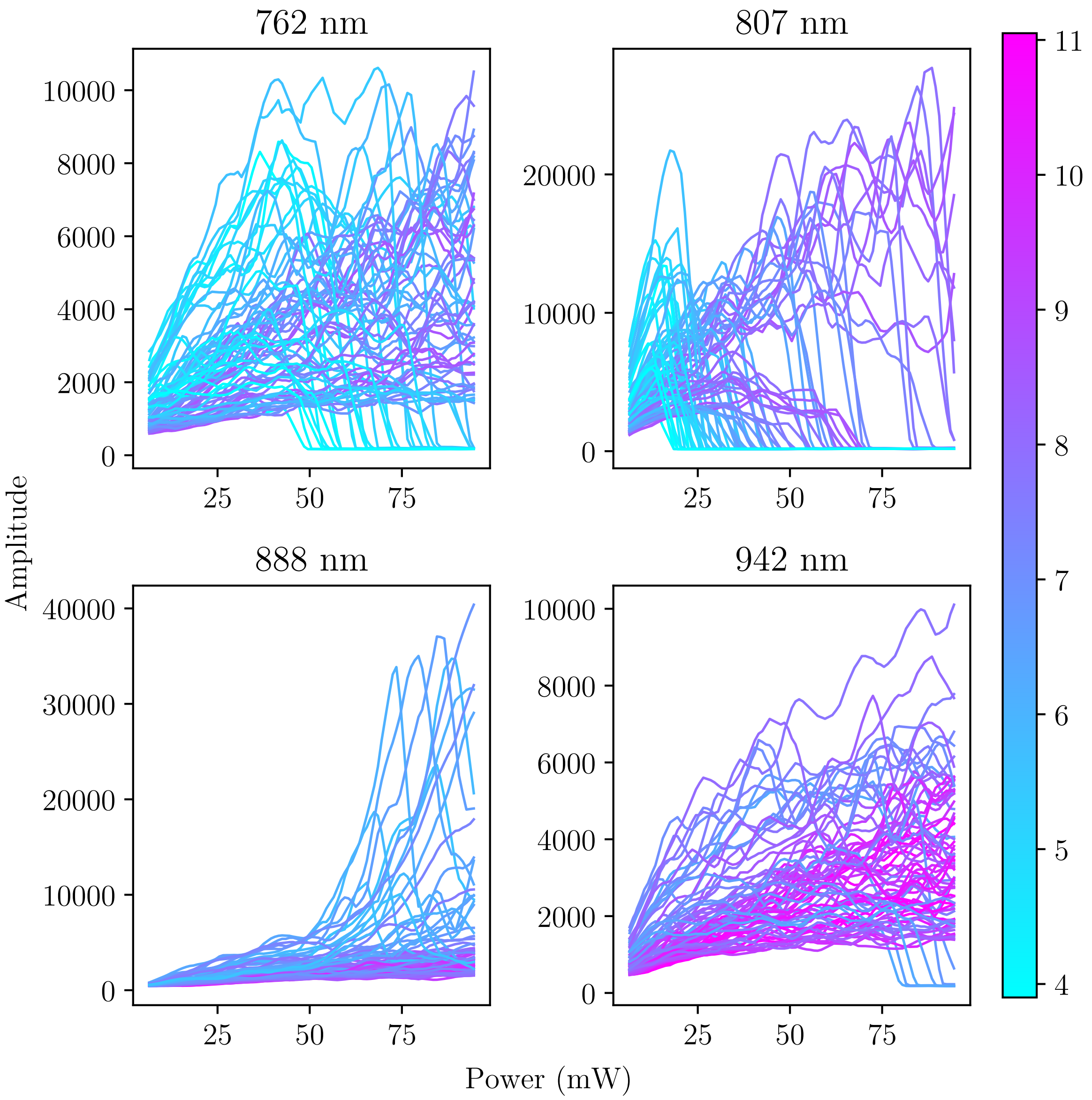

Figure 3.34 – Influence of distance and current in the LED over the quality of the PPG signal, infrared wavelengths

necessary to apply a correction factor the signal in order to compare the results of the different wavelength. In the following Figure 3.35, from the datasheet of the photodiode [39], we extract the corrections values.

The extracted values are given in the table 3.5. The corrections factors are calculated as showed in the equation 3.8, where C_λ is the correction factor and S_λ is the spectral

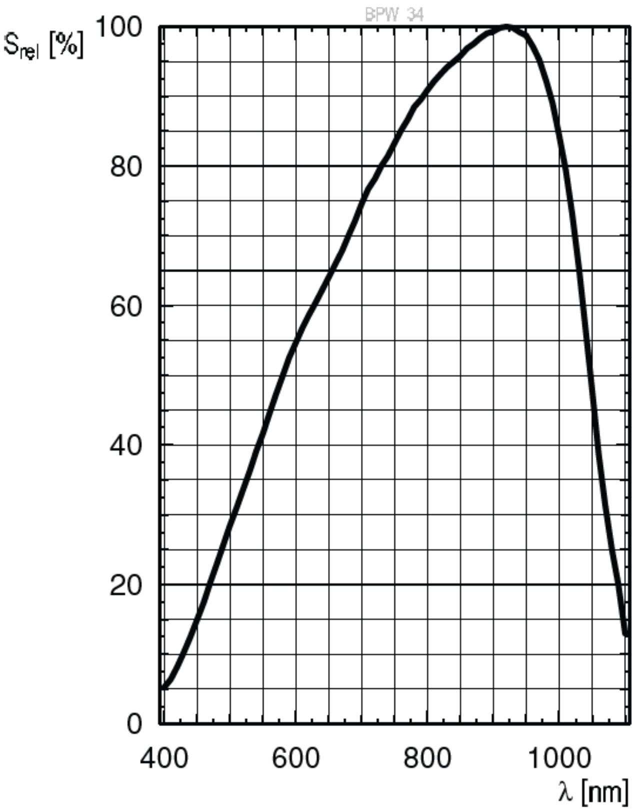

Figure 3.35 – Spectral sensitivity of the photodetector

sensitivity (in percents), of the wavelength λ.

$$C_\lambda = \frac{100}{S_\lambda} \tag{3.8}$$

Wavelengths (nm)	542	593	620	660	762	807	888	940
Spectral sensitivity (%)	39.7	53.7	58.9	66.8	85.7	91.9	98.9	98.2
Correction factors	2.519	1.862	1.699	1.497	1.167	1.088	1.012	1.019

Table 3.5 – Spectral sensitivity as given in the photodetector datasheet

Once everything is adjusted, we obtain the following Figures 3.36 and 3.37. In those figures, the orange line is the maximum along the 'Number of photon' axis. We see that like in the simulation, the greater the number of photon the better. Indeed, the greater the number of photon the greater the amplitude. In particular, at the distance where

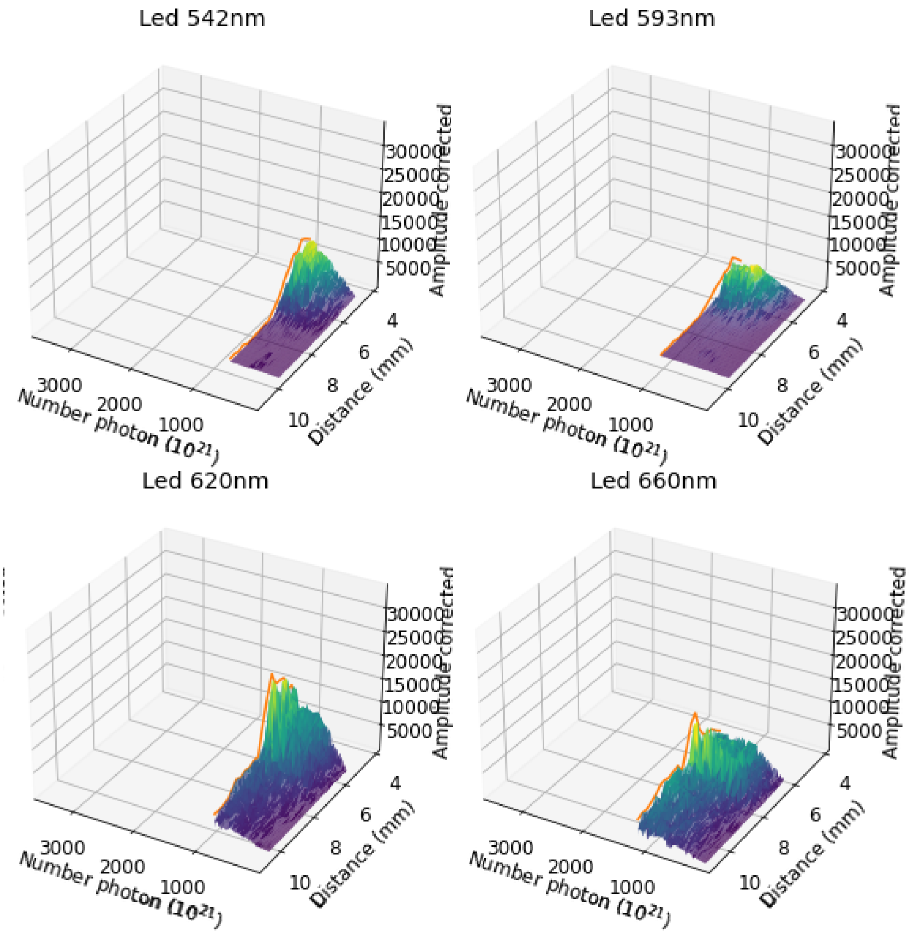

Figure 3.36 – Result of the experimentation once adjusted to be compared to the simulation, visible wavelengths.

it reaches its peak, the amplitude increases in proportion to the number of photons. It also seems that the optimal distance is equal or inferior to the tested distance. Indeed, in Figures 3.36 , 3.37, 3.31 and 3.32, we see that in general the shorter the distance the greater the AC value. This is particularly evident for the visible wavelengths and the 888 nm LED, where the peaks are clearly identifiable at the minimum distance tested. For the other wavelengths, the profile along the distance axis is flatter, making it more difficult to draw definitive conclusions.

The differences between the simulation and the experimentation can be explained by several factors such as the insufficient numbers of photons sent during the simulation, the simplification used in the simulation (such as the tissue is homogeneous), the saturation of the photodiode or even noise in the experimental signals.

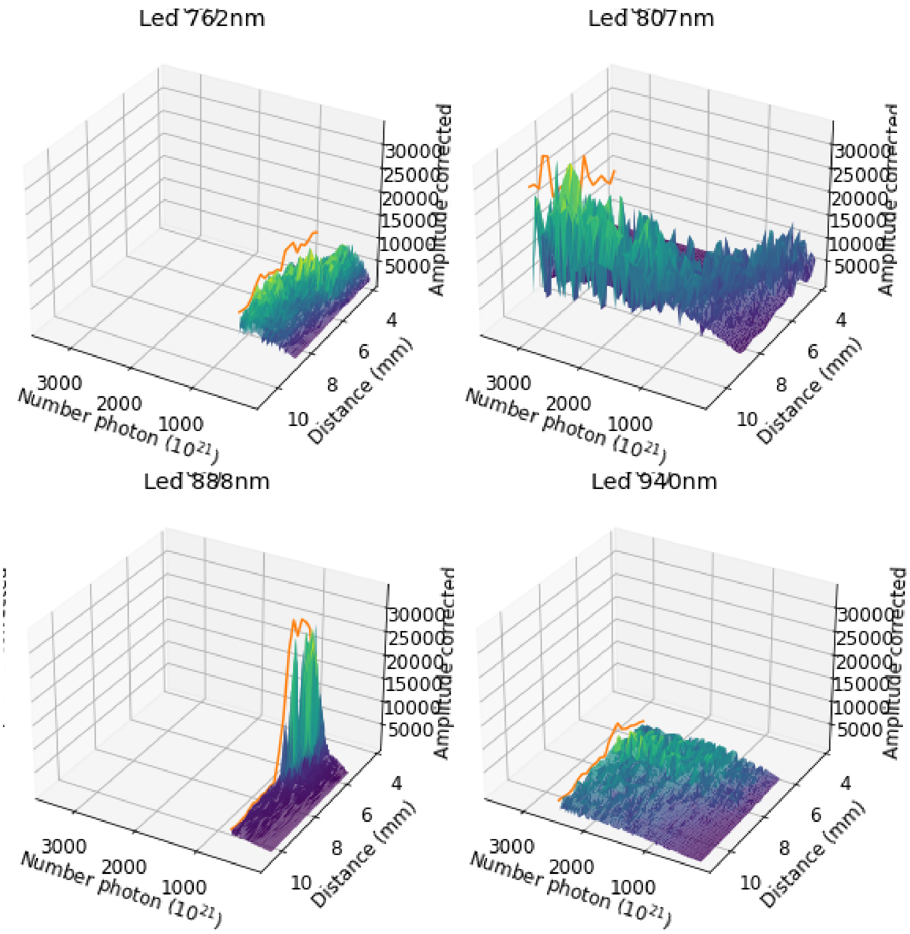

Figure 3.37 – Result of the experimentation once adjusted to be compared to the simulation, infrared wavelengths.

3.5.3 Determining the optimal distance using SEI metric for different sensor placement

To complement the previous experiment, a second study was conducted, this time focusing on determining the optimal distance based on sensor placement on the body. Given that different body regions have varying tissue compositions, the absorption and scattering of light can differ significantly with placement. This experiment employed a different metric and tested three distinct sensor placements: the finger, as a baseline, along with two additional locations specifically selected for their suitability in physical activity. The objective was to evaluate how these varying placements affect sensor performance, particularly in sports environments.

Metrics

The different metrics used are the PI, SNR and SEI as defined respectively by equations 1.5, 1.6 and 1.7.

$$\mathrm{PI} = \frac{\mathrm{AC}}{\mathrm{DC}} \tag{1.5}$$

$$\mathrm{SNR} = 20 \log \left(\frac{\mathrm{AC}}{Nph} \right) \tag{1.6}$$

Where Nph represents the noise level in the signal. Here, Nph is determined by recording a measurement with all the LEDs turned off, under the same conditions used for measuring the AC component. In this setup, only the noise is expected to be captured. The same filtering process applied to the AC signal is then applied to this noise measurement, and the amplitude of the resulting signal represents Nph.

$$\mathrm{SEI} = \mathrm{PI} \times \mathrm{SNR} \tag{1.7}$$

Here only the results for the SEI metrics will be presented. The results for the others metrics are in the Appendix 4.6.

Sensor placements

Figure 3.38 illustrates the sensor placement for the three experiments discussed in this subsection. In the first experiment, the sensor is placed on the finger, represented by the orange dot in the figure. The second experiment places the sensor on the upper arm, indicated by the blue star. The third experiment also involves the upper arm, but the placement is marked with a purple cross.

Results and interpretations

By examining the plot for the SEI, we observe distinct differences in performance between the visible and infrared wavelengths.

Let's first discuss the results for the visible wavelengths. For the finger placement, the first three wavelengths (542 nm, 593 nm, and 620 nm) show a clear trend where a shorter distance yields the best results, as high as 12. In contrast, for tests conducted on the upper arm, the results are more ambiguous and exhibit poorer performance. The flat profile and

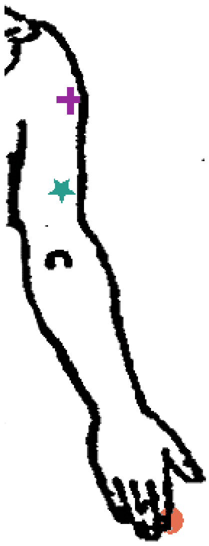

Figure 3.38 – Sensor placements for the three experimental conditions.

relatively low maximum value, such as 0.4 for the 542 nm wavelength, suggest that the optimal distance likely falls outside the range explored in this study, for the first upper arm placement. For the second upper arm placement, we observe that at wavelengths of 620 nm and 660 nm, a greater distance, beyond 8 mm, produces favorable results, with the SEI exceeding 1.5.

Additionally, we observe that, in general, increasing the LED calibration current generally leads to better outcomes, highlighting the importance of calibration intensity in optimizing signal quality.

For the infrared wavelengths, the optimal sensor distance, according to the SEI metric, tends to be greater than that for visible wavelengths. For instance, across all placements, the 762 nm wavelength appears to perform best at distances greater than 7 mm. A similar trend is observed for the 807 nm wavelength. For the 888 nm wavelength, the data suggests that the ideal parameters are a 6 mm distance and the highest possible LED calibration for finger placement, though the results for the upper arm are more ambiguous and less conclusive as they present a flat profile and lower SEI values, less than 4 against more than 10 for the wavelengths 762 nm, 807 nm and 888 nm.

The experimental results underscore the importance of sensor placement and calibration in achieving accurate measurements. The analysis of both visible and infrared wavelengths revealed distinct performance characteristics, with optimal distances varying

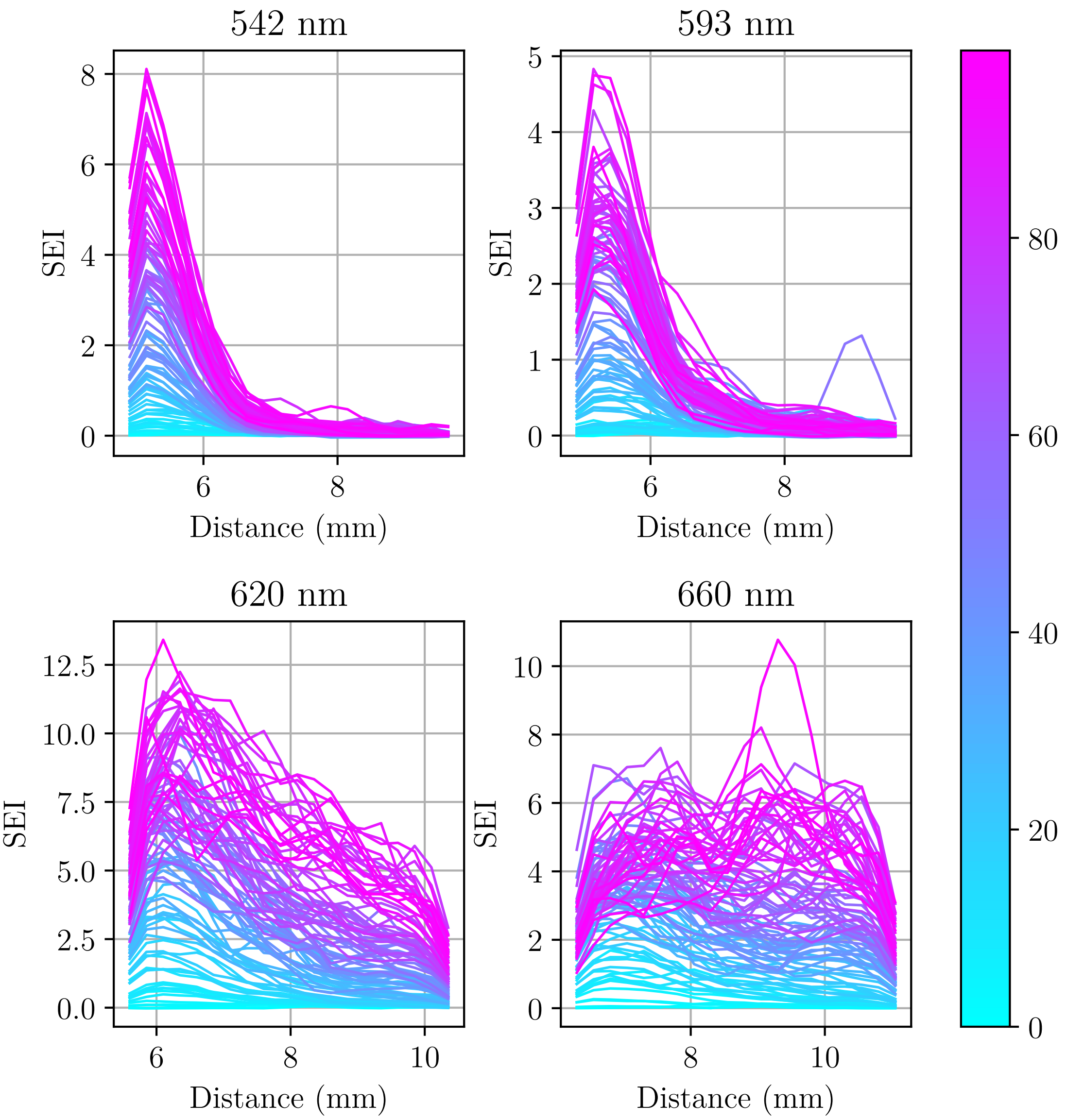

Figure 3.39 – SEI for finger placement experiment for visible wavelengths.

between different placements and wavelengths. Notably, the shorter distances for visible wavelengths on the finger yielded superior results, while the infrared measurements indicated that greater distances were beneficial.

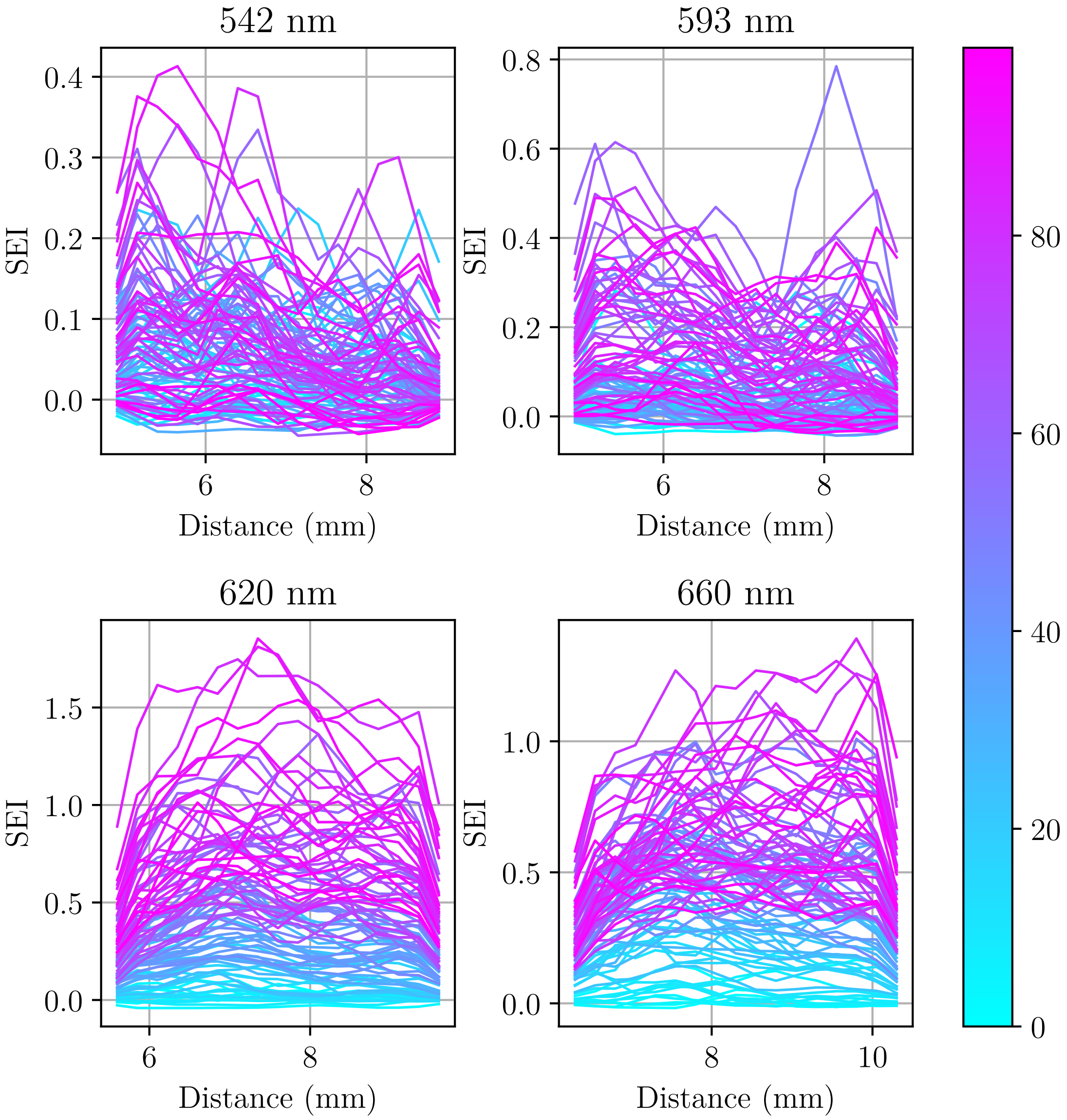

Figure 3.40 – SEI for first upper arm placement experiment for visible wavelengths.

3.6 Conclusion

In this chapter, we explored a hardware-driven approach to enhance the quality of the PPG signal at the point of acquisition, complementing traditional signal processing techniques. By verifying the linear relationship between LEDs command and illumination, we ensured the integrity of the hardware's basic functionality.

Through auto-calibration techniques, we fine-tuned the system's parameters to adapt

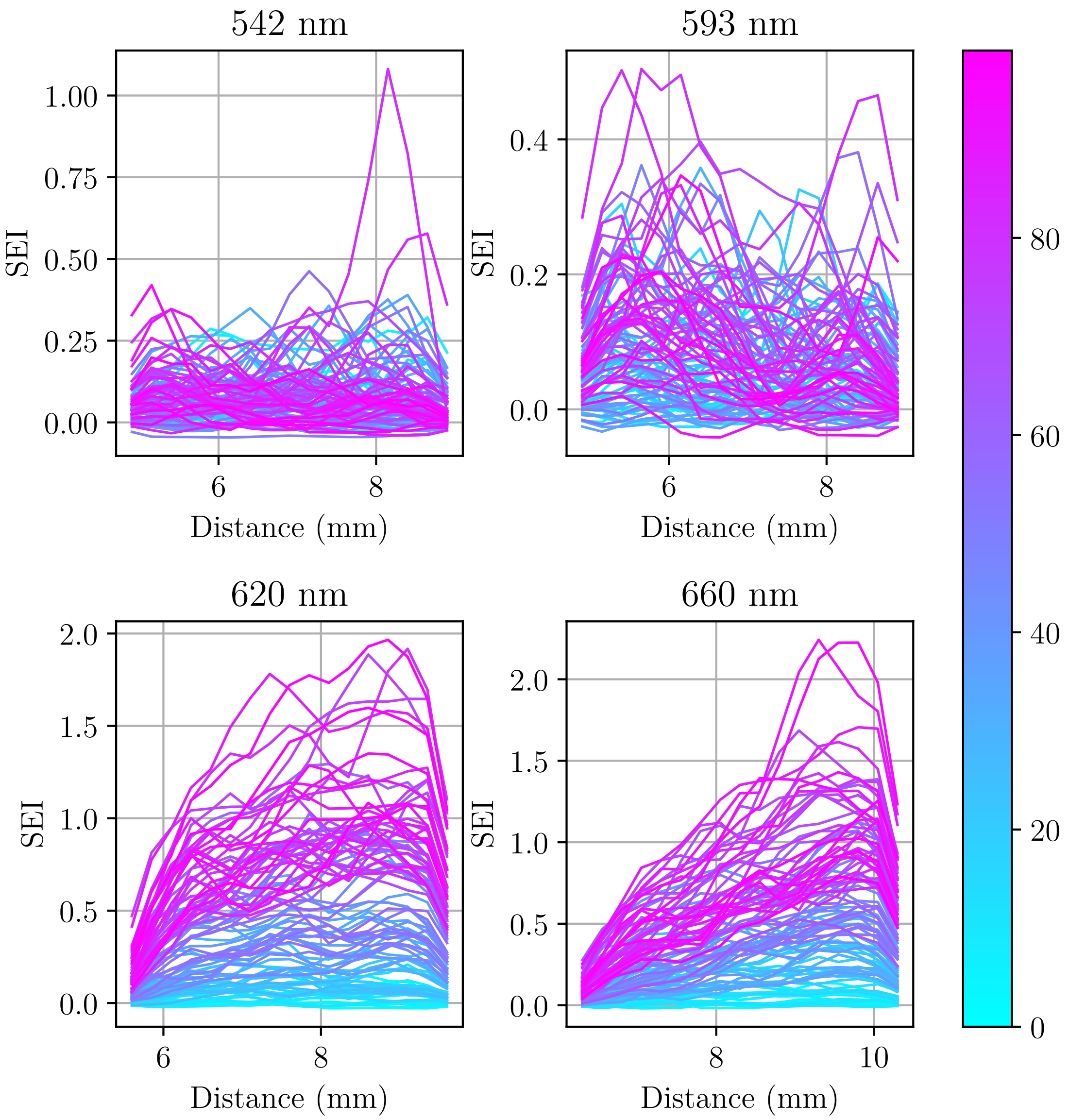

Figure 3.41 – SEI for second upper arm placement experiment for visible wavelengths.

to varying experimental conditions, ensuring consistent signal quality. Additionally, simulations and experimental investigations into the optimal distance between the LEDs and the photodiode have provided valuable insights into sensor placement, significantly improving measurement accuracy. Although the simulation and experimental results did not always align perfectly, they both indicated that for finger placement, the optimal distance is approximately 3 mm or less.

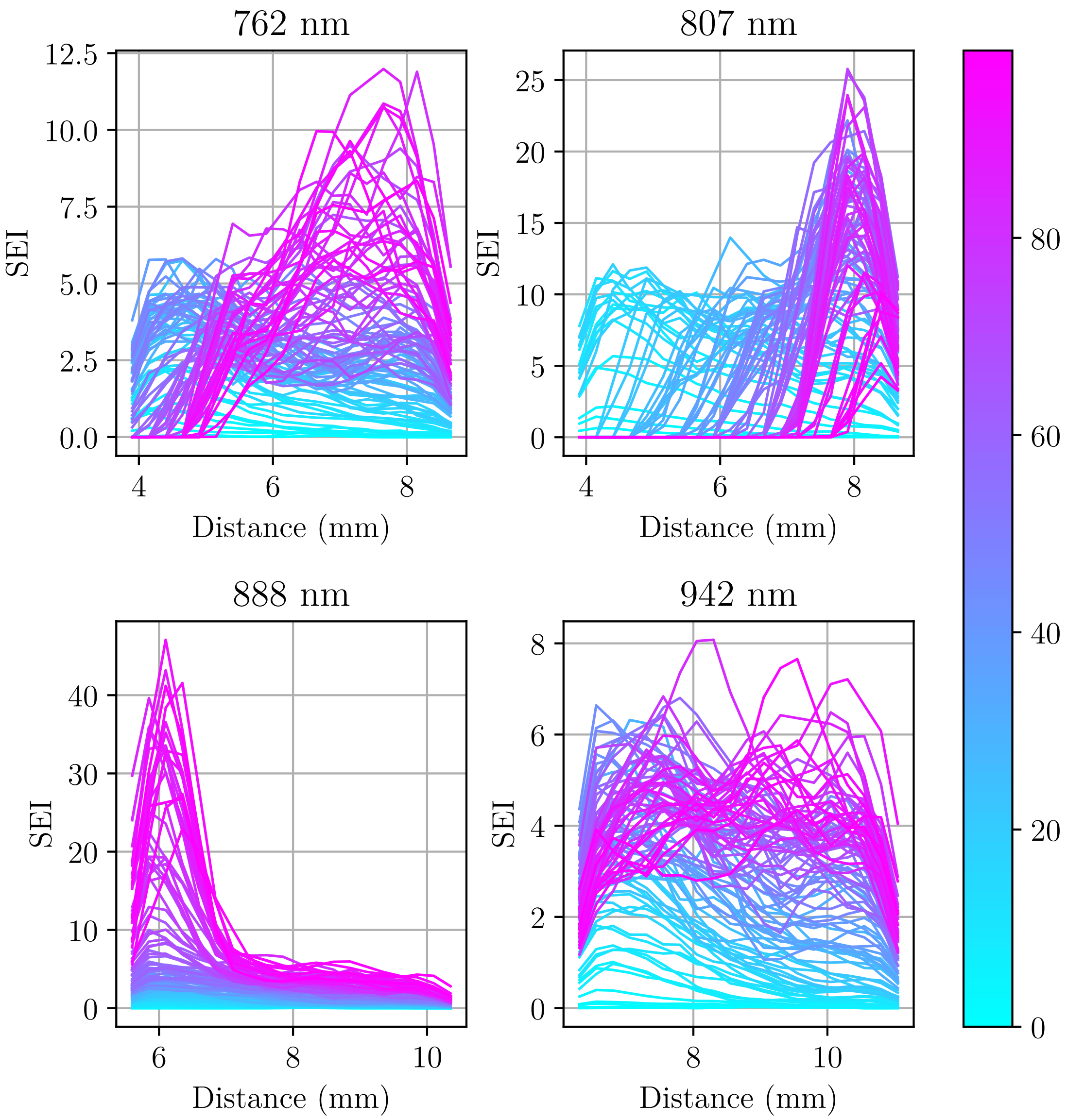

Figure 3.42 – SEI for finger placement experiment for infrared wavelengths.

Moreover, the experimental investigations allowed us to determine the best LED-photodiode distance for each specific placement. This is particularly beneficial in a sports setting, where the placement of PPG sensors differs from that of the finger. Our findings indicate that the optimal parameters, including the LED-photodiode distance and LED power, vary significantly from those for finger placement. Specifically, in most non-finger placements, the SEI tends to be lower, requiring a greater LED-photodiode distance to

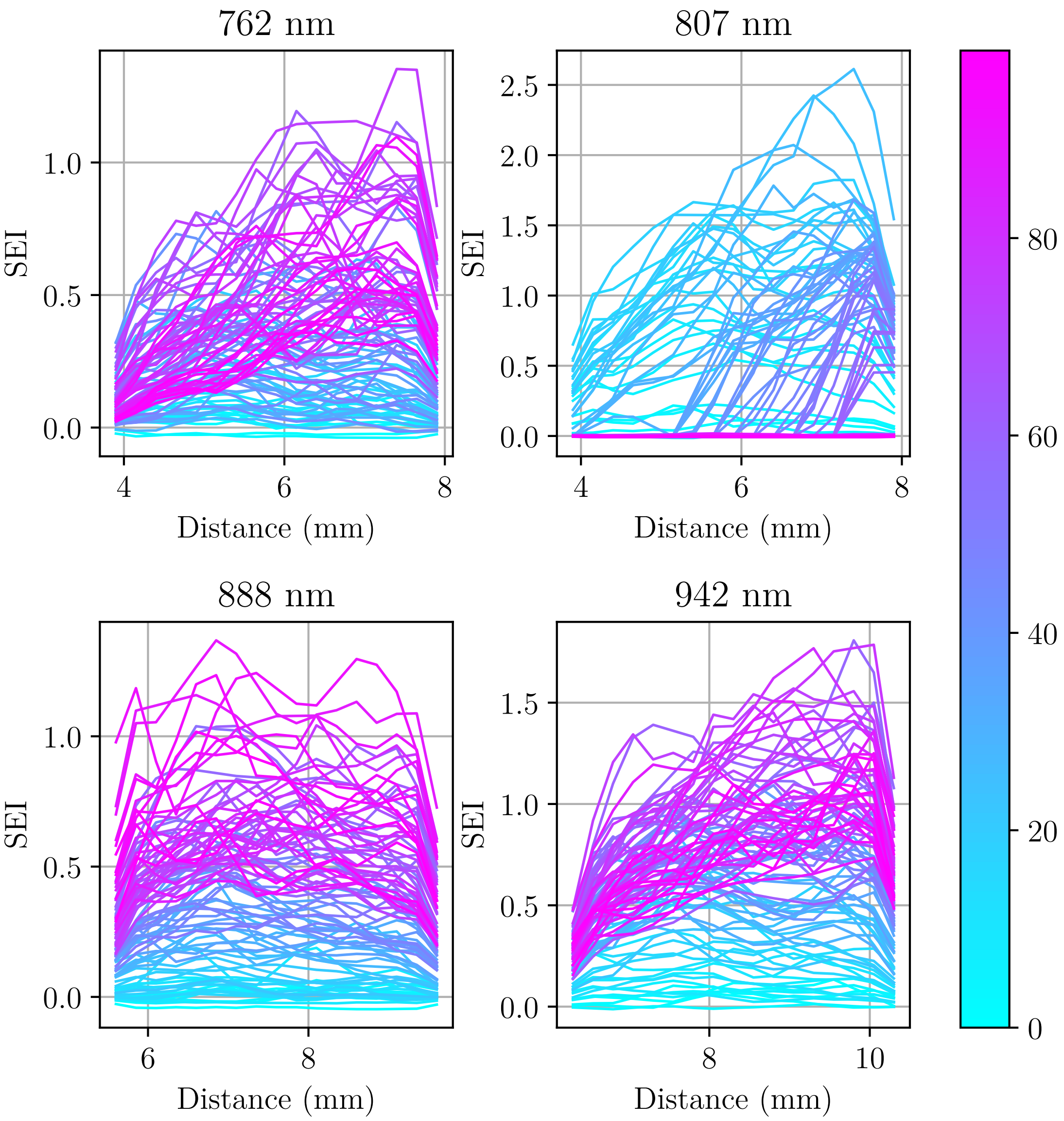

Figure 3.43 – SEI for first upper arm placement experiment for infrared wavelengths.

maintain signal quality.

Overall, the methodologies presented in this chapter demonstrate that a well-designed hardware system, coupled with thoughtful calibration and optimization, can significantly enhance the reliability and precision of PPG measurements.

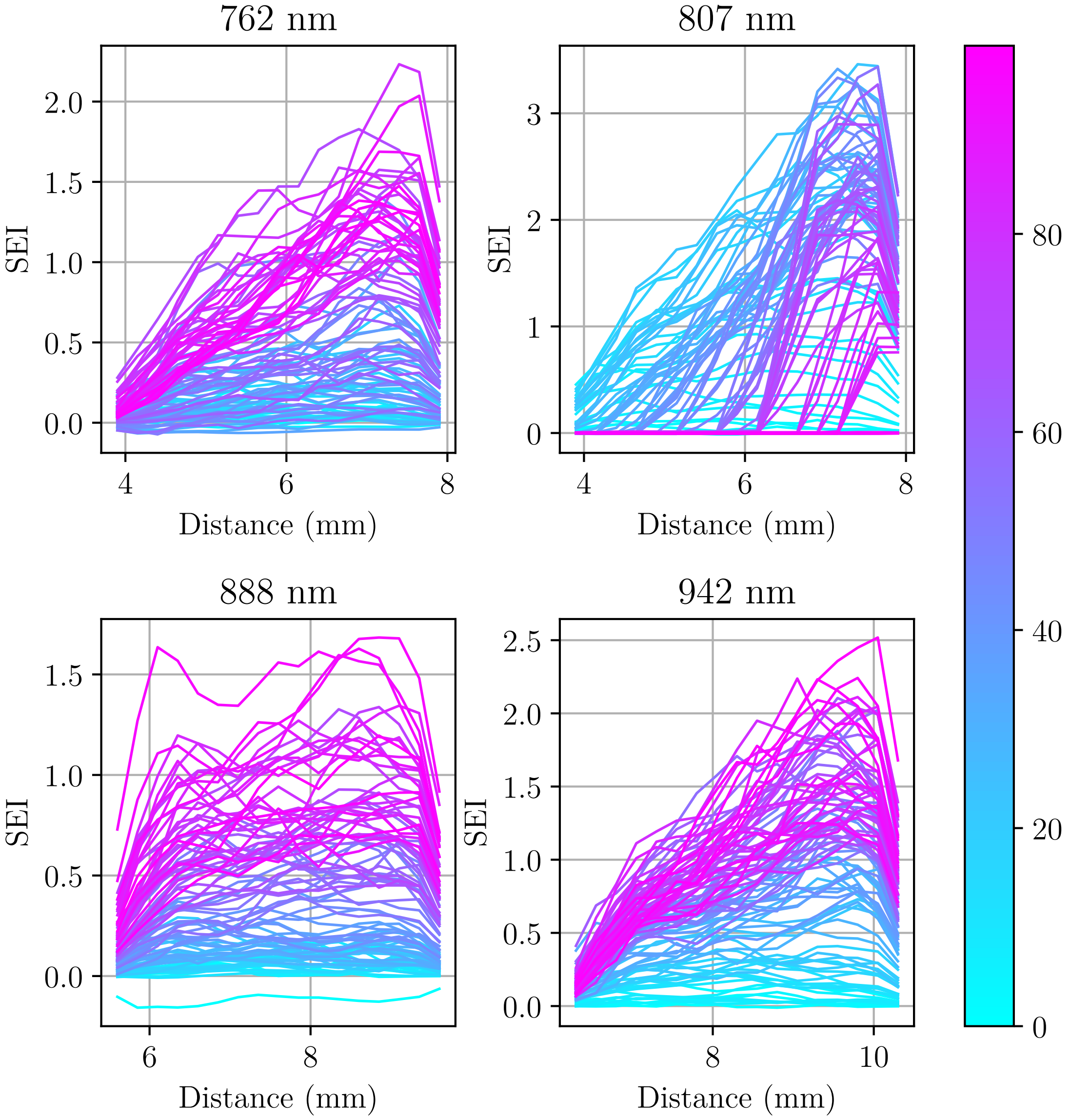

Figure 3.44 – SEI for second upper arm placement experiment for infrared wavelengths.

Chapter 4

MEASURES OF PHYSIOLOGICAL PARAMETERS

4.1 Introduction

After verifying the quality of the signal obtained with the platform, preliminary experiments are conducted to demonstrate a proof of concept. These experiments are essential for assessing the platform's capabilities. Given the significant resources required -time, personnel, materials, and test subjects- to fully conduct these experiments, preliminary or proof-of-concept experiments are carried out instead.

Three different types of parameters are studied using our platform. The first category is cardio-respiratory parameters, the most commonly evaluated using PPG. These parameters are relatively easy to assess, both in terms of the analysis required on the PPG signal and the resources necessary to evaluate the ground truth. In this category, both pulse/heart rate and breathing rate are demonstrated to be measurable using the sensor, in Section 4.2.

The second category includes SpO_2 and the measurement of relative hemoglobin concentrations. While SpO_2 is commonly assessed using the PPG signal, measuring dyshemoglobin concentrations requires a more advanced platform, like the one developed here. This system uses at least four different wavelengths, a necessity for accurately determining the concentrations of various hemoglobin variants due to the Beer-Lambert law. Hemoglobin in the blood exists in several forms, such as HbO_2, RHb, HbCO, and MetHb, each with different light absorption characteristics. The number of wavelengths used must match or exceed the number of hemoglobin variants to ensure enough data is gathered for accurate analysis. Each wavelength provides a unique absorption profile, contributing an equation to the system. By combining these equations, the system can solve for the concentrations of the different hemoglobin variants using a custom mathematical model. This is demonstrated in Section 4.3.

The final category, presented in Section 4.4 is glucose measurement. Historically, glucose has been measured using PPG with varying degrees of success. We believe that our platform enhance the precision of glucose measurement using PPG technology, partially thanks to the increase number of wavelengths.

To further expand the scope of our research, a comprehensive dataset will be created in collaboration with the Embedded Systems Laboratory (ESL) [16] at École polytechnique fédérale de Lausanne (EPFL) in Lausanne, Switzerland. This dataset will involve a large-scale data collection campaign using a wide variety of commercially available sensors, along with our custom platform. The data will be gathered from participants performing diverse everyday activities, such as walking, running, and driving, allowing for a more extensive evaluation of our platform against other sensors, including non-PPG sensors. This collaboration will not only enhance the reliability of our measurements but also provide valuable insights for improving the platform's performance in real-world scenarios. This dataset is presented in Section 4.5.

4.2 Cardio-respiratory parameters

The evaluation of the pulse/heart rate is the first experiment conducted using our platform. Two sensors are used simultaneously: our platform and an ECG system. The objective is to compare the performance of our platform against the gold standard of ECG.

An ECG works by detecting and recording the electrical activity of the heart through electrodes placed on the skin, which capture the heart's electrical impulses as it beats.

While ECG is considered the gold standard for heart rate monitoring due to its high accuracy, it comes with certain drawbacks, as stated in Subsection 1.2.1. ECG systems typically require electrode placement on the skin, which is cumbersome and uncomfortable, especially for long-term or continuous monitoring. The setup and maintenance of ECG systems is also complex and require specialized equipment and training.

In contrast, our platform offers a more user-friendly and non-invasive alternative. The results of this comparison are illustrated in Figure 4.1 and Figure 4.2. For the sake of simplicity, only the results of the LED with the wavelength of 660 nm is shown for our platform.

On Figure 4.1 the synchronized signals are shown, in addition the peaks of both signal are marked. On the x-axis, is the time in seconds and on the y-axis are the amplitude of the signal, with two different axes as the range of the signal are different. The information from the ECG sensor are in red and the information from the PPG sensor are in blue. We see that the peaks are synchronized.

To confirm this synchronicity, Figure 4.2 is produced. On this figure is plotted the instantaneous heart rate found by the two sensors, calculated as in Equation 4.1.

$$HR_i = \frac{60}{t_{i+1} - t_i} \text{ with } i \in [1, N_{beats} - 1] \tag{4.1}$$

with HR_i the instantaneous heart rate number i, t_i the time in seconds of the beat number i and N_{peaks} the number of beats.

The original data is marked with full line and a smoothed version is represented with a dashed line.

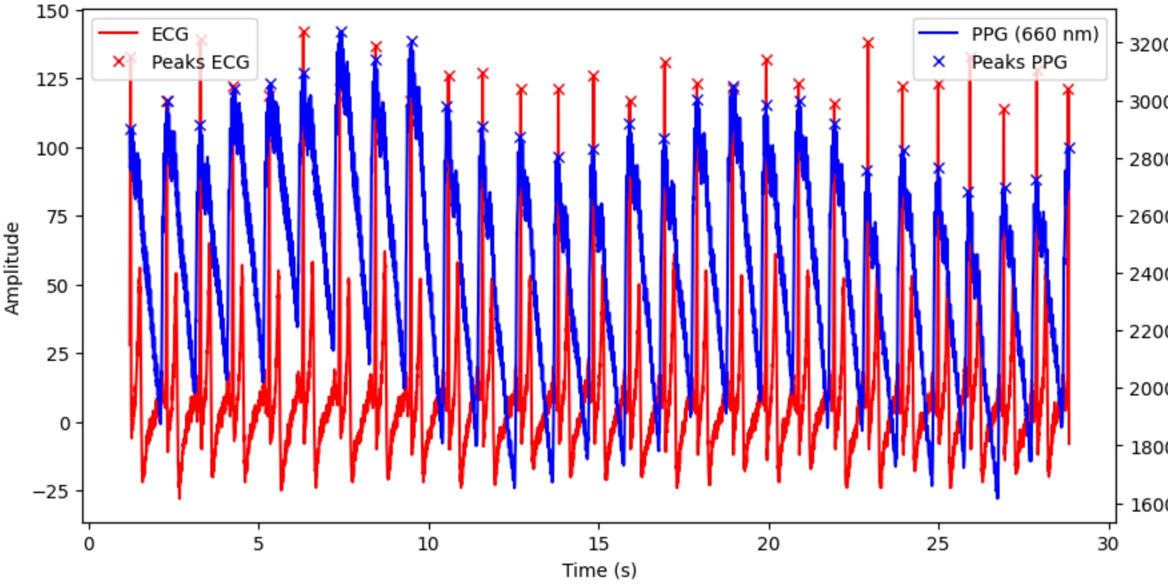

Figure 4.1 – Comparison between a ECG device and our platform PPG.

Our platform produces results similar to those of the ECG sensor in terms of heart rate evaluation. The quantitative comparison of instantaneous heart rates from both sensors yields a Mean Absolute Error (MAE) of 2.21 bpm, a Root Mean Squared Error (RMSE) of 2.59 bpm, and a Pearson Correlation Coefficient of 0.71. It should be noted that the ECG and PPG signals cannot provide exactly the same instantaneous HR due to differences in the physiological processes they measure and the locations from which they capture signals. While the ECG detects the electrical activity of the heart directly,

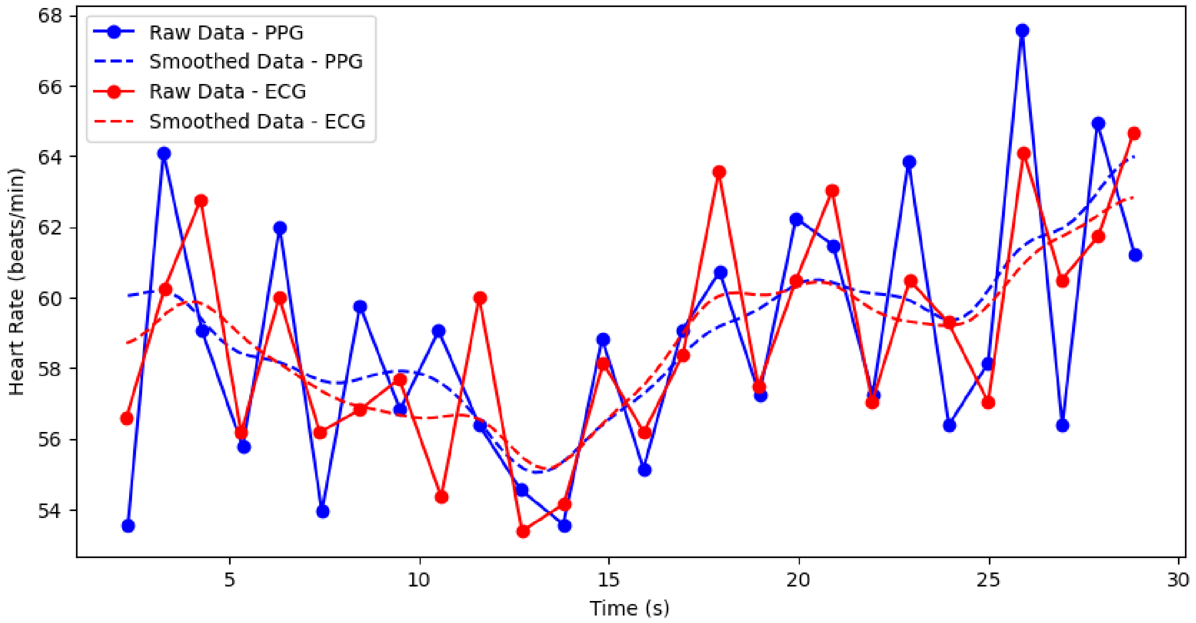

Figure 4.2 – Comparison evaluation HR between a ECG device and our platform PPG.

the PPG measures blood volume changes, which are influenced by vascular dynamics and may introduce slight delays, resulting in subtle discrepancies between the two signals. We present the smoothed data, as it is common practice for sensors to display a smoothed version of the signal, given that heart rate can vary due to breathing and other physiological factors.

The PPG signal is highly sensitive to respiration, influenced by it in several ways. As outlined in the state of the art, in Subsection 1.2.3, respiratory activity and the cardiac cycle induce three key modulations in the PPG signal: respiratory-induced intensity variation (BW), amplitude variation (AM), and frequency variation (FM). These modulations reflect changes in blood volume, pulse strength, and heart rate associated with the respiratory cycle. For the following experiment, the subject is asked to repeat breathing cycles consisting of 3 seconds of inspiration followed by 3 seconds of expiration.

We observe the signal obtained, for the LED with a wavelength of 940 nm, during this experiment on Figure 4.3. In this Figure the signal is represented by a continuous blue line. This signal is obtained with the first, full analog, version of the DC calibration which explain the slight decrease of the mean of the signal (due to the capacitors discharging). The platform different version are described in Section 2.4. The time is on the x-axis and the amplitude, the output of the ADC, is on the y-axis. The range of the amplitude given by the ADC is 0 to $2^{16} - 1$, meaning 65535.

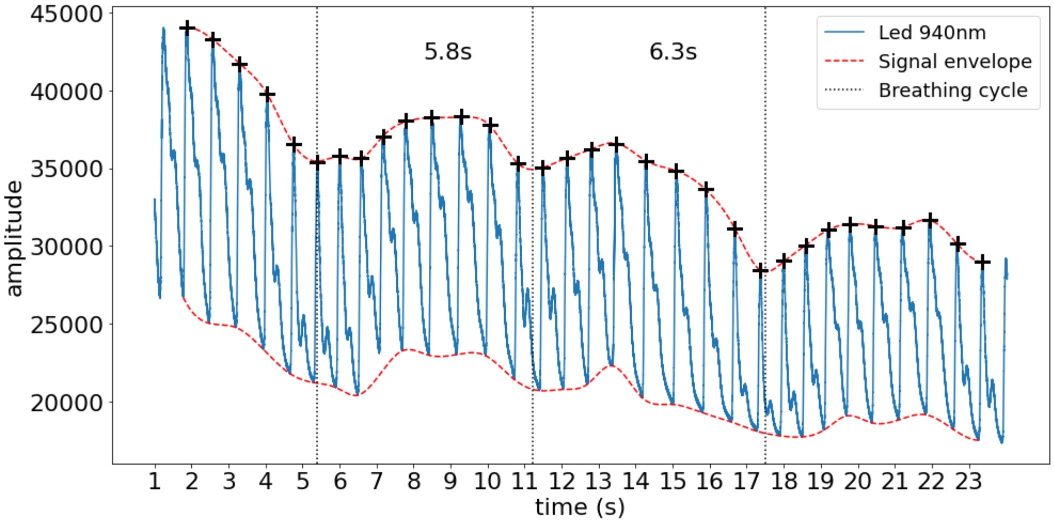

Figure 4.3 – Evaluation of the breathing rhythm with PPG signal.

The peaks and troughs are detected, and theirs locations are marked with black crosses. From those locations, two functions are calculated. One representing the extrapolation of the peaks and the other one the extrapolation of the troughs. These two functions frame the signal and represent its envelope. Those functions are represented in the plot by red dashed lines.

We observe that the envelope of the signal has a periodicity of about 6 seconds, which corresponds to the experimental conditions. To measure that, the troughs of the top of the envelope, meaning the extrapolation of the peaks, are located and the time between those troughs are measured. The first complete period is of 5.8 s and the second one of 6.3 s.

The breathing is thus well extractable from the signal obtained with the sensor.

In addition, on Figure 4.3, it is possible to see clearly the pulse rate by using the peaks of the signal.

4.3 Concentration of hemoglobins and SpO_2

The concentrations of hemoglobins in the blood are the perfect parameters to evaluate our platform as it requires a particularity of our platform : a greater number of wavelengths.

The aim is to develop an algorithm that takes advantage of 8 different wavelengths, from red to infrared, available on this device to determine SpO_2 and the concentration of dyshemoglobin. Our platform seeks to provide greater precision in measuring SpO_2 and to obtain more detailed information about blood components to improve health monitoring.

Indeed, as previously mentioned, in subsection 1.2.2, classical PPG has limitations when it comes to evaluating hemoglobin concentrations, with the primary challenge being the number of wavelengths used. Most PPG sensors, commonly employed as pulse oximeters, use only two wavelengths. This allows them to determine two unknowns: oxygenated and deoxygenated hemoglobin, by assuming the absence of other hemoglobin variants. However, to accurately measure multiple hemoglobin species, the system must provide at least as many wavelengths as there are unknowns, with each wavelength providing a unique equation necessary for precise concentration determination.

Unfortunately, the equations are not linear and there are different models in literature for the interaction between the light and biological tissue.

The first step consists in seeking a representative model in the form of a system of non-linear equations, the unknowns of which are the concentrations of the hemoglobins.

The second step is to verify the validity of the model found. Using data collected using the device, the result of the different models is being compared to the ground truth for the SpO_2.

4.3.1 History of the Beer-Lambert Law and evolution

The origin of the Beer-Lambert law dates back to 1729, with Bouguer's law, which relates the intensity of remaining light passing through a non-opaque liquid to the length of the path in the liquid via an exponential function. In 1760, Lambert expressed this relationship mathematically, resulting in Lambert's Law. By 1852, the concept of concentration was incorporated. Combining all the previous laws resulted in what is now known as the Beer-Lambert Law, as described in equation 1.2.

$$A = \epsilon \cdot c \cdot l \tag{1.2}$$

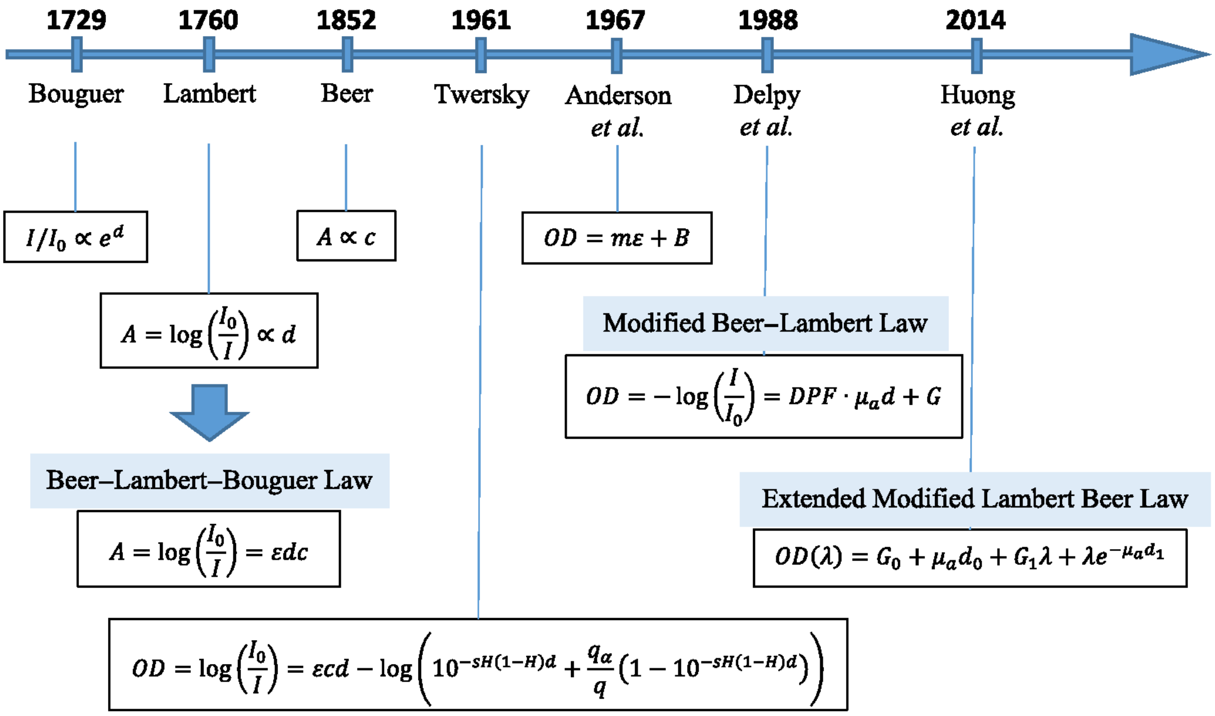

Figure 4.4 – Evolution of the Beer-Lambert Laws [38]

where:

A = Absorbance
ϵ = Molar absorptivity (extinction coefficient)
c = Concentration of the solution
l = Path length of the light through the solution

In 1962, Twersky introduced the idea of accounting for light intensity loss due to scattering by red blood cells, recognizing blood as the primary light absorber and diffuser in biological tissue. This law was reformulated and simplified five years later. In 1988, Delpy et al. incorporated tissue diffuse reflection into the law. Further extensions were made in 2014 to enhance the measurement quality of biological parameters by considering the dermis and epidermis [38].

The evolution of the Beer-Lambert law are illustrated in Figure 4.4.

4.3.2 Description of used models

The aim of this section is therefore to determine an 8-wavelength oximeter model. Indeed, as stated previously, we wish to stop neglecting the other hemoglobin (HbCO and MetHb). In consequence, it is necessary to create new models and to verify them. To do this, it is necessary to look at the modelling of biological tissues and to understand the different phenomena occurring in tissues. The different models use different version of the Beer-Lambert Law. The measured quantity is the variation of absorbance, meaning the difference of absorbance between the peaks and the troughs of the signal.

Several simplifications and assumptions are being made when developing models for hemoglobin concentration evaluation. Each combination of these simplifications leads to a distinct model. The various custom models, developed by Théo LANGÉ, during an internship under my supervision, are presented in the following sections. These models are ordered from the most simplified to the more general, with a detailed description of the assumptions that led to each model.

The goal of those models is to link the measurement that are done using the device, meaning the absorption of the light by the tissue, to the different levels of the hemoglobin.

Model 1: Extension of the Traditional Beer-Lambert Law

The first model is a straightforward extension of the currently used model, following the Beer-Lambert Law described in equation 1.2. In this model, the optical path l is assumed to be constant for all wavelengths. We only need to determine the extinction coefficient for the hemoglobin variants. The resulting equation is given by equation 4.2, where ΔA_{λ_i} represents the difference in absorbance for wavelength λ_i, $\epsilon_{Hb_j}(\lambda_i)$ is the extinction coefficient of the hemoglobin variant Hb_j at wavelength λ_i, and c_{Hb_j} is the concentration of Hb_j. This model serves as a baseline for understanding hemoglobin absorption.

$$\begin{pmatrix} \Delta A_{\lambda_1} \\ \vdots \\ \Delta A_{\lambda_n} \end{pmatrix} = \delta_l \times \begin{pmatrix} \epsilon_{Hb_1}(\lambda_1) & \dots & \epsilon_{Hb_m}(\lambda_1) \\ \vdots & \ddots & \vdots \\ \epsilon_{Hb_1}(\lambda_n) & \dots & \epsilon_{Hb_m}(\lambda_n) \end{pmatrix} \times \begin{pmatrix} c_{Hb_1} \\ \vdots \\ c_{Hb_m} \end{pmatrix} \tag{4.2}$$

Model 2: Variation of Optical Path with Wavelength

In the second model, we account for the variation of the optical path length based on the wavelength. This introduces more unknownsspecifically, the variation in optical path for the 8 wavelengths and 4 types of hemoglobinthan equations, with only 8 available. By leveraging the physical characteristics of the sensor, we estimate the variation in optical path using a Monte Carlo estimation method. The equation for this model is given by equation 4.3, where the symbols retain the same meaning as in equation 4.2, and Δl_{λ_i} denotes the difference in light path for wavelength λ_i. This model allows for a more nuanced understanding of how wavelength affects absorption.

$$\begin{pmatrix} \Delta A_{\lambda_1} \\ \vdots \\ \Delta A_{\lambda_n} \end{pmatrix} = \begin{pmatrix} \Delta l_{\lambda_1} & \dots & 0 \\ \vdots & \ddots & \vdots \\ 0 & \dots & \Delta l_{\lambda_n} \end{pmatrix} \times \begin{pmatrix} \epsilon_{Hb_1}(\lambda_1) & \dots & \epsilon_{Hb_m}(\lambda_1) \\ \vdots & \ddots & \vdots \\ \epsilon_{Hb_1}(\lambda_n) & \dots & \epsilon_{Hb_m}(\lambda_n) \end{pmatrix} \times \begin{pmatrix} c_{Hb_1} \\ \vdots \\ c_{Hb_m} \end{pmatrix} \tag{4.3}$$

Model 3: Incorporating Diffusion Effects

The third model incorporates the effects of diffusion. It is divided into two submodels, each considering different interpretations of what occurs during differentiation. One submodel treats diffusion as a change in path length, while the other treats it as a change in the extinction coefficients. The first submodel is represented by equation 4.6, where μ_{eff} is defined as described in equation 4.5, and Δl represents the variation in path length. The second submodel is articulated in equation 4.7. This model provides insight into how diffusion impacts absorbance measurements.

The characterization of biological tissues can be described by three key coefficients:

- The absorption coefficient, μ_a, which quantifies the tissue's ability to absorb light radiation.
- The scattering coefficient, μ_s, which describes the tissue's ability to scatter light.
- The anisotropy coefficient, g, which reflects how the light trajectory depends on the geometry and orientation of the tissue.

These three coefficients are fundamental in characterizing biological tissues, and their values may vary depending on the specific body region examined with an oximeter. Additionally, these parameters are essential in numerous models that describe tissue-light interactions. Accurately determining reliable values for these coefficients will significantly improve the precision of simulation results. From the scattering coefficient and the anisotropy coefficient, it is possible to define the reduced scattering coefficient, given by Equation 4.4

$$\mu_s' = \mu_s(1-g) \tag{4.4}$$

The effective extinction coefficient can also be defined, which describes the attenuation of light through tissues by accounting for both absorption and scattering phenomena, as in Equation 4.5.

$$\mu_eff = \sqrt{3\mu_a \times (\mu_a + \mu\prime_u)} \tag{4.5}$$

$$\Delta A_\lambda = \Delta l \times \mu_{eff} \tag{4.6}$$

$$\Delta A_\lambda = l \sum_{i=1}^{m} \frac{\delta \mu_{eff}}{\delta c_i} \Delta c_i \tag{4.7}$$

Model 4: Advanced Beer-Lambert Law

This model builds upon a more advanced interpretation of the Beer-Lambert Law, as described by equation 4.8. It is also divided into two submodels, depending on whether the DPF term is considered constant or variable. The two submodels are defined by equations 4.9 and 4.10. This approach addresses limitations in the traditional model by introducing additional complexity in the light absorption process.

$$A_\lambda = d \times DPF_\lambda \times \mu_a + B_\lambda \tag{4.8}$$

$$\Delta A_\lambda = dDPF_\lambda \sum_{i=1}^{m} \epsilon_{Hb_i}(\lambda) \Delta c_i \tag{4.9}$$

$$\Delta A_\lambda = d \sum_{i=1}^{m} (DPF_\lambda \times \epsilon_{Hb_i}(\lambda) + \frac{\delta DPF_\lambda}{\delta c_i} \mu_a) \Delta c_i \tag{4.10}$$

Model 5: Enhanced Beer-Lambert Law with Effective Absorption Coefficient

The fifth model is a further enhancement of the fourth model, substituting μ_a with μ_{eff}. Similar to the previous model, it is divided into two submodels based on the constancy of the DPF term. The equations for these submodels are provided in 4.11 and 4.12. This model offers a refined approach to understanding light absorption in the context of different hemoglobin variants.

$$\Delta A_\lambda = dDPF_\lambda \sum_{i=1}^{m} \frac{\delta \mu_{eff}}{\delta c_i} \Delta c_i \tag{4.11}$$

$$\Delta A_\lambda = d\sum_{i=1}^{m}(DPF_\lambda \frac{\delta\mu_{eff}}{\delta c_i} + \frac{\delta DPF_\lambda}{\delta c_i})\Delta c_i \tag{4.12}$$

Additional Information

The models that assume a varying path length based on wavelength present a scenario where the number of unknowns exceeds the number of equations. For these cases, the path length is estimated using the technique demonstrated in Section 3.4.

During the optimization process to solve the models, certain limitations are imposed on the system:

- The concentrations must be positive numbers.
- Concentrations must be significantly larger than their variation during a cardiac cycle.
- The concentrations of dyshemoglobin and reduced hemoglobin must not exceed 10% of the concentration of oxygenated hemoglobin, as the subjects are healthy.
- The average concentration of hemoglobin in human blood is approximately 11 $g \cdot L^{-1}$.

These limitations are translated in equation 4.13, with the concentration in $mol \cdot L^{-1}$.

$$\begin{cases} c_{Hb_i} \geq 0 & \forall i \\ |\Delta c_{Hb_i}| \leq 10^{-4} c_{Hb_i} & \forall i \\ c_{Hb_i} \leq 0.1 \times c_{HbO_2} & \forall i \neq O_2 \\ 10^{-4} \leq \sum_{i=1}^{m} c_{Hb_i} \leq 10^{-2} & \forall i \end{cases} \tag{4.13}$$

4.3.3 Experimental results of the models

In Figure 4.5, we observe the saturation levels, SpO_2, calculated over the 10 cardiac cycles. Additionally, the boxplots associated to the SpO_2 value are represented in Figure 4.6. The boxplots provide a clearer visualization of how the calculated values relate to the average across the 10 cycles.

By incorporating all relevant hemoglobin types in the estimation of HbO_2 and Hb levels, we aimed to achieve more precise results. The results are presented in Figure 4.5 and 4.6. On the x-axis of Figure 4.5 are the beats of the heart. On the y-axis, is the level of SpO_2. On the x-axis of Figure 4.6, are represented the models used and on the y-axis, the level of SpO_2.

When comparing the results shown in Figure 4.5 for the different models, we observe that the SpO_2 values obtained using Model 1 are consistently around 96% for all 10 cardiac cycles. However, the lack of variation across cycles suggests that this model may not be robust enough to capture fluctuations in absorbance. As expected, this model seems unsuitable for the current scenario, as it assumes a non-diffusive medium and that the wavelength has no influence on the optical path.

In contrast, Models 2 and 3.1 exhibit lower variance compared to the other systems, indicating more stability in the calculated saturation values. Additionally, the average saturation from Model 2 is higher than that of the other models. Thus, Model 2 appears to be the most suitable for our problem. Unfortunately, we did not have reference saturation values for comparison, preventing us from drawing definitive conclusions about the accuracy of these models. However, the results we obtained seem consistent with typical saturation values found in the literature.

While the PPG-derived SpO_2 estimates appear coherent and consistent with expected physiological parameters, their accuracy is difficult to confirm due to the challenge of obtaining a reliable ground truth. Indeed, the study of other hemoglobins (HbCO and MetHb) is challenging because obtaining significant variations in these levels requires putting the test subject in danger. In fact, a few percent of those hemoglobins can cause different symptoms that go from feeling uneasy to death.

4.4 Glucose

In this section, we focus on the measurement of glucose levels, a critical physiological parameter that has historically been challenging to evaluate using PPG technology. Glucose measurement via PPG is particularly difficult due to the complexity of the signal and the low concentration of glucose compared to other blood constituents. However, one key advantage of PPG is that it is a non-invasive technique, offering significant benefits in terms of patient comfort and ease of monitoring.

As illustrated in Figure 4.7, the variation in blood sugar levels over a half-day period in a healthy subject is shown. This subject will serve as the reference for all subsequent measurements. The x-axis represents time, while the y-axis denotes glucose concentration in $mg \cdot dl^{-1}$. The red hatched zones mark meal times, illustrating the effect of food intake on glucose levels. During this period, the glucose concentration fluctuates between 96 and 123 $mg \cdot dl^{-1}$, which is typical for a healthy individual.

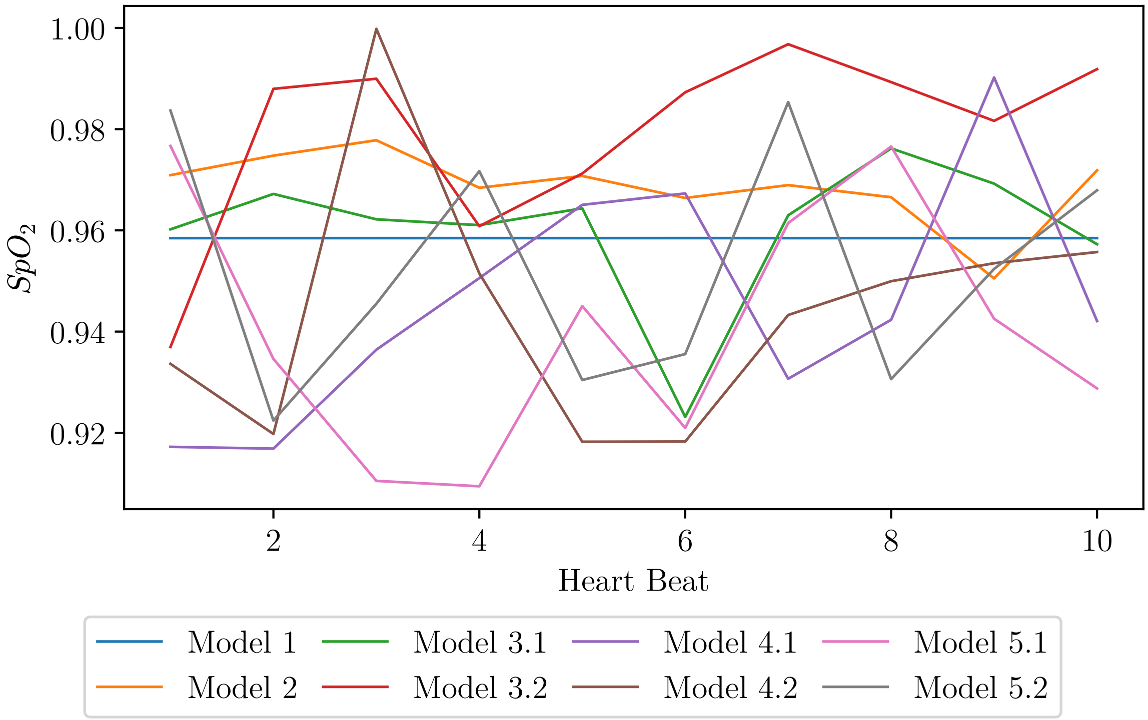

Figure 4.5 – Functional saturation in oxygen SpO_2

4.4.1 Experimental protocol

Over a period of few days, multiple times a day, a blood sample and a measurement with the platform are done simultaneously on a subject. The times of sampling are chosen to ensure a variety of blood sugar levels by for example taking samples right after a meal or after a fasting period (like in the morning before the first meal). The blood sample is used to obtain a reading of the blood sugar level using an Accu-Chek Performa Nano glucose meter [1]. The link between the two measurement are made using two metadata files, using as a key the time of the measurements. A total of 34 samples are taken.

After the collect the signal of the PPG is processed, different features are extracted, and then the data is used to train and verify machine learning model in order to predict the glucose levels from the features, as discussed in the next subsections.

4.4.2 Methods for Evaluating Glucose Levels

To estimate glucose levels, various features are extracted from the PPG signal. A comprehensive set of features, consistent with those reported in the literature [44, 20, 50],

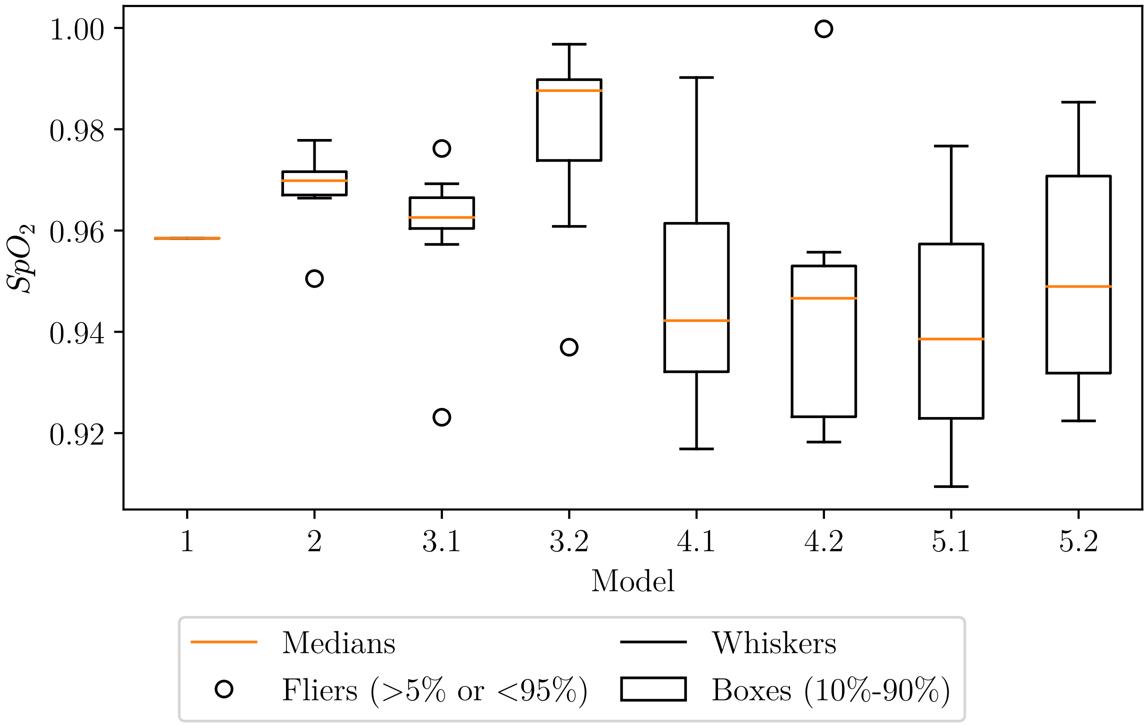

Figure 4.6 – Boxplots of the functional saturation in oxygen

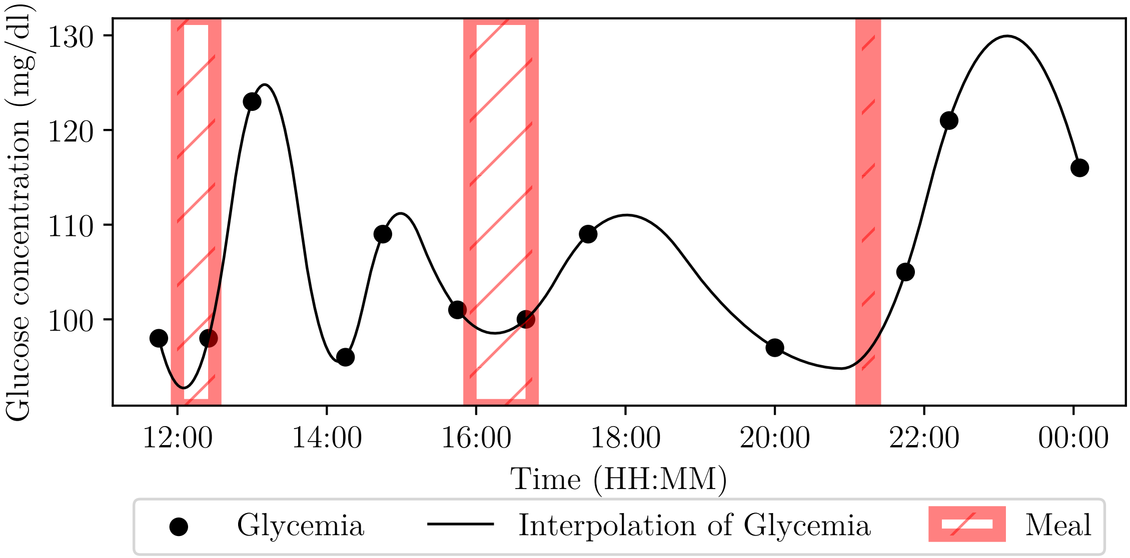

Figure 4.7 – Variation of blood sugar levels during half a day

are analyzed to identify the most effective feature set for glucose detection. The dataset consists of 34 measurements, divided equally into 17 for training and 17 for validation.

This separation enables cross-validation, ensuring robust evaluation of the feature set's performance.

Choice and extraction of the features

Here, we present the details of the features utilized, and the methods employed for their calculation.

First the position of the local maxima and minima of the signal are extracted. From those value we extract the following features :

Number of peaks (N_{peaks}): The number of peaks in the signal, which indicates how many local maxima are present.

With the position of the local maxima, the instantaneous heart rate is extracted. The values extracted are called as in the equation 4.14.

$$HR_i, \text{ with } i \in [2, N_{peaks}] \tag{4.14}$$

Where HR_i is the instantaneous heart rate of the beat i and N_{peaks} is the number of heart rate measurements.

Mean heart rate ($\overline{HR}$): The mean heart rate is the average heart rate over a period of time, calculated as:

$$\overline{HR} = \frac{1}{N_{peaks} - 1} \sum_{i=2}^{N_{peaks}} HR_i \tag{4.15}$$

Where HR_i is the instantaneous heart rate of the beat i and N_{peaks} is the number of heart beats found.

Variance heart rate (HR_{var}): The variance of the heart rate measures the variability of heart rate over the duration of the experiment. It is calculated as:

$$HR_{var} = \frac{1}{N_{peaks} - 1} \sum_{i=2}^{N_{peaks}} (HR_i - \overline{HR})^2 \tag{4.16}$$

where HR_i is the heart rate at beat i, $\overline{HR}$ is the mean heart rate, and N_{peaks} is the number of heart beats found.

Then the **Power Spectral Density (PSD)** and a **Kaiser-Teager Energy (KTE)** operator of the signal is calculated. The PSD allows the observation of the distribution of energy over different frequency components of a signal. The KTE operators are commonly used to determine the energy profiles of signals.

Then the kurtosis, the mean and the variance of those two functions are calculated.

The kurtosis indicates the "tailedness" of a function. It is a measure of whether the data are heavy-tailed or light-tailed relative to a normal distribution. The equation 4.17 describes the calculation for the kurtosis.

$$x_{kur} = \frac{N \sum_{i=1}^{N} (x_i - \overline{x})^4}{\left(\sum_{i=1}^{N} (x_i - \overline{x})^2\right)^2} - 3 \tag{4.17}$$

Where x_{kur} is the kurtosis of the function x, x_i represents the individual data points, $\overline{x}$ is the mean of the data, and N is the number of data points

Subsequently, the first beat is extracted, and a double Gaussian mixture model is fitted to this beat, from which the parameters of the mixture are extracted.

Double Gaussian Mixture: A double Gaussian mixture model consists of two Gaussian components combined to better fit a dataset that shows a bimodal distribution. The probability density function (PDF) of a Gaussian mixture model is given by:

$$p(x) = w_1 \frac{1}{\sqrt{2\pi\sigma_1^2}} \exp\left(-\frac{(x-\mu_1)^2}{2\sigma_1^2}\right) + w_2 \frac{1}{\sqrt{2\pi\sigma_2^2}} \exp\left(-\frac{(x-\mu_2)^2}{2\sigma_2^2}\right) \tag{4.18}$$

where w_1 and w_2 are the weights of the two Gaussian components, μ_1 and μ_2 are their means, and σ_1 and σ_2 are their standard deviations.

In addition, the quadratic error between the double Gaussian mixture model and the real beat is calculated.

Quadratic error (MSE): The quadratic error, also known as mean squared error (MSE), measures the average of the squares of the errors between predicted and actual values. It is calculated as in 4.19.

$$MSE = \frac{1}{N} \sum_{i=1}^{N} (y_i - \hat{y}_i)^2 \tag{4.19}$$

where y_i is the actual value, $\hat{y}_i$ is the predicted value, and N is the number of observations.

In summary, the features used are :

— Number of peaks (N_{peaks})
— Mean heart rate ($\overline{HR}$)
— Variance heart rate (HR_{var})
— The kurtosis of the PSD (PSD_{kur})
— The mean of the PSD (PSD_{mean})

- The variance of the PSD (PSD_{var})
- The kurtosis of the KTE (KTE_{kur})
- The mean of the KTE (KTE_{mean})
- The variance of the KTE (KTE_{var})
- Weight of the first Gaussian (w_1)
- Weight of the second Gaussian (w_2)
- Mean of the first Gaussian (μ_1)
- Mean of the second Gaussian (μ_2)
- Standard deviation of the first Gaussian (σ_1)
- Standard deviation of the second Gaussian (σ_2)
- Quadratic error of the Gaussian Mixture Model (MSE)

All those features are calculated for each wavelength.

Choice of the machine learning algorithm

Several machine learning algorithms are tested to evaluate their performance on the dataset:

- Linear Regression: A fundamental algorithm used as a baseline model to find the linear relationships within the data.
- Random Forest: An ensemble learning method that leverages multiple decision trees to enhance prediction accuracy and manage overfitting.
- Support Vector Regression (SVR): A robust algorithm designed to handle non-linear relationships by maximizing the margin of tolerance and minimizing error.

Each algorithm is carefully chosen to explore different aspects of the data, from linear patterns to complex, non-linear interactions.

4.4.3 Results on determination of glucose level using the advanced platform

Presentation of the evaluation metrics

Four evaluation metrics are selected to assess the model performance : R^2, MSE, mARD, and the Clarke Error Grid.

In the context of machine learning cross-validation, the coefficient of determination, denoted as R^2, plays a crucial role in evaluating model performance. R^2, as described by Equation 4.20, measures the proportion of variance in the dependent variable that can be explained by the independent variables used in the model. It effectively quantifies how well the model replicates the observed outcomes, with a value ranging from 0 to 1. A higher R^2 value indicates that the model explains a larger portion of the variance, suggesting better predictive accuracy.

$$R^2 = 1 - \frac{\sum_{i=1}^{n}(y_i - \hat{y}_i)^2}{\sum_{i=1}^{n}(y_i - \bar{y})^2} \tag{4.20}$$

Where y_i represents the actual values, $\hat{y}_i$ the predicted values, and $\bar{y}$ the mean of the actual values. This metric is especially valuable in cross-validation as it helps to identify models that not only fit the training data well but also generalize effectively to unseen data.

It is important to note that R^2 can sometimes yield negative values. This occurs when the predictions being compared to the outcomes are not derived from a model-fitting procedure using those data. In such cases, the mean of the data provides a better fit to the outcomes than the fitted function values, according to this criterion.

In statistics, the MSE of an estimator measures the average of the squares of the errors, meaning the average squared difference between the estimated values and the actual values. The formula for MSE is given by Equation 4.21.

$$\mathrm{MSE} = \frac{1}{n}\sum_{i=1}^{n}(y_i - \hat{y}_i)^2 \tag{4.21}$$

Where y_i represents the actual values, and $\hat{y}_i$ the predicted values.

MSE serves as a key measure of the quality of an estimator. As it is derived from the square of Euclidean distance, MSE is always positive and decreases as the prediction error approaches zero. MSE is also the second moment (about the origin) of the error, meaning it incorporates both the variance of the estimator (how widely the estimates vary across different samples) and its bias (how far off the average estimated value is from the true value). Moreover, since MSE have the same units as the square of the quantity being estimated, taking its square root yields the root-mean-square error (RMSE), which have the same units as the estimated quantity. In the case of an unbiased estimator, the RMSE is equivalent to the standard error, providing a measure of the standard deviation of the estimator. The MSE highlights the model's prediction accuracy.

Another commonly used evaluation method in clinical studies for assessing device accuracy is the mARD. mARD quantifies the average percentage difference between a device's measurement (or test result) and a reference measurement, particularly at normal to high glucose levels. The formula for mARD is as given by Equation 4.22:

$$mARD = \frac{1}{n}\sum_{i=1}^{n}\left|\frac{y_i - \hat{y}_i}{y_i}\right| \times 100\% \tag{4.22}$$

where y_i denotes the reference (actual) values, and $\hat{y}_i$ represents the device's measured values.

A lower mARD value indicates a closer alignment between the device and the reference/comparator measurement, signifying higher accuracy.

The mARD evaluates the relative deviation of predictions from actual values, providing an intuitive understanding of the model's performance in percentage terms.

Finally, the Clarke Error Grid Analysis, introduced in 1987, is a methodological framework designed to assess the clinical accuracy of patient-reported blood glucose estimates in comparison to values obtained from blood glucose meters. Initially, it was used to evaluate the clinical accuracy of these estimates, against a reference standard. Over time, the Clarke Error Grid Analysis has become widely recognized as a gold standard for evaluating the precision and accuracy of blood glucose meters [33]. The Clarke Error Grid is presented in Figure 4.8.

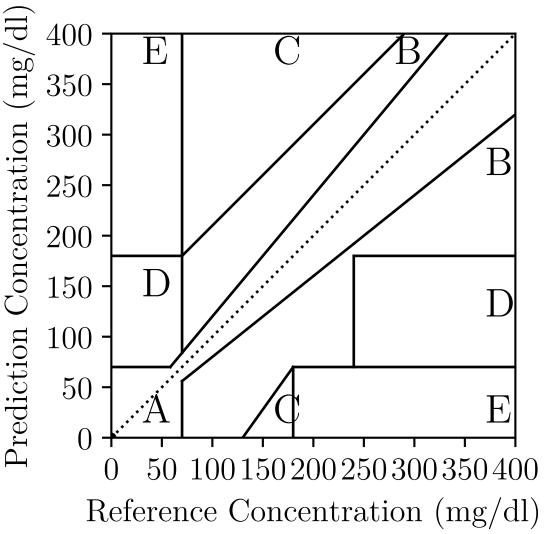

Figure 4.8 – Empty Clarke Error Grid

The grid is divided into five regions (A through E) that categorize the clinical significance of the error in blood glucose measurements. Zone A represents values that are

	Linear Regression	Random Forest	SVR	Naive Method
R^2	-2642595.60	-0.73	-0.27	-0.63
MSE	138804901.12	91.11	66.92	85.75
mARD (%)	4902.72	8.26	7.12	8.06

Table 4.1 – Comparison of R^2, MSE and mARD over 17 samples test (with 17 train samples)

clinically accurate, where errors have no significant impact on treatment decisions. Zone B includes values that are slightly erroneous but would lead to minor or no adverse outcomes. In contrast, Zone C indicates values that could result in overcorrecting or failure to detect significant glucose deviations, potentially leading to inappropriate treatment. Zone D represents dangerous errors that could lead to life-threatening decisions, while Zone E involves errors that would result in confusion between hypoglycemia and hyperglycemia.

By classifying measurement errors into these distinct zones, the Clarke Error Grid provides a comprehensive understanding of the impact that inaccuracies in blood glucose readings might have on patient care, ensuring that both healthcare providers and device manufacturers can assess the practical usability of glucose meters in clinical settings. This framework has since been adapted for evaluating other medical devices where accurate readings are critical to patient safety and treatment outcomes.

Experimental results

The results for the R^2 , MSE, and mARD metrics are summarized in Table 4.1, providing a comprehensive comparison of the model performances.

The result on the Clarke Error Grid are presented in Figure 4.9. The red dots correspond to points that couldn't be properly represented because there are outside the Clarke Error Grid, meaning more than 400 $mg \cdot dl_{-1}$ or less than 0 $mg \cdot dl_{-1}$.

In addition to the three previously method, a fourth method called 'Naive Method' is tested. This method consists of providing, during the testing phase, the mean of the glucose readings obtained during the training.

The Linear Regression give aberrant value, some are even negative, which is not possible. This proves that if the glucose level can be read from the PPG sensor, it can not be found through a simple linear relation with the selected features.

The Random Forest and the SVR give similar good results. The dots are all in zone A, which the best zone, as stated previously. In addition, they have a mARD under 9,

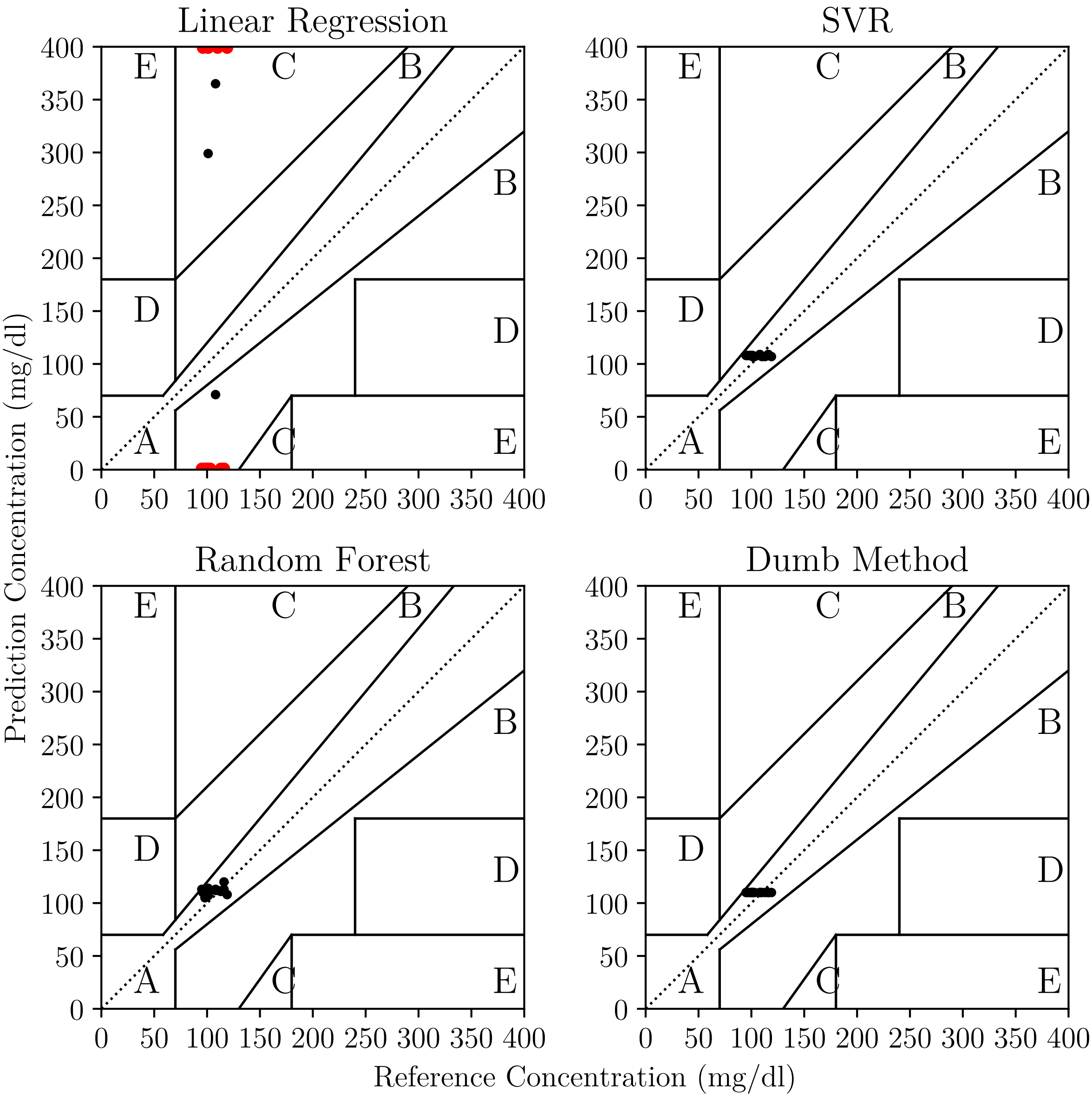

Figure 4.9 – Clarke Error Grid for different method on one subject.

which is a very good result but the R^2 coefficients is negative.

The fact that this 'Naive Method' have as good result as the best of the Random Forest and the SVR, corroborate the negative R^2 of the other methods, and tell us that the variation in glucose level of the subject is not great enough to judge the quality of the methods for the glucose estimation with this dataset.

A study is done, to determine the number of estimator necessary for the Random

Forest. The results are showed in Figure 4.10. For all metrics, the performance stabilizes around 100 estimators, indicating diminishing returns beyond this point.

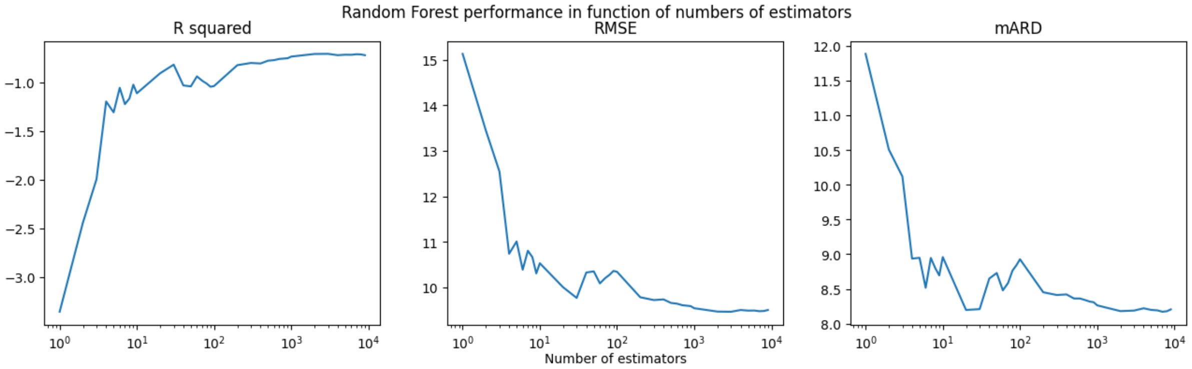

Figure 4.10 – Performance random forest in function of numbers of estimator

4.5 Creation of a Dataset in Collaboration with the ESL

To gather a comprehensive dataset, a measurement campaign has been planned in collaboration with the ESL at EPFL. This dataset will include data collected from a wide range of commercially available sensors alongside our custom-made PPG sensor. The inclusion of different types of sensors, including non-PPG sensors, will allow for rigorous comparison and validation of our sensor. Moreover, the data will be collected during various everyday activities and sports tasks, ensuring a diverse range of physiological parameters and conditions.

4.5.1 Global Platform Developed by ESL

In the context of this research, the global platform developed by ESL plays a pivotal role in enabling efficient and scalable sensor integration. This platform is specifically designed to address the challenges associated with multi-sensor synchronization, providing a versatile and low-power solution. By offering modularity and flexibility in sensor placement, the system ensures seamless data acquisition from a variety of sensors, making it a valuable tool for monitoring physiological parameters in diverse applications. This subsection explores the platform's key features and benefits.

Key features include:

- SPI communication for reliable data transfer between sensor modules and the central unit.
- Data synchronization across multiple sensors to ensure temporal accuracy.
- A low-power design, optimized for continuous and long-term data collection.

The platform integrates the following sensors:

- Inertial Measurement Unit (IMU)
- ECG
- PPG
- Accelerometer (ACG)
- Respiration (RSP)
- Electromyography (EMG)
- Skin Temperature (SkT)

The system is modular, meaning it consists of a central board with an MCU, power supply, and battery. Individual sensor modules are connected to this central board and are placed strategically on the body, as shown in Figure 4.11. For the dataset, two units will be used: one on the chest and one on the wrist.

4.5.2 Enhancement of the Platform for Real-World Data Collection

To integrate seamlessly with the ESL platform, several enhancements are made to our PPG sensor. ESL has developed an electronic board that centralizes data from multiple sensors, and our sensor is upgraded to ensure compatibility with their system.

Key improvements include:

- The development of an SPI communication interface, partly motivated by this collaboration, allowing efficient data transmission to ESL's board.
- The use of medical-grade resin for the sensor probe, ensuring compliance with medical standards and facilitating easy cleaning.
- Optimization of the probe's form factor for better integration into ESL's modular platform, as show in Figure 4.12.

In Figure 4.12, the probe design prior to the collaboration is shown on the left, while the newly developed, custom-made probes are displayed on the right. The new round form factor not only integrates more seamlessly into larger platforms but also ensures

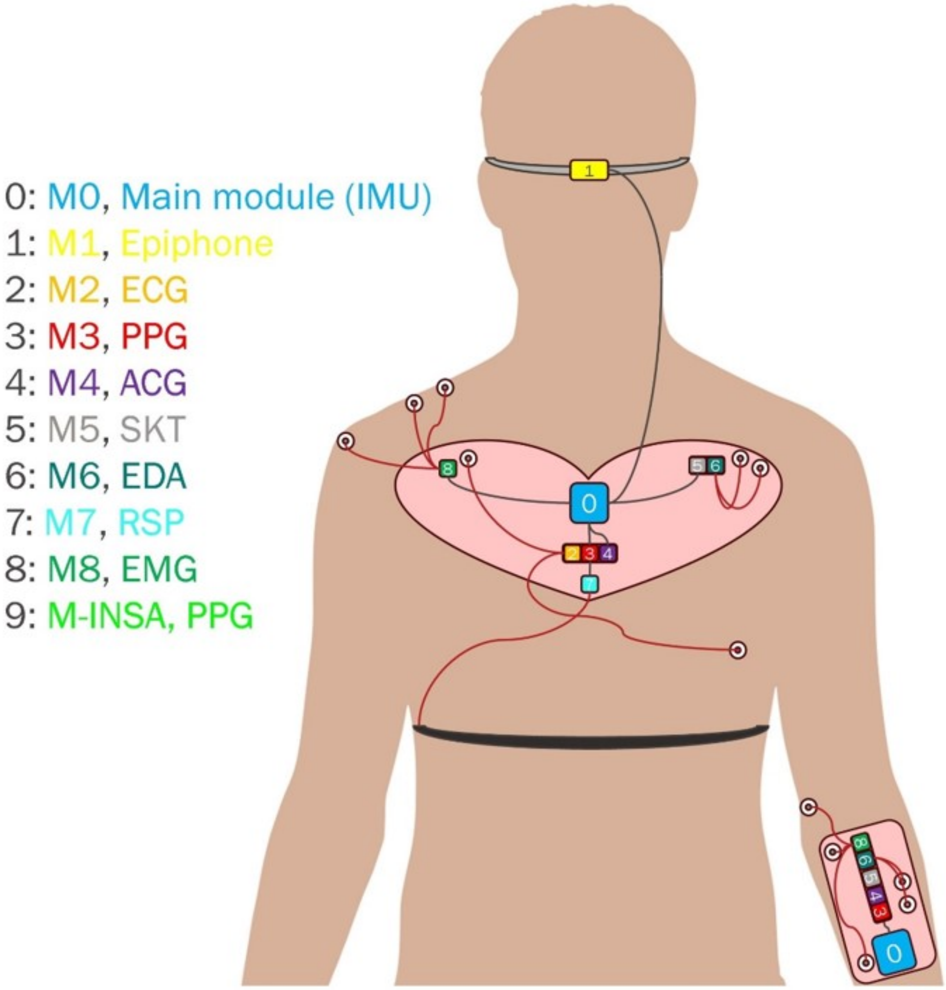

Figure 4.11 – Provisional placement and choice of sensors for the dataset.

more even distribution of pressure, improving both comfort and measurement consistency. Additionally, the upgraded connectors provide a significantly more robust and durable connection, better suited to the mobile and wearable nature of the PPG sensor, enhancing its reliability in real-world, nomadic applications.

These improvements are crucial for ensuring that our sensor functions effectively within the overall platform, making it suitable for real-world data collection campaigns.

4.5.3 Protocol for Data Collection

Participants from EPFL will be recruited to perform a variety of activities while wearing the full sensor suite. The chosen activities represent common daily tasks and

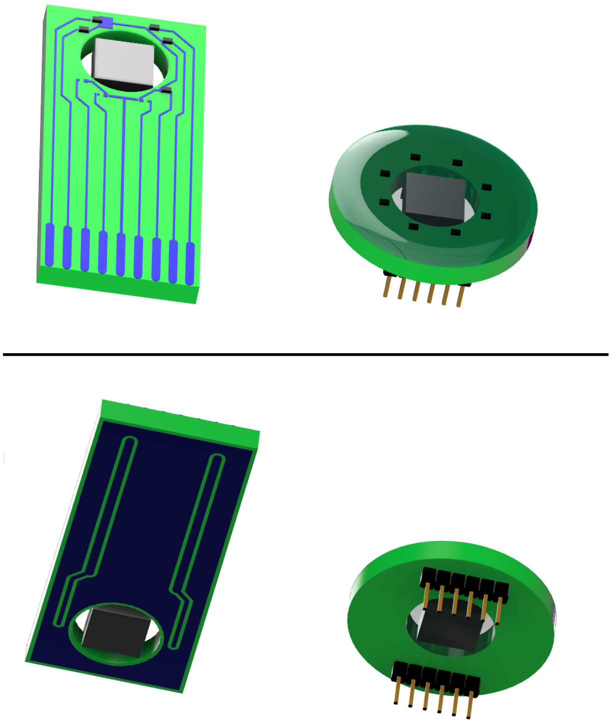

Figure 4.12 – Optimization of the probe's form factor for better integration into ESL's modular platform.

physical exercises, ensuring a wide range of physiological responses are captured.

The activities include:

- Driving
- Eating
- Walking
- Running
- Playing table football (Babyfoot)

Participants will wear the global platform, including all sensors, for continuous measurement throughout these activities. This protocol is designed to provide a rich dataset covering various physical and physiological conditions, enabling robust analysis of sensor performance and inter-sensor comparison.

4.6 Conclusion

Among the three avenues explored, cardio-respiratory parameters are successfully evaluated using the sensor. The evaluation of SpO_2 and other hemoglobin concentrations also showed promising results, demonstrating coherence with biological expectations, even though they are not compared against the gold standard. Due to the previously mentioned challenges, assessing the precision of glucose measurement using the platform remains difficult.

These experiments represent only a fraction of the PPG sensor's potential, highlighting its versatility and adaptability. Further in-depth experiments and additional research are essential to fully explore and unlock the sensor's capabilities, offering opportunities for broader applications and deeper insights into physiological monitoring.

In addition, the planned dataset collection in collaboration with the Embedded Systems Laboratory (ESL) will provide a crucial opportunity for further validation. By incorporating a broad range of physiological sensors and collecting data from participants engaged in various daily and physical activities, this dataset will allow a more thorough comparison of our platform against other well-established sensors. The diversity and volume of the collected data will help to refine the algorithms and potentially unlock new insights.

CONCLUSION AND FUTURE WORK

Conclusion

This thesis has explored the development and enhancement of PPG technology, focusing on improving the accuracy and reliability of physiological measurements, such as heart rate, respiratory rate, hemoglobin concentrations, and glucose levels. The research has demonstrated that PPG offers a valuable, non-invasive approach to monitoring various physiological parameters, with significant potential for applications in both medical and consumer contexts.

The ability of PPG to capture modulations related to breathing patterns and cardiac activity makes it a powerful tool for assessing respiratory efficiency and overall health. Despite challenges such as signal interference and calibration difficulties, the research has shown that PPG provides valuable insights into heart rate variability and blood glucose levels. The application of PPG in glucose monitoring is particularly promising, although achieving accurate measurements remains challenging due to issues related to tissue optics and sensor calibration.

The accuracy of PPG measurements is found to be influenced by several factors, including wavelength selection, the distance between LEDs and photodetectors, and calibration for individual physiological variations.

Through the development of a new PPG platform, this research has addressed several limitations of current devices. The platform incorporates multiple wavelengths (more than four), higher frequency (up to 10kHz), and higher resolution, all while maintaining portability. It supports the capture and storage of raw data and embedded signal processing with a general-purpose processor. The software developed for the platform prioritizes user experience, demonstrating a seamless integration of user-friendly interfaces with sophisticated measurement and data management capabilities.

The quality enhancement functions of the platform, including calibration of the DC level and optimization of the distance between the LED and photodiode, are tested and found to be efficient. Additionally, the platform successfully evaluated cardio-respiratory parameters, SpO_2, and hemoglobin concentrations, showing promising results consistent with biological expectations. However, assessing the precision of glucose measurements remains a challenge, requiring further large-scale experiments to confirm the platform's potential in non-invasive glucose evaluation.

In 2022, after the start of this thesis, Maxim Integrated introduced a new evaluation kit, the MAXREFDES280, designed for the rapid assessment of the MAX86171, a state-of-the-art low-noise PPG sensor. This evaluation band integrates a 3-axis accelerometer, four photodiodes, and eight LEDs, optimizing it for advanced biometric monitoring. The LEDs' configuration consists of two Osram SFH 7013 Red/IR/Green LED packages, where the Red operates at 655 nm, the Green at 530 nm, and the Infrared Emitter at 940 nm [41]. Additionally, the kit includes two green LEDs emitting at 536 nm [40].

The MAX86171 itself is a highly efficient, ultra-low-power optical data acquisition system, designed to cater to diverse optical sensing applications. It provides a versatile platform with nine LED driver output pins, programmable via three high-current, 8-bit LED drivers. On the receiver side, it features two low-noise charge-integrating front-ends, each equipped with independent 19.5-bit analog-to-digital converters (ADCs) and advanced ambient light cancellation (ALC) circuitry, enhancing measurement accuracy under varying light conditions [28]. The release of the MAXREFDES280 underscores the relevance and timeliness of the work presented in this thesis. Many of the advanced features introduced in this evaluation kit, such as multi-wavelength sensing and low-noise optical signal acquisition, and more recently, the power efficiency, closely align with the design principles and innovations developed for the platform created during this research. However, it is important to highlight that the platform developed in this thesis offers significant advantages, particularly its open hardware nature. All components and design aspects of this platform are fully available and modifiable, allowing the research community to freely adapt and enhance the system for future investigations. This open-source approach not only fosters innovation but also ensures that the platform can evolve to meet the demands of various applications, ensuring its long-term utility and adaptability in both research and practical deployments.

Future Work

Looking forward, this research opens up several promising avenues for future exploration. One of the immediate next steps involves leveraging the developed PPG sensor in new projects at EPFL, where it will be used alongside other advanced measurement devices to build a comprehensive dataset. This dataset will play a pivotal role in refining the sensor's performance, enhancing the accuracy of physiological measurements, and expanding its applicability in both sports and medical domains.

Moreover, the continuation of this work in a post-doctoral context will focus on real-world applications, particularly within the framework of the IH2A chair. This cross-disciplinary initiative aims to address mobility and accessibility challenges by co-developing assistive technologies with researchers, clinicians, and end-users. A key aspect of this research will involve studying the user acceptance of the sensor, with special emphasis on its use during para-sports activities, and evaluating its potential for monitoring stress and glucose levels in individuals with disabilities.

In parallel, collaboration with industry partners such as *Innove* offers exciting opportunities. *Innove* specializes in real-time data transmission for various IoT applications, and our sensor technology could be integrated into their platform for advanced sports performance monitoring or continuous medical diagnostics. This synergy has the potential to enhance the impact of our system by making the data more accessible and actionable.

Furthermore, national projects, like those funded by the French National Research Agency (ANR) under the PEPR SantéNum initiative, present valuable opportunities to extend this research. With a focus on developing multi-scale digital twins for personalized health monitoring and treatment, future proposals could explore how the developed sensor fits within this innovative ecosystem, contributing to both clinical and assistive technologies.

It is also worth mentioning the significant role of the EUR Digisport program in supporting this work. The funding provided by Digisport not only facilitated the technical development of the sensor but also aligned with their broader mission to foster innovation at the intersection of sports and digital technology. The prototype created during this thesis represents a strong foundation for further development, with future miniaturization efforts (see Subsection 2.4.5) paving the way for wider adoption in sports and health applications.

BIBLIOGRAPHY

---

[1] *Accu-Chek Performa Nano Blood Glucose Meter*, `https://www.accu-chek.co.uk/products/meters/accu-chek-performa-nano`, (visited on 09/10/2024).

[2] Ajmal et al., « Monte Carlo analysis of optical heart rate sensors in commercial wearables: the effect of skin tone and obesity on the photoplethysmography (PPG) signal », *in*: *Biomed. Opt. Express* 12.*12* (Dec. 2021), pp. 7445–7457, DOI: `10.1364/BOE.439893`, URL: `https://opg.optica.org/boe/abstract.cfm?URI=boe-12-12-7445`.

[3] Ludvik Alkhoury et al., « Heart-rate tuned comb filters for processing photoplethysmogram (PPG) signals in pulse oximetry », *in*: *Journal of Clinical Monitoring and Computing* 35.*4* (Aug. 2021), pp. 797–813, ISSN: 1573-2614, DOI: `10.1007/s10877-020-00539-2`, URL: `https://doi.org/10.1007/s10877-020-00539-2`.

[4] John Allen et al., « Age-related changes in pulse risetime measured by multi-site photoplethysmography », *in*: *Physiological Measurement* 41.*7* (Aug. 2020), Publisher: IOP Publishing, p. 074001, ISSN: 0967-3334, DOI: `10.1088/1361-6579/ab9b67`, URL: `https://dx.doi.org/10.1088/1361-6579/ab9b67` (visited on 07/11/2024).

[5] GARY G. BERNTSON, JOHN T. CACIOPPO, and KAREN S. QUIGLEY, « Respiratory sinus arrhythmia: Autonomic origins, physiological mechanisms, and psychophysiological implications », *in*: *Psychophysiology* 30.*2* (1993), pp. 183–196, DOI: `https://doi.org/10.1111/j.1469-8986.1993.tb01731.x`, eprint: `https://onlinelibrary.wiley.com/doi/pdf/10.1111/j.1469-8986.1993.tb01731.x`, URL: `https://onlinelibrary.wiley.com/doi/abs/10.1111/j.1469-8986.1993.tb01731.x`.

[6] *BITalino FAQs*, `https://bitalino.com/documentation/faqs`, Accessed: 2022-11-11.

[7] Kang-Ming Chang and Keng-Ming Chang, « Pulse Rate Derivation and Its Correlation with Heart Rate », *in*: *Journal of Medical and Biological Engineering* 29 (Jan. 1, 2009), pp. 132–137.

[8] Safa Cherif, « Effective signal processing methods for robust respiratory rate estimation from photoplethysmography signal », Theses, Ecole nationale supérieure Mines-Télécom Atlantique, Oct. 2018, URL: `https://tel.archives-ouvertes.fr/tel-02160161`.

[10] JinGuo Dong, « The role of heart rate variability in sports physiology (Review) », *in*: *Exp Ther Med* 11.*5* (May 2016), pp. 1531–1536, DOI: `10.3892/etm.2016.3104`, URL: `https://doi.org/10.3892/etm.2016.3104`.

[13] E. Randy Eichner, « L'ANÉMIE ET LE DOPAGE SANGUIN », *in*: *Sports Science* 14.*2* (2001).

[14] M. Elgendi, « Optimal Signal Quality Index for Photoplethysmogram Signals », *in*: *Bioengineering (Basel)* 3.*4* (Sept. 2016).

[15] Mohamed Elgendi, « On the analysis of fingertip photoplethysmogram signals », eng, *in*: *Current cardiology reviews* 8.*1* (Feb. 2012), pp. 14–25, ISSN: 1875-6557, DOI: `10.2174/157340312801215782`, URL: `https://doi.org/10.2174/157340312801215782`.

[16] *ESL | Laboratoire des systèmes embarqués*, https://www.epfl.ch/labs/esl/fr/esl-laboratoire-des-systemes-embarques/, (visited on 09/24/2024).

[17] *File:Wiggers Diagram.svg - Wikipedia*, Mar. 20, 2012, URL: `https://commons.wikimedia.org/wiki/File:Wiggers_Diagram.svg` (visited on 07/08/2024).

[18] A. Fusco et al., « On how to extract breathing rate from PPG signal using wearable devices », *in*: *2015 IEEE Biomedical Circuits and Systems Conference (BioCAS)*, Oct. 2015, pp. 1–4, DOI: `10.1109/BioCAS.2015.7348369`.

[19] *Guidelines for the Opto-Mechanical Integration of Heart-Rate Monitors in Wearable Wrist Devices | Analog Devices*, URL: `https://www.analog.com/en/resources/technical-articles/guidelines-for-the-optomechanical-integration-of-heartrate-monitors-in-wearable-wrist-devices.html` (visited on 07/08/2024).

[20] Aminah Hina and Wala Saadeh, « A Noninvasive Glucose Monitoring SoC Based on Single Wavelength Photoplethysmography », *in*: *IEEE Transactions on Biomedical Circuits and Systems* 14.*3* (June 2020), Conference Name: IEEE Transactions on Biomedical Circuits and Systems, pp. 504–515, ISSN: 1940-9990, DOI: `10.1109/TBCAS.2020.2979514`, URL: `https://ieeexplore-ieee-org.rproxy.insa-rennes.fr/document/9028112` (visited on 08/06/2024).

[21] Aminah Hina and Wala Saadeh, « Noninvasive blood glucose monitoring systems using Near-Infrared technology-A review », en, *in*: *Sensors (Basel)* 22.*13* (June 2022), p. 4855.

[22] Fu-Hsuan Huang et al., « Analysis of Reflectance Photoplethysmograph Sensors », *in*: *International Journal of Biomedical and Biological Engineering* 5.*11* (2011), pp. 622–625, ISSN: eISSN: 1307-6892, URL: `https://publications.waset.org/vol/59`.

[23] W. Johnston and Y. Mendelson, « Extracting heart rate variability from a wearable reflectance pulse oximeter », *in*: *Proceedings of the IEEE 31st Annual Northeast Bioengineering Conference, 2005.* Apr. 2005, pp. 157–158, DOI: `10.1109/NEBC.2005.1431971`.

[24] Yung-Hua Kao, Paul C.-P. Chao, and Chin-Long Wey, « Design and Validation of a New PPG Module to Acquire High-Quality Physiological Signals for High-Accuracy Biomedical Sensing », *in*: *IEEE Journal of Selected Topics in Quantum Electronics* 25.*1* (Jan. 2019), pp. 1–10, ISSN: 1558-4542, DOI: `10.1109/JSTQE.2018.2871604`.

[25] Yung-Hua Kao et al., « A new reflective PPG LED-PD sensor module for cuffless blood pressure measurement at wrist artery », *in*: *2017 IEEE SENSORS*, Oct. 2017, pp. 1–3, DOI: `10.1109/ICSENS.2017.8234348`.

[26] J G Kim and H Liu, « Variation of haemoglobin extinction coefficients can cause errors in the determination of haemoglobin concentration measured by near-infrared spectroscopy », *in*: *Physics in Medicine and Biology* 52.*20* (Sept. 2007), pp. 6295–6322, DOI: `10.1088/0031-9155/52/20/014`, URL: `https://doi.org/10.1088/0031-9155/52/20/014`.

[27] Bojan Makivic, M.D. Niki, and Monte Willis, « Heart Rate Variability (HRV) as a Tool for Diagnostic and Monitoring Performance in Sport and Physical Activities », *in*: *Journal of Exercise Physiology Online* 16 (Jan. 2013), pp. 103–131.

[28] *MAXREFDES280 | reference design | Analog Devices*, URL: `https://www.analog.com/en/resources/reference-designs/maxrefdes280.html#rd-overview` (visited on 07/11/2024).

[29] Elisa Mejía-Mejía et al., « Pulse rate variability in cardiovascular health: a review on its applications and relationship with heart rate variability », *in*: *Physiological Measurement* 41.*7* (Aug. 11, 2020), 07TR01, ISSN: 1361-6579, DOI: `10.1088/1361-`

`6579/ab998c`, URL: `https://iopscience.iop.org/article/10.1088/1361-6579/ab998c` (visited on 07/08/2024).

[30] Y. Mendelson and C. Pujary, « Measurement site and photodetector size considerations in optimizing power consumption of a wearable reflectance pulse oximeter », *in*: *Proceedings of the 25th Annual International Conference of the IEEE Engineering in Medicine and Biology Society (IEEE Cat. No.03CH37439)*, Proceedings of the 25th Annual International Conference of the IEEE Engineering in Medicine and Biology Society (IEEE Cat. No.03CH37439), vol. 4, ISSN: 1094-687X, Sept. 2003, 3016–3019 Vol.4, DOI: `10.1109/IEMBS.2003.1280775`, URL: `https://ieeexplore-ieee-org.rproxy.insa-rennes.fr/document/1280775` (visited on 07/08/2024).

[31] David J Meredith et al., « Photoplethysmographic derivation of respiratory rate: a review of relevant physiology », *in*: *Journal of medical engineering & technology* 36.*1* (2012), pp. 1–7.

[32] Gian Mario Migliaccio et al., « Sports Performance and Breathing Rate: What Is the Connection? A Narrative Review on Breathing Strategies », *in*: *Sports* 11.*5* (May 10, 2023), p. 103, ISSN: 2075-4663, DOI: `10.3390/sports11050103`, URL: `https://www.ncbi.nlm.nih.gov/pmc/articles/PMC10224217/` (visited on 07/10/2024).

[33] Timothy E. Morey, Nikolaus Gravenstein, and Mark J. Rice, « Let's Think Clinically Instead of Mathematically About Device Accuracy », *in*: *Anesthesia & Analgesia* 113.*1* (2011), ISSN: 0003-2999.

[34] Andrea Nicolò et al., « The Importance of Respiratory Rate Monitoring: From Healthcare to Sport and Exercise », *in*: *Sensors (Basel, Switzerland)* 20.*21* (Nov. 9, 2020), p. 6396, ISSN: 1424-8220, DOI: `10.3390/s20216396`, URL: `https://www.ncbi.nlm.nih.gov/pmc/articles/PMC7665156/` (visited on 07/10/2024).

[35] Meir Nitzan, Igor Faib, and Haim Friedman, « Respiration-induced changes in tissue blood volume distal to occluded artery, measured by photoplethysmography », *in*: *Journal of biomedical optics* 11.*4* (2006), pp. 040506–040506.

[36] Meir Nitzan, Ayal Romem, and Robert Koppel, « Pulse oximetry: fundamentals and technology update », eng, *in*: *Medical devices (Auckland, N.Z.)* 7 (July 2014), pp. 231–239, ISSN: 1179-1470, DOI: `10.2147/MDER.S47319`, URL: `https://doi.org/10.2147/MDER.S47319`.

[37] Meir Nitzan et al., « Measurement of oxygen saturation in venous blood by dynamic near IR spectroscopy », *in*: *Journal of Biomedical Optics* 5.*2* (2000), pp. 155–162, DOI: `10.1117/1.429982`, URL: `https://doi.org/10.1117/1.429982`.

[38] Ilze Oshina and Janis Spigulis, « BeerLambert law for optical tissue diagnostics: current state of the art and the main limitations », *in*: *Journal of Biomedical Optics* 26.*10* (2021), p. 100901, DOI: `10.1117/1.JBO.26.10.100901`, URL: `https://doi.org/10.1117/1.JBO.26.10.100901`.

[39] *OSRAM DIL, BPW 34 Photodiodes - ams-osram - ams*, ams-osram, URL: `https://ams-osram.com/products/photodetectors/photodiodes/osram-dil-bpw-34` (visited on 08/06/2024).

[40] *OSRAM FIREFLYő, CT DBLP31.12 Color LEDs - ams-osram - ams*, ams-osram, URL: `https://ams-osram.com/products/leds/color-leds/osram-firefly-ct-dblp31-12` (visited on 07/11/2024).

[41] *OSRAM Multi Chip LED, SFH 7013 Multi color LEDs - ams-osram - ams*, ams-osram, URL: `https://ams-osram.com/products/leds/multi-color-leds/osram-multi-chip-led-sfh-7013` (visited on 07/11/2024).

[42] N. Pinheiro et al., « Can PPG be used for HRV analysis? », *in*: *2016 38th Annual International Conference of the IEEE Engineering in Medicine and Biology Society (EMBC)*, 2016 38th Annual International Conference of the IEEE Engineering in Medicine and Biology Society (EMBC), Orlando, FL, USA: IEEE, Aug. 2016, pp. 2945–2949, ISBN: 978-1-4577-0220-4, DOI: `10.1109/EMBC.2016.7591347`, URL: `http://ieeexplore.ieee.org/document/7591347/` (visited on 07/04/2024).

[43] K. Ashoka Reddy et al., « A Novel Calibration-Free Method of Measurement of Oxygen Saturation in Arterial Blood », *in*: *IEEE Transactions on Instrumentation and Measurement* 58.*5* (June 2009), pp. 1699–1705, ISSN: 1557-9662, DOI: `10.1109/TIM.2009.2012934`.

[44] Shantanu Sen Gupta et al., « Towards non-invasive blood glucose measurement using machine learning: An all-purpose PPG system design », *in*: *Biomedical Signal Processing and Control* 68 (2021), p. 102706, ISSN: 1746-8094, DOI: `https://doi.org/10.1016/j.bspc.2021.102706`, URL: `https://www.sciencedirect.com/science/article/pii/S1746809421003037`.

[45] Ville-Pekka Seppä et al., « Assessment of Breathing Parameters during Running with a Wearable Bioimpedance Device », *in*: *4th European Conference of the International Federation for Medical and Biological Engineering*, ed. by Jos Vander Sloten et al., Berlin, Heidelberg: Springer Berlin Heidelberg, 2009, pp. 1088–1091, ISBN: 978-3-540-89208-3.

[46] Ángel Solé Morillo et al., « PPG EduKit: An Adjustable Photoplethysmography Evaluation System for Educational Activities », *in*: *Sensors* 22.*4* (2022), p. 1389.

[47] Toshiyo Tamura et al., « Wearable photoplethysmographic sensorspast and present », *in*: *Electronics* 3.*2* (2014), pp. 282–302.

[48] *Thorlabs - S401C Thermal Power Sensor Head, Surface Absorber, 0.19 - 20 Mm, 10 µW - 1 W, Ø10 Mm*, https://www.thorlabs.com, (visited on 09/23/2024).

[49] Wilbert Villena Gonzales, Ahmed Toaha Mobashsher, and Amin Abbosh, « The Progress of Glucose Monitoring-A Review of Invasive to Minimally and Non-Invasive Techniques, Devices and Sensors », *in*: *Sensors (Basel, Switzerland)* 19.*4* (Feb. 2019), E800, ISSN: 1424-8220, DOI: `10.3390/s19040800`, URL: `https://europepmc.org/articles/PMC6412701`.

[50] Gaobo Zhang et al., « A Noninvasive Blood Glucose Monitoring System Based on Smartphone PPG Signal Processing and Machine Learning », *in*: *IEEE Transactions on Industrial Informatics* 16.*11* (Nov. 2020), Conference Name: IEEE Transactions on Industrial Informatics, pp. 7209–7218, ISSN: 1941-0050, DOI: `10.1109/TII.2020.2975222`, URL: `https://ieeexplore-ieee-org.rproxy.insa-rennes.fr/document/9005207` (visited on 08/06/2024).

[51] Yue Zhao et al., « Optimal hemoglobin extinction coefficient data set for near-infrared spectroscopy », eng, *in*: *Biomedical optics express* 8.*11* (Sept. 2017), 29188110[pmid], pp. 5151–5159, ISSN: 2156-7085, DOI: `10.1364/BOE.8.005151`, URL: `https://doi.org/10.1364/BOE.8.005151`.

[52] W.G Zijlstra and A Buursma, « Spectrophotometry of Hemoglobin: Absorption Spectra of Bovine Oxyhemoglobin, Deoxyhemoglobin, Carboxyhemoglobin, and Methemoglobin », *in*: *Comparative Biochemistry and Physiology Part B: Biochemistry and Molecular Biology* 118.*4* (1997), pp. 743–749, ISSN: 1096-4959, DOI: `https://doi.org/10.1016/S0305-0491(97)00230-7`, URL: `https://www.sciencedirect.com/science/article/pii/S0305049197002307`.

PUBLICATION

[9] Flavie Durand De Gevigney et al., « A Highly Configurable Platform for Advanced PPG Analysis », *in*: *Design and Architectures for Signal and Image Processing*, ed. by Tiago Dias and Paola Busia, vol. 14622, Cham: Springer Nature Switzerland, 2024, pp. 3–14, ISBN: 978-3-031-62873-3 978-3-031-62874-0, DOI: `10.1007/978-3-031-62874-0_1`, (visited on 09/28/2024).

[11] Flavie Durand de Gevigney et al., « Advanced Photodetector for Athlete Monitoring », *in*: *EMBC*, Sydney, Australia, July 2023, URL: `https://hal.science/hal-04582259`.

[12] Flavie Durand de Gevigney et al., « Photodétecteur Paramétrable Avancé », *in*: *GRETSI*, ed. by GRETSI-Groupe de Recherche en Traitement du Signal et des Images, vol. 2023–1231, Grenoble, France, Aug. 2023, p. 645–648, (visited on 09/28/2024).

Appendices

SPI

Introduction

Overview

This document describes the custom communication protocol used in our system. The protocol includes various commands for configuration and data transfer, allowing flexible communication between devices.

Features

- Flexible
- Precise

Signal Descriptions

Signal Name	Direction	Description	Voltage Levels
SCLK	Input	Serial Clock	0V, 3.3V
MOSI	Input	Master Out Slave In	0V, 3.3V
MISO	Output	Master In Slave Out	0V, 3.3V
SS	Input	Slave Select	0V, 3.3V

Table 2 – Signal Descriptions

Commands

Command Structure

Commands are composed of an opcode followed by one or more arguments. The general format is:

```
<Opcode> <Argument 1> <Argument 2> ... <Argument N>
```

Command List

Command Name	Opcode	Description
WRITE_CONFIG	0x01	Writes a value to a configuration register.
READ_CONFIG	0x02	Reads a value from a configuration register.
CALIBRATION	0x03	Launch a calibration of the LED on the device.
LAUNCH_MEASURE	0x04	Launch a measure on the device.
READ_DATA	0x05	Reads data from the measure from the device.
RESET	0xFF	Resets the device.

Table 3 – Command List

WRITE_CONFIG Command

- **Opcode**: 0x01
- **Description**: Writes a value to a specified configuration register.
- **Arguments**:
  - Register Address (1 byte)
  - Data (1 byte)
- **Example**:

  `0x01 0x05 0x53`

  This command writes the value 0x53 to the register at address 0x05. Meaning the current in the LED 1 is set to 83mA.
- **Notes**: The registers are detailed in the Section 4.6. For a more in detail example of how to this command, check the section 4.6.

READ_CONFIG Command

- **Opcode**: 0x02
- **Description**: Reads a value from a specified configuration register.
- **Arguments**:
  - Register Address (1 byte)
- **Example**:

  `0x02 0x05`

This command reads the value from the register at address 0x05. Meaning reading the current in the LED 1.

- **Notes**: The registers are detailed in the Section 4.6. For a more in detail example of how to this command, check the Section 4.6.

CALIBRATION Command

- **Opcode**: 0x03
- **Description**: Launch a calibration of the LED on the device.
- **Example**:

  `0x03`

  This command launches a calibration of the LEDs. It will automatically update the current LED registers (see Section 4.6, in particular 4.6).

LAUNCH_MEASURE Command

- **Opcode**: 0x04
- **Description**: Launch a measure on the device.
- **Arguments**:
  - Number of seconds MSB (1 byte)
  - Number of seconds LSB (1 byte)
- **Example**:

  `0x04 0x0E 0x10`

  This command launches a one-hour measure.

READ_DATA Command

- **Opcode**: 0x05
- **Description**: Read packets from the device.
- **Arguments**:
  - Number of packets (1 byte)
- **Example**:

  `0x05 0x0E`

  This command asks the transmission of 14 packets from the device.
- **Notes**:

- This command should be used only after the LAUNCH_MEASURE command (see 4.6).
- There is enough internal storage on the device for the user to only request the packets when needed. There is very little risk of losing data.

RESET Command

- **Opcode**: 0x06
- **Description**: Perform a soft reset of the device, all the parameters are set to theirs defaults values (except the Ids), all measures, and calibrations are stopped.
- **Example**:

  `0x06`

  This command performs a soft reset.

Configuration Registers

Those registers are to be used in combination with the command WRITE_CONFIG (see 4.6) and READ_CONFIG (see 4.6).

Register Address	Default Value	Description
0x00	0x75	Mode and Frequency register (see 4.6)
0x01	0xFF	LEDs activation register (see 4.6)
0x02	0x00	Packet number register (Read only) (see 4.6)
0x04-0x0B	0x00	LED(0-8) current register (see 4.6)
0x0C	0x00	Running status register (see 4.6)
0x0D	0x00	Current Calibration Id (see 4.6)
0x0E	0x00	Current Measure Id (see 4.6)

Table 4 – Register Map

0x00 Register: Mode and Frequency

The ‘0x00‘ register is used to configure the mode and frequency of the device. It is composed of 4 bits for the mode and 4 bits for the frequencies as follows:

Bit Position	7	6	5	4	3	2	1	0
Categories		Mode			Frequencies			
Bit Name	X	ACDC	DC	AC	freq[3]	freq[2]	freq[1]	freq[0]

Table 5 – 0x00 Register: Mode and Frequency

Mode Configuration

The ‘Mode‘ bits (ACDC, DC, AC) determine the operating mode of the device:

— **ACDC** (bit 6): Specifies whether ACDC mode is enabled.
— **DC** (bit 5): Specifies whether DC mode is enabled.
— **AC** (bit 4): Specifies whether AC mode is enabled.

Frequencies Configuration

The ‘Frequency‘ bits (freq[3], freq[2], freq[1], freq[0]) determine the frequency settings. The value formed by these bits corresponds to a specific frequency as shown in the table below:

freq[3]	freq[2]	freq[1]	freq[0]	Frequency (Hz)
0	0	0	0	Undefined
0	0	0	1	50 Hz
0	0	1	0	100 Hz
0	0	1	1	200 Hz
0	1	0	0	400 Hz
0	1	0	1	800 Hz
0	1	1	0	1000 Hz
0	1	1	1	1500 Hz
1	0	0	0	2000 Hz
1	0	0	1	2500 Hz
1	0	1	0	3000 Hz
1	0	1	1	4500 Hz
1	1	0	0	Undefined
1	1	0	1	Undefined
1	1	1	0	Undefined
1	1	1	1	Undefined

Table 6 – Frequency Interpretation

The frequency is determined by interpreting the 4-bit binary value and using the lookup table to find the corresponding frequency in Hz.

0x01 Register: LEDs activation

The ’0x01’ register is used to configure the active LEDs for the next measure on the device. It is composed as follows:

Bit Position	7	6	5	4	3	2	1	0
Categories	Infrared				Visible			
Bit Name	led[7]	led[6]	led[5]	led[4]	led[3]	led[2]	led[1]	led[0]
Wavelength (nm)	940	888	807	762	660	620	593	542

Table 7 – 0x01 Register: LEDs activation

0x02 Register: Packet Number

The ‘0x02‘ register is used to read the number of packets ready to be transferred that are stored in the device’s memory. This register is read-only.

— If the value stored in this register is ‘0xFF‘, it indicates that there are 255 or more packets ready to be transferred.

— Any other value (0x00 to 0xFE) represents the exact number of packets ready to be transferred.

Note : This value is automatically change during a measure, each time a new packet in available, the number of this register is increased by one (if not already at 0xFF).

0x04-0x0B Register: LED(0-8) Current

The ‘0x04‘ to ‘0x0B‘ registers are used to configure and read the current in each of the LEDs. Each register corresponds to one LED, starting from ‘0x04‘ for LED 0 and ending at ‘0x0B‘ for LED 7.

Each register is 8 bits long and can hold a value between 0 and 100, representing the current in the respective LED. The value 0 corresponds to no current, while the value 100 corresponds to the maximum current.

Register Address	0x04	0x05	0x06	0x07	0x08	0x09	0x0A	0x0B
LED Number	LED 0	LED 1	LED 2	LED 3	LED 4	LED 5	LED 6	LED 7

Table 8 – LED Current Register Mapping

The bit structure of each LED current register is as follows:

Bit Position	7	6	5	4	3	2	1	0
Bit Name	Current Value							

Table 9 – Bit Structure of LED Current Registers

The 8-bit value stored in each register directly corresponds to the current level of the associated LED, with the value range as follows:

— **0**: No current (LED is off)

— **1-99**: Proportional current levels

— **100 and more**: Maximum current (100mA)

For example, if register ‘0x04‘ (LED 0) contains the value ‘50‘ (0x32), it means that LED 0 is operating at 50% of its maximum current. If register ‘0x05‘ (LED 1) contains the value ‘100‘ (0x64), it means that LED 7 is operating at its maximum current (100 mA). If the register ‘0x0B‘ (LED 7) contains the value ‘137‘ (0x89), it means that LED 7 is operating at its maximum current (100 mA).

This setup allows for fine control over the brightness of each LED by adjusting the current values in their respective registers.

Note : Those values are automatically determined during the calibration phase, it is not necessary for the user to manually set them. This is an advanced configuration.

0x0C Register: Running Status

The ‘0x0C‘ register is used to read the status of the device. This register provides critical information about the current operating state of the device. The possible status codes are:

— **0x00: Ready** The device is ready to receive a command for calibration or measurement.

— **0x01: Calibrating** The device is currently performing a calibration operation, it is not ready to receive a command.

— **0x02: Measuring** The device is currently performing a measurement operation, it is not ready to receive a command.

— **0x03 - 0xFF: Other** The device is currently performing an undefined task, it is not ready to receive a command.

0x0D Register: Current Calibration ID

The ‘0x0D‘ register is used to read the current calibration ID. Each time a calibration is started, a unique calibration ID is generated and associated with that particular calibration session. This ID serves as a reference for linking the calibration data received from the device to the data stored on the device.

When writing in this register, if the data given correspond to an already attributed calibration, the current LED registers (0x04-0x0B, see 4.6) will be set to the value of the corresponding calibration.

By using the calibration ID, users can accurately track and manage multiple calibration events, ensuring that the correct data is associated with each calibration process. This is particularly useful for maintaining the integrity and traceability of calibration records.

0x0E Register: Current Measurement ID

The ‘0x0E‘ register is used to read the current measurement ID. Similar to the calibration ID, a unique measurement ID is generated each time a measurement is started. This ID is associated with the specific measurement session and allows users to link the received measurement data to the stored data on the device.

Similarly to the calibration ID, when writing a valid ID into the register, all the parameters (registers 0x00 to 0x0D, see Section 4.6) will be set to match the ones used during the measure.

The measurement ID ensures that users can accurately track and reference individual measurement events, facilitating better data management and analysis. This is crucial for applications where precise measurement tracking and data correlation are required.

Protocol Description

Data Transfer

The device works in full duplex mode and shouldn’t be used in half duplex mode.

Each sample is 16 bits long. The number of samples per packet depends on the modes activated (AC, DC, and ACDC) and the number of LEDs activated (0 to 7 LEDs). Each packet consists of 64 samples.

To better understand the data transfer format, we introduce the concept of a "mega-sample." A mega-sample is defined as the aggregated samples of all LEDs for all activated modes within a single sample interval. This means that one mega-sample contains the samples for all LEDs in each activated mode.

To calculate the size of a mega-sample:

— Each sample is 16 bits (2 bytes) long.

— A maximum of 3 modes (AC, DC, ACDC) can be activated simultaneously.

— A maximum of 8 LEDs can be activated (LED 0 to LED 7).

The formula to calculate the total number of bytes in a mega-sample is:

$$\text{Mega-sample Bytes} = \text{Number of LEDs} \times \text{Number of Modes} \times \text{Bytes per Sample}$$

Plugging in the maximum values:

- Number of LEDs: 8
- Number of Modes: 3
- Bytes per Sample: 2

$$\text{Maximum size Mega-sample} = 8 \times 3 \times 2 = 48 \text{ bytes}$$

Each packet consists of 64 such mega-samples. Therefore, to calculate the maximum number of bytes used to transmit a packet, we use the following formula:

$$\text{Total Bytes per Packet} = \text{Mega-sample Bytes} \times \text{Samples per Packet}$$

Given that each packet contains 64 mega-samples:

$$\text{Maximum Total Bytes per Packet} = 48 \times 64 = 3072 \text{ bytes}$$

Thus, the maximum number of bytes used to transmit a packet is 3072 bytes.

Clock Polarity and Phase

- Clock Polarity (CPOL): 1
- Clock Phase (CPHA): 1

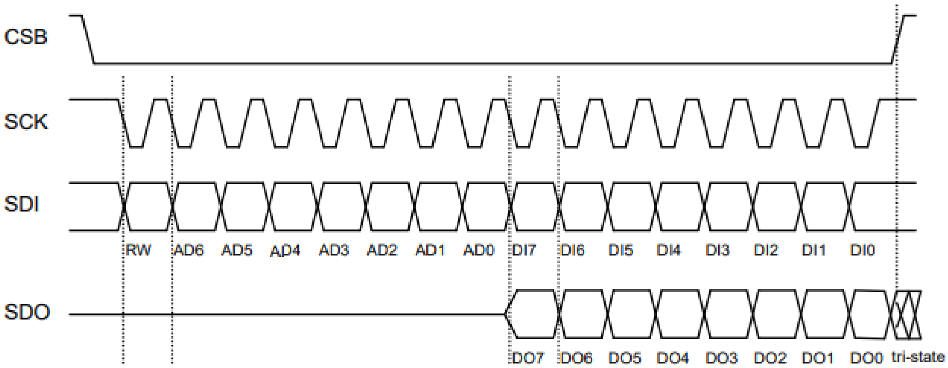

Figure 13 – SPI Timing Diagram

Electrical Characteristics

Voltage and Current Specifications

Parameter	Absolute Min	Recommended Min	Absolute Max	Recommended Max
I/O Voltage (V)	-0.4	0.2	3.4	3.75

Table 10 – Electrical Characteristics

Connectors

The SPI wires on this device are accessible through a USB-C female connector. The specific pin assignments are detailed in Table 11. In the table, the wires specifically used for SPI and general communication are highlighted in bold.

USBC pins	**Description**	**USBC-3**	**Interface**	**Comments**
A1	GND1.1	GND	GND	
A2	SSTXP1	SCL	I2C	Not used
A3	SSTXN1	SDA	I2C	Not used
A4	VBUS1.1	3.3V		Do not use
A5	**CC1**	**SCLK, SCL**	**SPI**	**Clock of the SPI**
A6	**DP1**	**SDI (MISO)**	**SPI**	**MISO of the SPI**
A7	**DN1**	**SDO (MOSI)**	**SPI**	**MOSI of the SPI**
A8	SBU1	CSB1	SPI	Do not use
A9	VBUS1.2	3.3V		Do not use
A10	SSRXN2	CSB2	SPI	Do not use
A11	SSRXP2	FCLK	Clock	Clock for all peripheral sensors
A12	GND1.2	GND	GND	
B1	GND2.1	GND	GND	
B2	SSTXP2	CLK	PDM	Do not use
B3	SSTXN2	Data	PDM	Do not use
B4	VBUS2.1	3.3V		Do not use
B5	**CC2**	**USB3_GP1**	**GPIO**	**Chipselect for the SPI**
B6	**DP2**	**USB3_GP2**	**GPIO**	**Interrupt signal to main SoC**
B7	DN2	USB3_GP3	GPIO	Do not use
B8	SBU2	USB3_GP4	GPIO	Do not use
B9	VBUS2.2	3.3V		Do not use
B10	SSRXN1	Start	GPIO	Hard Reset from Main SoC
B11	**SSRXP1**	**Reset**	**GPIO**	**Hard Reset from Main SoC**
B12	GND2.2	GND	GND	
SH	Shield	Shield	GND	

Table 11 – USBC Pin Configuration

Timing Specifications

Parameter	Value
Clock Frequency (fSCLK)	2MHz

Table 12 – Timing Specifications

Application Examples

Example 1: Configuration

This example demonstrates how to configure the device to activate certain LEDs and set the mode and frequency.

— **Step 1.1: Set Mode and Frequency**

```
0x01 0x00 0x76
```

This command writes the value ‘0x76‘ to the register at address ‘0x00‘, which sets the mode to ACDC (bit 6), DC (bit 5) and AC (bit 4) and the frequency to 1000 Hz (bits 3-0).

— **Step 1.2: Activate LEDs**

```
0x01 0x01 0x8F
```

This command writes the value ‘0x8F‘ to the register at address ‘0x01‘, which activates LEDs 0, 1, 2, 3 and 7 (bits 0, 1, 2, 3, and 7).

— **Step 1.3: Calibrate LEDs**

```
0x03
```

This command launches the calibration of the LEDs.

The Figure 14 is the full chronograph of this first example. At the end of the proposed configuration :

— All the mode are activated (ACDC, AC and DC).

— The sampling frequencies is set to 1000 Hz.

— The LEDs 0, 1, 2, 3, and 7, (meaning the 542 nm, 593 nm, 620 nm, 660 nm and 940 nm LEDs

- The currents in the LEDs (registers ‘0x04‘ to ‘0x0C‘) are set to maximize the quality of the signal.

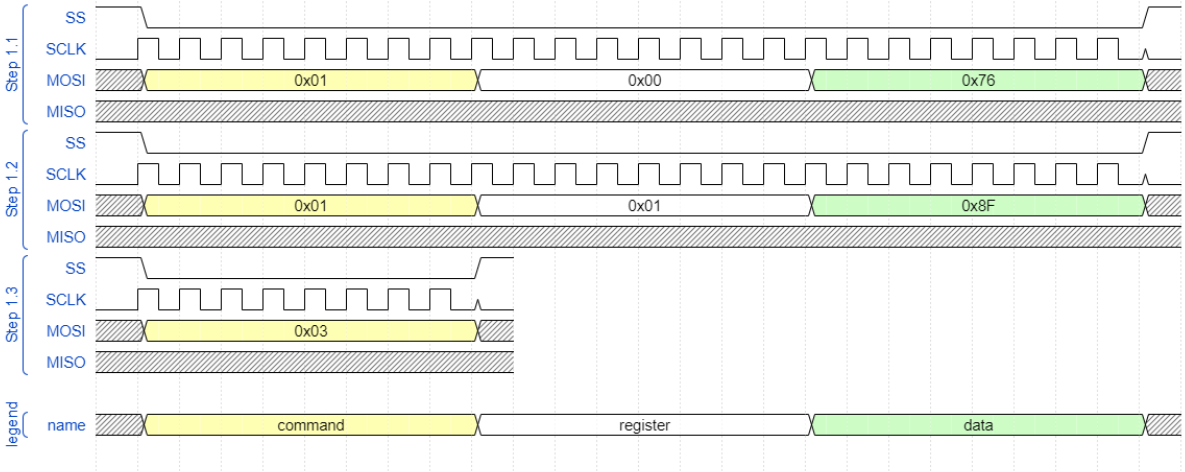

Figure 14 – Example 1 chronograph

Example 2: Full Measure for 30 Minutes

This example demonstrates how to launch a measure for 30 minutes and then read the data.

- **Step 2.1: Launch Measure**

  ```
  0x04 0x07 0x08
  ```

  This command launches a measure for 30 minutes (0x0708 in hexadecimal represents 1800 in decimal).

- **Step 2.2: Read Number of Packet Available**

  ```
  0x02 0x02
  ```

  This command requests the number of packets available on the device.

- **Step 2.3: Read Data**

  ```
  0x05 0xFF
  ```

  This command requests the transmission of 255 packets from the device. If more data is available, additional read commands will be necessary.

The Figure 15 is the full chronograph of this second example. In practice, the best scenario to get 30 min measure, you need to :

- (optional) Follow the first example to set the parameters.
- Follow the Step 2.1.
- Get the number of packet left nPacket by following the Step 2.2.
- While nPacket is not zero:
    - Follow Step 2.3 to retrieve nPacket packets.
    - Get the number of packet left nPacket by following the Step 2.2.

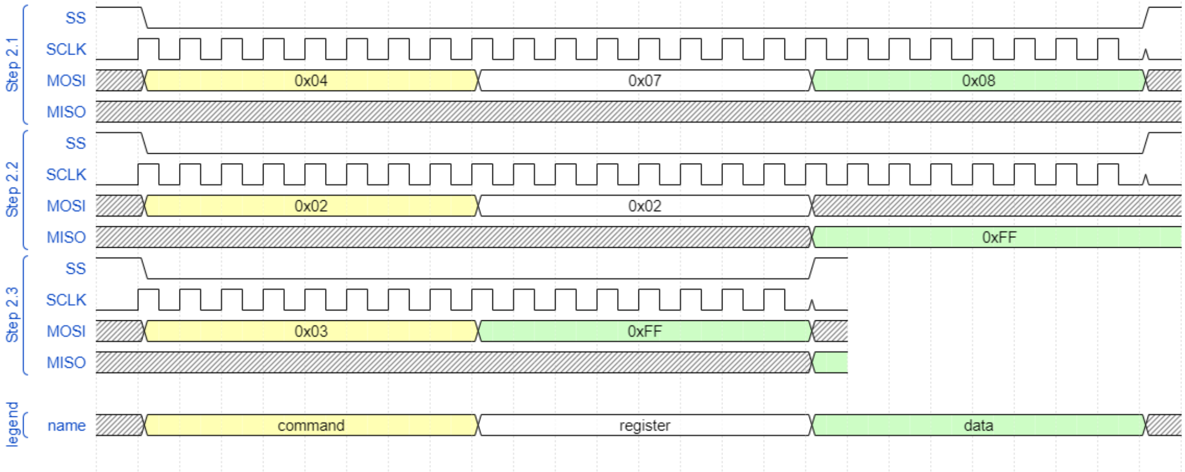

Figure 15 – Example 2 chronograph

Example 3: Configuration reading

This example demonstrate how to read the complete set of parameters used during a particular measure (here the measure with the ID equal to 4).

- **Step 3.1: Check if the device is not running (optional)**

  ```
  0x02 0x0C
  ```

  This command reads the register 0x0C, meaning the running status register (see 4.6). Here we are excepting 0x00 as an answer, as it indicated that the device is ready to receive others commands.

- **Step 3.2: Change the measure ID**

  ```
  0x01 0x0E 0x04
  ```

  This command set the measure ID to 4, if a measure ID equal to 4 already exist then all the registers will be set to match the condition of the measure.

- **Step 3.3: Read the calibration ID (optional)**

```
0x02 0x0D
```

This command reads the calibration ID (of the measure 4).

- **Step 3.4: Read the calibration**

  ```
  0x02 0x04
  0x02 0x05
  0x02 0x06
  0x02 0x07
  0x02 0x08
  0x02 0x09
  0x02 0x0A
  0x02 0x0B
  ```

  Those commands reads the currents in the LEDs starting from LED 0 to LED 7 (see 4.6).

- **Step 3.5: Read the mode and the frequency**

  ```
  0x02 0x00
  ```

  This command read the mode and the frequency (see 4.6).

- **Step 3.6: Read the LEDs activation**

  ```
  0x04 0x01
  ```

  This command read the LEDs activation, meaning which LEDs where used during the measure (see 4.6).

Note : The steps 3.3 to 3.6 can be done in any order.

PI AND SNR METRICS FOR THE EVALUATION OF THE OPTIMAL LED-PHOTODIODE DISTANCE

Here are presented the PI and SNR metrics for the evaluation of the optimal LED-photodiode distance.

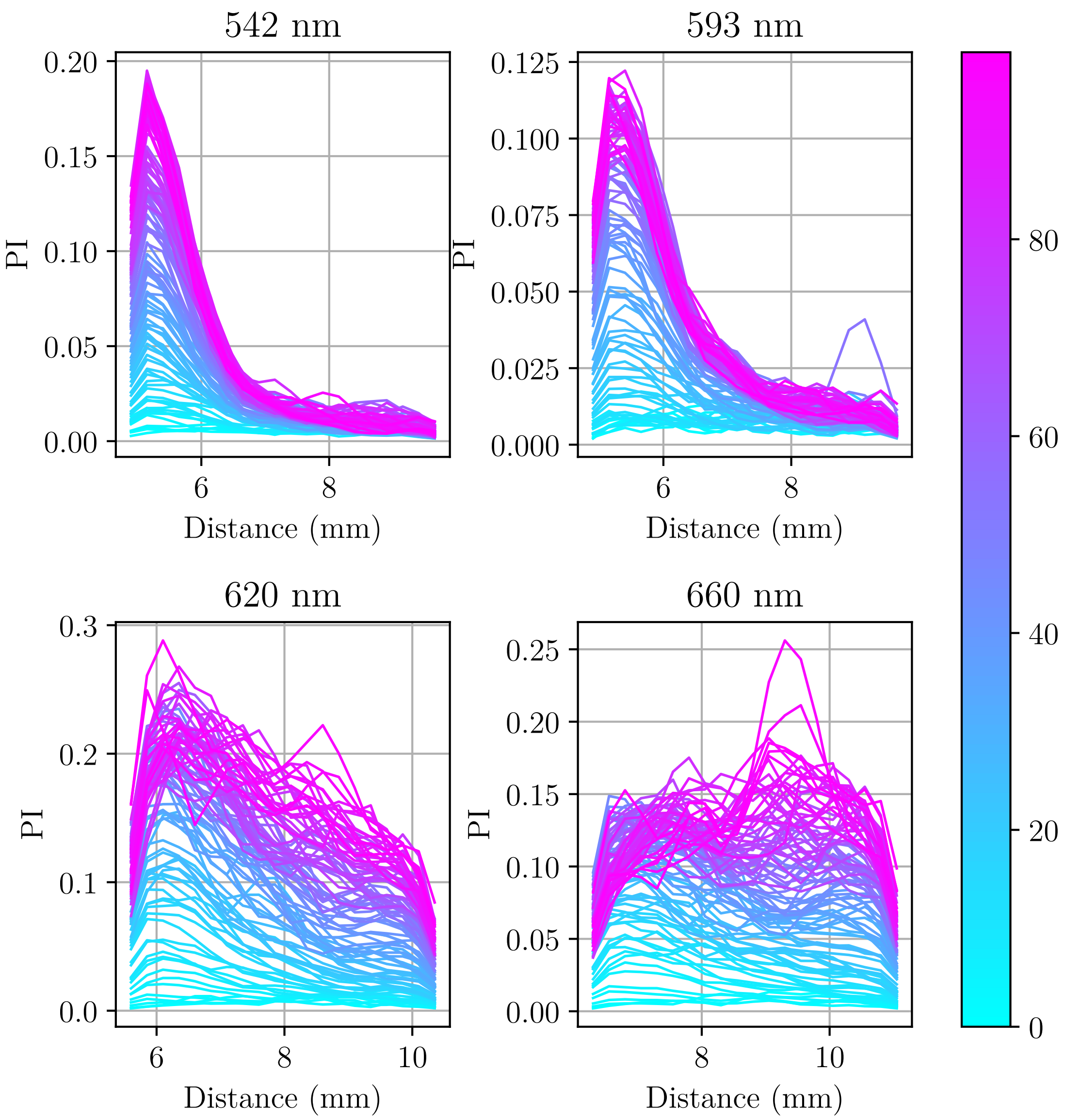

Figure 16 – PI for finger placement experiment for visible wavelengths.

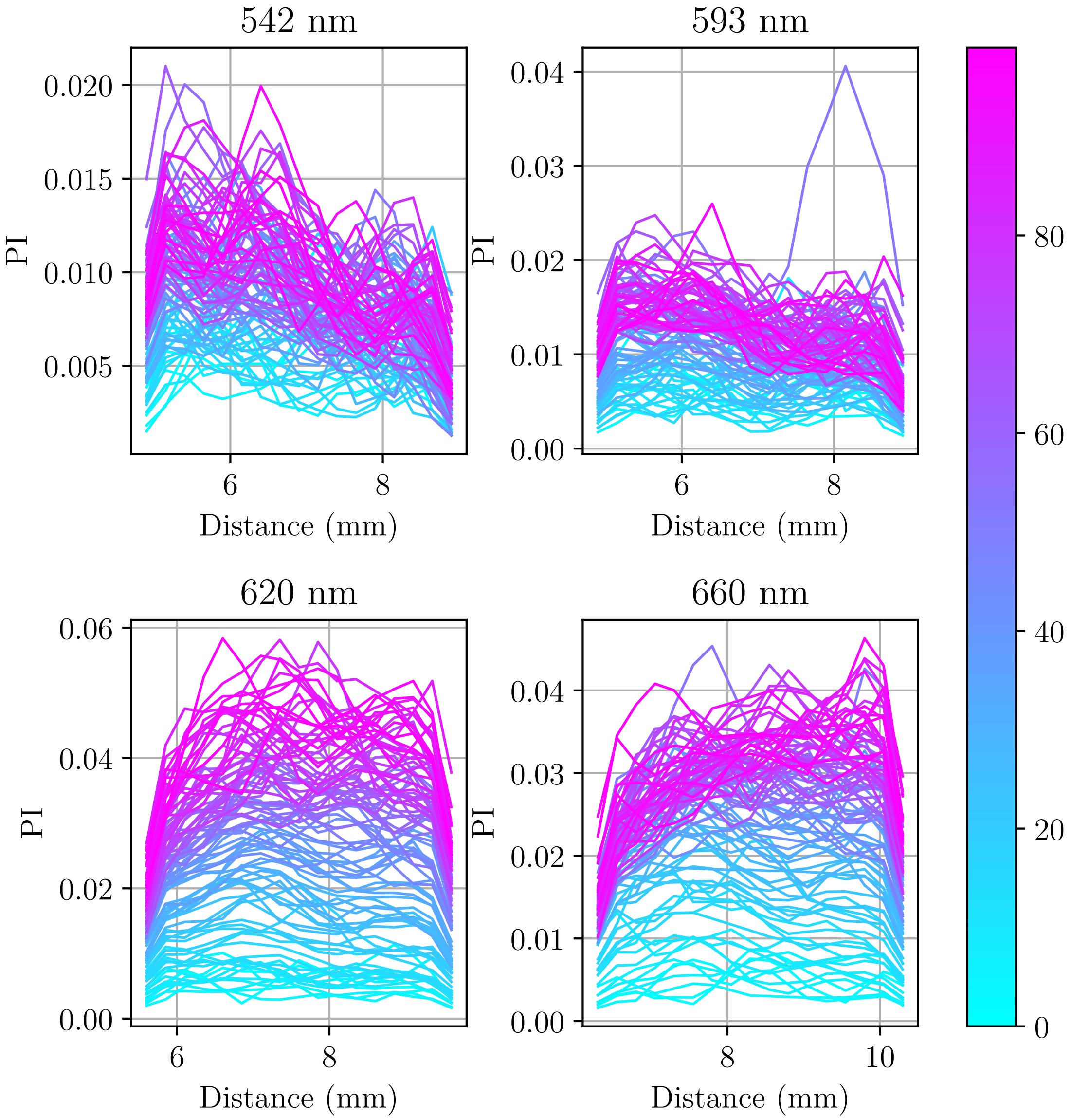

Figure 17 – PI for first upper arm placement experiment for visible wavelengths.

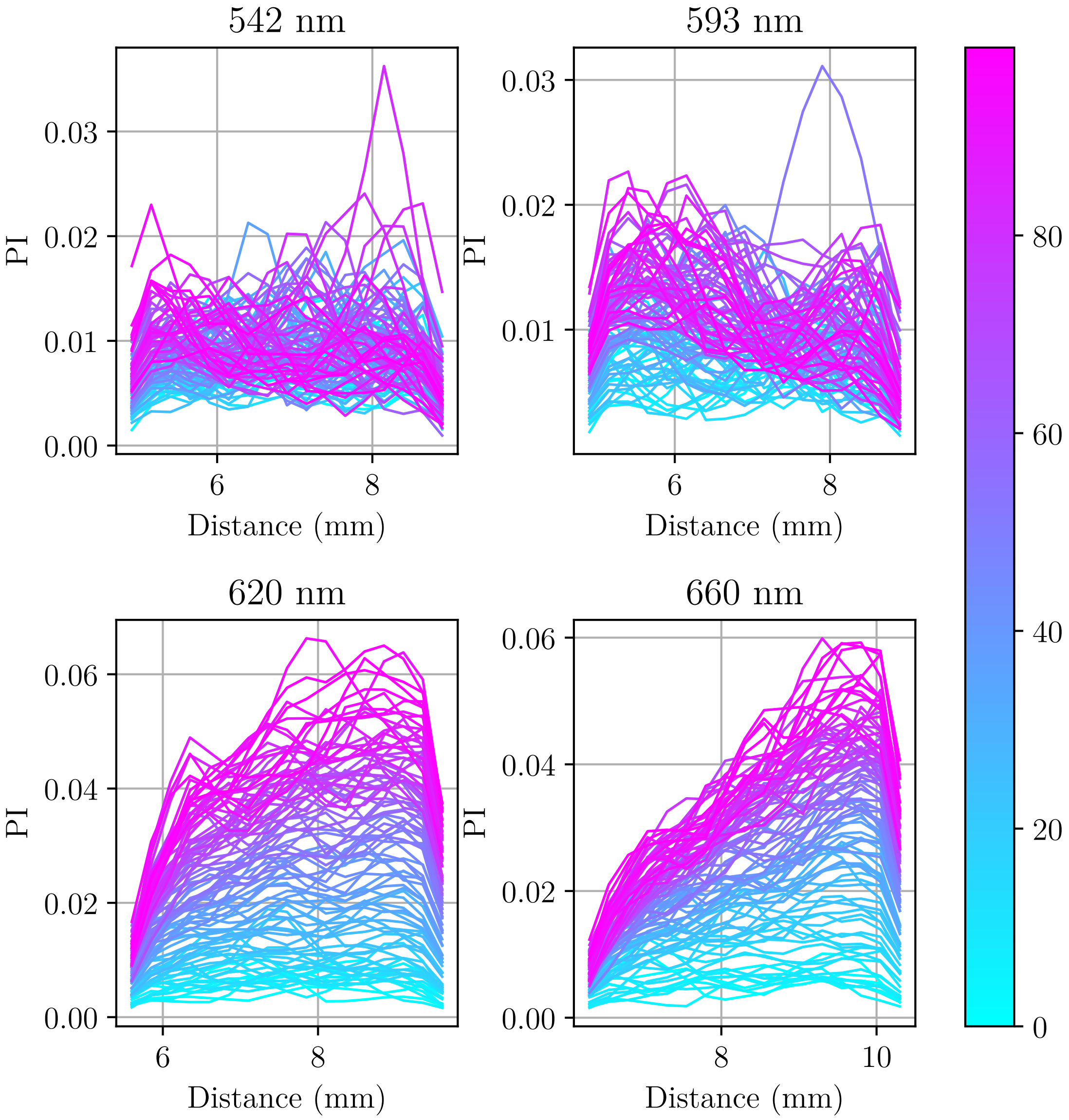

Figure 18 – PI for second upper arm placement experiment for visible wavelengths.

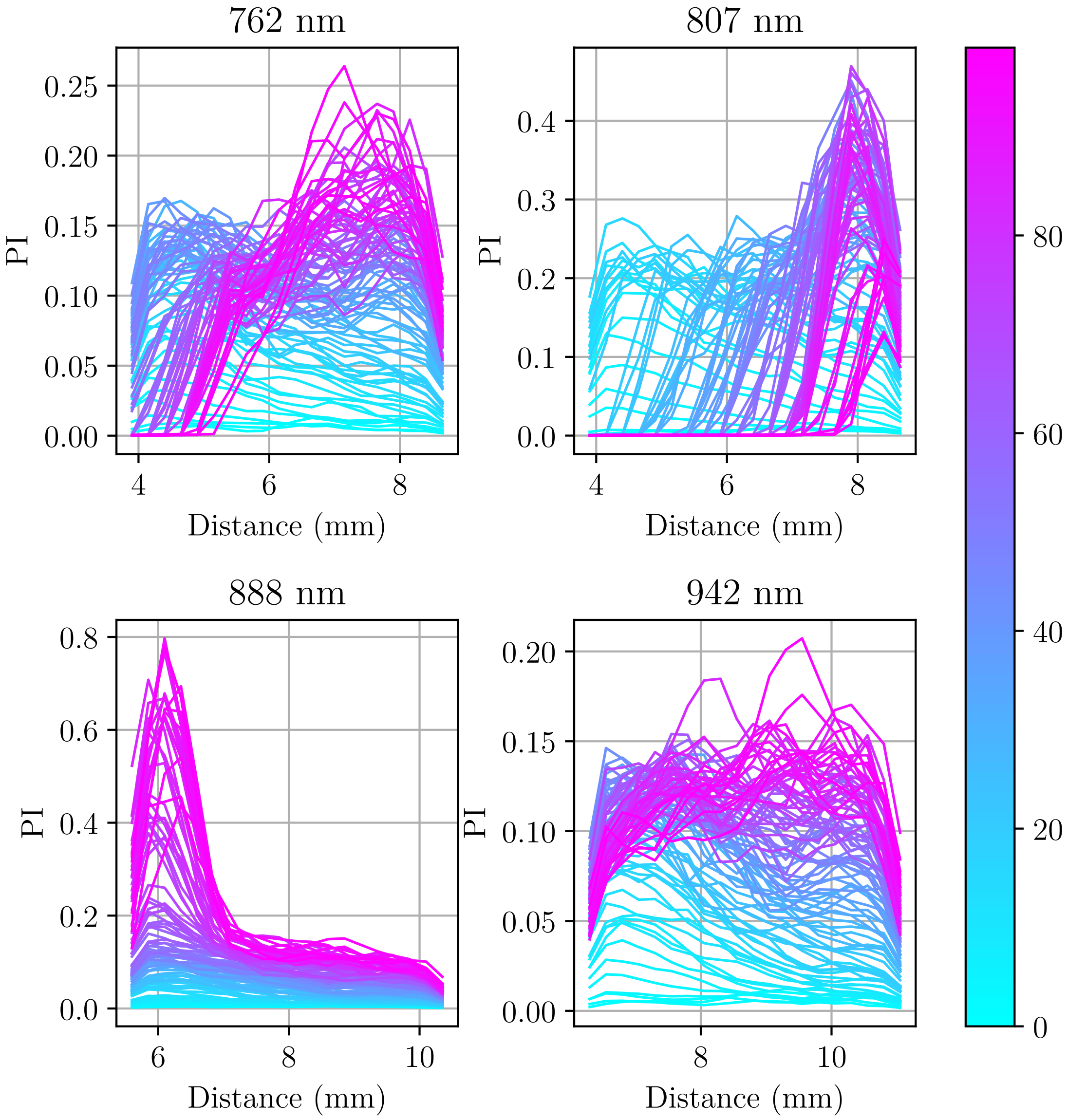

Figure 19 – PI for finger placement experiment for infrared wavelengths.

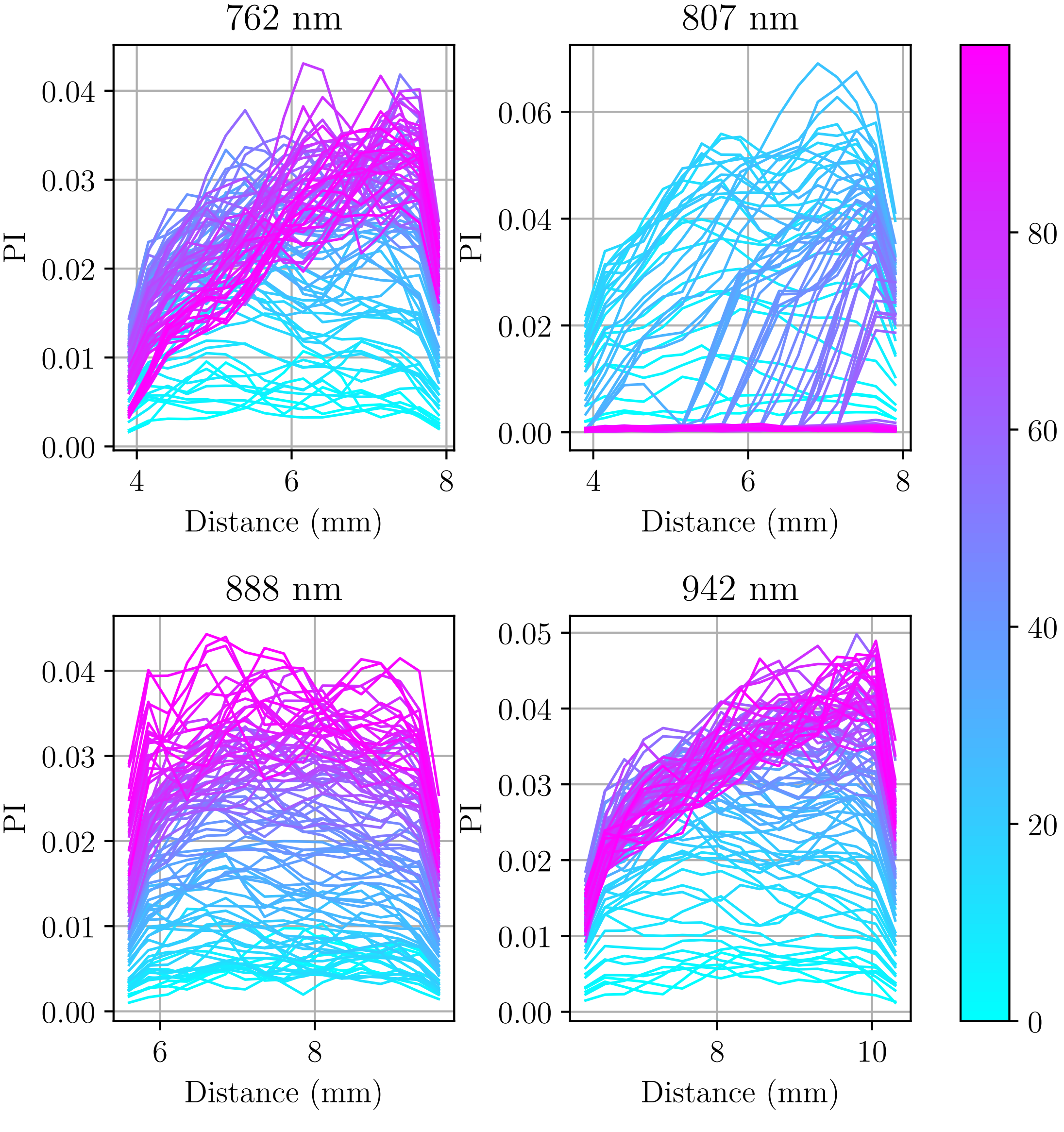

Figure 20 – PI for first upper arm placement experiment for infrared wavelengths.

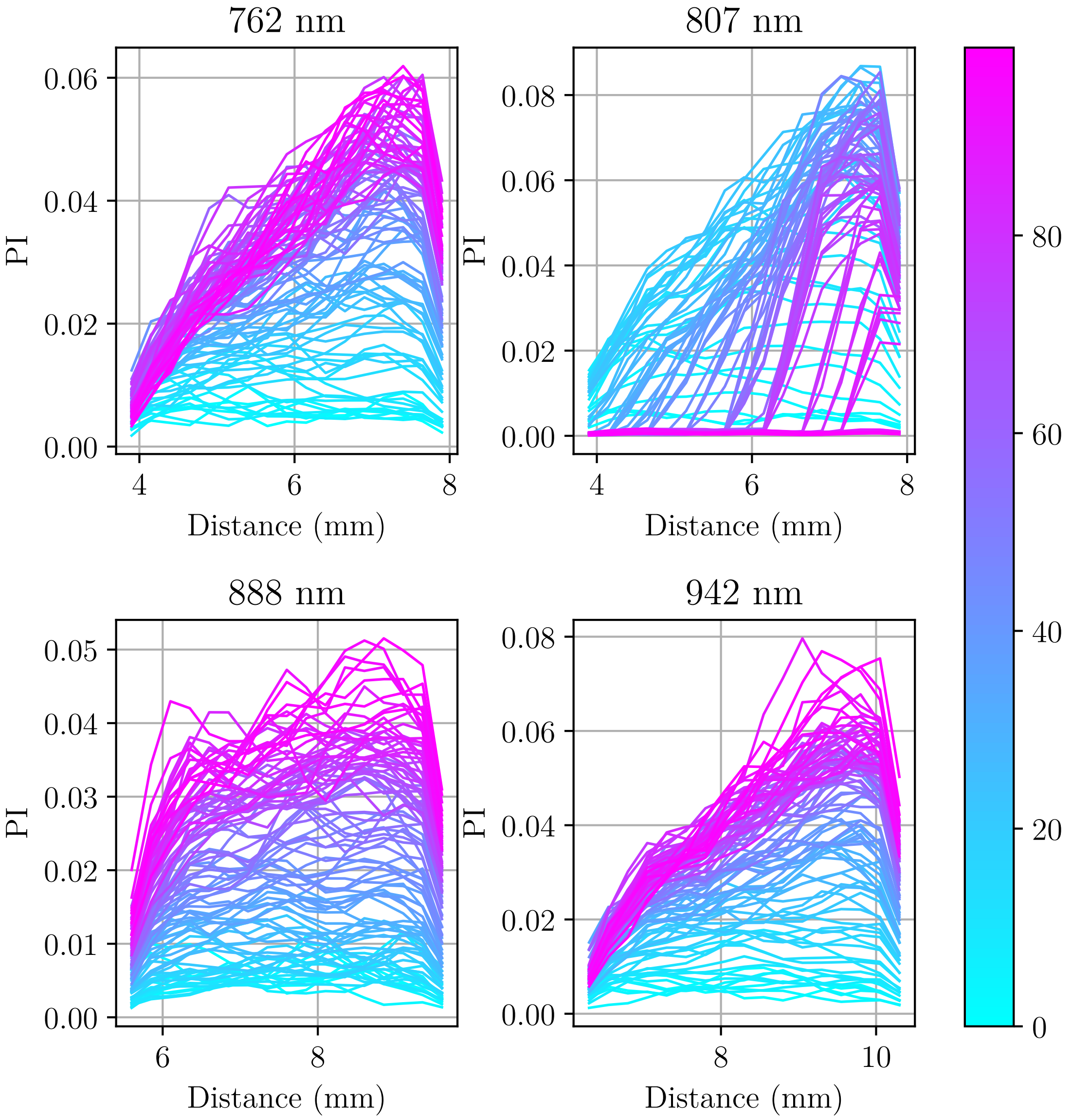

Figure 21 – PI for second upper arm placement experiment for infrared wavelengths.

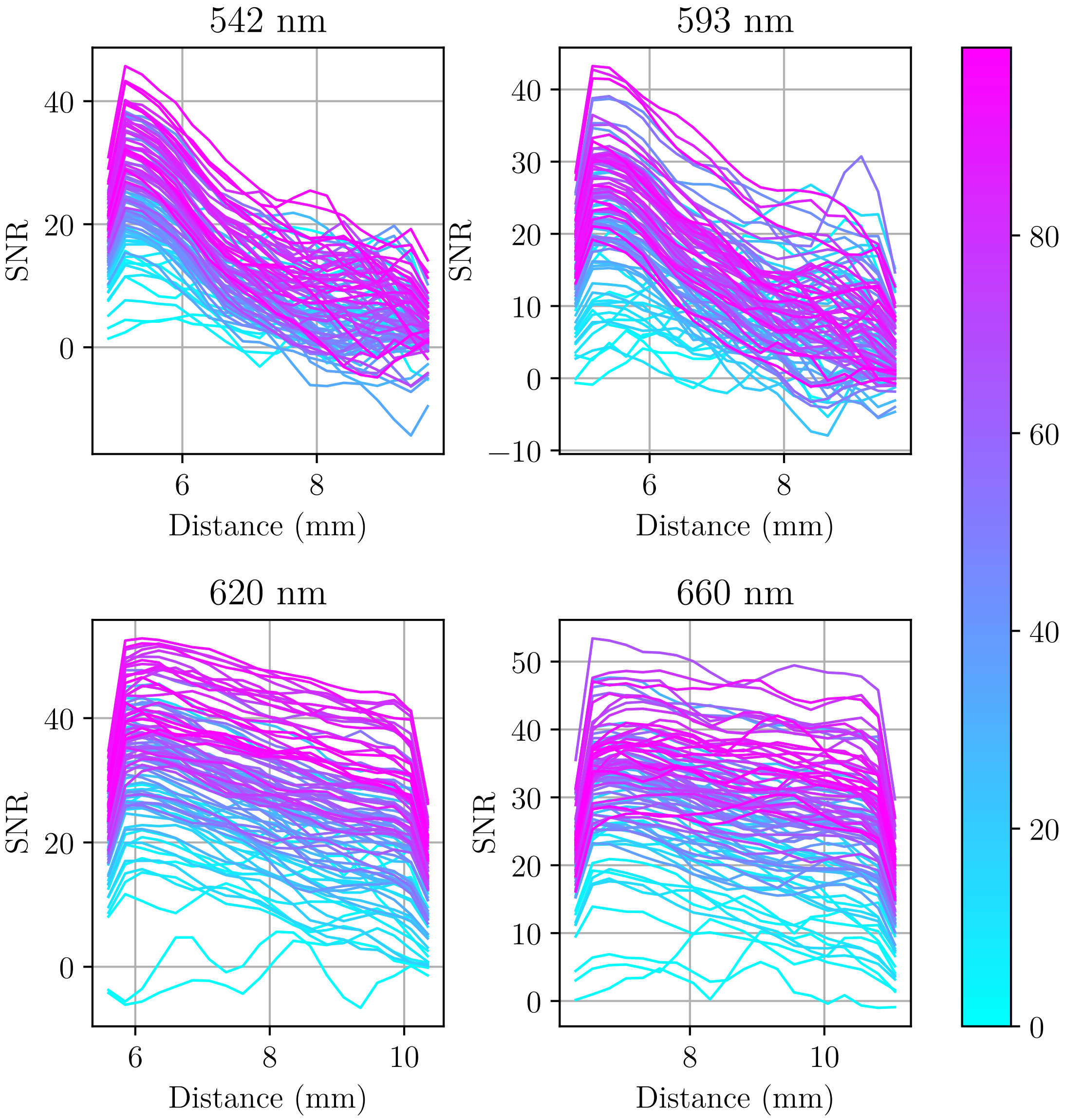

Figure 22 – SNR for finger placement experiment for visible wavelengths.

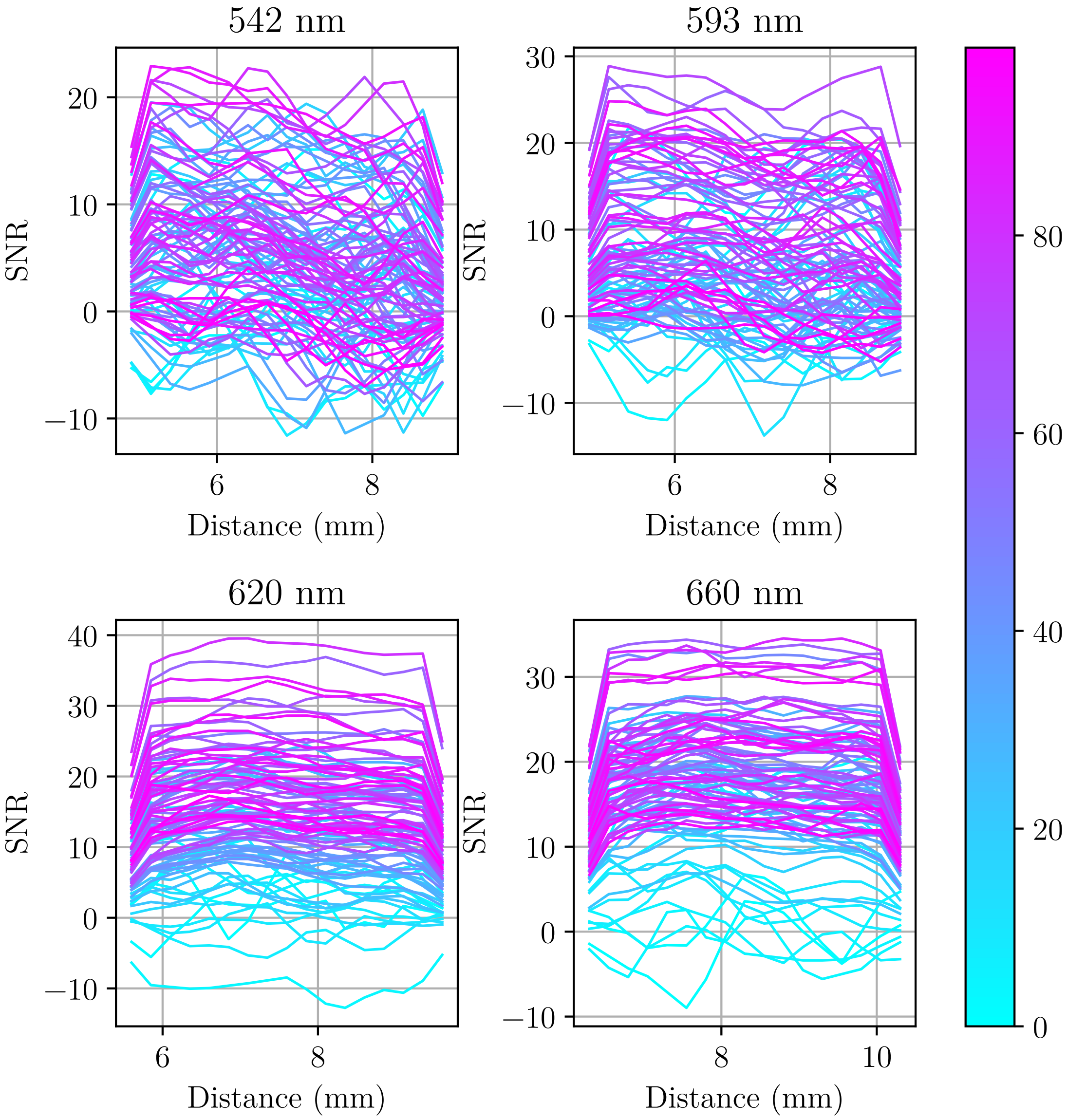

Figure 23 – SNR for first upper arm placement experiment for visible wavelengths.

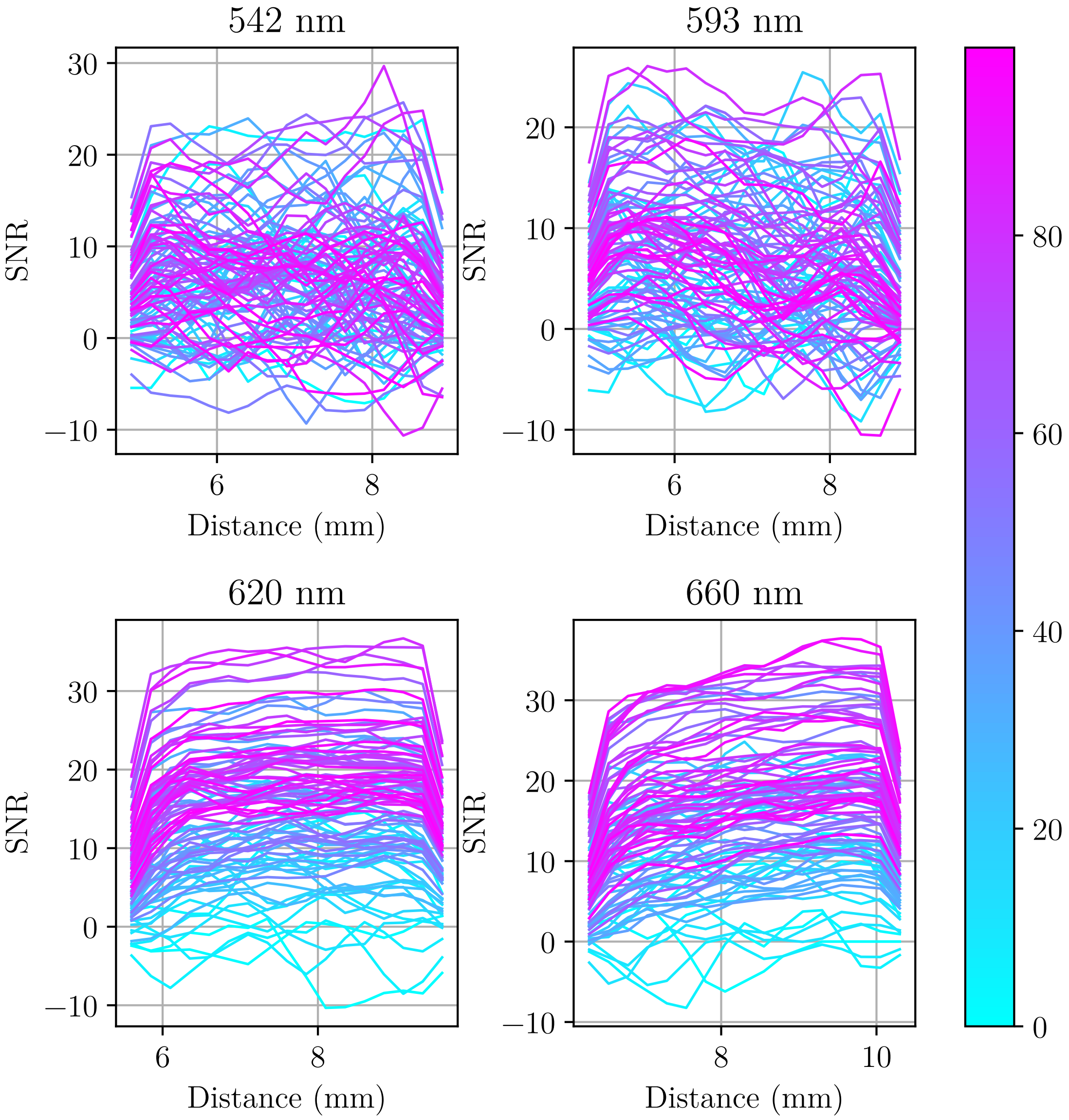

Figure 24 – SNR for second upper arm placement experiment for visible wavelengths.

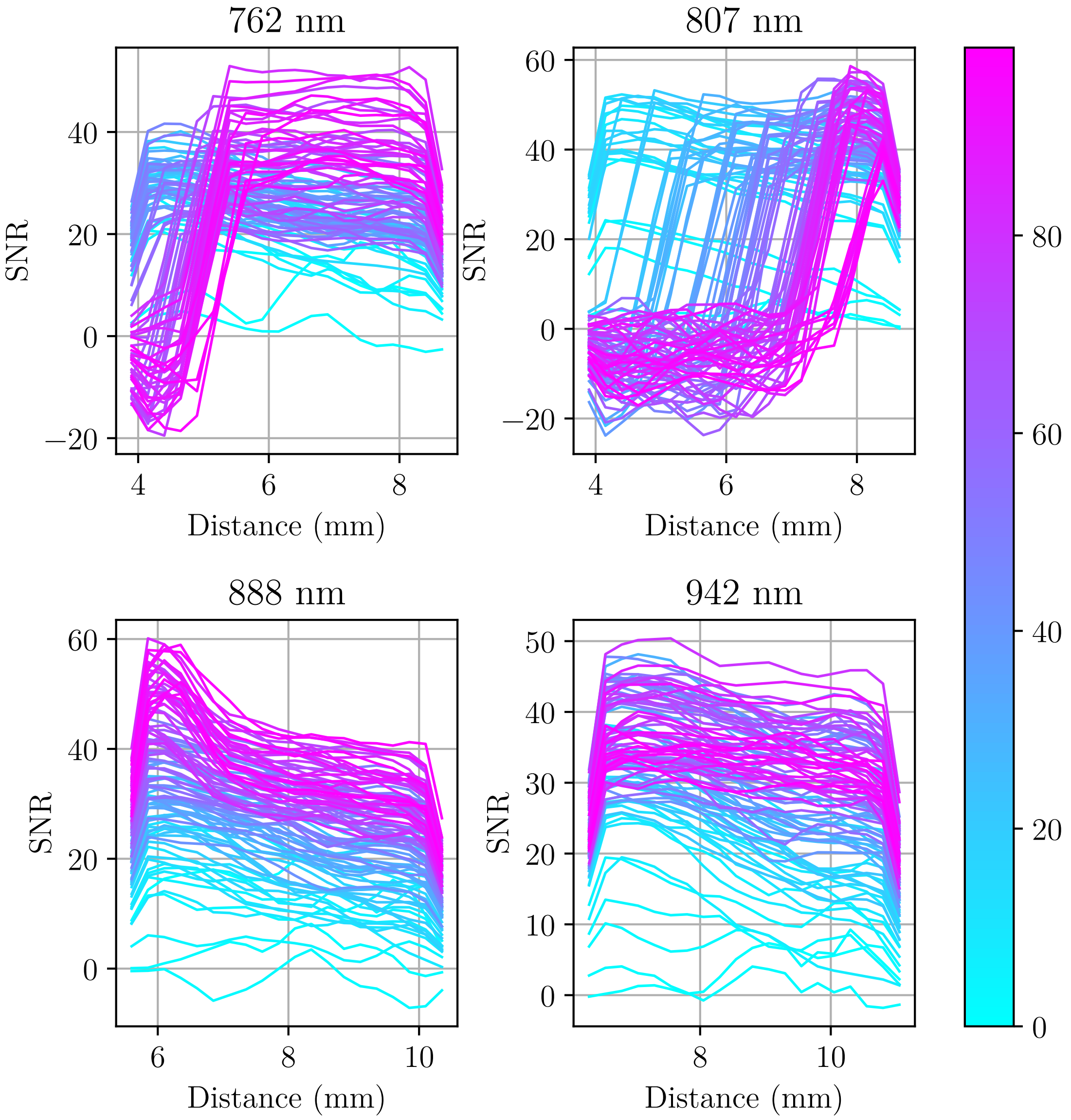

Figure 25 – SNR for finger placement experiment for infrared wavelengths.

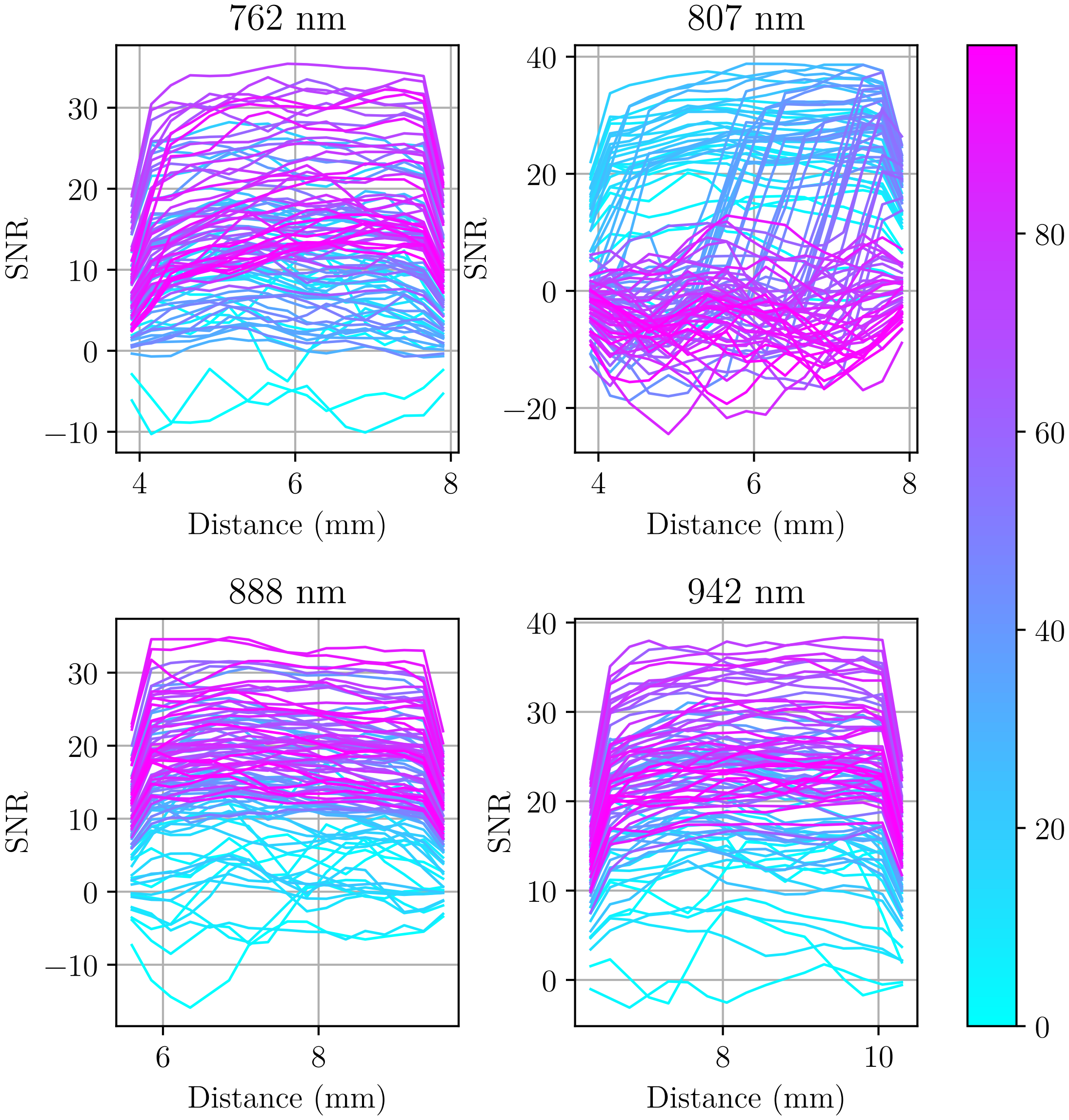

Figure 26 – SNR for first upper arm placement experiment for infrared wavelengths.

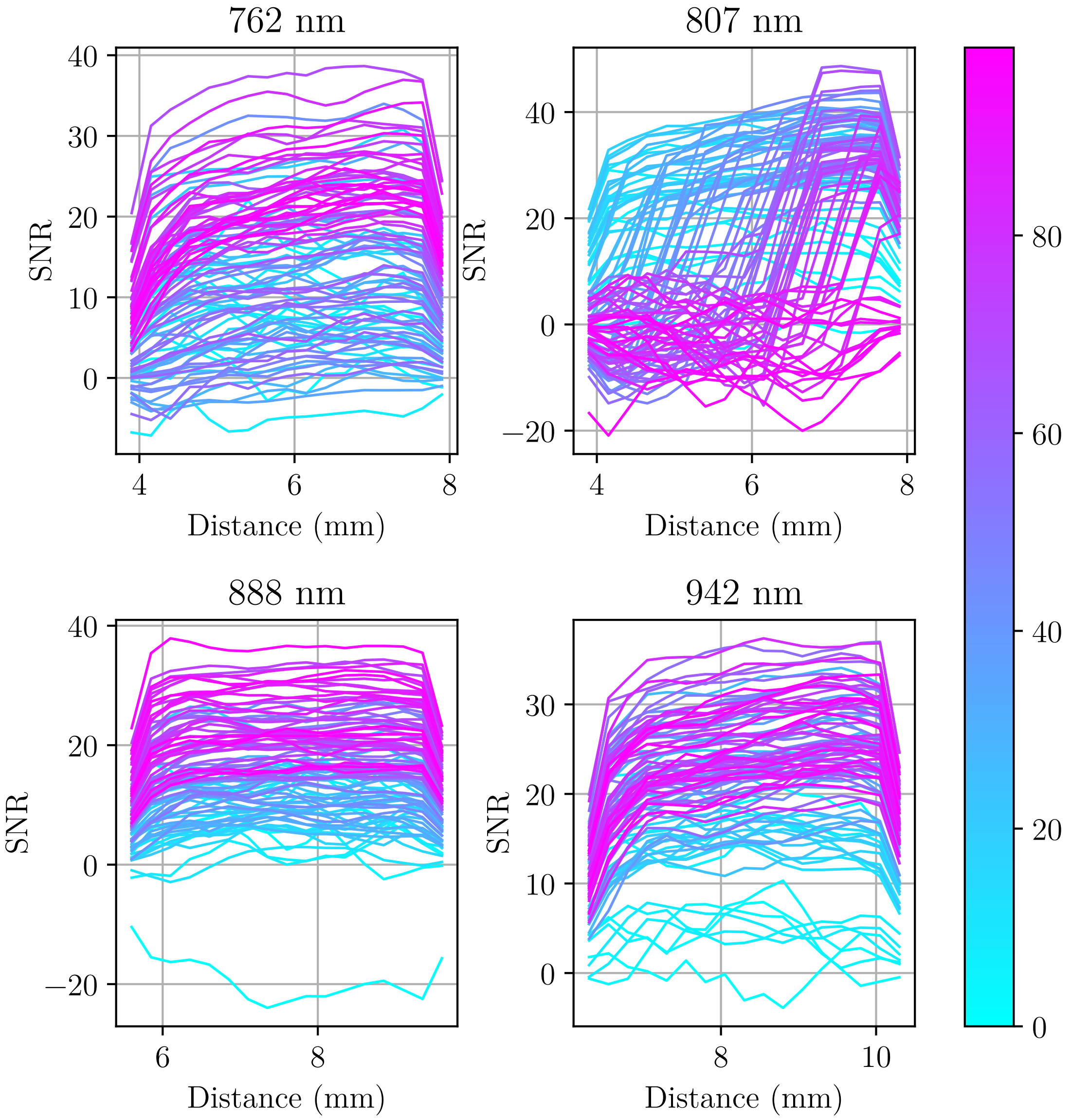

Figure 27 – SNR for second upper arm placement experiment for infrared wavelengths.

COLLEGE MATHS, TELECOMS
DOCTORAL INFORMATIQUE, SIGNAL
BRETAGNE SYSTEMES, ELECTRONIQUE

INSA INSTITUT NATIONAL
DES SCIENCES
APPLIQUÉES
RENNES

Titre : Photodétecteur avancé pour le suivi athlète

Mot clés : Photoplethysmography PPG Multi-wavelength Mixed Signal Heart Rate SpO2.

Résumé : L'intérêt croissant pour les applications de santé a fait de l'ingénierie biomédicale l'une des disciplines à la croissance la plus rapide de ces dernières années. PPG est l'une de ces tendances puisque les capteurs PPG sont intégrés dans de nombreux appareils tels que les smartwatches ou les oxymètres. En raison de sa polyvalence, PPG est la technique de choix pour la surveillance non invasive des signes vitaux tels que la fréquence cardiaque, la fréquence respiratoire, la saturation en oxygène du sang et la pression artérielle. Cependant, les oxymètres de pouls commerciaux utilisent souvent des techniques propriétaires d'acquisition et de visualisation des données, ce qui rend difficile, voire impossible, le traitement des signaux numériques sur les données brutes. Cet article présente une plateforme matérielle pour l'exploration de nouvelles analyses de signaux biologiques basées sur PPG. L'originalité de la plateforme est d'étendre le nombre de longueurs d'onde à 8 et de permettre le paramétrage de l'acquisition en choisissant la fréquence d'échantillonnage. Cela permet d'adapter le capteur PPG aux besoins d'analyse sur l'ensemble du signal ou d'effectuer des mesures de haute précision. L'acquisition de données précises lors d'activités sportives a fait l'objet d'une grande attention.

Title: Advanced photodetector for athlete monitoring

Keywords: Photoplethysmography PPG Multi-wavelength Mixed Signal Heart Rate SpO2.

Abstract: Growing interest in healthcare applications has made biomedical engineering one of the fastest growing disciplines in recent years. PPG is one of these trends since PPG sensors are embedded into many devices like smartwatches or oximeters. Due to the versatility of PPG, it is the technique of choice for the non-invasive monitoring of vital signs such as heart rate, respiratory rate, blood oxygen saturation and blood pressure. However, commercial pulse oximeters often use proprietary data acquisition and visualization techniques, making digital signal processing on raw data difficult or impossible. This paper presents a hardware platform for the exploration of new biological signal analysis based on PPG. The originality of the platform is to expand the number of wavelengths to 8 and to allow the parameterization of the acquisition by choosing the sample rate. This allows the PPG sensor to be adapted to the needs of analysis on the whole signal or perform high precision measurements. Much consideration has been given to the accurate data acquisition during sports activities.